

CHARACTERIZATION OF COAL SULFUR FUNCTIONAL FORMS
BY PROGRAMMED-TEMPERATURE OXIDATION

R. B. LaCount, D. G. Kern, W. P. King, T. K. Trulli, D. K. Walker*

ViRoLac Industries, Waynesburg, PA 15370

and

Dept. of Chem., Waynesburg College, Waynesburg, PA 15370.

* Dept. of Computer Science, Marshall University, Huntington, WV 25755

Keywords: coal analysis, sulfur, oxidation

ABSTRACT

This paper describes the current status for characterization of coal by using a multiple sample controlled-atmosphere programmed-temperature oxidation (CAPTO_m) instrument. Distinctive gas evolution patterns are observed among coals of different rank and between raw and treated coals. In addition to resolved SO₂ peaks, assignable to the oxidation of pyrite and the decomposition of sulfate, two others, assignable to organic structures in the coals, are observed. Coals from the Argonne Premium Coal Sample Program have been characterized by this technique.

INTRODUCTION

Interest continues to be strong in methods to reduce the levels of SO₂ and NO_x in the atmosphere as a route to reduce acid deposition. This interest intensified development of advanced coal cleaning technologies which, in turn, generated a need for suitable analytical techniques to monitor progress of the work. A number of these analytical techniques, including CAPTO were reviewed in a previous report¹. This work utilized a CAPTO instrument designed to characterize multiple coal samples in either an oxidative or pyrolysis mode. The instrument has been used in an oxidative mode to characterize the sulfur functional forms for the Argonne Premium Coal Samples.

EXPERIMENTAL

The CAPTO technique is used to characterize coals, treated coals, and other high molecular weight substances reduced to a particle top size of -60 mesh, or smaller. For oxidative characterization, the sample is thoroughly dispersed in a diluent (to reduce exotherms that occur during oxidation), inserted near the center of a quartz tube and positioned in a horizontal "primary" furnace. The sample is exposed simultaneously to a linear increase in temperature (normally 3°C/min) up to 1000°C and to a mass flow controlled oxygen stream of 100 mL/min. The gases flow through a catalytic "secondary" furnace held at 1050°C and through a heated transfer line for analysis using a Fourier Transform Infrared (FTIR) spectrometer equipped with multiple gas cells. The system shown in Figure 1 is designed to characterize four samples simultaneously. A single sample system has been previously described¹.

Using the multiple sample CAPTO instrument in oxidative mode, characterization of the sulfur functionality was completed for the eight coals available from the Argonne Premium Coal Sample Program.

DISCUSSION

The distinctive gas evolution patterns observed among coals of different rank and between raw and treated coals have been related to the structural entity producing each peak^{1,2}. The SO₂ evolution peaks obtained from oxidation of coal pyrite and decomposition of sulfate are resolved and appear at temperatures distinct from those observed from combustion of the organic

structures in coal¹. Two major SO₂ evolution maxima resulting from organic structures are observed. Each of these peaks has CO₂ and H₂O associated with it, implying that the organic matrix is oxidized in stages. Using model systems for comparison, these two major evolution maxima have been related to the probable structural types producing the evolutions. The temperatures observed for the evolution maxima are sensitive to the experimental conditions¹.

Previous ¹³C CP-MAS n.m.r. work² was completed on coal samples both before and after a CAPTO experiment that was terminated at 400°C. The n.m.r. spectra prior to the experiment indicated the presence of both aromatic and non-aromatic structures ($f_a = 0.69$). After the sample was exposed to CAPTO conditions up to 400°C, the spectra revealed an essentially unchanged aromatic region; however, the non-aromatic region had been almost totally eliminated ($f_a = 0.87$). Thus, the lower temperature CO₂ and SO₂ evolutions resulting from organic structures were attributed to carbon and sulfur lost primarily from oxidation of non-aromatic coal structures. The CO₂ and SO₂ evolutions from organic structures above 400°C were attributed primarily to carbon and sulfur lost during oxidation of the aromatic coal matrix. We still believe this to be a generally valid premise, and it is supported by the H/C ratio of 0.7 observed for the evolved gas at 400°C². As also noted in the earlier work, stable aryl sulfides and sulfones oxidize above 400°C and should be included along with thiophenic structures in what we term "aromatic" sulfur.

The Argonne Premium Coal Sample Program coals were characterized using the multiple sample CAPTO instrument. One example, the absorbance/temperature CAPTO profiles for the Illinois No. 6 Argonne Premium Coal Sample is shown in Figure 2. The SO₂ evolution profile shows a peak at 274°C produced from oxidation of non-aromatic organic sulfur structures and a peak at 404 °C from the aromatic organic sulfur structures. The peaks at 439°C and 469°C are both derived from oxidation of pyrites and the small evolution at 580°C is produced from decomposition of iron sulfate. The CO₂ and H₂O evolution profiles are also monitored and shown in Figure 2. Each profile shows a major peak related to oxidation of non-aromatic organic structures and aromatic organic structures. The ratio of non-aromatic/aromatic carbon or hydrogen is readily available from these profiles in addition to a continuous plot of the H/C ratio.

The relative areas of non-aromatic organic, aromatic organic, pyritic, and sulfate sulfur from the CAPTO evolution profiles were related to the ASTM total sulfur values of the Argonne coals for a comparison of sulfur forms. The preliminary results are shown in Table 1. As noted in Table 1 the Wyodak-Anderson and Beulah-Zap coals produced an additional SO₂ peak in the temperature range where SO₂ evolution from decomposition of several inorganic sulfates³ is observed.

CONCLUSIONS

Quantitative studies are in progress to evaluate the CAPTO technique as a one-step determination of the organic, inorganic, and total sulfur present in coals and treated coals. The multiple sample CAPTO instrument has been used to characterize the sulfur forms of the Argonne Premium Coal Samples and the preliminary results are reported.

ACKNOWLEDGEMENTS

This work has been supported in part by Department of Energy SBIR Phase II Grant No. DE-FG01-90ER81055 and in part by the Ben Franklin Technology Center of Western Pennsylvania through Pennsylvania's Ben Franklin Partnership Program. The authors wish to thank the Pittsburgh Energy Technology Center (PETC) and specifically Sidney Friedman, Robert Warzinski, and Bernard Blaustein for their interest and support in the early phases of the work. The authors also thank Waynesburg College for its cooperation and support.

We are grateful to Dr. Karl S. Vorres for providing the Argonne National Laboratory Premium Coal Samples. We also wish to acknowledge the efforts of K. D. Robertson and T. J. Schroyer toward development of the multiple sample CAPTO instrument.

REFERENCES

1. LaCount, R. B., Kern, D. G., King, W. P., LaCount, R. B. Jr., Miltz, D. J. Jr., Stewart, A. L., Trulli, T. K., Walker, D. K., Wicker, R. K., "Advances in Coal Characterization by Programmed-Temperature Oxidation", Prepr. Pap. - Am. Chem. Soc., Div. Fuel Chem. 1991, 33(3), 1217.
2. LaCount, R. B., Anderson, R. R., Friedman, S., Blaustein, B. D., "Sulfur in Coal by Programmed - Temperature Oxidation", Fuel, 66, 909 (1987).
3. LaCount, R. B., Gapen, D. K., Dell, David A., Simpson, F. W., Helms, Charles A., "Thermal Oxidative Degradation of Coal as a Route to Sulfur Functionality: An Initial Study", New Approaches in Coal Chemistry, eds., B. D. Blaustein, B. C. Bockrath, S. Friedman, A.C.S. Symposium Series, 169, 415 (1981).

Table 1

DETERMINATION OF SULFUR FORMS OF THE ARGONNE PREMIUM COALS
RELATIVE TO ASTM TOTAL SULFUR (mf basis)

Argonne Premium Coal Sample	Wt% Total Sulfur	% Pyrite	% Non-Aromatic	% Aromatic	% Sulfate
Pocahontas #3, VA	0.66	0.09	0.13	0.44	nd.
Upper Freeport, PA	2.32	1.64	0.25	0.43	<0.01
Pittsburgh #8, PA	2.19	1.54	0.20	0.43	0.02
Lewis.-Stock., WV	0.71	0.26	0.08	0.37	nd.
Blind Canyon, UT	0.62	0.29	0.10	0.23	nd.
Illinois #6, IL	4.83	2.65	0.56	1.62	<0.01
Wyodak-Anders., WY*	0.63	0.19	0.11	0.15	0.02
Beulah-Zap, ND**	0.80	0.25	0.27	0.16	nd.

* 0.16% Sulfur evolved at 832°C.

** 0.12% Sulfur evolved at 756°C.

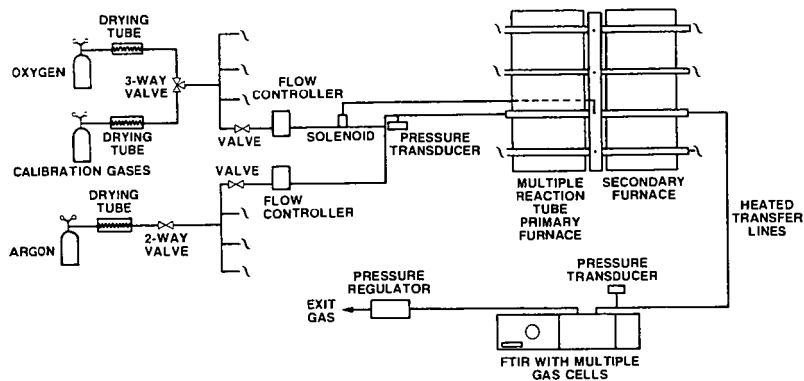


Figure 1. Flow system for the multiple sample controlled-atmosphere programmed-temperature oxidation (CAPTO) instrument.

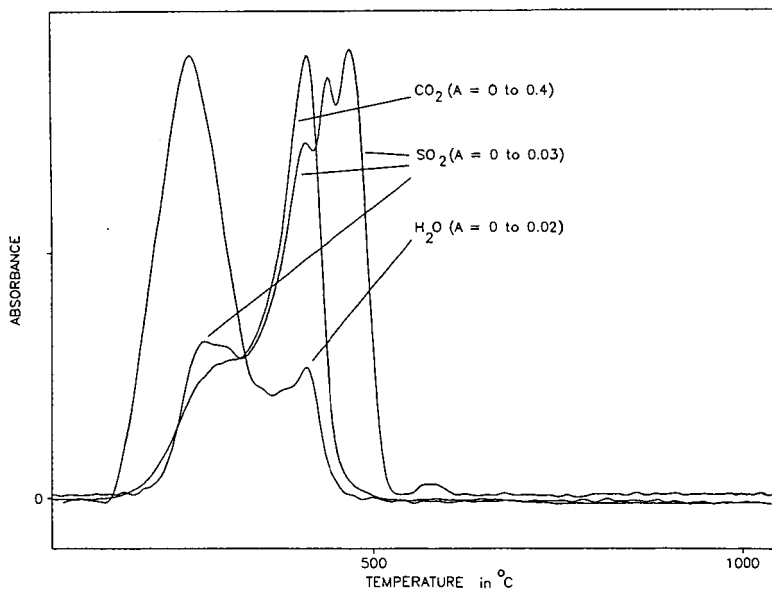


Figure 2. CAPTO evolution profiles from the Illinois No. 6 Argonne Premium Coal Sample.

DETECTION OF ORGANIC SULFUR BY ^{15}N AND ^{19}F NMR VIA FORMATION OF IMINOSULFURANES

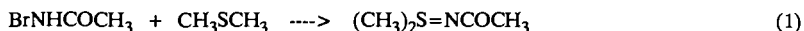
James A. Franz, John C. Linehan and Claude N. Lamb

Pacific Northwest Laboratory
Battelle Memorial Institute
P. O. Box 999
Richland, Washington 99352

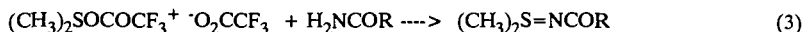
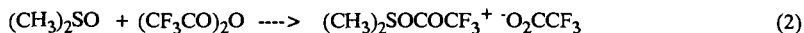
INTRODUCTION

Determination of the forms of organic sulfur in coal remains a topic of wide interest in coal science. Recent efforts to characterize organic sulfur include analysis by XANES (1-3), pyrolytic methods (4-7), mass spectrometric analysis of coal extracts (8), and preparation of ^{13}C -labelled sulfonium salts from organic sulfides (9). Direct observation of the ^{33}S nucleus by NMR is unsatisfactory, due to low natural abundance, poor receptivity, and unfavorable quadrupolar relaxation properties. ^{13}C NMR is of limited utility for the indirect analysis of sulfur, since ^{13}C chemical shifts for carbons with sulfur substituents are similar to those of carbons with carbon substituents. The aim of the present study is to develop NMR methods for characterization of organic sulfur functional groups which do not suffer from the ambiguities of pyrolytic and hydrolytic methods. Thus, we have examined the potential for spectroscopic discrimination of categories of organic substituents at sulfur by conversion of organic sulfides to iminosulfuranes, $\text{R}_2\text{S}=\text{NR}$, for analysis by ^{15}N NMR spectroscopy (10). In this paper, we present results of measurement of ^{15}N chemical shifts for various alkyl and aryl substituents at sulfur. We discuss a second approach under study, the attachment of ^{19}F labels to groups attached to sulfur, with *chemical* selectivity providing the basis for structural discrimination.

Iminosulfuranes have been prepared from the reaction of N-haloamides with dialkyl sulfides (eq 1) (11). The reaction is selective for dialkyl sulfides: diaryl sulfides and aryl alkyl sulfides are unreactive.

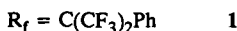


Iminosulfuranes have been prepared by the reaction of sulfoxides with trifluoroacetic anhydride or oxalyl chloride (eqs 2-3) (12). The intermediate sulfonium salt formed in eq. 2 can be trapped at low temperature (-60°C) with an appropriate amide to form the iminosulfurane (eq 3). At temperatures above -30°C , the intermediate undergoes the Pummerer rearrangement (eq 4).

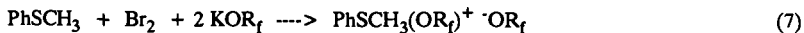




Finally, diaryl sulfides can be converted to diaryldialkoxysulfuranes ($\text{R}_f = \text{C}(\text{CF}_3)_2\text{Ph}$) by reaction with bromine or chlorine and a suitable alkoxide in dry aprotic solvents (ether, tetrahydrofuran, CCl_4). The diaryldialkoxo sulfuranes, e.g., **1**, can be isolated or easily prepared *in situ* for reaction with a wide variety of amides and amines to form iminosulfuranes (eq 6) (13). The acidic alcohol R_fOH is conveniently removed by basic aqueous extraction. The main requirements for application of this reaction in a coal product environment are (1) the absence of water, which hydrolyzes sulfuranes to sulfoxides, and (2) phenolic OH groups and other active hydrogen-containing groups must be alkylated to prevent oxidation.



In this paper, we examine the possibility of discriminating between diaryl sulfides and alkyl sulfides by converting diaryl sulfides to iminosulfuranes, while arylalkyl sulfides are selectively converted to the Pummerer rearrangement product under the same reaction conditions. Sulfonium salts formed from arylalkyl sulfides (eq 7) do not form iminosulfuranes when the R_fO^- anion is present (eq 8), but rather undergo efficient Pummerer rearrangement (eq. 9). In this paper, we extend recent work which



determined ^{15}N chemical shifts for simple diaryl and dialkyl iminosulfuranes to include the dibenzothiophene structure, and we demonstrate introduction of ^{19}F and ^{15}N labels in iminosulfuranes prepared from diphenyl sulfide and dibenzothiophene. We examine reaction of a mixture of sulfides leading to selective iminosulfurane formation from a diaryl sulfide and Pummerer rearrangement from an arylalkyl sulfide. These reactions provide a strategy for *chemical* discrimination between dibenzothiophene, simple diaryl sulfides, aryl alkyl sulfides, and dialkyl sulfides.

EXPERIMENTAL

Preparation of Dibenzothiophene-N-(2,2,2-trifluoroacetyl) Iminosulfurane. The following is a representative procedure for preparation of iminosulfuranes. 2,2,2-Trifluoroacetamide (Aldrich) was dissolved in ether and decanted from an insoluble component.

The alkoxide $K^+ \cdot OC(CF_3)_2Ph$ (KOR_f) was prepared by heating R_fOH (1 eq.) and aqueous KOH (0.95 eq) at 100 °C and 10^{-2} Torr in a round bottom flask equipped with a vacuum adapter, with two interruptions to grind the white alkoxide cake to powder, following published procedures (13,14). The apparatus, reagents and solvents were rigorously dried. However, the white alkoxide powder can be quickly (less than 3-4 minutes) transferred in the open air for weighing into reaction flasks without appreciable yield losses. Similarly, solvents and reagents were quickly transferred to the oven-dried reaction flask through the air, followed by nitrogen purge of the reaction medium. Thus, dibenzothiophene (1.5 g, 8.15 mmol), and KOR_f (4.6g, 16.3 mmol) were dissolved in ca. 60 mL of dry tetrahydrofuran (Aldrich, stored over type 3A molecular sieves) in a 3-neck 100 mL round bottom flask equipped with two serum caps and a vacuum adapter. Chlorine (0.35 mL at -78°C, 8.1 mmol), was condensed in a calibrated trap and swept into the solution in a nitrogen stream via syringe needle. (When bromine was substituted for chlorine, no iminosulfurane was formed from dibenzothiophene in reactions using ether, CCl_4 , or THF solvents.) The reaction mixture was stirred for 5 min. A THF solution of 2,2,2-trifluoroacetamide (0.92 g, 8.1 mmol) was added, and the solution was warmed to room temperature. THF was removed by rotary evaporation, and methylene chloride, 80 mL, was added. After extraction with 10% aq. KOH twice to remove acidic R_fOH , and once with water, the CH_2Cl_2 solution was dried over anhydrous $MgSO_4$ and concentrated to give crystalline product, 2.2 g (90% yield). The iminosulfurane was sparingly soluble in diethyl ether. Recrystallization from ether gave fine needles, mp 215-217°C, 1.8 g. ^{13}C NMR (75 MHz, $CDCl_3$, ppm using $CDCl_3$ center line at 77 ppm): 168.9 (quartet, $J_{CF}=35.8$ Hz), 138.6, 135.6, 133.4, 130.4, 129.0, 122.7, 117.1 (quartet, $J_{CF}=288$ Hz). ^{19}F NMR (282 MHz), singlet at -73.5 ppm from $CFCl_3$. 1H NMR (300 MHz, $CDCl_3$, ppm from TMS), 8.15 ppm (2H, d, $J=7.9$ Hz), 7.92 (2H, d, $J=7.7$ Hz), 7.71 (2H, d of t, $J=7.6, 0.9$) 7.57 (2H, d of t, $J=0.9, 7.9$ Hz).

Preparation of Other Iminosulfuranes. ^{15}N -Acetamide (Cambridge Isotope Laboratories) was recrystallized from $CHCl_3$ -ether for preparation of ^{15}N -acetyl iminosulfuranes. S,S-Diphenyl-N-(2,2,2-trifluoroacetyl) iminosulfurane (mp 88.5-89.5 °C), dibenzothiophene- ^{15}N -acetyl iminosulfurane (mp 165-165.5° C), and S,S-diphenyl- ^{15}N -acetyl iminosulfurane (mp 94-95°C) (10) were also prepared by the method described above. Spectroscopic details will be published in detail elsewhere. Excellent crude yields of ca. 90% were achieved in all cases, with final isolated yields of pure product of typically greater than 75%. CCl_4 and diethyl ether can be substituted for THF. Unlike dibenzothiophene, diphenyl sulfide can be converted to iminosulfuranes using either bromine or chlorine. In general, iminosulfuranes can be recrystallized from ether/pentane (13).

Pummerer Rearrangement of Thioanisole. An ether solution of thioanisole was exposed to a 10% excess of Br_2 or Cl_2 at -78°C, followed by two equivalents of KOR_f in ether. ^{13}C NMR analysis revealed clean, quantitative conversion to the Pummerer rearrangement product, $PhSCH_2OC(CF_3)_2Ph$, isolated as a clear liquid after a workup similar to that of the iminosulfuranes. ^{13}C NMR, 75 MHz, $CDCl_3$, ppm using $CDCl_3$ centerline at 77.0 ppm, 133.8, 131.9, 130.3, 129.1, 128.8, 128.3, 128.0, 127.2, 122.3 (quartet, CF_3 , $J_{CF}=290$ Hz), 83.2 (heptet, $J_{CF}=28.5$ Hz), 72.2. ^{19}F NMR (282 MHz), singlet at

-71.2 ppm from internal CFCl_3 . The 70 eV mass spectrum gave a strong molecular ion at m/e 366 and fragments at 227, 207, 177, 123, 109, and 77.

Reaction of mixture of Diphenylsulfide and Thioanisole. An equimolar mixture of diphenylsulfide and thioanisole were treated with Cl_2 , KOR_p and excess H_2NCOCF_3 in dry THF at -78°C . After the standard workup, the reaction mixture was examined by ^{13}C and ^{19}F NMR. This revealed complete conversion of thioanisole to the Pummerer product, $\text{PhSCH}_2\text{OR}_p$ and 60% conversion of diphenylsulfide to the iminosulfurane.

Conversion of Diphenylsulfide to S,S-Diphenyl- ^{15}N -acetylminosulfurane in the Presence of Illinois No. 6 Methylated Asphaltenes. Argonne premium coal no. 301 was heated for 15 min at 435°C in tetralin (1 g coal/1.75 g tetralin) in a stainless steel tubing bomb. The products were extracted with THF. The THF solution was poured into excess hexane to precipitate asphaltenes and preasphaltenes. A sample of 0.8 g of the product in 30 mL THF was stirred overnight with 10 g $^{13}\text{CH}_3\text{I}$ and 1.9 g KOH in 2.5 mL water. THF was removed, and a CHCl_3 solution of the products was concentrated and thoroughly dried under vacuum at 100°C . ^{13}C NMR revealed 70% O-alkylation (50-70 ppm) and 30% C-alkylation (10-50 ppm). A mixture of 0.39 g methylated coal product, 1.8 g KOR_p , 0.49 g Ph_2S in 10 mL CCl_4 and 2 mL benzene were treated with 0.2 mL Br_2 . The reaction mixture warmed noticeably. The ^{15}N -labelled acetamide, 0.2 g, was added, the mixture was shaken for 30 min, and worked up in the standard way. Examination of a CDCl_3 solution of the products by ^{13}C and ^{15}N NMR, revealed ca. 70% conversion of Ph_2S to $\text{Ph}_2\text{S}=\text{NCOCH}_3$.

RESULTS AND DISCUSSION

Spectroscopic Discrimination of Sulfur Functional Groups. ^{15}N Chemical Shifts for N-acetylminosulfuranes. As shown in Table I, ^{15}N chemical shifts for S,S-dialkyl and S,S-diaryl N-acetylminosulfuranes span a narrow range of only ca. 10 ppm, with no separation of aryl from alkyl substituents, although changes in the nitrogen substituent lead to a chemical shift range of about 100 ppm on going from N-benzyl to N-aryl to the N-acetyl substituent. In this paper, we have added data for the dibenzothiophene structure to previously reported data (10). Overall, these data indicate that the substituent at sulfur exerts little effect on the ^{15}N chemical shift, and that no simple spectroscopic discrimination of sulfur substituents into aryl or alkyl substituents will be accomplished using ^{15}N NMR, at least for the N-acetyl substituent.

Chemical Discrimination of Sulfur Functional Groups. ^{19}F Chemical Shifts. Organic sulfides differ greatly in their reactivity to oxidizing reagents. Thus, a strategy for discrimination of sulfur functional groups using NMR spectroscopy uses chemical selectivity to attached spectroscopically distinct groups to different categories of organic sulfur. The ^{13}C and ^{19}F chemical shifts of the methyl and trifluoromethyl groups of N-acetyl and N-trifluoroacetyl iminosulfuranes are unaffected by changes in the sulfur substituents. As shown in Table I, the ^{19}F shifts of N-trifluoroacetyl groups attached to diphenyl sulfide or dibenzothiophene are nearly identical. Diaryl sulfides in a coal-derived mixture thus may be expected to yield iminosulfuranes which will appear closely

clustered at about -73.5 ppm in the ^{19}F spectrum compared to CFCl_3 , and Pummerer rearrangement products will appear around -73.5 ppm with the present choice of fluorinated alkoxide. Dibenzothiophene structures can be discriminated from diphenyl sulfide structures by selection of Br_2 or Cl_2 as an oxidant. Aryl alkyl and dialkyl sulfides are converted to Pummerer products in the sulfurane-forming reaction. Finally, dialkyl sulfides are converted to iminosulfuranes using N-bromo amides, but arylalkyl and diaryl sulfides do not react, providing a means for selective detection of dialkyl sulfides. Each of these categories of selective reaction can be used to introduce a unique ^{19}F or ^{15}N label. Introduction of two distinct ^{19}F labels for diaryl and alkyl aryl sulfides is demonstrated by the reaction of a mixture of diphenyl sulfide and thioanisole giving S,S-diphenyl-N-(2,2,2-trifluoroacetyl) iminosulfurane (^{19}F resonance at -73.5 ppm from CFCl_3) and $\text{PhSCH}_2\text{OC}(\text{CF}_3)_2\text{Ph}$ (-71.2 ppm from CFCl_3), respectively. Although the sulfurane-forming reactions may appear rather exotic for application to coal, we have shown in model compound experiments that the reactions can be successfully carried out in the presence of methylated preasphaltenes and asphaltenes, and are simple bench-top procedures.

SUMMARY

We have synthesized new iminosulfuranes from a variety of diaryl- and dialkyl sulfides and dibenzothiophene. The pattern of ^{15}N chemical shifts indicates that functional groups attached to sulfur are not simply resolved into aryl and alkyl groups. Thus, resolution of sulfur functional groups using ^{15}N NMR via iminosulfurane does not appear practicable. However, iminosulfurane formation, together with the N-haloamide reaction and the Pummerer rearrangement, provides pathways for chemical discrimination of different sulfur substituents using unique ^{15}N - or, ^{19}F -labelled fragments for different categories of sulfur functional groups. In efforts currently underway, we are applying these reactions to methylated extracts and conversion products of the high-organic-sulfur containing Yugoslavian Rasa and Spanish Mequinenza lignites.

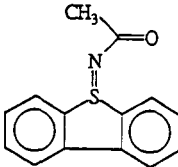
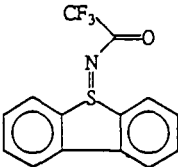
ACKNOWLEDGEMENT

This work was supported by the Office of Energy Research, U. S. Department of Energy, under Contract DE-ACO6-76RLO 1830. The authors thank Dr. Ana B. Garcia of the Instituto Nacional Del Carbon, Oviedo, Spain for providing us with a sample of the Mequinenza lignite, and Dr. Curt M. White of the Pittsburgh Energy Technology Center for providing a sample of the Rasa lignite.

REFERENCES

1. George, G. N., Gorbaty, M. L., J. Amer. Chem. Soc. 1989, 111, 3182.
2. George, G. N., Gorbaty, M. L., Kelemen, S. R., Sansone, M. Energy & Fuels, 1991, 5, 93-97.
3. Kelemen, S. R., George, G. N., Gorbaty, M. L., Fuel, 1990, 69, 939.
4. Calkins, W. H., Torres-Ordenez, R. J., Jung, B., Gorbaty, M. L., George, G. N., and Kelemen, Proc. 1991 International Conf. Coal Science, S. R. Butterworth-Heinemann Ltd., Linacre House, Jordan Hill, Oxford OX2 8DP, 1991, pp. 985-988, and references therein.
5. Calkins, W. H., Prepr. Fuel Div. Am. Chem. Soc., 1985, 30(4), 450-465.
6. Calkins, W. H., Energy & Fuels, 1987, 1, 59.
7. Torres-Ordenez, R. J., Calkins, W. H., and Klein, M. T., ACS Symposium Series 429, Ch. 17, June 1990.
8. White, C. M., Douglas, L. J., Anderson, R. R., Schmidt, C. E., and Gray, R. J. ACS Symposium Series 1990, 429, 261-286.
9. Green, T. K., Lloyd, W. G., Gan, L., Whitley, P., and Wu, K. Prepr. Fuel Div. Am. Chem. Soc. 1992, 37(2), 664-669.
10. Franz, J. A., Lamb, C. N., and Linehan, J. C. Proc. 1991 International Conf. Coal Science, S. R. Butterworth-Heinemann Ltd., Linacre House, Jordan Hill, Oxford OX2 8DP, 1991, 977-980.
11. Kise, H., Whitfield, G. F., and Swern, D., J. Org. Chem. 1972, 37, 1121-1128.
12. Huang, S. L., and Swern, D. J. Org. Chem. 1978, 43, 4537-4538 and Sharma, A. K., Ku, T., Dawson, A. D. and Swern, D. J. Org. Chem. 1975, 40, 2758-2764.
13. Franz, J. A., and Martin, J. C. J. Am. Chem. Soc. 1975, 97, 583-591 and 6137-6144.
14. Martin, J. C.; Arhart, R. J.; Franz, J. A.; Kaplan, L. J.; and Perozzi, E. F. Organic Syntheses, 1977, 57, pp. 22-26, John Wiley & Sons, New York, New York.

Table I. ^{15}N and ^{19}F Chemical Shifts of Iminosulfuranes and a Pummerer Rearrangement Product

Iminosulfurane	^{15}N Chemical Shifts ^a	^{19}F Chemical Shifts ^b
$\text{Ph}_2\text{S}=\text{NC}(\text{CH}_3)_3$	-293.5	
$\text{Ph}_2\text{S}=\text{NCH}_2\text{Ph}$	-330.4	
$\text{Ph}_2\text{S}=\text{NPh}$	-284.0	
$(\text{CH}_2)_4\text{S}=\text{NCOCH}_3$	-217.8	
$\text{Ph}_2\text{S}=\text{NCOCH}_3$	-227.6	
$(\text{PhCH}_2)_2\text{S}=\text{NCOCH}_3$	-228.9	
	-219.0	
$\text{Ph}_2\text{S}=\text{NCOCF}_3$		-73.52
		-73.45
$\text{PhSCH}_2\text{OC}(\text{CF}_3)_2\text{Ph}$		-71.2
<hr/>		
^a ppm from CH_3NO_2	^b ppm from CFCl_3	

Sulfur Speciation of Desulfurized Coals by XANES Spectroscopy

G.P. Huffman, S.A. Vaidya, N. Shah, and F.E. Huggins
CFMLS, 233 Mining & Minerals Res. Bldg., University of Kentucky,
Lexington, KY 40506-0107

Keywords: XANES, sulfur, XAFS, desulfurized

ABSTRACT

Least square analysis of the x-ray absorption near edge structure (XANES) region of sulfur K-edge x-ray absorption fine structure (XAFS) spectra can provide a quantitative analysis of both the organic and inorganic functional forms of sulfur in coal. In the current article, this method is applied to speciation of the sulfur forms in a number of desulfurized coals. The samples investigated include specimens treated with boiling perchlorethylene, samples subjected to selective chemical reactions, samples subjected to molten caustic leaching, and biologically desulfurized coals. In all cases, analysis of the XANES provides a reasonably quantitative speciation of the changes in the sulfur forms resulting from the various treatments.

INTRODUCTION

In the past several years, it has been demonstrated that sulfur K-edge x-ray absorption fine structure (XAFS) spectroscopy can be used to speciate all of the major functional forms of sulfur. Two primary methods of analysis have been used: direct least squares analysis of the x-ray absorption near edge structure (XANES) [1-3] and a third derivative treatment of the XANES [4-6]. With the least squares analysis approach, it is possible to quantitatively determine the percentages of the total sulfur present in five principal organic functional forms and several inorganic forms with an accuracy of ± 5 -10%.

An obvious application of this capability is the investigation of the changes in sulfur forms produced by desulfurization treatments. Particularly of interest are treatments aimed at removing organic sulfur. In the current paper, we present the results of XANES analysis of coals subjected to a variety of chemical and biological desulfurization treatments.

EXPERIMENTAL PROCEDURE AND SAMPLE DESCRIPTION

The samples investigated were prepared in several laboratories. The desulfurization procedures have been described in detail elsewhere and will not be discussed here. Samples studied included coals treated by boiling perchlorethylene (PCE) prepared in the laboratories of Prof. Sunyu Lee[7] and Dr. Melissa Chou[8], specimens treated with single electron transfer and strongly basic reagents in the laboratory of Dr. Kuntal Chatterjee and Prof. Leon Stock [7-11], samples subjected to biological desulfurization by Dr. John Kilbane [12], and samples treated by molten caustic leaching [13] provided by Mr. Phil Goldberg of the Pittsburgh Energy Technology Center.

The sulfur K-edge XAFS spectroscopy was carried out at beamline X-19A at the

National Synchrotron Light Source (NSLS) at Brookhaven National Laboratory. To minimize x-ray absorption, the x-ray beam at X-19A is maintained in machine vacuum all the way from the synchrotron ring to the experimental hutch, and is thereafter maintained in a helium atmosphere. All spectra were taken in the fluorescent mode using a Stearn-Heald ionization detector [14]. The x-ray energy was varied from approximately 100 eV below to about 400 eV above the sulfur K-shell absorption edge (2472 eV) using a Si (111) double crystal monochromator.

RESULTS AND DISCUSSION

Biologically Desulfurized Samples: Previously, we have used XANES to examine a number of biologically solubilized and desulfurized samples [2]. The primary conclusion of that earlier work was that biological agents did not discriminate greatly between different functional forms of sulfur, and little if any organic sulfur was removed by biological treatment. More recently, however, XANES has been used to examine several samples subjected to biotreatment using the microbe *Rhodococcus rhodochrous*, as discussed in detail elsewhere by Kilbane [12].

Typical fitted XANES spectra of a control sample and a biotreated sample of an Illinois #6 coal are shown in Figure 1. Prior to treatment, most of the pyrite was removed from the coal. The results are summarized in Table I and Figure 2. In both examples, it is seen that a substantial reduction in organic sulfur was accomplished. However, it is evident from Figure 2 that the relative amounts of the different functional forms of organic sulfur were essentially unchanged, within the standard error ($\pm 5\%$). It therefore appears that all of the organic sulfur functional forms were reduced approximately equally by the treatment [12].

Coals Subjected to Molten Caustic Leaching: A molten caustic leaching process for removal of both ash and sulfur from coal has been developed by TRW Corporation [13]. The fitted XANES obtained from a Kentucky #9 coal subjected to this process is shown in Figure 3. It is evident that the sulfur has undergone considerable oxidation. The results obtained by quantitative analyses of the XANES are summarized for three coals in Table 2: a Kentucky #9 coal and a Pittsburgh #8 coal subjected to the molten caustic leaching process, and the Pittsburgh #8 coal prior to leaching [1]. It is evident that the forms of sulfur are drastically changed and reduced by this rather severe process. In particular, no pyrite or organic sulfide remain, and thiophenic sulfur, which is the dominant organic sulfur form in the original coals is reduced to only about 0.1% in the treated coals. Elemental sulfur, sulfone, and sulfate are the dominant sulfur species remaining, indicating severe oxidation.

Perchloroethylene Treated Samples: We have examined a number of samples before and after treatment with PCE. For the samples investigated to date, it is concluded that the primary effect of the treatment is to remove elemental sulfur. Typical results for a number of samples are summarized in Table 3. It is seen that elemental sulfur is the primary sulfur form removed for all of the samples which exhibited a decrease in sulfur due to PCE treatment. It is also noted that all of these samples contain a significant amount of sulfate, indicative of substantial oxidation. In two cases, a fresh coal is compared to the sample before PCE treatment. It appears that an oxidative step is essential to produce the elemental sulfur that is removed by the PCE treatment. It is known that oxidation of pyrite will

produce both sulfate and elemental sulfur [15]. The current XANES data, however, have not included enough fresh coals before the oxidative step to conclude whether or not any significant amount of organic sulfur is being converted to elemental sulfur in this step. A more detailed paper is in preparation summarizing our results on PCE treated coals [16].

Coals Treated with Single Electron Transfer(SET) and Basic Reagents:

Chatterjee and Stock have discussed the removal of organic sulfur from coal by treatment with SET [9] and strongly basic reagents [10]. A suite of these desulfurized coals were previously examined by XANES spectroscopy by Chatterjee et al. using the third derivative method of XANES analysis developed by Gorbaty et al. [11]. We have examined the same suite of samples independently using the least squares analysis approach for deconvolution of the XANES. The results are summarized in Table 4.

The results for the raw Illinois no. 6 coal, obtained from the Argonne Premium Coal Sample Bank, are similar to those we have reported earlier [1], except for the presence of some sulfate. After treatment with lithium aluminum hydride (LAH), all of the pyrite and most of the sulfate have disappeared; additionally, the percentage of organic sulfide appears to have decreased relative to thiophenic sulfur. Following the SET treatment, the thiophenic sulfur percentage is significantly decreased, while the BASE treatment produces a substantial decrease in the sulfidic sulfur. This is exactly as proposed by Stock and Chatterjee [6,7] and as previously observed by the third derivative treatment of the XANES data of Gorbaty [11]. However, the results are obscured somewhat by the appearance of an unidentified sulfide which gives an s→p peak in the spectrum at -0.5 eV. Presumably, this is a potassium sulfide, in view of the nature of the chemical treatment. Since we have not conclusively identified this phase and have not determined a coefficient for conversion of its peak area percentage to sulfur percentage, we have simply assumed a conversion coefficient of 1.0 to derive the values in Table 4. This should not significantly affect the relative percentages of the other functional forms of sulfur, however.

For the samples treated with SET then BASE, and with BASE then SET, the thiophenic sulfur is markedly decreased in both cases, but there does not appear to be any decrease in the organic sulfide. In this regard, however, it should be noted that the accuracy of our method with an unknown inorganic sulfide present is not better than about ±10%.

The final two treatments indicated in Table 4 both produce significant sulfur oxidation and a decrease in thiophenic sulfur, by 50% for the last treatment. In the last treatment, it is seen that the process also produced a significant amount of elemental sulfur.

ACKNOWLEDGEMENT

This research was supported by the Office of Exploratory and Applied Research of the Electric Power Research Institute under EPRI Contract No. RP-8003-20. We are grateful to Prof. Sunyu Lee, Dr. Melissa Chou, Dr. John Kilbane, Mr. Phil Goldberg, Prof. Leon Stock and Dr. Kuntal Chatterjee for providing samples for this investigation.

REFERENCES

1. Huffman, G.P.; Mitra, S.; Huggins, F.E.; Shah, N.; Vaidya, S.; Lu, F. *Energy & Fuels* **1991**, *5*, 574.
2. Huggins, F.E.; Mitra, S.; Vaidya, S.; Taghiei, M.M.; Lu, F.; Shah, N.; Huffman, G.P. *Processing and Utilization of High Sulfur Coal IV*, Dugan, P.R.; Quigley, D.A.; Attia, Y.A.; Eds.; Elsevier Sci. Pub., **1991**, *4*, 13.
3. Taghiei, M.M.; Huggins, F.E.; Shah, N.; Huffman, G.P. *Energy & Fuels*, **1992**, *6*, 293-300.
4. George, G.N.; Gorbaty, M.L. *J. Am. Chem. Soc.*, **1989**, *111*, 3182.
5. Gorbaty, M.L.; George, G.N.; Kelemen, S.R. *Fuel*, **1989**, *69*, 939.
6. Gorbaty, M.L.; George, G.N.; Kelemen, S.R. *Fuel*, **1989**, *69*, 945.
7. Lee, S.; Fullerton, K.L.; Kesawan, S.K. *Proceedings: Fourteenth Annual EPRI Conference on Fuel Science*, Ed., Lebowitz, H.E., 1990, EPRI GS-6827, pp. 7-1-7-24.
8. Chou, Melissa; Work in progress.
9. Chatterjee, K.; Wolny, R.; Stock, L.M. *Energy & Fuels*, **1990**, *4*, 402.
10. Chatterjee, K.; Stock, L.M. *Energy & Fuels*, **1991**, *5*, 704-707.
11. Chatterjee, K.; Stock, L.M.; Gorbaty, M.L.; George, G.N.; Kelemen, S.R. *Energy & Fuels*, **1991**, *5*, 771-773.
12. Kilbane, J.J.; *Proceedings: 1991 Second International Symposium on the Biological Processing of Coal*, Ed., S. Yunker; EPRI GS-7482, 1991, pp. 5-1-5-18.
13. Anastasi, J.L.; Barrish, E.M.; Coleman, W.B.; Hart, W.D.; Jonis, J.F.; Ledgerwood, L.; McClanathan, L.C.; Meyers, R.A.; Shih, C.C.; Turner, W.B. *Processing and Utilization of High Sulfur Coals III*; Eds., Markuszewski, R.; Wheelock, T.D.; Elsevier Sci. Pub., 1990, 371-377.
14. Lytle, F.W.; Greegor, R.B.; Sandstrom, D.R.; Marques, E.C.; Wong, J.; Spiro, C.L.; Huffman, G.P.; Huggins, F.E. *Nucl. Instrum. Methods*, **1988**, *226*, 542.(26).
15. Duran, J.E.; Mahasay, S.R.; Stock, L.M. *Fuel*, **1986**, *65*, 1167-1168.
16. Huggins, F.E.; Vaidya, S.; Shah, N.; Lu, F.; Huffman, G.P.; paper in preparation.

**Table 1: Sulfur Analytical Data - Biotreated Coals
Samples from J. J. Kilbane (I.G.T.)**

	III. #6 Coal Control	III. #6 Coal Biotreated	III. #6 Coal Control	III. #6 Coal Biotreated
Total S, Wt%	3.45	1.03	3.00	2.14
Organic S, Wt%	3.20	0.92	2.54	1.72
Pyritic S, Wt%	0.25	0.15	0.50	0.45

Table 2: Sulfur Forms in Gravimelt Coals from XANES Analysis

% of Total Sulfur in Different Forms

	Pittsburgh #8 2.19 wt% S	Gravimelt Pgh#8 0.43 wt% S	Gravimelt KY#9 0.70 wt% S
Pyrite	52	0	0
Elem. Sulfur	0	28	37
Org. sulfide	13	0	0
Thiophene	35	19	16
Sulfonate	0	16	14
Sulfate	0	37	33

Table 3. Weight percentages of sulfur contained in different functional forms for a number coals before and after PCE treatment, as determined from the XANES spectra. Precision estimated as ± 0.2 wt. %

<u>Sample</u>	<u>Pyrite</u>	<u>Elemental S</u>	<u>Sulfide</u>	<u>Thiophene</u>	<u>Sulfone</u>	<u>Sulfate</u>
IBC-104 fresh	2.22*	0.0	0.72	1.18	0.0	0.11
IBC-104 2wk ox before	2.17*	0.0	0.61	1.07	0.0	0.12
IBC-104 2wk ox after	2.18*	0.0	0.61	1.12	0.0	0.07
IBC-104 5yr ox before	1.40*	0.17	0.53	0.86	0.13	1.01
IBC-104 5yr ox after	1.40*	0.0	0.56	0.88	0.07	0.41
Ohio #5/#6 before	0.79*	0.26	0.50	1.00	0.14	0.82
Ohio #5/#6 after	0.87*	0.0	0.54	1.04	0.04	0.29
Freeport, before	1.8*	-	0.65	0.85	0.0	0.2
Freeport, after	1.9*	0.0	0.25	0.7	0.0	0.25
Freeport, before	0.95*	0.87	0.05	0.25	0.05	0.82
Freeport, after	0.94	0.25	0.07	0.35	0.08	1.15
Indiana #5, before	0.85*	0.35	0.4	0.4	0.05	0.45
Indiana #5, 30 min PCE treatment	0.85*	0.2	0.3	0.4	0.05	0.45
Indiana #5, after	0.85*	0.0	0.25	0.4	0.05	0.35

*Pyritic sulfur values from Mössbauer spectroscopy.

*ASTM chemical analysis value

Table 4. Percentages of total sulfur contained in different functional forms ($\pm 5-10\%$).

<u>Sample</u>	<u>Inorganic Sulfide</u>	<u>Elemental Sulfur</u>	<u>Organic Sulfide</u>	<u>Thiophenic Sulfur</u>	<u>Sulfoxide</u>	<u>Sulfone</u>	<u>Sulfate</u>
Illinois No. 6 raw coal	48 - pyrite	0	18	26	0	0	9
Lithium aluminum hydride (LAH) treated coal	0	0	25	66	4	3	2
SET-treated coal	15 - unk.	0	25	36	5	15	4
BASE-treated coal	18 - unk.	0	13	49	7	8	5
SET, then BASE	21 - unk.	0	24	21	11	13	10
BASE, then SET	0	9	26	36	7	9	13
Pyrite free coal + nickelocene + LAH in THF (24 hr, 67°C)	6 - unk.	0	24	47	13	9	1
Pyrite-free coal + K + naphthalene + BASE in heptane (24 h, 98°C), protonated	0	23	21	32	5	10	10

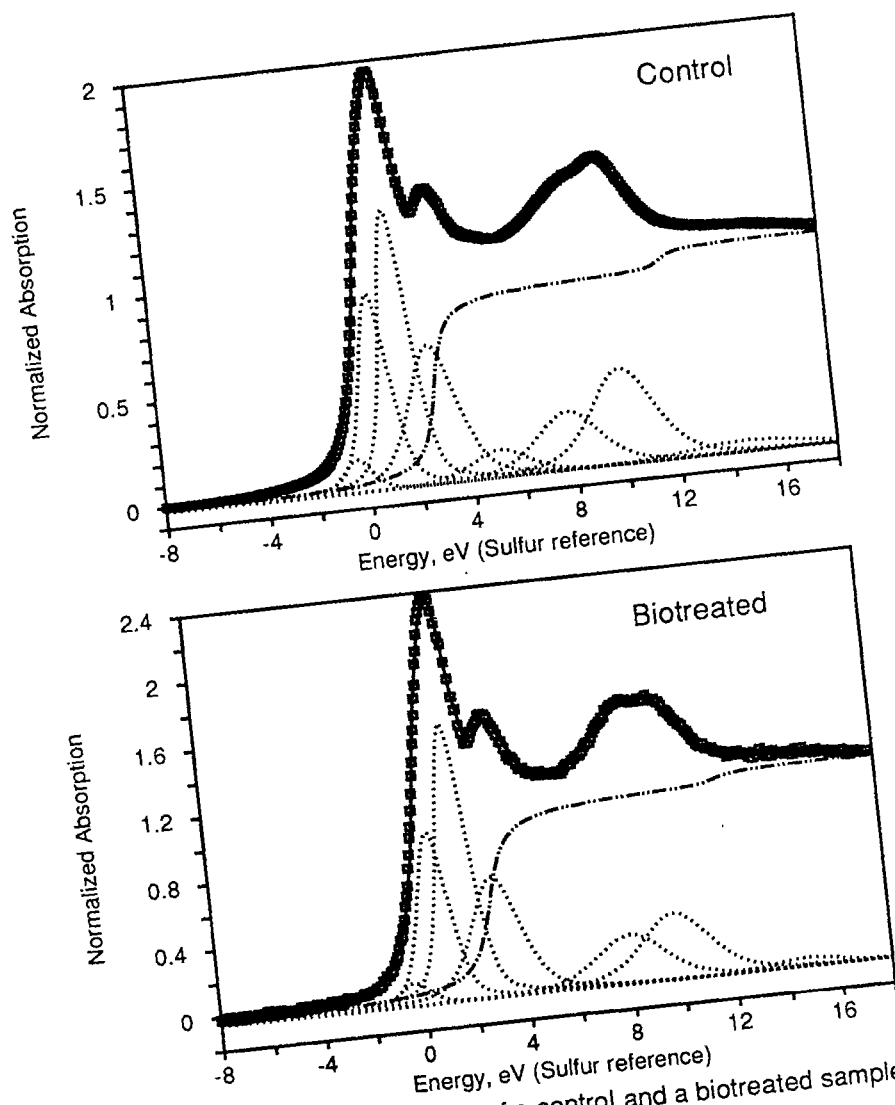


Fig 1: S K-edge XANES spectra of a control and a biotreated sample of Illinois #6 coal.

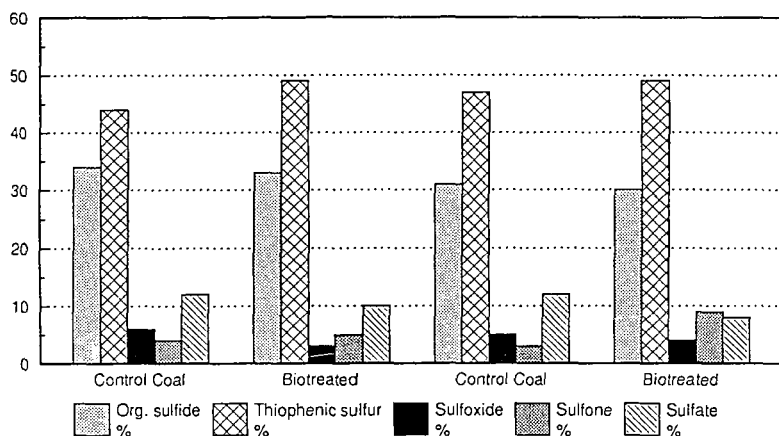


Fig. 2: Percentages of organic functional forms of sulfur in control and biotreated Illinois #6 samples as determined from the S K-edge XANES analyses.

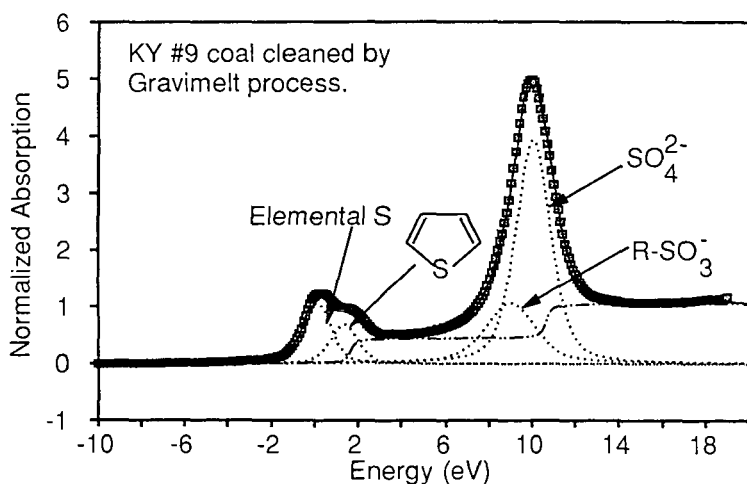


Fig. 3: Sulfur XANES spectrum of coal cleaned by molten caustic leaching.

Nitrogen Chemical Structure in Petroleum Asphaltenes and Coal by X-Ray Absorption Spectroscopy

Sudipa Mitra Kirtley,^{@*} Oliver C. Mullins,[@] Jan van Elp,^{*} & Stephen P. Cramer^{*#}

[@]Schlumberger-Doll Research, Ridgefield, CT 06877;

^{*}Lawrence Berkeley Laboratory, Berkeley, CA 94720;

[#]University of California, Davis, Davis, CA 95616

Keywords: nitrogen, XANES, fossil-fuel

ABSTRACT

Nitrogen chemical structure in fossil-fuel samples has been determined using x-ray absorption near-edge structure (XANES) spectroscopy. XANES data on three petroleum asphaltenes, a coal, and a number of nitrogen model compounds have been analyzed by comparing normalized areas under corresponding resonances in the spectra of the fossil-fuel samples and the model compounds. In the asphaltene and coal samples, we find that nitrogen occurs mostly in aromatic forms; very little or no evidence of saturated amines is found. The coal and asphaltenes show substantial quantities of pyrrole and pyridine fractions, and the pyrrole content is found to be greater than or equal to the pyridine content in all cases. XANES methodology is shown to be promising for the investigation of nitrogen structures in fossil-fuels, similar to its success in determining sulfur forms in similar samples over the past decade.

INTRODUCTION

Heteroatom chemistry of the heavy ends of petroleum and of coals has long been of interest for both processing and environmental concerns.^{1,2} However, the study of the heteroatom chemistry in these fossil fuels is problematic. Nondestructive chromatographic methods are largely precluded due to the high molecular weights of these materials. Spectroscopic studies, particularly of nitrogen and sulfur, are difficult due to the low concentration of the heteroatoms and the elemental nonspecificity of many spectral methods. X-ray methods are element specific, and x-ray photoelectron spectroscopy (XPS) methods have been employed to study nitrogen in coals. However, XPS studies to date have suffered from the lack of resolution; peak separations from different chemical forms of nitrogen are comparable to or less than peak widths.^{3,4} Additionally, XPS is particularly sensitive to surface effects. Here we report the study of nitrogen chemistry in three petroleum asphaltenes and in a coal using x-ray absorption near-edge structure (XANES). Nitrogen K-edge XANES spectra are found to have distinct and well resolved features which allow identification of the corresponding chemical forms of nitrogen. The fossil fuel spectra are satisfactorily interpreted in terms of two different kinds of aromatic model compounds, pyrrole and pyridine analogues. In both the asphaltene and coal samples, these aromatic nitrogen fractions

account for all of the nitrogen, and there are no indications of saturated amines. The coal and asphaltene samples differ in that the asphaltene has a greater fraction of pyrrolic nitrogen while the coal has comparable fractions of pyrrolic and pyridinic nitrogen fractions.

Over the past decade, XANES has emerged as perhaps the most powerful tool⁵ for the analysis of sulfur in coals,⁶⁻¹¹ coal macerals,¹⁰ and petroleum asphaltenes.^{12,13} This is a moderately sensitive, nondestructive and element-specific method that relies on changes in positions and shapes of spectral features near the K-edge (or other edge), that depends on the chemical environment. In coals,^{7,10} the organic and inorganic fractions of sulfur have been determined. In both coals⁸⁻¹¹ and asphaltenes,^{12,13} the fractions of sulfidic and thiophenic forms of sulfur have been resolved. Different oxidized forms of sulfur have been readily identified in coals⁸⁻¹⁰ and asphaltenes.¹³ Although x-ray absorption methods have been very useful in the determination of the chemical forms of sulfur,⁵⁻¹³ the application of XANES to the study of nitrogen in asphaltenes and coals is more difficult due to the low energy of the nitrogen K edge. Recent availability of high resolution soft x-ray beam lines¹⁴ and of efficient fluorescence detectors¹⁵ facilitates nitrogen XANES studies.

EXPERIMENTAL SETUP

Measurements were performed at the National Synchrotron Light Source at Brookhaven National Laboratories using the AT&T Bell Lab's 'Dragon' beam line (U4B).¹⁴ Typical incident x-ray resolution in the experiments was 0.14 eV. The powdered samples were placed on silicon supports using nitrogen-free double-stick tape. The sample was then placed in the vacuum chamber fitted with a cryopump which maintained the pressure at $\sim 10^{-9}$ torr. Energy calibration was performed using zinc octaethylporphyrin which has a resonance at 399.72 eV. Fluorescence detected x-ray absorption spectra were obtained using a seven element Ge detector,¹⁵ with single channel analyzers set to select the shaped pulses corresponding to the nitrogen K α emission.¹⁵ The coal sample was obtained from Argonne National Labs (Pittsburgh #8), the asphaltenes were prepared from crude oils from California, USA (CAL), France (FRA), and Kuwait (UG8), by 40cc/g dilution with n-heptane, and the pure model compounds were obtained from the Aldrich Chemical Company.

RESULTS AND DISCUSSION

Figure 1 compares the fluorescence excitation spectra of the petroleum asphaltenes and Pittsburgh #8 coal.¹⁶ (Figure 1 also shows the composite spectrum consisting of the weighted sum of the spectra of acridine and carbazole, see below). Three distinct spectral regions are apparent in all spectra, at 399.5 eV, 403 eV, 408 eV. To assign these features, we have resorted to the fluorescence detected x-ray absorption spectra of model compounds, as shown in figure 2. Acridine, a pyridine analogue, has a particularly strong resonance at ~ 399 eV which is assigned to a $1s \rightarrow \pi^*$ transition.¹⁷ Carbazole, a pyrrole analogue, has a strong resonance at ~ 403 eV which is also assigned to a $1s \rightarrow \pi^*$ resonance.¹⁷ 1,3,5-

tribenzylhexahydro-1,3,5-triazine, a saturated amine, exhibits only a broad σ resonance at ~408 eV, a slightly lower energy than the σ resonances of the aromatic compounds.¹⁷ The π^* resonances of the two different types of aromatic compounds are well resolved which is advantageous for interpreting the data.

There is a clear correspondence in the spectra between the peaks of the aromatic compounds with peaks of asphaltenes and coal in figure 1. Assuming the oscillator strengths of these transitions remain in constant ratio with post threshold continuum absorption at 420 eV, these spectra can be used to quantitatively determine the various nitrogen fractions. Small energy shifts between peaks in the spectra of models and fossil fuel samples are observed. Furthermore, peak widths in the spectra of the fossil fuel samples are somewhat larger than for the pure model compounds. Therefore, we did not simply fit the asphaltene and coal spectra with sums of model spectra. We fit all spectra with a sum of Lorentzian peaks and an arc-tangent step function. We used peak areas normalized by the step height to determine nitrogen fractions in the fossil fuels. For the asphaltene and coal spectra, the area of the lowest energy resonances at ~399.7 eV was assigned to the pyridine analogue, thereby determining the pyridine fraction. The resonances near 403.5 were assigned to both pyridine (already determined) and pyrrole. The contribution of pyridine to the area of the broad peak centered at ~403.5 eV was subtracted and the remaining peak area was assigned to the pyrrole analogue, thereby determining the pyrrole fraction. Likewise, the peak area of the 409 eV peak was assigned to both aromatics (already determined) and the saturated amine. The contribution of the aromatics to the very broad peak at ~409 eV was subtracted and any remaining, unaccounted for peak area was assigned to the saturated amine.

The fitting procedure resulted in the following peak positions (listed in eV). UG8 asphaltene: 399.3, 399.8, 402.55, 403.4, 406.77, 408.0, 410.8, 412.5, 415.5 and step 408.6; FRA asphaltene: 399.6, 402.2, 403.2, 406.5, 407.8, 412.8, and step 408.6; CAL asphaltene: 399.8, 402.4, 403.5, 406.2, 407.4, 412.3, 416.9, and step 408.3; Pittsburgh #8 coal: 399.5, 400.05, 402.7, 404.05, 407.08, 408.2, 412.9, and step 408.6; acridine: 399.25, 399.6, 401.8, 403.3, 406.4, 407.9, 408.9, 412.9 and step 408.6; carbazole: 402.3, 403.2, 404.2, 406.1, 408.0, 410.4, 413.3, 418.4, and step 408.4; and tribenzylhexahydrotriazine: 402.3, 402.9, 405.3, 407.5, 410.0, 413.3, and step 408.5.

The normalized fractional forms of nitrogen are for CAL: 50% pyridine, 48% pyrrole, and saturated amine 2%, for FRA: 40% pyridine, and 60% pyrrole, for UG8: 37% pyridine, 63% pyrrole, and for coal: 47% pyridine, 53% pyrrole. The error estimate, based on the unnormalized nitrogen fraction, is considered to be about 10%. Figure 1 shows the similarity of the overall features of the spectra of the fossil fuels, although there are some differences in peak positions and widths. For the sake of comparison, a weighted spectral sum with 42% acridine and 58% carbazole (fractional values intermediate between coal and asphaltene results) is also shown. Examination of a greater selection of model compounds may reduce

discrepancies between spectra of fossil fuels and the spectral sum of model compounds. The coal and the three asphaltenes exhibit appreciable fractions of both pyrrolic and pyridinic nitrogen, with the pyrrolic nitrogen content being either greater than or equal to the pyridinic content in all four samples. Little evidence of saturated amine is found in any sample. XPS methods employing pyrrole and pyridine models have been used to study coal-derived materials,^{3,4} and coals.⁴ Coal asphaltenes³ were found to contain 49-62% and coals⁴ 65-85% pyrrolic nitrogen, the rest being assigned to pyridine analogues in both cases. Our determination of pyrrolic and pyridinic nitrogen fractions for our asphaltene samples is similar to the XPS results for coal asphaltenes, and the pyrrolic estimate for our coal is somewhat lower than the XPS coal results. Uncertainties exist in the XPS results as a result of resolution difficulties. For all asphaltenes and coals, the nitrogen is much more aromatic than the (organic) sulfur where large sulfidic fractions are found. Additionally, for asphaltenes, the fraction of aromatic nitrogen is much larger than the fraction of aromatic carbon (~40%), whereas in coal, such a comparison can not be easily made, since the aromatic carbon content varies significantly among different coals.¹⁸

CONCLUSIONS

Nitrogen XANES methods are powerful for determining different chemical forms of nitrogen in asphaltenes and coals. The high degree of specificity of this technique coupled with the well resolved resonances of various forms of nitrogen provide one of the best methods for differentiating nitrogen chemical forms in fossil fuels. Aromatic pyrrolic and pyridinic nitrogen are the most prevalent forms of nitrogen found in the asphaltenes and coal; pyrrolic nitrogen is generally more abundant than pyridinic nitrogen, although considerable variability is observed in the pyrrole and pyridine fractions of nitrogen in the asphaltene and coal samples. Little evidence of saturated amines is found in these fossil-fuel samples. Non-destructive and direct XANES methodology for nitrogen characterization in amorphous fossil-fuel samples is shown to be very successful, and holds promise for further work in this area.

Acknowledgments

Research carried out at the National Synchrotron Light Source at Brookhaven National Laboratory which is supported by U.S. Dept. of Energy, Division of Material Science and Division of Chemical Science. SPC acknowledges support by Lawrence Berkeley Lab, Exploratory Research Fund and by the National Institutes of Health, Grant GM-44380.

References

- 1) Coal Science II, H.H. Schobert, K.D. Bartle, and L.J. Lynch Eds., ACS symp. Series #461 Amer. Chem. Soc., Washington D.C., (1991)
- 2) Chemistry of Asphaltenes, J.W. Bunger, N.C. Li, Eds., Amer. Chem. Soc., Washington, D.C., (1981)
- 3) S. Wallace, K.D. Bartle, D.L. Perry, Fuel, 68, 1450, (1989)
- 4) P. Burchill, Intl. Conf. Coal Science, J.A. Moulijn et al eds., Elsevier Pub., Amsterdam, 5, (1987)
- 5) L.M. Stock, R. Wolny, B. Bal, Energy & Fuels, 3, 651, (1989)
- 6) Z. Hussain, E. Umbach, D.A. Shirley, J. Stohr, J. Feldhaus, Nucl. Instrum. Methods. Phys. Res. 195, 115, (1982)
- 7) C.E. Spiro, J. Wong, F. Lytle, R.B. Greegor, D. Maylotte, S. Lampson, Science 226, 48, (1984)
- 8) G.P. Huffman, F.E. Huggins, H.E. Francis, S. Mitra, and N. Shah, Coal Science and Tech.16: Proc. and Util. of High Sulfur Coals III, 21, (R. Markuszewski et al eds.), 21, (1990)
- 9) M.L. Gorbaty, G.N. George, S.R. Kelemen, Fuel, 69, 1065, (1990)
- 10) G.P. Huffman, S. Mitra, N. Shah, S. Vaidya, and F. Lu, Energy & Fuels, 5, 574, (1991)
- 11) G.N. George, M.L. Gorbaty, S.R. Kelemen, and M. Sansone, Energy & Fuels, 5, 93, (1991))
- 12) G.N. George, M.L. Gorbaty, J. Amer. Chem. Soc., 111, 3182, (1989)
- 13) G.S. Waldo, O.C. Mullins, J.E. Penner-Hahn, S.P. Cramer, Fuel, 71, 53, (1992)
- 14) C.T. Chen, Nucl. Instrum. Methods Phys. Res. A, 256, 595 (1987); C.T. Chen, F. Sette, Rev. Sci. Instrum. 60, 1616, (1989)
- 15) S.P. Cramer, O. Tench, M. Yocum, H. Craner, L. Rogers, V. Radeka, O.C. Mullins, and S. Rescia, X-Ray Absorption Fine Structure - Proc. 6th Intl. XAFS Conf., S.S. Hasnain, Ed., Ellis Horwood Chichester, 640, (1991)
- 16) Using x-ray absorption tables (J.J. Yeh, I. Lindau, Atomic Nuc. Data Tables, 32, 1, (1983)), maximum nonlinearities from concentration effects in the model compound spectra are calculated to be ~7% and were corrected

for in the data using Eqn. 23, in J. Goulon, C. Goulon-Ginet, R. Cortes, J.M. Dubois, *J. Physique*. 43, 539, (1982)

17) J.L. Dehmer, A.C. Parr, S.H. Southworth, Ch. 5 in *Handbook on Synchrotron Radiation*, Vol. 2, G.V. Marr Ed., North-Holland, Amsterdam, (1987)

18) R.M. Davidson, *Coal Science*, Vol. 1, I. G. Dryden Ed., Academic Press Inc., 83, (1982)

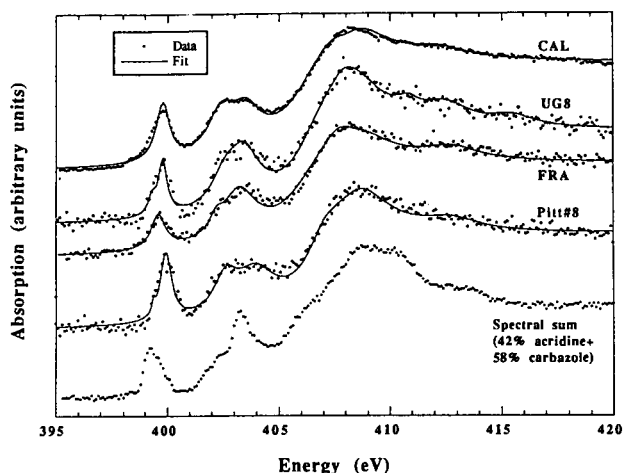


Figure 1. Nitrogen K-edge absorption spectra of three asphaltene samples: CAL, FRA, and UG8, and one coal sample: Pittsburgh #8. Dots are data and the solid lines are fits consisting of a sum of lorentzians and an arc-tan function. Also shown (at the bottom) is the weighted sum of the spectra of a pyridine analogue, acridine (42%), and a pyrrole analogue, carbazole (58%).

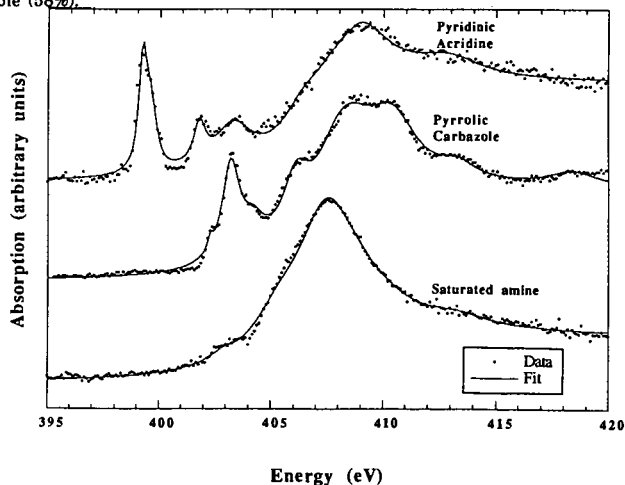


Figure 2. Nitrogen K-edge absorption spectra of three model compounds used to fit the fossil fuel spectra, acridine - a pyridine analogue, carbazole - a pyrrole analogue, and tribenzylhexahydrotriazine - a saturated amine. Dots are data and the solid lines are fits consisting of a sum of lorentzians and an arc-tan function.

APPLICATION OF XAFS SPECTROSCOPY TO THE SPECIATION OF CRITICAL TRACE ELEMENTS IN COAL UTILIZATION

Frank E. Huggins, Naresh Shah, Jianmin Zhao, Fulong Lu, and G. P. Huffman,
University of Kentucky, Lexington, KY 40506.

Keywords: XAFS spectroscopy, chromium, arsenic, trace elements, coal

ABSTRACT

The environmental impact of specific trace element species in coal utilization and waste disposal depends not only on the abundance, but also on the form(s) of occurrence of the element present in such materials. While there are a number of analytical methods for determining the abundance of trace elements in coal, there are very few methods available for determining the form of occurrence (speciation) of a trace element in coal at abundances as low as 10 ppm. In this report, the potential of XAFS spectroscopy for trace element speciation is demonstrated by means of measurements on two important trace elements, arsenic and chromium, in coal and ash.

INTRODUCTION:

In the United States in recent years, almost one billion tons of coal have been mined each year, of which 85-90% is used for electrical power generation [1]. Combustion of such huge tonnages of coal has the potential to release vast amounts of undesirable elements into the U.S. environment. For example, for an element such as arsenic that occurs in many U.S. coals only at the 10 - 50 ppm level [2,3], there is the potential for 10,000 - 50,000 tons of arsenic to be released to the environment from coal utilization annually. Some of the arsenic may be removed by coal washing, some will be trapped in the solid products (ash and slag) of coal combustion, some will be collected in fly ash, and some will escape to the environment in combustion gases and fugitive emissions. The collected wastes from coal washing and combustion are often dumped into ash settling ponds, where, due to aqueous leaching of the wastes, there is additional opportunity for arsenic to enter the environment through groundwater. Such a scenario will be followed by many of the eleven trace metal species identified as potentially hazardous to the environment by the 1990 Amendments to the Clean Air Act.

It is clear that the environmental impact and hazard assessment of a specific element in coal combustion is a highly complex issue. For instance, it is apparent that minimization of an element's contribution to degradation of air quality either by coal cleaning prior to combustion or by efficient capture of fly ash and effluent gases in scrubbers after combustion may exacerbate problems with groundwater quality because of the leaching and reactivity characteristics of higher amounts of the element in cleaning or combustion wastes. Moreover, little is known about the forms-of-occurrence of most trace elements in coal, ash and other wastes and how such factors might influence the behavior of the element during combustion and its segregation into various solid and gaseous forms during cleaning, combustion, and waste disposal.

In order to understand the behavior of a given element in coal combustion and waste disposal and perhaps remedy some of the potential problems associated with environmental contamination by hazardous trace elements, it is not enough just to determine the amount of an element in the coal and various waste fractions. It is essential to know also how the element

occurs in the coal and other fractions. The mode or form of occurrence of the element in the coal (i.e., whether the element forms a specific mineral, whether it is dispersed within a particular host mineral or in the coal macerals, with which fraction of the coal the element is associated, in which oxidation state the element occurs in the coal, etc.) controls to a great extent the potential hazard posed by the element to human health and the environment.

There are many different methods of quantitatively determining the amount of an element in coal; such methods include atomic absorption, X-ray fluorescence, instrumental neutron activation analysis, proton induced X-ray or gamma-ray emission, inductively coupled plasma techniques, etc. However, there are very few methods for determining the forms of occurrence of a trace element in materials as complex as coal, ash, slags, and solutions (e.g. leachates). A technique that has excellent demonstrated potential for investigating the forms of occurrence of trace elements in coal and other materials is X-ray absorption fine structure (XAFS) spectroscopy [4-6]. This technique has the ability to focus on a specific element in a material and to provide detailed information relevant to the local bonding and structure of the element in the material, from which the form of occurrence can usually be deduced. Furthermore, this technique is both direct and nondestructive. In this report, the application of XAFS spectroscopy to the speciation of trace element species is demonstrated by a preliminary survey investigation of chromium and arsenic in coal and ash. Both of these elements have been identified as potentially hazardous to the environment in the 1990 Amendments to the Clean Air Act.

EXPERIMENTAL:

Samples: For this survey study, coal samples were obtained from a variety of sources. Samples unusually high in arsenic (up to 2,000 ppm) were provided by Dr. Leslie Ruppert at the U.S. Geological Survey [7]; the Upper Freeport coal in the Argonne Premium Coal Sample Bank (APCSB), which has an arsenic content of 17 ppm [3], was also investigated as its abundance of arsenic is more typical of that in the majority of U.S. coals. This coal was also subjected to laboratory float/sink tests; a 1.6 float sample, a 1.6 sink - 2.85 float sample, and a 2.85 sink sample were prepared by centrifugation using perchloroethylene (C_2Cl_4 , sp. gr. 1.6) and bromoform ($CHBr_3$, sp. gr. 2.85) as the heavy liquid separation media. A raw coal with a typical (≈ 20 ppm) chromium content and the corresponding clean coal after treatment by the spherical oil agglomeration process (SOAP) and the resulting ash samples were obtained from combustion studies performed at Physical Sciences, Inc., by Dr. J. Helble; coals with somewhat higher than average chromium contents (up to 140 ppm) were obtained from the Penn State Coal Bank.

XAFS Spectroscopy: XAFS spectroscopy was performed at beam-line X-19A at the National Synchrotron Light Source, Brookhaven National Laboratory. For chromium in coals and ash samples, the absorption of X-rays was measured over the spectral range from 5.9 keV to 6.2 keV; over the X-ray absorption near-edge structure (XANES) region (5.97 to 6.03 keV), absorption data were collected every 0.2 eV. For arsenic in coals and ash samples, the absorption of X-rays was measured over the spectral range from 11.75 keV to 12.0 keV; over the XANES region (11.85 to 11.90 keV), absorption data were collected every 0.25 eV. Absorption of the X-rays was measured by means of a thirteen-element germanium array detector [8] that detected the fluorescent X-rays only in a specified tunable energy window that corresponded to the energy of the chromium or arsenic fluorescent K_{α} X-rays. In addition, the appropriate 6p vanadium or germanium filter was used to minimize background. Up to ten scans were recorded and summed for the weakest absorbers. The spectral summations, the pulse-height windowing, and the low-energy filtering all contributed to enhance the signal-to-noise ratio of the trace element spectra. For reference standards, conventional ion chambers were used to measure both the fluorescent and absorption XAFS spectra in a single scan. Depending on the amount of arsenic or chromium

in the standard, the standard was diluted in graphite to optimize the absorption spectrum. As is normally done, the chromium or arsenic XAFS spectra were divided into separate XANES and, where feasible, EXAFS regions and standard XAFS analysis methods were employed to analyze the spectral regions. The arsenic K-edge XANES spectra shown in this report are calibrated with respect to a zero energy point (11.867 keV) defined as the position of the white line in the spectrum of As_2O_3 that was run simultaneously with all arsenic spectra. The zero energy point (5.989 keV) for chromium was defined as the first inflection point in the XAFS spectrum of chromium metal foil.

RESULTS AND DISCUSSION:

Arsenic: Arsenic K-edge XANES spectra for three high arsenic coals from Alabama are shown in Figure 1. It is clear, by inspection, that the spectra are the combination of at least two distinct forms-of-arsenic as the white line features (the prominent peaks near 0 eV) consist of two components. All standards with a single oxidation state of arsenic investigated to date merely give a single component white line, the position of which shifts to higher energy with increasing formal oxidation state of the arsenic atom. Based on comparison of peak positions with standards, the lower-energy component is assigned to arsenic substituting for sulfur in the pyrite structure and the higher-energy component to arsenic in the arsenate anion (AsO_4^{3-}). Furthermore, the radial structure functions (RSFs) derived from the EXAFS region for the high-arsenic coals also show two peaks at the appropriate distances for As-O bonds in arsenate anions and for As-Fe(S) bonds in pyrite (Figure 2). The relative heights of the two peaks in the XANES spectra show the same order as the relative heights of the corresponding peaks in the RSFs.

Arsenic K-edge XANES spectra of three Upper Freeport APCSB coal fractions are shown in Figure 3. In comparison to Figure 1, the signal-to-noise ratio is significantly lower, but the spectra are still informative. In the two fresh samples, there is essentially only one white line component, which arises from arsenic associated with pyrite; only a trace amount (<5% of the arsenic) is present in arsenate form, as indicated by the very small peak on the higher energy side of the white line. The arsenic XAFS spectra of these samples were measured just a few days after opening the APCSB vials. Similar measurements made on whole coal and float/sink samples of the Upper Freeport coal from APCSB vials that had been opened six months previously and left exposed to the laboratory atmosphere showed much greater amounts of arsenate, as for example in the spectrum of the oxidized 2.85 sink sample in Fig. 3. An ash sample prepared from an unrelated Upper Freeport coal showed that all of the arsenic was present in the arsenate form (bottom spectrum, Fig. 3).

Chromium: It is a relatively easy matter to discriminate by means of XAFS spectroscopy among the two most common oxidation states of chromium, Cr^{3+} and CrO_4^{2-} , found in natural and environmental samples. Chromium XAFS spectra of two chromic oxide and two chromate samples are shown in Figure 4. The chromate oxidation state is characterized by the presence of a large pre-edge feature at about 0 eV that is highly distinctive of first series transition metal $3d^0$ species in tetrahedral coordination by oxygen anions. In addition, it should be noted that the maximum absorption in the chromate species occurs at about 40 - 50 eV, at which energy a minimum in the absorption occurs for the Cr^{3+} compounds. These observations appear to be quite general and to apply to all the chromium standards so far examined.

Figures 5 and 6 show chromium XAFS spectra obtained for coal and ash samples. In Figure 5 are shown spectra for the parent Illinois #6 coal and the SOAP cleaned coal. These spectra are virtually identical in appearance and clearly demonstrate that all (>95%) of the chromium is present in the Cr^{3+} oxidation state. In addition, the abundance of chromium in the two samples is essentially the same. These observations suggest that there is only one significant

chromium form of occurrence and that it is not strongly associated with the mineral matter, otherwise the chromium abundance would have dropped significantly upon cleaning and the XAFS spectrum would have shown significant variation. Chromium in the ash sample is also predominantly Cr^{3+} , although the spectral shape differs somewhat from that of the coal samples. The chromium XAFS spectra of the high chromium bituminous coals (Ohio #5 and Illinois #6) shown in Figure 6 are very similar to those shown in Figure 5. The spectrum of the anthracite sample, although similar to those of the bituminous coals, exhibits a somewhat sharper white line peak.

CONCLUSIONS:

This survey study demonstrates that XAFS spectroscopy is capable of obtaining significant information on the oxidation state and form of occurrence of trace elements that exist in coal at about the 10 ppm level. This information complements conventional analytical data on trace element abundances and provides additional information for evaluation of the potential environmental hazard of specific elements in coal combustion. For example, of the two oxidation states of chromium considered here, the CrO_4^{2-} oxidation state is both toxic and carcinogenic, whereas the Cr^{3+} oxidation state at such low concentration levels (<100 ppm) does not pose a significant health risk [9]. If the results of this study can be considered to be general, then the absence of the chromate state in both coal and ash would imply that the hazard posed by chromium in coal utilization is minimal. In contrast, the investigation of arsenic in coal and ash by XAFS reveals significant oxidation of the arsenic associated with pyrite to arsenate (AsO_4^{3-}) species that can be easily leached from coal wastes and which may pose a significant health hazard.

Acknowledgements:

We are grateful to Dr. L. F. Ruppert (U.S. Geological Survey) and Dr. J. Helble (Physical Sciences, Inc.) for their donation of analyzed samples for this study. This study was supported by the Office of Exploratory Research of the Electric Power Research Institute (Palo Alto, CA) under EPRI Contract No. RP-8003-20, and by the U.S. Department of Energy (Pittsburgh, PA) under DOE Contract No. DE-AC22-86pc90751. The XAFS spectra were obtained at the National Synchrotron Light Source at Brookhaven National Laboratory, which is supported by the U.S. Department of Energy.

References:

1. 1992 Keystone Coal Industry Manual, MacLean Hunter Publications, Chicago, IL (1992).
2. H.J. Gluskoter, R.R. Ruch, W.G. Miller, R.A. Cahill, G.B. Dreher, and J.K. Kuhn, Illinois State Geological Survey, Circular 499, 154 pp., (1977).
3. C.A. Palmer, *Energy & Fuels*, **4**, 436-439, (1990).
4. J. Wong, C.L. Spiro, D.H. Maylotte, F.W. Lytle, and R.B. Gregor, in EXAFS and Near-Edge Structure III, (eds. K.O. Hodgson, B. Hedman, and J.E. Penner-Hahn), Springer Proc. Phys. **2**, 362-367, (1984).
5. J.E. Silk, L.D. Hansen, D.J. Eatough, M.W. Hill, N.F. Mangelson, F.W. Lytle, and R.B. Gregor, *Physica B (Proceedings, XAFS V)*, **158**, 247-248, (1989).
6. F.E. Huggins, G.P. Huffman, and S.H. Bauer, *J. Coal Qual.*, **8**(3,4), 119, (1989).
7. L.F. Ruppert, J.A. Minkin, J.J. McGee, and C.B. Cecil, *Energy & Fuels*, **6**, 120-125, (1992).
8. S.P. Cramer, O. Tench, N. Yocum, and G.N. George, *Nucl. Instr. Meth.* **A266**, 586-591, (1988).
9. N. Tietz (Ed.), "Clinical Guide to Laboratory Tests", (2nd. Edition), W. B. Saunders, Philadelphia, PA, (1990).

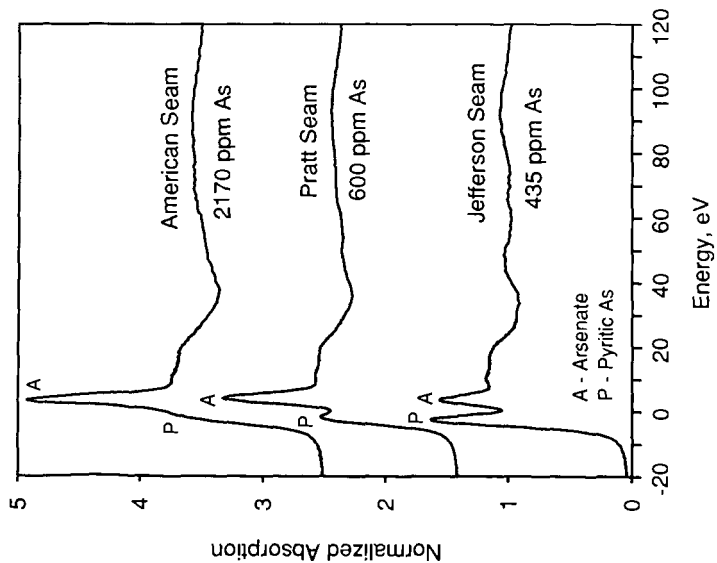


Figure 1: As K-edge XANES spectra of three high arsenic coal fractions from bituminous coal seams in Alabama.

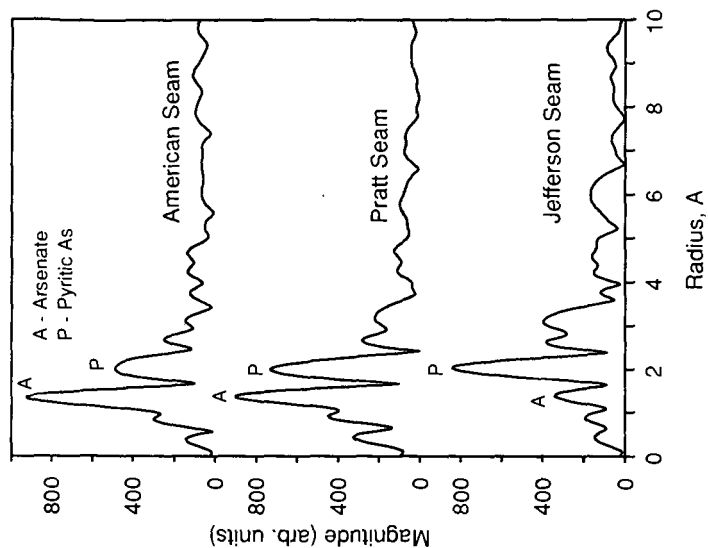


Figure 2: RSFs derived from EXAFS regions of As XAFS spectra for high arsenic coal fractions from Alabama.

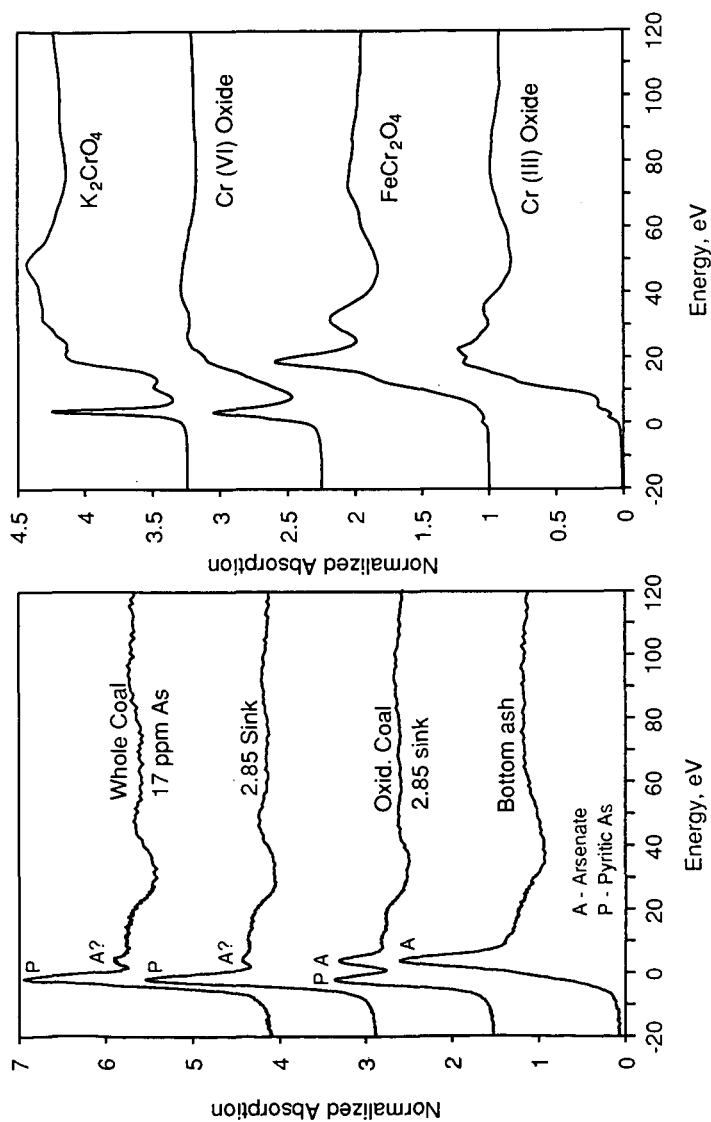


Figure 4: Cr K-edge XANES spectra of two chromic and two chromate oxide reference standards.

Figure 3: As K-edge XANES spectra of three Upper Freeport coal fractions and an ash sample.

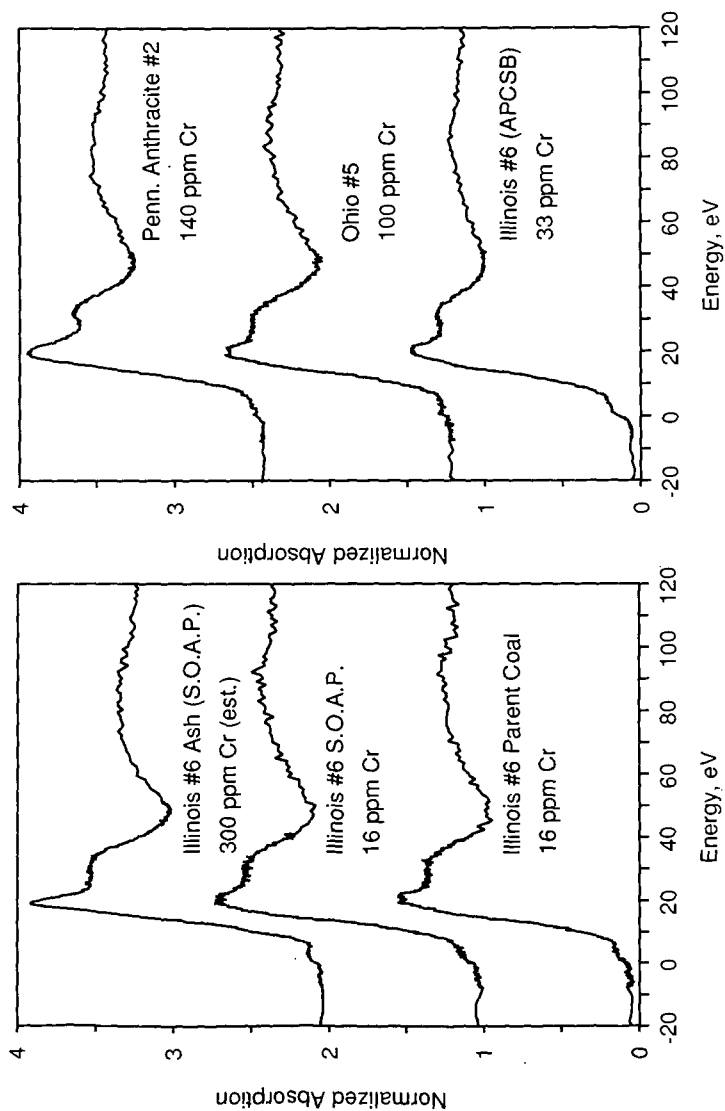


Figure 5: Cr XANES spectra of Illinois #6 parent coal, a cleaned coal, and a derived ash sample.

Figure 6: Cr XANES spectra of three high chromium coal samples.

MULTI-ELEMENTAL ANALYSIS OF ARGONNE PREMIUM COAL SAMPLES BY SIMULTANEOUS PROTON-INDUCED GAMMA-RAY/X-RAY EMISSION SPECTROMETRY

A. S. Wong and J. D. Robertson

*Department of Chemistry and Center for Applied Energy Research
University of Kentucky, Lexington, KY 40506-0055*

Keywords: Argonne Premium Coals; trace elements; PIXE/PIGE

INTRODUCTION

Although the Argonne Premium whole coal samples are widely used by the coal research community,¹ relatively little work has been done on determining the trace element composition of these materials. Of the more than 340 references in the Users Handbook for these reference materials,² only three papers report trace-element concentration data. Instrumental neutron activation analysis (INAA)³, inductively coupled argon plasma-atomic emission spectrometry (ICAP-AES)⁴ and X-ray fluorescence spectrometry (XRF)⁵ have been applied to the Argonne Premium coal samples. The INAA measurements were performed on the whole coals while the XRF and ICAP-AES measurements utilized ashed samples.

We have used external beam proton-induced gamma-ray and X-ray emission (PIGE/PIXE) analysis to determine the concentration of 28 minor and trace elements in 8 Argonne Premium whole coal samples. Briefly, PIGE and PIXE are rapid, nondestructive multielemental analysis techniques that can be *instrumentally* applied to coal, fly ash, and coal derived materials. Because PIGE and PIXE can be applied to whole coal, they can, like INAA, be used to measure elements that might be volatilized during ashing. The other chief advantage of these two ion beam analysis techniques is that they are free of the chemical interference effects that arise in the elemental analysis of such complex matrices by more traditional methods such as ICAP-AES and GF-AAS. In principle, PIXE is capable of determining the concentration of all elements from sodium through uranium with relatively uniform sensitivity. In practice, up to 20 elements are commonly determined per irradiation at fractional mass sensitivities of 1.0 to 10.0 ppm. Unlike PIXE, the sensitivity of PIGE varies greatly from element to element. It does, however, provide concentration information for the light elements lithium, fluorine, sodium and aluminum in these samples.

EXPERIMENTAL PROCEDURE

Sample Preparation. The samples were oven dried for 24 hours at 105 °C and prepared by pelletizing *c.a.* 200 mg of the coal (-100 mesh) in a 13 mm stainless steel die at 90 Mpa. Single and multielemental graphite standards were used in the thick-target PIXE analysis. High purity graphite powder (-100 mesh) was spiked with single (CaCl₂ and KCl) and NIST multielement SRM spectrometric solutions (SRM 3172 and 3174) and dried at 105° for 24 hours. The spiked graphite was then mixed in a methacrylate vial on a mixer mill for 30 minutes and pressed into a 13-mm diameter pellet.

Thick-Target PIGE/PIXE Analyses. The measurements were performed at the University of Kentucky 7.5 MV Van de Graaff accelerator.⁶ The γ -rays were detected with a

HpGe detector with a full-width-half-maximum (FWHM) resolution of 1.87 keV at 1274 keV which was placed 3.0 cm from the target at an angle of 90° relative to the beam direction. The X-rays were detected with a Si(Li) detector with a FWHM resolution of 165 eV at 5.90 keV that was placed 5.4 cm from the target at an angle of 45°. A 700 µm thick mylar filter and a 10 µm thick Cr critical absorber were placed in front of the Si(Li) detector to reduced the bremsstrahlung background and the intensity of Fe X-rays. A total of five irradiations were performed; the critical absorber was removed during two of the irradiations in order to determine the concentration of Cr. All irradiations were performed at 2.5 MeV (on target) with an external proton beam in helium using on-demand beam pulsing. The beam, normal to the target surface, was rastered over the sample at 1 Hz irradiating a spot of 5 mm by 7 mm. The proton beam current, on the extraction foil, ranged from 50 to 100 nA and the irradiation times ranged from 10 to 15 min. per sample. Rather than adjust the beam current to maintain a constant count rate, a pulser was used to correct for the dead time in the PIGE spectra. In this case, the dead time in the PIGE spectra was less than 3% for all coal samples. The accuracy of the measurements was determined by analyzing three NIST coal SRM's (1632a, 1632b, 1635).

RESULTS and DISCUSSION

PIGE Analysis. A typical PIGE spectrum of an Argonne Premium coal sample is shown in Figure 1. The nuclear reactions utilized in the PIGE measurements were ${}^7\text{Li}(p,p_1){}^7\text{Li}$, $E_\gamma = 478$ keV; ${}^{19}\text{F}(p,p_2){}^{19}\text{F}$, $E_\gamma = 197$ keV; ${}^{23}\text{Na}(p,p_1){}^{23}\text{Na}$, $E_\gamma = 439$ keV; and ${}^{27}\text{Al}(p,p_2){}^{27}\text{Al}$, $E_\gamma = 1013$ keV. The concentrations of Li, F, Na and Al were determined by comparison of the normalized γ -ray yields with those obtained from either the NIST 1632a or NIST 1635 coal SRM's. In the comparative method, the concentration of an element (C) is determined by:

$$C = C_{\text{std}} \cdot (Y \cdot S) / (Y_{\text{std}} \cdot S_{\text{std}})$$

where Y is the normalized γ -ray, S is the stopping power of the proton beam (at 2.5 MeV), and C_{std} is the concentration of the element in the standard. NIST 1632a was used as the reference standard for Li and Na in all samples. The Argonne samples with a F concentration of less than 100 ppm and an Al concentration of less than 1 wt. percent were compared to NIST 1635. The PIGE results given in Table I are the average values obtained from 7 irradiations of each Argonne sample. The errors are reported as the standard error of the mean.

The sensitivities for these four light elements in whole coal samples are: Li, 5 ppm; F, 5 ppm; Na, 10 ppm; and Al, 200 ppm. These limits of detection (LOD) are based upon a minimum observable peak area of 3**vbkg** where **bkg** is the background over 1 FWHM about the γ -ray peak's centroid. The relative standard deviation, based upon counting statistics, for a single measurement ranged from 2% to 20%.

The Na concentration values given in Table I agree well with the values determined both by INAA³ and ICAP-AES⁴ and the Al values are in good agreement with those obtained by ICAP-AES.⁴ In the case of Li, the PIGE values for two of the Argonne coals (POC and UT) agree with the FAAS results of Doughten and Gillison.⁴ For the remaining six samples, the PIGE results are consistently lower than the FAAS values. Similarly, the F values given in Table I for the ND, POC, and UT samples are in good agreement with the ISE results of Doughten and Gillison.⁴ Our results for the remaining five samples are, again, considerably lower than the ISE values.

PIXE Analysis. A typical PIXE spectrum of an Argonne Premium coal sample is shown in Figure 2. A comparison of our thick-target PIXE results with the literature values for the NIST SRM's⁷ are given in Table II. With the exception of Cr, Ge, and Th, the values obtained by PIXE in this study agree, within the error bars reported, with the literature values for the NIST SRM's.

The results of the PIXE analysis for 24 minor and trace elements in the Argonne premium coal samples are given in Table I. The errors are the standard error of the mean from the 7 irradiations. In the majority of cases, the PIXE results agree, within the error bars reported, with the values obtained by INAA³ and ICAP-AES.⁴

CONCLUSION

The concentrations of 28 minor and trace elements in 8 Argonne premium coal samples have been determined by simultaneous PIXE/PIGE analysis. In general, the PIXE/PIGE results agree with the values obtained by INAA³ and ICAP-AES.⁴ However, additional analyses are needed to resolve the discrepancy between the Li and F concentration values reported in this work and by Doughten and Gillison.⁴ From previous work on the determination of F in similar reference materials,⁸ we would suggest that a series of pyrohydrolysis measurements could resolve the differences observed for fluorine.

ACKNOWLEDGEMENTS

This work was supported by the DOE Kentucky EPSCoR Doctoral Traineeship Program. We are indebted to H. Francis from the Kentucky Geological Survey for providing the Argonne coal samples used in this work.

REFERENCES

1. Vorres, K. S., *Energy and Fuels* 4, 420 (1990).
2. Vorres, K.S. Users Handbook for the Argonne Premium Coal Sample Program, Argonne National Laboratory, Argonne, IL, ANL/PCSP-89/1 and Newsletter.
3. Doughten, M. W. and Gillison, J. R., *Energy and Fuels* 4, 426 (1990).
4. Palmer, C. A., *Energy and Fuels* 4, 436 (1990).
5. Evans, J. R., Sellers, G. A. and Johnson, R. G., *Energy and Fuels* 4, 440, (1990).
6. Robertson, J.D., Bates, J.B., Dudney, N.J. and Zuhr, R.A., *Nucl. Instr. and Meth. B56/57*, 722 (1991).
7. Gladney, E.S., O'Malley, B.T., Roelandts, I. and Gills, T. E., Standard Reference Materials Compilation of Elemental Concentration Data for NBS Clinical, Biological, Geological and Environmental Standard Reference Materials. NBS Spec. Publ., 260-111, (1987).
8. Wong, A.S., Lurding, E.A., Robertson, J.D. and Francis, H., to appear in the proceedings of The 2nd Int. Conf. on the Elemental Analysis of Coal and Its By Products, G. Vourvopoulos, ed. (1992).

Table 1a. Concentrations of elements ($\mu\text{g/g}$) in 8 Argonne premium coal samples by PIGE/PIXE.

Element	WV	ND	POC	UT	PITT	IL	UF	WY
Li	36 ± 2	**	5 ± 1	5 ± 1	26 ± 3	21 ± 4	26 ± 8	17 ± 2
Na	340 ± 30	5600 ± 500	760 ± 30	1300 ± 170	320 ± 30	1000 ± 55	355 ± 30	1110 ± 90
Al*	2.96 ± 0.12	0.44 ± 0.05	0.53 ± 0.01	0.39 ± 0.03	0.89 ± 0.06	1.14 ± 0.07	1.58 ± 0.09	0.80 ± 0.03
F	130 ± 30	35 ± 6	20 ± 4	56 ± 7	90 ± 40	86 ± 7	86 ± 12	56 ± 9
K	4700 ± 460	320 ± 80	225 ± 90	264 ± 40	1090 ± 30	2330 ± 50	2300 ± 250	230 ± 65
Ca*	0.05 ± 0.01	1.44 ± 0.05	0.42 ± 0.01	0.43 ± 0.02	0.21 ± 0.02	0.88 ± 0.06	0.35 ± 0.01	1.13 ± 0.07
Ti	2860 ± 270	202 ± 6	360 ± 20	217 ± 4	550 ± 30	610 ± 20	620 ± 50	610 ± 50
Cr	37 ± 2	4 ± 1	8 ± 2	7 ± 1	18 ± 1	36 ± 4	23 ± 3	7 ± 1
Mn	12 ± 2	85 ± 9	12 ± 1	5 ± 1	20 ± 4	87 ± 7	27 ± 6	23 ± 5
Fe*	0.39 ± 0.06	0.05 ± 0.03	0.57 ± 0.02	0.28 ± 0.02	1.11 ± 0.01	2.01 ± 0.01	1.35 ± 0.1	0.38 ± 0.01
Co	9.4 ± 3.7	**	3.2 ± 1.4	1.3 ± 0.3	1.5 ± 0.7	**	**	1.0 ± 0.6
Ni	14 ± 3	3.3 ± 0.1	4.1 ± 0.7	5.1 ± 0.1	4.7 ± 0.8	15 ± 3	9.4 ± 1.2	3.5 ± 2.1
Cu	20 ± 4	4.2 ± 1.1	12 ± 1	5.4 ± 0.4	5.1 ± 1.6	7.7 ± 1.1	12 ± 1	15 ± 5
Zn	12 ± 1	5.7 ± 2.5	4.3 ± 1.3	6.8 ± 2.1	9.7 ± 2.1	130 ± 20	18 ± 3	23 ± 7

* Concentrations in weight percent.

** Below detection limit.

Table 1b. Concentrations of elements ($\mu\text{g/g}$) in 8 Argonne premium coal samples by PIGE/PIXE.

Element	WV	ND	POC	UT	PITT	IL	UF	WY
Ga	10 ± 1	**	2.1 ± 0.1	1.5 ± 0.2	3.8 ± 0.6	3.9 ± 0.6	4.3 ± 0.1	3.5 ± 0.5
Ge	1.3 ± 0.8	**	0.8 ± 0.7	**	1.1 ± 0.5	7.0 ± 0.4	4.0 ± 1.3	3.5 ± 0.8
As	6.9 ± 0.4	3.3 ± 0.1	6.9 ± 0.4	1.2 ± 0.8	4.5 ± 0.4	3.2 ± 1.4	11 \pm 1	3.5 ± 0.4
Se	8.0 ± 0.9	2.2 ± 1.2	2.1 ± 0.5	1.9 ± 0.6	2.2 ± 1.0	3.1 ± 0.4	1.4 ± 0.5	1.2 ± 0.1
Br	13 ± 2	0.9 ± 0.4	40 ± 3	1.6 ± 0.4	12 ± 1.5	4.6 ± 0.5	50 \pm 2	2.1 ± 1.1
Rb	34 ± 4	0.9 ± 0.2	6.1 ± 1.3	0.7 ± 0.2	6.7 ± 0.2	16 \pm 2	17 \pm 3	9.6 ± 1.2
Sr	65 ± 5	650 ± 50	100 \pm 2	72 \pm 4	68 \pm 7	28 \pm 1	53 \pm 1	240 \pm 50
Y	12 \pm 1	2.4 ± 1.3	5.8 ± 0.7	2.1 ± 0.5	3.4 ± 0.5	3.7 ± 0.7	11 \pm 1	4.3 ± 1.0
Zr	72 \pm 9	16 \pm 5	12 \pm 2	24 \pm 2	19 \pm 3	16 \pm 2	16 \pm 1	20 \pm 3
Mo	**	**	3.3 ± 1.8	**	**	5.7 ± 0.8	1.5 ± 0.2	2.1 ± 0.4
Ba	140 ± 40	480 ± 60	130 \pm 50	32 \pm 7	37 \pm 6	**	88 \pm 11	270 \pm 31
Pb	3.6 ± 0.6	0.2 ± 0.1	1.3 ± 0.7	1.9 ± 0.6	3 \pm 0.9	2.5 ± 0.8	1.5 ± 0.4	1.4 ± 0.5
Th	4.4 ± 1.0	**	**	0.9 ± 0.2	1.3 ± 0.9	**	2.4 ± 0.5	2.0 ± 0.9
U	1.7 ± 0.7	**	**	**	1.2 ± 0.4	1.7 ± 0.4	2.9 ± 0.8	1.4 ± 0.8

** below detection limit.

Table II. Concentrations of elements ($\mu\text{g/g}$) in NIST coal standards by PIGE/PIXE.

Element	NIST 1632b	NIST 1632a	NIST 1635
K	716 \pm 14 [748 \pm 28]	4310 \pm 310 [4110 \pm 60]	101 \pm 50 [96 \pm 16]
Ca*	0.22 \pm 0.01 [0.20 \pm 0.01]	0.25 \pm 0.02 [0.24 \pm 0.02]	0.55 \pm 0.06 [0.54 \pm 0.03]
Ti	436 \pm 7 [454 \pm 17]	1707 \pm 11 [1750]	187 \pm 11 [202 \pm 6]
Cr	11 \pm 2 [11]	28 \pm 3 [34.3 \pm 1.5]	4 \pm 1 [2.5 \pm 0.3]
Mn	8 \pm 3 [12.4 \pm 1.0]	24 \pm 5 [28 \pm 2]	23 \pm 7 [21.4 \pm 1.5]
Fe*	0.74 \pm 0.02 [0.76 \pm 0.05]	1.10 \pm 0.03 [1.11 \pm 0.02]	0.23 \pm 0.02 [0.24 \pm 0.05]
Cu	5.1 \pm 0.8 [6.3 \pm 0.3]	14 \pm 2 [15.9 \pm 1]	4.8 \pm 2.3 [3.6 \pm 0.3]
Zn	14 \pm 2 [11.9 \pm 0.8]	26 \pm 1 [28 \pm 2]	6.0 \pm 1.4 [4.7 \pm 0.5]
Ga	2.6 \pm 0.2 ---	8.8 \pm 0.9 [8.49]	1.4 \pm 0.5 [1.05]
Ge	2.7 \pm 0.2 ---	3.3 \pm 0.1 [2.5]	1.1 \pm 0.6 [0.5]
As	3.8 \pm 1.1 [3.7 \pm 0.1]	9.3 \pm 1.6 [9.3 \pm 1.0]	** [0.4 \pm 0.2]
Se	1.7 \pm 1.1 [1.3 \pm 0.1]	2.4 \pm 0.5 [2.6 \pm 0.7]	0.8 \pm 0.5 [0.9 \pm 0.3]
Br	18 \pm 1 [17]	41 \pm 1 [41 \pm 2]	1.4 \pm 0.6 [1.4 \pm 0.4]
Rb	** [5.1 \pm 1.1]	32 \pm 8 [30 \pm 2]	0.8 \pm 0.1 [0.9 \pm 0.1]
Sr	98 \pm 2 [102]	77 \pm 3 [85 \pm 6]	139 \pm 14 [121 \pm 19]
Zr	13 \pm 1 ---	52 \pm 5 [53 \pm 5]	17 \pm 4 [16 \pm 2]
Ba	60 \pm 6 [67.5 \pm 2.1]	140 \pm 50 [120 \pm 15]	45 \pm 16 [73 \pm 5]
Th	** [1.3 \pm 0.1]	3.7 \pm 0.1 [4.5 \pm 0.1]	1.4 \pm 0.7 [0.6 \pm 0.1]
U	** [0.4 \pm 0.1]	1.2 \pm 0.3 [1.3 \pm 0.1]	1.1 \pm 0.5 [0.2 \pm 0.1]

[] NIST compilation value* Concentrations in weight percent **Below detection limit.

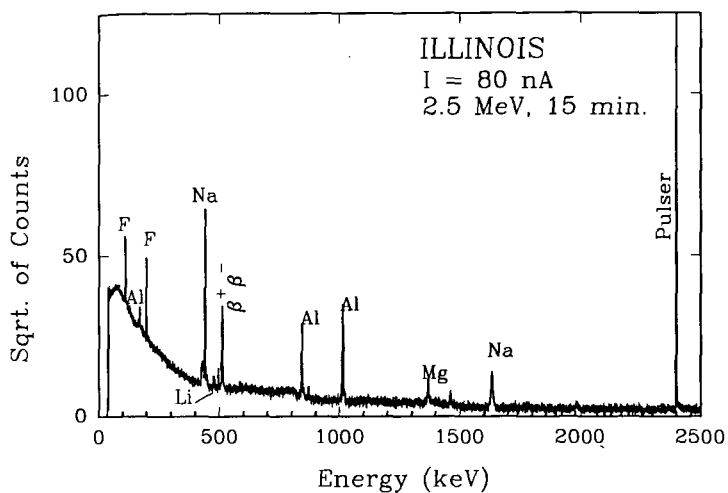


Figure 1. PIGE spectrum of an Argonne premium coal sample.

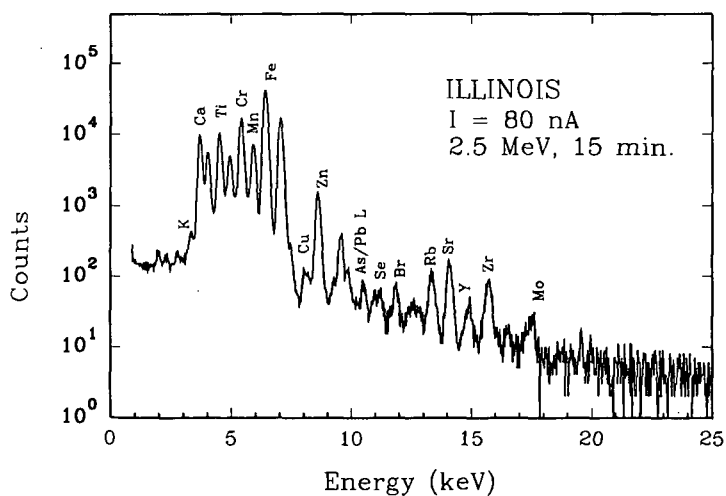


Figure 2. PIXE spectrum of an Argonne premium coal sample with 700 μm mylar and 10 μm Cr filters

STM CHARACTERIZATION OF COAL STRUCTURES, DERIVED EXTRACTS, MODEL
COMPOUNDS, AND GASIFIED CARBONS:

Edwin J. Hippo, Neil Murdie, Jane F. Byrne, and Eric B. Sebok
Mechanical Engineering and Energy Processes
Southern Illinois University, Carbondale
Illinois 62901

KEYWORDS: Scanning Tunneling Microscopy

ABSTRACT

Techniques for characterizing coal and coal derived structures using scanning tunneling microscopy are being developed. These techniques allow surface structures of coal to be viewed with a fraction of an angstrom resolution. Images of inertinite structures have been obtained. A monolayer of THF extract from an Illinois #6 coal was deposited on HOPG and images obtained. One of the difficulties in interpreting the images is lack of knowledge about the tunneling efficiencies of various functional groups. Model compounds are being deposited onto well oriented surfaces and images at different bias and gain settings are being obtain to determine if spectral analysis can spot oxygen, sulfur, and nitrogen atoms in their various chemical forms thought to be present in coal. Analysis of pits formed from the gasification of HOPG have shown that oxygen complexes can be identified, pitting mechanisms can be followed and initial direction of gasification can be deduced. There is some evidence that oxygen complexes can form between carbon atoms of two different planes.

INTRODUCTION

The scanning tunneling microscope (STM) was invented in 1982 by Binnig and Rohrer(1), who were awarded the Nobel Prize in physics for their work. The STM operates on the principle that a tunneling current can be established between an anatomically sharp tip and the surface electronic orbitals near the Fermi level of a sample(2). An image is obtained by scanning the tip across a samples surface with the use of a set of three piezo electric crystals(3). A voltage is applied to the crystal controlling the z-direction (the distance between the tip and the sample surface). The tip is then lowered until the tip crashes into the surface(non-conducting material) or a tunneling current is established(conducting material). Once the current is established, work functions can be measured over a certain spot or xyz images can be obtained. The images are obtained by one of two operating modes. In the constant current mode varying voltages are applied to the x and y crystals which drives the tip first across the surface in the x-direction and then increments the y-spacing and drives the tip in the reverse x-direction. A feedback loop measures current and adjusts the voltage on the z-direction crystal. This raises and lowers the tip. Since current is highly dependent on distance from the surface, the variation in z-distance allows a constant current to be maintained. A computer keeps

track of the z variations in a xy matrix which is transformed by using Fourier analysis into a three dimensional image. A second mode of operations employs a constant z-setting and as the tip moves variations in current are recorded. The current xy matrix is then converted to an image.

The actual image obtained is a charge density map of the eigen states localized above a surface(4). This means that the images should be viewed in terms of electronic interactions(5,6). Interpretation of the images is therefore dependent on complex theories. Although this should be kept in mind, the images can be viewed as simple atomic geometries (5,6). For well ordered systems including silicon, gold, platinum and highly ordered graphite(7,8,9, and 10) the atomic spacings and orbital shapes agree with X-ray, and TEM data, and HMO theory.

STM is dependent on the conductivity of the sample being imaged. However if a sample is non-conducting then atomic force microscopy (AFM) can be used (11-15). AFM is a closely related offshoot of STM. It drags a diamond tip across the sample surface and measures the repulsion of the tip from the sample surface. The tip is set on a cantilever and a laser beam is used to measure the deflection of the cantilever. This technique is not as highly developed as STM imaging but has been used to investigate structures of polymers and ceramics.

Depending on scan size of the STM image; resolution as low as 0.01 nanometers for lateral and 0.001 nm for vertical measurements can be obtained. Scan size can be varied from 14x14 microns to 2x2 nanometers. The depth of resolution is much greater than for SEM and TEM. In addition little or no sample preparation is required and the instrument can be operated under ambient environments with little sample preparation. Thus, surfaces can be examined in far greater detail than previously and with much less degradation of the sample. These capabilities make STM an ideal candidate for application to in situ coal structure determinations and the study of coal reactions in various conversion technologies.

The purpose of this paper is to describe some preliminary work on applying STM to coal analysis and utilization technology. To the authors knowledge this is the first work to obtain actual images of coal and coal derived materials. The paper also discusses methods used to follow gasification of highly oriented pyrolytic graphite(HOPG).

EXPERIMENTAL

All STM nanographs were obtained using a nanoscope II scanning tunneling microscope manufactured by Digital Instruments of Santa Barbara Ca. Details of the operating procedures can be found in reference (16). The HOPG was obtained from Union Carbide. An Illinois #6, IBCSP 101, coal was used to obtain extract and Maceral concentrates. Maceral concentrates were obtained employing a density gradient centrifugation procedures described elsewhere(17,18). THF extraction was carried out in a soxhlet extractor for 48 hours. About 20 grams of coal are extracted with 150 mls of THF. The average yield is 16% solubles based on weight of dry solids recovered after extraction.

STM ANALYSIS OF COAL

The first attempt to image coal was made by polishing a block of coal, painting the back of the block with a conducting paint, and mounting the block on the STM base. Blocks were mounted with the tip perpendicular and parallel to the bedding plane. The instrument allows various gains and bias to be set along with scan rate and size. The tip crashed into the surface whenever engagement was attempted.

During engagement the tip is lowered manually to within 250 microns of the surface using a set of position bolts which are turned to raise or lower three ball bearings on which the STM scan head sets. The software package is then activated and automatically lowers the tip to the surface. As the tip approaches the surface it will begin to tunnel if the sample is conducting but the program will continue to lower the tip into the sample if a tunneling current is not established. Since the tip must be atomically sharp, lowering the tip too far will blunt the tip and good images will not be obtained with that tip. Since tips are expensive, this approach was abandoned after 20 attempts.

Next, particles of whole coal were scattered on the STM base. The coal was ground in a fluid energy mill prior to mounting. The smaller particles of coal were expected to be more conductive. A scan of the base was made to determine its structure before attempting to analyze the coal particles. During engagement the tip would either push particles aside and engage the base, or pin a particle and bend the tip.

Steel slides were then prepared, painted with conducting paint and coal dust was sprayed over the wet surface. This method produced a sample which could be imaged. Blank painted slides were also imaged. Although there are some differences between the blank slides and the images obtained with whole coal particles, it is difficult to describe these (slides will be shown at the presentation). The percentage of successful engagements range between 50 and 70%. To obtain a clearer understanding of what was imaged, the process was repeated on sporinite, cutinite, vitrinite, inertinite, and mineral concentrates. The liptinites and mineral fractions could not be engaged. The Vitrinite concentrates had a 40% engagement rate and the inertinite had a 90% engagement rate. This follows the general order of conductivity of the macerals. Since most of the mineral in this coal was clay this fraction was also expected to be nonconductive.

Because of the problem with imaging the painted surfaces as well as coal particles, another approach was attempted. Coal macerals were physically pressed into a wafer with the aid of a hydraulic press. The back of the wafer was painted and the sample was mounted. Engagement was obtained for the inertinite wafer only. The images obtained with the inertinite wafer were identical to those obtained from the painted slide method. Not much can be said about the chemical structures imaged at this point. This is because there is little known about tunneling of organic structures. A good deal of model compound work will need to be carried out. It can be said that the imaged orbitals vary a great deal but the significance of these variations can not be estimated at this time. More can be said about the size and shape of the pore openings. When scanned on the nanometer range; pore diameter ranges between 5 to 20 angstroms. About half of the pores

have circular openings and half slit shape openings. Area of the slit shaped openings were greater than those of the circular openings.

SOLVENT DEPOSITION

Those carbon materials which are unsuitable for STM studies due to their poor conductivity, porosity, and surface heterogeneity may be imaged, in some cases, by depositing a dissolved portion (from solution) onto HOPG in very small amounts. The tetrahydrofuran (THF) soluble portion of Herrin, IL No.6 coal, as well as materials such as n-dotriacontane ($n\text{-C}_{25}$), which readily dissolve in heptane, were analyzed. These solvents (THF and heptane) do not alter the HOPG surface. Blank experiments were carried out by pipeting drops of solvent on newly cleaved HOPG surfaces. After the solvent evaporates the hexagonal basal plane image of the HOPG is observed. This is somewhat unexpected because even the purest solvent contain some residual material. A quick calculation shows that the concentration is high enough to more than cover the HOPG surface. However, their usage did not effect STM images. Upon evaporation solvent/solute mixtures left behind deposited material that could be imaged.

The THF extract was diluted from its original concentration of about 0.02 gram/ml by an approximate ratio of 10:1. A portion of this solution was further diluted to approximately 100,000:1 in increments of 10:1, until STM images showed only a thin layer deposited onto the HOPG. Deposition was carried out using a pipette to place a drop of the diluted solution onto the HOPG. The THF was allowed to evaporate, leaving behind a thin layer of coal extract. The specimen could then be placed directly onto the sample stage for STM imaging. This technique is suitable for molecules with large atomic weights which adsorb strongly to the graphite surface.

Although areas could be imaged where more than a single monolayer are present these images where chaotic and individual structures were not easily recognized. A monolayer of the deposited material (or scattered areas of monolayer) gave very clear images. Various aromatic compounds are evident, as well as side-chains branching off from these rings. The images are easily differentiated from the defined HOPG basal plane surface. HOPG is an ideal substrate for organic molecules which align with the basal plane and adsorb fairly strongly, depending on the size and planarity of the molecule.

The n-dotriacontane/heptane solution was created by dissolving n-dotriacontane in heptane. This solution was deposited onto the HOPG with a micropipette. The sample was then placed directly onto the sample stage for STM imaging.

The $n\text{-C}_{25}$ on the surface of the HOPG gave spacings of 0.30 nm, instead of 0.25 nm, between hexagon centers of the HOPG. An elliptical shape of many of the atoms was due to the hydrogen atoms attached to the carbon atoms, and the carbon atoms themselves are imaged as one. A somewhat repeating pattern on the surface was observed and believed to be due to the fact that the $n\text{-C}_{25}$ molecules align themselves along the carbon atoms of the top basal plane layer. Other compounds such as steroids, acids, alcohols have

been imaged by others using a similar technique(19). Other model compounds such as dibenzothiophene,, thiols, carbazol and others scheduled for analysis in the near future.

GASIFICATION OF HOPG

In this portion of the program HOPG was exposed to air oxidation at 650°C in a TGA system until 5 and 30% burnoff was reached. After various exposure times the size, shape, and distribution of pits and the linear dimension of the graphite were determined. The STM was used to image the pits, determine the direction of oxygen attack and to determine the amount and type of oxygen complexes on the surfaces of the graphite. In the initial stage of pit formation at 5% burnoff, the pits seem to align in a parallel orientation. Also some pits extend 3-5 layers deep without enlarging. The familiar large hexagonal pits are formed by the 30% weight loss level. A zoom into the base of the pits formed at 30% weight loss showed that although the large scale hexagonal morphology is observed; attack on pristine planes is linear. Long parallel high points were observed at the end of narrow elongated pits. These high points or streaks were originally thought to be carbon atoms but cross-sectional analysis showed them to have bond lengths indicative of adsorbed oxygen molecules. The length of the streaks are multiples of 4.2 angstroms which indicate attack parallel to the 101 face. We are not sure if this is indicative of catalytic attack or if the highly oriented graphite contains a large amount of elongated crystalites. It is possible to measure bond length and depth of penetration using the cross sectional analysis routines which were provided with the STM. By measuring heights from the base of pits it is possible to obtain an idea of the composition of the atoms in the pit. For example, if the vertical distance is 3.35 angstroms then the pit is one layer deep assuming that the atoms at the pit base are carbon. Likewise an atom appearing 6.7 angstroms above the pit floor would be a carbon atom 2 layers above the floor of the pit. It is interesting to note that 3.53 and 3.22 angstroms are encountered in measurements more often than 3.35(the ideal basal plane spacing) These measurements are probably the results of edge carbon atoms wagging up or down around the pit edge. This is reasonable. In fact, edge sites on a graphite model behave the same way. Also values between these measurements are not encountered very often. Thus, any multiple of 0.35 plus or minus the wag distance of 0.12 angstroms is likely to be carbon. Alternately measurements of 3.35 multiples plus or minus 0.75 and 1.5 are observed. these appear to be oxygen complexes. These values appear over and over again. The large pits have nearly vertical walls (slope > 75°) these walls are over 500 layers deep. Cross sectional analysis of smaller pits vary in angle depending on size. Some are steep like the larger pits but some have gentle slopes which seem to indicate that oxygen forms adsorbed species between layers. A similar effect was observed on edge cite studies(20.).

CONCLUSIONS

STM has been shown to be a powerful tool for exploring atomic structures of coal and graphite. Additional work is required to assign structures, but the techniques developed in this study demonstrate that it is possible to image coal and coal derived material.

ACKNOWLEDGEMENTS

This work has been sponsored by the Department of Mechanical Engineering and Energy Processes Southern Ill. University. Dr. Robert Clarkson of Univ. of Ill. and Dr. J. Crelling of SIU supplied pressed wafers.

REFERENCES

1. G. Binnig and H. Rohrer, Scanning Tunneling Microscopy, *Helv. Phys. Acta.*, **55**, pp.726-735 (1982)
2. P. C. W. Davies, Quantum Mechanics, Routledge and Kegan Paul, London, U.K. (1984).
3. P.K. Hansma, J. Tersoff, "Scanning Tunneling Microscopy". *Journal of Applied Physics*. **61**(2), pp. R1-R3, January 15, 1987.
4. C.J. Chen. "Theory of Scanning Tunneling Spectroscopy". *Journal of Vacuum Science and Technology*. Vol. A **6**(2),
5. P. Batra, et al. "A Study of Graphite Surface with STM and Electronic Structure Calculations". *Surface Science*. Vol. **181**, pp. 126-138, 1987.
6. S. Gauthier, et al. "A Study of Graphite and Intercalated Graphite by STM". *Journal of Vacuum Science and Technology*. A **6**(2), pp. 360-362, Mar./Apr. 1988.
7. R.M. Tromp, et al. "Atomic and Electronic Contributions to Si(111)-(7X7) STM Images". *Physical Review*. **B15**, Vol. **34**, No. **2**, pp. 1388-1391, 1986.
8. P. N. First, J.A. Stroscio, R. A. Dragoset, D. T. Pierce, and R. J. Celotta, *Physical Review Letters*, **63**, No. **13**. pp. 1416-1419(1989).
9. J. Schneir, H. H. Harary, J. A. Dagata, P. K. Hansma, and R. Sonnefeld, *Scanning Microscopy*, **3**, No. **3**, pp. 719-724(1989)
10. Sebok, E.B., Hippo, E.J., Murdie, N., Byrne, J.F., and Rehak, J., "Scanning Tunneling Microscopy of Various Carbon Materials," *Materials Technology Center 7th Annual Conference*, 111-117, SIUC, April 10-11, 1991.
11. P.K. Hansma, et al. "Scanning Tunneling Microscopy and Atomic Force Microscopy: Application to Biology and Technology". *Science*. Vol. **242**, pp. 209-216, Oct. **14**, 1988.
12. I.P. Batra, S. Ciraci. "Theoretical STM and AFM Study of Graphite Including Tip-Surface Interaction". *Journal of Vacuum Science and Technology*. A **6**(2), pp. 313-318, Mar./Apr. 1988.
13. R. Pool. "Children of the STM". *Science*. Vol. **247**, pp. 634636, Feb. **9**, 1990.
14. E. Meyer, J. Frommer. "Forcing Surface Issues". *Physical World*. pp. 46-49, Apr. 1991.

15. A.L. Wersenhorn, et al. "Molecular Resolution Images of Langmuir-Blodgett Films and DNA by Atomic Force Microscopy". *Langmuir*. Vol. 7, No. 1, pp. 8-12, 1991.
16. Digital Instruments, Nanoscope II Instruction Manual, Version 5, 6780 Cortona Dr., Santa Barbara, California, 93117.
17. Crelling, J.C., Hippo, E.J., Woerner, B.A., and West, D.P., "Combustion Characteristics of Selected Whole Coals and Macerals," *Fuel* (in press).
18. Hippo, E.J., Crelling, J.C., and Mukherjee, J., "Desulfurization of Single Coal Macerals," *Fuel Processing Technology*, 27, 287-305, 1991.
19. J. P. Rabe, and S. Buchholz, *Science*, 253 pp. 424-426, July 1991.
20. Sebok, E.B., Hippo, E.J., Byrne, J.F., Rehak, J., and Murdie, N., "Scanning Tunneling Microscopy of Various Carbon Materials," *Proceedings of 20th Biennial Conference on Carbon*, 418-419, Santa Barbara, CA, June 24-28, 1991.

AN APPARATUS FOR IN-SITU HIGH TEMPERATURE/HIGH PRESSURE ESR SPECTROSCOPY AND ITS APPLICATIONS IN COAL CONVERSION STUDIES

Manjula M. Ibrahim and Mohindar S. Seehra, Physics Department,
West Virginia University, Morgantown, WV 26506

Keywords: hydroliquefaction, coal, free radicals, ESR

Abstract

An apparatus for carrying out in-situ ESR (Electron Spin Resonance) spectroscopy studies from ambient to 500°C and for gaseous pressures up to 800 psi at x-band frequencies (~9 GHz) is described. ESR signals can be monitored as a function of time, temperature or pressure in the above stated ranges. Using this apparatus, results on the hydrogenation of a Blind Canyon coal carried out at 440°C in hydrogen pressures up to 600 psi, and with and without the shell 324 catalyst (presulfided $\text{NiMo}/\text{Al}_2\text{O}_3$), are described. A non-linear decrease of the free radical density with H_2 pressure is observed and the catalyst increases the free radical density. Significance of these results is discussed.

Introduction

The fundamental mechanisms of coal pyrolysis and direct hydroliquefaction are believed to involve free radicals and the interaction of the free radicals with available hydrogen.^(1,2) Generally accepted view of pyrolysis is that thermally generated free radicals extract internal hydrogen from coal to form tar or combine with other coal molecules to form high molecular weight char. In hydroliquefaction, when hydrogen is available readily from a donor solvent and/or molecular H_2 , free radicals extract this hydrogen to produce low molecular weight product.^(1,2) In order to provide direct evidence for these views, direct and in-situ monitoring of the free radicals during pyrolysis and hydroliquefaction is necessary. In previous papers from this laboratory,⁽³⁻⁷⁾ we have used the in-situ ESR (electron spin resonance) spectroscopy of free radicals in coals to investigate pyrolysis and the effect of zinc halide catalysis in coal conversions. These studies were however carried out either in vacuum-sealed samples or in flowing gases (N_2 and H_2). Since direct hydroliquefaction is usually carried out under high pressures (1000-3000 psi) of hydrogen, it is essential to carry out ESR measurements under the realistic conditions of high temperatures/high pressures. Here we describe a microwave cavity system in which in-situ ESR spectroscopy can be carried out at temperatures up to 500°C and gaseous pressures up to 800 psi (pressures are limited by the use of the pyrex tubes). The design of our apparatus differs significantly from that reported by Petrakis and Grandy⁽²⁾ but somewhat similar to that described by Yokono et al.⁽⁸⁻¹⁰⁾ The major improvement in our apparatus is that pressure can be varied in-situ at a given temperature. Using this apparatus, we have investigated the hydrogenation of a Blind Canyon coal as a function of H_2 pressure at 440°C, with and without a catalyst. This apparatus, along with the results of these experiments, are described in this paper.

High Temperature/High Pressure ESR Cavity System

The high temperature/high pressure ESR cavity system consists of three primary units: (i) A rectangular TE_{102} cavity in which the field modulation coils are located outside the cavity and a circular hole through the center of the cavity which allows the insertion of the quartz dewar and the sample; (ii) A heating unit external to the cavity (see Fig. 1) and purchased from Wilmad Glass Co. in which a flowing N_2 gas over a voltage-controlled chromel heater is used to deliver heat to the sample without heating the microwave cavity; and (iii) a high pressure unit (Fig. 2) to which a pyrex ESR tube is attached which can be inserted in the TE_{102} cavity. If the sample is to be exposed to a flowing gas (such as N_2 or H_2), then the high pressure unit is replaced by the flow-chamber unit shown in Fig. 3, a description of which was also given in our recent paper.⁷ Thus in this apparatus, the cavity remains at ambient temperature and pressure and no cooling coils as for example used in the design by Yokono et al.⁽⁸⁻¹⁰⁾ are used anywhere in the apparatus. The system is pressurized directly from a gas cylinder and so the pressure can be easily changed during the course of the experiment. The maximum pressure is limited by the strength of the ESR tube and in our experiments, the pyrex and quartz tube could not withstand pressures beyond 800 psi. To attain higher pressures, search for a better non-conducting material for the ESR tube is underway.

There are several special features of the high pressure unit which deserve special mention. As shown in Fig. 2, the ESR tube is screwed to a stainless steel (#316) tube which in turn is connected to a high pressure gage and a valve to let in or shut off the gas supply. A Swagelok quick-connector connects this attachment to a stainless-steel bellow-type tube leading to the gas cylinder. To secure the sample tube firmly with the attachment, a stainless steel nut is glued to the tube using a high pressure glue (Torr-seal by Varian) and a stainless-steel block holds the tube below the nut giving additional support. The large temperature gradient between the bottom of the tube where the sample is kept and the top of the tube where the high pressure attachment is connected eliminated the need for any cooling of the tube. The high-temperature quartz dewar which is inserted in the hole of the TE_{102} cavity, has an evacuated double-wall ensuring only minimal heat transfer from the sample to the cavity. The gage connected to the tube enables direct reading of the inside pressure during experiment. Since inserting a thermocouple inside the cavity distorts the microwave signal, the thermocouple is placed outside, just at the cavity entrance. The temperature is calibrated by an initial run with an additional thermocouple inside the sample, the experiment being carried out under realistic identical conditions. In the heater unit, the temperature is controlled by the voltage input to the heater, controlled by a variable transformer. For each data point, at least 10 minute interval is allowed to ensure temperature stability.

Experimental Procedures

All experiments reported here were carried out with the Blind Canyon coal, DECS-17, obtained from the coal bank of the Pennsylvania State University. In Table I, we list the proximate analysis, the ultimate analysis and the maceral content of this coal as provided by the coal bank. A presulfided catalyst, Shell #324 ($NiMo/Al_2O_3$) was obtained from the Consolidated Coal Co. An x-ray diffractogram of this catalyst is shown in Fig. 4. Not all the Al_2O_3 oxides lines are observed. From the two prominent lines observed near $2\theta \approx 46^\circ$ and $2\theta \approx 67^\circ$ and

using the Scherrer eq. $L = (0.9)\lambda/\beta \cos\theta$ (where L is the particle dimension, β is the corrected linewidth and λ is the x-ray wavelength) and the procedures outlined in our recent paper,⁽¹¹⁾ we find $L = 38 \text{ \AA}$ for the $2\theta \approx 38^\circ$ line and $L = 42 \text{ \AA}$ for the $2\theta \approx 67^\circ$ line. These measurements show that for the 324 catalyst, the average particle size $\approx 40 \text{ \AA}$. In our experiments, the 324 catalyst was dry mixed with the coal, in the ratio of 2.1% by weight of the coal.

The free radical density N is calculated by double integration of the derivative ESR spectra using an on-line computer and comparing it with a standard.⁽⁴⁾ Also the values of N are corrected for the Curie-law variation of the spins with temperature i.e. $N = N_T(T/RT)$, where N_T is the measured value at a temperature T in degrees Kelvin and RT is the room temperature in degrees Kelvin. If there is no change in the free radical concentration with temperature, then N will be independent of temperature and a plot of N vs T will be a horizontal line. To account for any changes in mass with temperature, thermogravimetric studies using the Mettler 3000 TG system were done. Typically 10 mg of the sample was heated in an alumina cell from 30°C to 600°C at a heating rate of $10^\circ\text{C}/\text{min.}$, in flowing N_2 and H_2 gases.

Results and Discussion

In Figs. 5 and 6, results of the thermogravimetric studies of the change in weight of the coal and the coal with catalyst, as a function of temperature and in flowing N_2 and H_2 gas, are shown. Two results are evident: more volatiles are lost in H_2 flow and second, the catalyst significantly reduces the evolution of volatiles in the presence of N_2 . These data were used to correct the free radical density N/mass for experiments carried out in N_2 and H_2 flow.

In Fig. 7, we have plotted N against temperature for the Blind Canyon coal under three conditions: (i) sample sealed under vacuum; (ii) experiments in flowing N_2 ; and (iii) experiments in flowing H_2 . For these cases, the variations of N with temperature are similar except above about 400°C , where N is lower in H_2 flow. This difference persists (shown in insert) even after applying the mass correction for N_2 and H_2 flow experiments. The lowering of N in H_2 flow is presumably due to capping of the free radicals by H_2 . Discussion of this variation of N with T , somewhat similar to the observation in other coals, is given in our earlier publications.^(3,4)

The effect of 2.1% loading of the coal with the 324 catalyst on N is shown in Fig. 8 where the experiments were carried out in flowing H_2 gas and the data are corrected for the change in mass from Figs. 5 and 6. These studies clearly show an additional mechanism for the generation of the free radicals by the catalyst. No additional details about this mechanism are, however, available at this time.

Since most of the experiments in direct coal liquefaction are carried out above 400°C and in H_2 pressures, we studied the variation of N as a function of pressure but at a fixed temperature of 440°C . A novel feature of our apparatus is that pressures can be varied in-situ. Results of N vs pressure are shown in Fig. 9, for the cases of coal and coal with catalyst in both H_2 and Ar gases. We used Ar gas suspecting that N_2 may have some effect on N . However later experiments showed that just as in Ar gas, there is no variation of N with N_2 pressure either. In H_2 pressure, however, there are significant changes in N with pressure as the

results in Fig. 9 show. For the coal alone, N decreases nearly linearly with P with initial pressures, approaching saturation above 400 psi. For the catalyst loaded coal sample, N increases slightly with initial pressures of H_2 but above 150 psi, N decreases nearly linearly with H_2 pressure. From these experiments, it is quite evident that molecular H_2 caps at least some of the free radicals whereas in the presence of the 324 catalyst, an additional mechanism for the generation of free radicals is operative.

There are only two reports available in literature on the variation of N with pressure in coals. Earlier studies by Petrakis and Grandy⁽²⁾ were done at two pressures viz. 1200 and 1600 psi of H_2 gas in the presence of tetralin. These studies showed no change in N with pressure, although the presence of tetralin which is an excellent hydrogen donor might have obscured the effect of H_2 . On the other hand, it is possible, that as we observe in Fig. 9, the effect of H_2 is saturated above about 400 psi in the absence of a catalyst. Yokono et al⁽⁸⁻¹⁰⁾ measured N at 6 and 13 MPa of H_2 and N_2 (1 MPa \approx 145 psi) and found that H_2 aids in capping some of the free radicals. The results presented here in Fig. 9 are unique in that for the first time, a systematic study of N with H_2 pressure in the absence of tetralin is now available.

The results presented above have demonstrated that molecular H_2 is involved in free radical quenching reactions, supporting the hypothesis forwarded by Vernon.⁽¹²⁾ More recent studies on model compounds by McMillan et al⁽¹³⁾ and by Shin et al⁽¹⁴⁾ on the Argonne coals have shown that hydrogen can also take part in the hydrogenolysis of strong Car-Calk bonds. Similar observations were made on hybrid studies in which known structures were either mixed with⁽¹⁵⁾ or grafted to coal.⁽¹⁶⁾ Although there is no direct proof of hydrogenolysis from our studies, the quenching of the thermally generated free radicals upon hydrogenation is quite evident. In addition, significant enhancement of the free radical density in the presence of 2.1% loading of the coals by the 324 catalyst provides strong evidence for catalytic cracking of coals. There is some evidence from the data in Fig. 9 that for initial H_2 pressure, this catalytic hydrogenolysis is more significant than the quenching mechanism for hydrogenation. Additional experiments in the presence of hydrogen donor solvents such as tetralin are now planned to further elucidate these mechanisms.

Acknowledgments

The authors thank C. Weber, T. Milam and C. Sicina for their assistance in fabricating the high temperature/high pressure apparatus, and S. D. Brandes of Consolidated Coal Co. for providing the Shell 324 catalyst used in these experiments. This research was sponsored by the U.S. Department of Energy under DOE Contract No. DE-FC22-90PC90029.

References

1. Neavel, R. C. Fuel 1976, 55, 237-242.
2. Petrakis, L. and Grandy, D. W. 'Free Radicals in Coals and Synthetic Fuels' 1983 (Elsevier Science Publication Co. N.Y.).
3. Seehra, M. S.; Ghosh, B.; and Mullins, S. E. Fuel 1986, 65, 1315-1316.
4. Seehra, M. S. and Ghosh, B. J. Anal. Appl. Pyrolysis 1988, 13, 209-220.
5. Seehra, M. S.; Ghosh, B.; Zondlo, J. W.; and Mintz, E. A. Fuel Process. Technol. 1988, 18, 279-286.
6. Ibrahim, M. M.; Seehra, M. S.; and Keogh, R. Fuel Process. Technol. 1990, 25, 215-226.
7. Ibrahim, M. M. and Seehra, M. S. Energy & Fuels 1991, 5, 74-78.
8. Yokono, T.; Iyama, S.; Sanada, Y.; Shimokawa, S.; and Yamada, E. Fuel 1986, 65, 1701-1705.
9. Yokono, T.; Iyama, S.; Sanada, Y.; and Makino, K. Carbon 1984, 22, 624-626.
10. Yokono, T.; Iyama, S.; Makino, K.; and Sanada, Y. Fuel 1985, 64, 1014-1026.
11. Ibrahim, M. M. and Seehra, M. S. J. Mater. Res. 1992, 7, No. 7 (in press).
12. Vernon, L. W. Fuel 1980, 59, 102-106.
13. McMillen, D. F.; Malhotra, R.; Hum, G. P.; and Chang, S. J. Energy & Fuels 1987, 1, 193-198.
14. Shin, S.-C.; Baldwin, R. M.; and Miller, R. L. Energy & Fuels 1989, 3, 71-76.
15. McMillen, D. F.; Malhotra, R.; Chang, S. J.; Ogier, W. C.; Nigenda, S.E.; and Fleming, R. H. Fuel 1987, 66, 1611-1618.

Table 1: Relevant analysis of Blind canyon coal-DECS-17. Data obtained from Penn State Coal Bank.

proximate analyses (DAF %)		ultimate analysis (DAF %)		maceral content (DMMF vol%)	
volatile	50.04	C	81.61	inertinite	2.1
fixed C	44.93	H ₂	6.21	exinite	11.2
		N ₂	1.38	vitrinite	79.7
		total S	0.47	fusinite	6.0
		O ₂ (diff)	10.33		

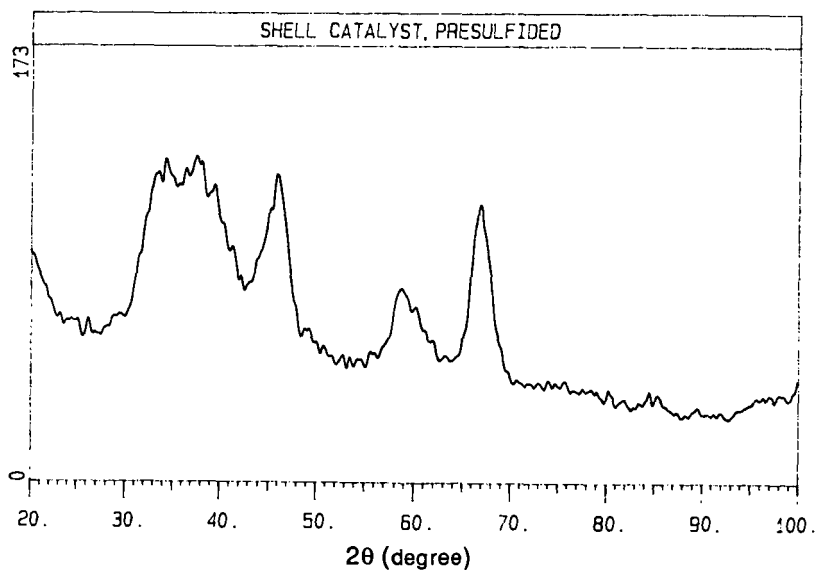


Figure 1: X-ray powder diffractogram of the catalyst, shell 324.

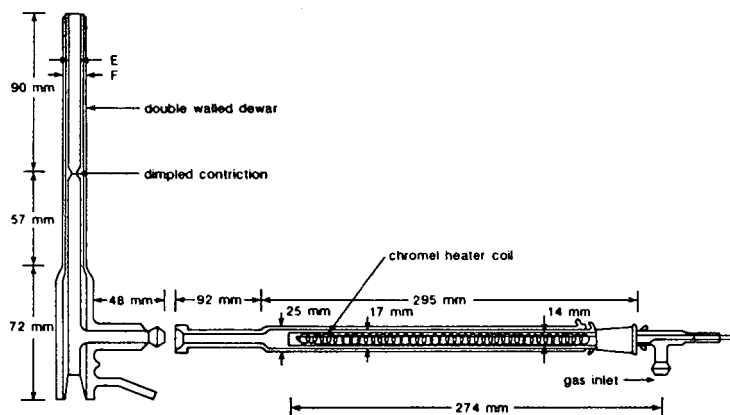


Figure 2: Block diagram of the high temperature dewar for ESR cavity

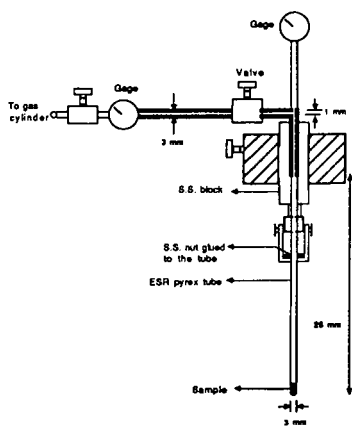


Figure 3 : Block Diagram of the high pressure set up fabricated for in-situ experiments up to 800 psi of any gas and up to 500 °C

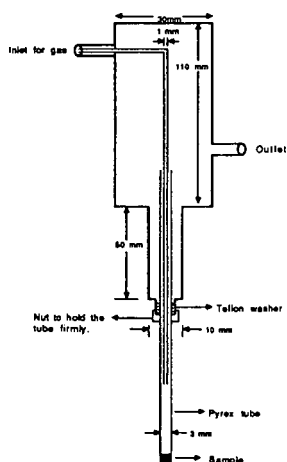


Figure 4 : Diagram of the flow chamber used for experiments under flowing gas.

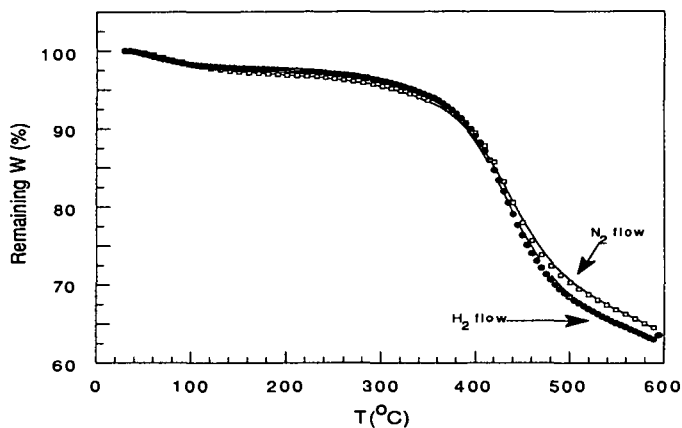


Figure 5: Remaining weight of blind canyon coal plotted against temperature, from TG experiments under nitrogen/hydrogen flow.

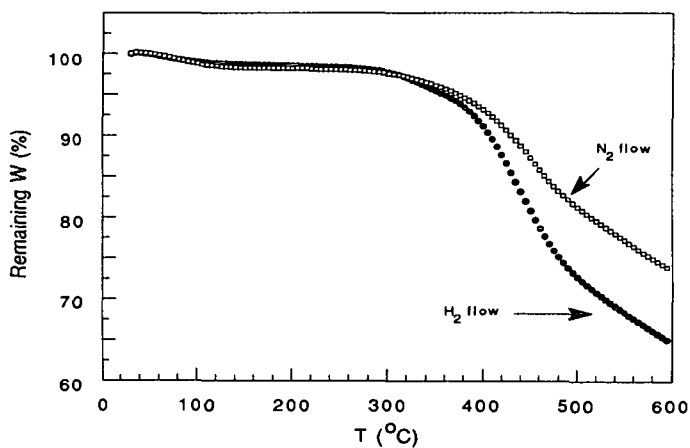


Figure 6: Variation of remaining weight with temperature for blind canyon coal mixed with 2.1% shell 324, under nitrogen/hydrogen flow.

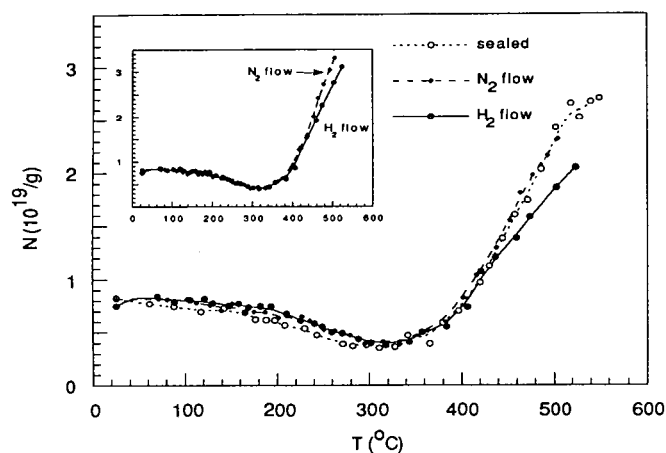


Figure 7: Variation of N with T for blind canyon coal. Plot after applying mass correction is shown in the insert.

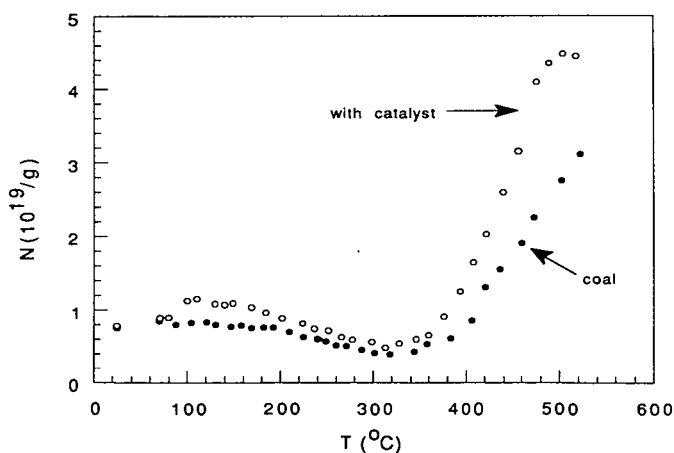


Figure 8: Variation of N with temperature for blind canyon with and without shell catalyst 324, in hydrogen flow. The values of N are corrected for the change in mass from TG data.

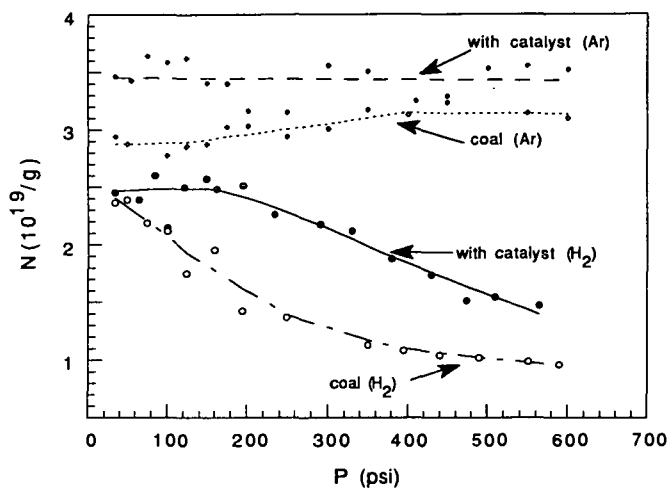


Figure 9: Variation of N with argon/hydrogen pressure for blind canyon coal with and without the shell catalyst 324.

VERY HIGH FREQUENCY EPR SPECTRA OF ORGANIC SULFUR COMPOUNDS

Wei Wang,^a R. B. Clarkson,^a F. P. Auteri,^a
P. Kovacs,^a M. V. Williamson,^a and R. L. Belford^a

^aIllinois EPR Research Center; Departments of ^aVeterinary Clinical Medicine, and

^bChemistry, University of Illinois, 505 S. Mathews, Urbana, IL 61801

Key Words: Sulfur (organic), thiophenic radical cations, EPR (ESR)

ABSTRACT

Radical cations formed from several sulfur-containing heterocyclic aromatic compounds have been studied, both as subjects in their own right and as models for organic sulfur in coal. Since for most organic radicals, the g shift and g anisotropy are expected to be small, they have seldom been resolved at conventional X-band (9.5 GHz) EPR. Our very high frequency (VHF) EPR spectrometer (W-band, 95 GHz) provides a tenfold increase in spectral resolution, which enables us to obtain, for the first time, the principal g matrices of thiophenic radical cations in amorphous or disordered state. The EPR experimental results are presented, along with observation of certain trends of g shift and g anisotropy among the homologous series.

INTRODUCTION

Identification of the chemical forms of sulfur-containing heterocyclic aromatic compounds in coal continues to be a challenging problem. Our previous studies¹ hypothesized that the very high frequency (VHF) EPR spectra of Illinois #6 coal could be approximated by superposition of two main classes of organic radicals. The first class was polycyclic aromatic hydrocarbon radicals and the second was the radicals from heterocyclic aromatic compounds containing sulfur, oxygen, or nitrogen. It was suggested that the spin-orbit coupling from sulfur could be responsible for the low field feature of the W-band spectra of the coal.

In order to fully explore this hypothesis, we are investigating a number of sulfur- and oxygen-containing organic radical ions by VHF EPR spectroscopy. The goal is to obtain their anisotropic g -factors and to assess the influence of heavy atoms such as sulfur and oxygen and extent of aromatic conjugation on EPR parameters, especially g anisotropy and EPR line-shape. Here we present some of our experimental results on cation radicals from thiophenic compounds.

The g -factor, one of the most important and fundamental EPR parameters, characterizes the position of a resonance signal: $g = h\nu/\beta B_0$, where B_0 is external magnetic field strength at the resonance (also called spectral center or resonance field center). A g -factor for a molecule containing an unpaired electron is generally viewed as characteristic of its electronic structure. But there are several reasons which can prevent the g -factor from being a straightforward and definitive structural indicator.

For most organic radicals, g -factors are very close to the free-electron value ($g_0 = 2.00232$). The g shift, $\Delta g = g - g_0$, is consequently small. A typical Δg for carbon centered radicals is ca. 20×10^{-5} and only several-fold greater for heterocyclic containing oxygen or sulfur. Experimentally resolving such small g shifts is difficult, especially in non-single-crystal solids (powders, frozen solutions, glasses) where the situation is more complicated.

Since for most cases, g -factors are intrinsically anisotropic, due to spin-orbit coupling, the resonance field positions vary with the orientation of the molecules in the external magnetic field. Therefore, g is represented as a matrix with three principal values. If molecules are tumbling rapidly, then the g matrix is motionally averaged to a single average (scalar) value $\langle g \rangle = (g_1 + g_2 + g_3)/3$, where $\langle g \rangle$ determines the averaged resonance line center. In a disordered solid, the resonance spectrum will be a superposition of the individual absorption spectra of the variously-oriented molecules. In the typical macroscopically isotropic specimen, the whole ensemble assumes with equal probability every possible orientation relative to the external magnetic field. The resulting composite is known as a powder spectrum. Principal g matrix values or components can still be resolved providing that extreme g values differ enough. But as stated earlier, for most organic radicals the g values are all quite close together. Thus, under the effect of other line broadening mechanisms, powder spectra of organic radicals often show a single, featureless (and boring) line with varied width and symmetry and very limited information content, as illustrated in Fig. 1(a).

One possible way to overcome this problem is to work at higher magnetic fields (requiring higher microwave frequency) to enhance the spectral resolution.² From the simple resonance condition one can see easily that the difference in resonance fields corresponding to slightly different g -factors is proportional to the product of the microwave frequency with the difference in g -factors. Therefore the spectral resolution will be enhanced by a factor of 10 in going from X-band (9.5 GHz) to W-band (95 GHz) providing the line does not broaden substantially with microwave frequency. Fig. 1(b) demonstrates this greatly enhanced g -resolution.

Thiophenic compounds have been thought to be abundant in Illinois coal³. Upon chemical oxidation on catalyst surface or UV irradiation in boric acid glass, such compounds yield immobilized and extremely long-lived cation radicals suitable for EPR studies. EPR spectra of the radical cations so prepared from thiophene and four more structurally related compounds were obtained at both X-band and W-band frequencies. The principal g matrix components obtained from analyses of these spectra are reported here. We have found in the literature no previous reports of g matrices for these radicals.

EXPERIMENTAL SECTION

Thiophene (THI), benzothiophene (BTH), dibenzothiophene (DBT) and benzo[*b*]naphtho-[2,1-*d*]thiophene (BNT) were purchased from Aldrich; dinaphthylene thiophene (DNT), from ICN. The highest commercially available grades (typically 99+% pure) were obtained and used without further purification.

To generate free radical ions, we have tried several different methods. Two of them proved to be quite versatile and thus are used routinely. The first is chemical oxidation at a metal oxide

catalyst surface with O_2 ; the catalysts can be either alumina or alumina/silica like Houdry M46. The second is UV photolysis in boric acid glass. Both methods can produce sufficient populations of stable radical ions in a powder or glassy matrix, thus mimicking the disordered state of chemical species in coal.

In method I, γ -alumina from Akzo was loaded into an EPR tube attached to a three-way Y-shaped connector with a connector to vacuum line and a septum seal. After the alumina was calcined at ca. 650 °C for 12 hours, a small amount of gaseous oxygen was let in for about 4 hours. The benzene solution of the thiophenic compound was injected onto the alumina to form a suspension. Over some time (a few minutes to several days), the color developed which indicates formation of radical ions. The suspension was then freeze-thaw-pumped (three cycles) to deplete the oxygen. The EPR tube was then flame-sealed. A W-band sample prepared this way can be used in both X-band and W-band resonators.

In method II, a mixture of powdered boric acid and the desired thiophenic compound (1000:1 mole ratio) is heated to the melting point of boric acid (ca. 180 °C). The molten mass is allowed to cool to a glass, broken into small fragments or crashed into fine powder, and loaded into a quartz sample tube. The tube is placed in a Ray-O-Net irradiation unit and subjected to UV irradiation at 254 nm for 30 minutes. The sample tube is then removed and sealed for analysis. Samples of cation radicals still give the same strong EPR signal even one year after their preparations.

X-band spectra were obtained from a Varian E-line 12" EPR spectrometer outfitted with a tracking Varian NMR gaussmeter and a Fluke frequency counter. Different microwave levels were used to ensure no power saturation, and different magnetic field modulation amplitudes were used to find the best balance between S/N and resolution. W-band EPR was performed on a locally-built spectrometer described elsewhere (reference 1). All radicals have been prepared at least three times and each sample run at least four times.

The resolution of W-band spectra is usually so high that one can read the principal g matrix directly, which is impossible at much lower frequencies. Nevertheless, a computer-assisted analysis using an EPR powder spectrum simulation program² was still performed to confirm the direct measurements.

RESULTS AND DISCUSSION

The g-shifts at W-band and X-band and the measured principal g-matrix components of the heterocyclic sulfur cation radicals are summarized in Figs. 2 and 3.

The g shifts measured at X-band seems compare well with those measured at W-band. Actually, g shift measurement at W-band have more than three times better accuracy than at X-band, because not only is the W-band g shift calculated as an average of three separately measured individual matrix components, each better defined spectroscopically than the line center measured at X-band. It is rather difficult to define the resonance center for a usually broad and asymmetric line.

There is a general agreement between g shifts measured for the alumina surfaces and those for the corresponding boric acid glasses (Fig. 2). But this agreement should not be viewed as proving that these two different preparations yield precisely the same radical species; comparison of the full g -matrices would be much more revealing. Moreover, careful analysis of the g matrices might result in additional information on these radical ions.

It is also observed that g shift or g matrix components do not follow a monotonic trend among our series (Fig. 2). Rather, the g shift starts from THI, rises up, peaked at DBT, then falls down toward DNT. Also, the lowest field g matrix component g_1 and g_2 behave similarly while g_z stays constantly near the free-electron g value (Fig. 3). The latter is expected because all these radicals are planar π radicals, where delocalized p_z electrons have zero shift on g_z .

The fact that both g shift and two of the three principal g -matrix values vary substantially with the number of fused benzene rings is very encouraging. It demonstrates that W-band EPR spectroscopy of these organic sulfur radicals is very sensitive to their structures. Thus the EPR parameters of those model compounds, especially anisotropic g values, have the potential to help identify the sulfur-containing heterocyclic moieties in coal. Clearly, studies on more model compounds are needed in order to build a library of VHF EPR spectra. We are currently investigating a dozen more alkyl-thiophenes or benzothiophenes as well as an analogous furanic series.

Based on notions including 'frozen orbitals' and additive property of g shifts, Stone⁴ proposed the g shift of aromatic hydrocarbon to be $\Delta g = b + \lambda C$ where λ is the coefficient in the simple Hückel Molecular Orbital (HMO) energy expression $E = \alpha + \lambda\beta$, where α and β are the Coulomb and resonance integral, respectively; b and c are empirical parameters. Fig. 4 shows the measured g shift plotted against λ from HMO's. It seems that four of the five points fall into a straight line in this particular sulfur heterocyclic series. We are a bit surprised by this observation in view of the crudity of this simple treatment. We cannot guarantee that this 'correlation' is not accidental; more experimental examples are required to establish a generalization at a high level of confidence.

Fig. 5, 6, and 7 show g matrix components (g_1 , g_2 and g_3), g shift, and g_{xy} anisotropy vs. spin density calculated by McLachlan's method of perturbation on HMO⁵. Fig. 5 indicates that both g_1 and g_2 increase with the π spin density, with g_1 faster than g_2 . Fig. 6 shows that the g shift also increases with the π spin density at the sulfur atom. From Fig. 7 one sees that the difference between g_1 and g_2 (so called xy anisotropy) increases with the π spin density at the sulfur atom. These probably suggest that one of the g matrix components g_1 is more sensitive to the change of π spin density distribution in the aromatic ring. One tentative conclusion from these comparisons of theory and experimental data is that one of the g matrix components, g_1 , is more sensitive to the change of π spin density distribution in the aromatic ring than the others. We are currently using more elaborate MO calculations to examine how structural features other than the number of benzene rings should affect the anisotropic g values.⁶

SUMMARY

Radical cations prepared from thiophene and some of its aromatic homologues were studied by

a novel technique — VHF (W-band) EPR spectroscopy. The first unambiguous results on principal g matrices and g shifts for these species are presented. Since the EPR parameters determined from W-band spectra of these compounds prove very sensitive to their molecular structure, this technique is promising for the nondestructive analysis of the chemical forms of organic sulfur in coal, where nearly identical g -factors have been observed and correlated with organic sulfur content¹.

ACKNOWLEDGEMENT

Facilities of the Illinois EPR Research Center (IERC), partially supported by the National Institutes of Health, Division of Research Resources under BRTP Grant RR01811 were used in this work. The authors thank Prof. Mark J. Nilges, Illinois EPR Research Center, for many helpful discussions and for his key role in the design and improvement of the W-band spectrometer. This work was prepared with the support, in part by grants made possible by the Illinois Department of Energy and Natural resources through its Coal Development Board and Center for Research on Sulfur in Coal, and by the U. S. Department of Energy (Grant Number DE-FG22-91PC91334). However, any opinions, findings, conclusions, or recommendations expressed herein are those of the authors, and do not necessarily reflect the views of IDENR, CRSC, and the DOE.

REFERENCES

1. R. B. Clarkson, W. Wang, M. J. Nilges, and R. L. Belford, in *Processing and Utilization of High-Sulfur Coal*, R. Markuszewski and T. D. Wheelock, Eds., Elsevier: Amsterdam, 1990; pp. 67-79.
2. R. L. Belford, R. B. Clarkson, J. B. Cornelius, K. S. Rothenberger, M. J. Nilges, and M. D. Timken, in *Electron Magnetic Resonance of the Solid State*, J. A. Weil, Ed., Chemical Institute of Canada: Ottawa, 1987; p 21.
3. A. Attar, and F. Dupuis, *Am. Chem. Soc. Div. Fuel Chem. Preprints*, **24**, 166 (1979)
4. A. J. Stone, *Mol. Phys.* **6**, 509 (1963)
5. The calculation was based on HMO and McLachlan parameters taken from P. D. Sullivan, *J. Am. Chem. Soc.*, **90**, 3618 (1968)
6. W. Wang, Ph.D. Thesis, University of Illinois, Urbana, IL (1992).

Fig. 1. EPR spectra of dibenzothiophene (DBT) cation radical in boric acid glass. a) At X-band, b) At W-band.

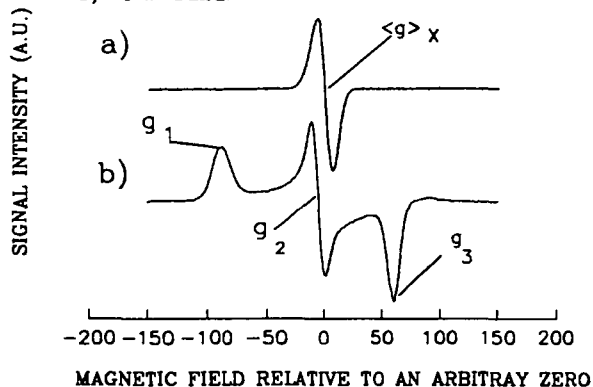


Fig. 2. g-shifts of thiophenic cation radicals on alumina (A) surface and in boric (B) acid glass.

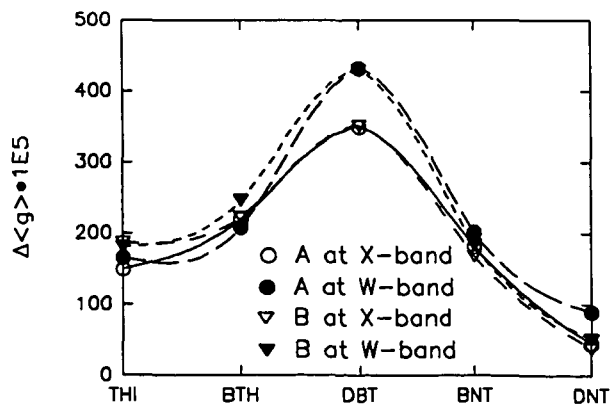


Fig. 3. Measured three principal g -matrix components, (A) on alumina (B) in boric acid glass

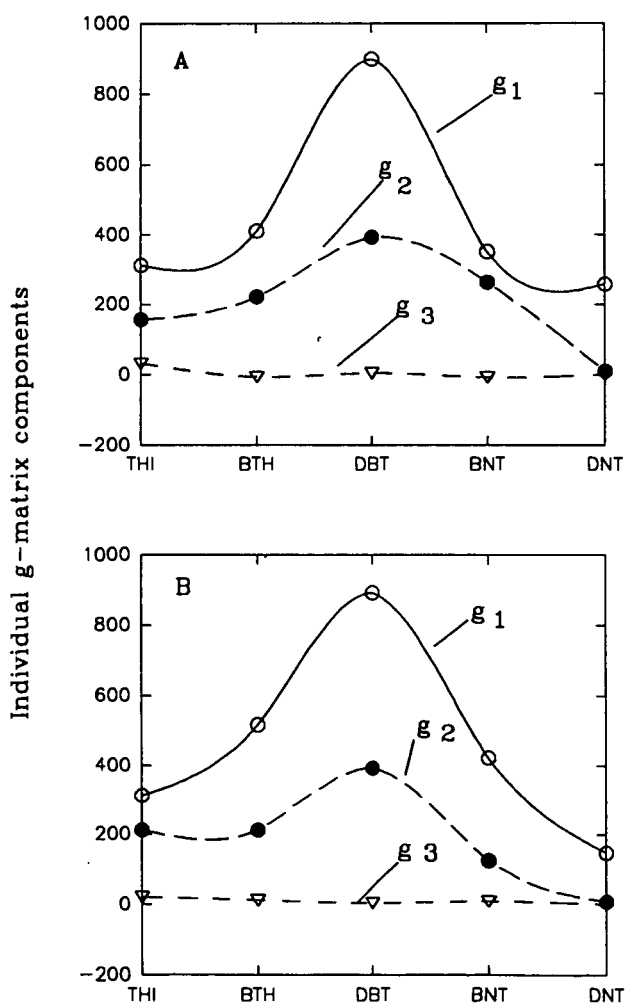
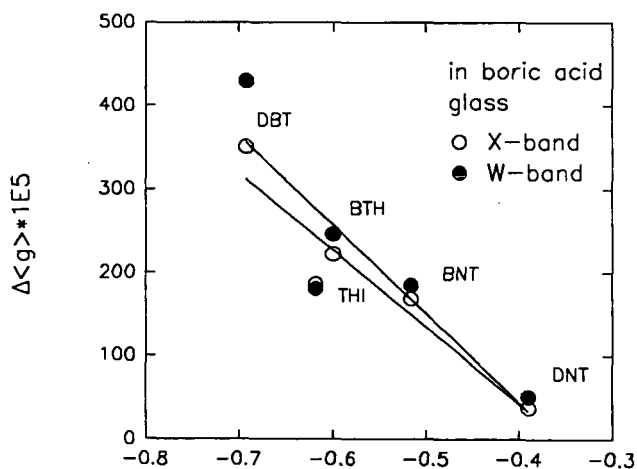
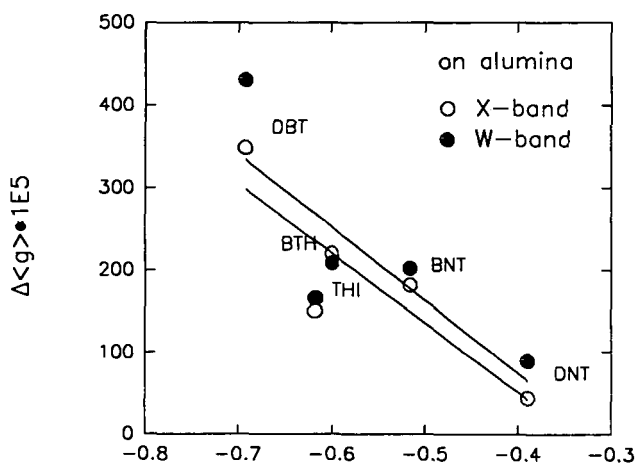


Fig. 4. Experimental g-shifts plotted against λ in HMO calculation.



λ in HMO

Fig. 5. A plot of principal g-matrix components against calculated π spin density on sulfur

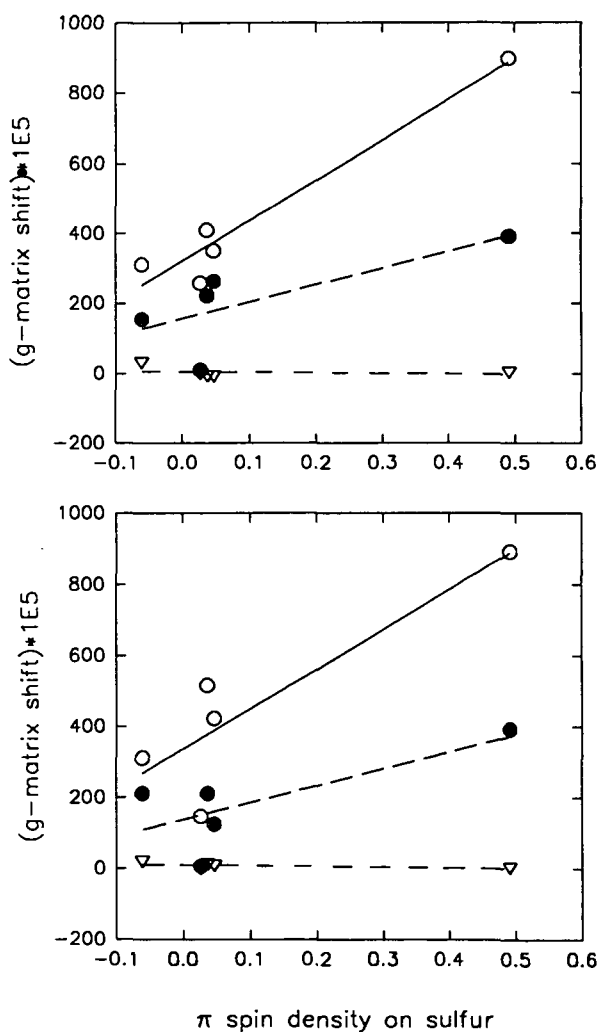


Fig. 6. A plot of g-shift at W-band vs. calculated π spin density on sulfur

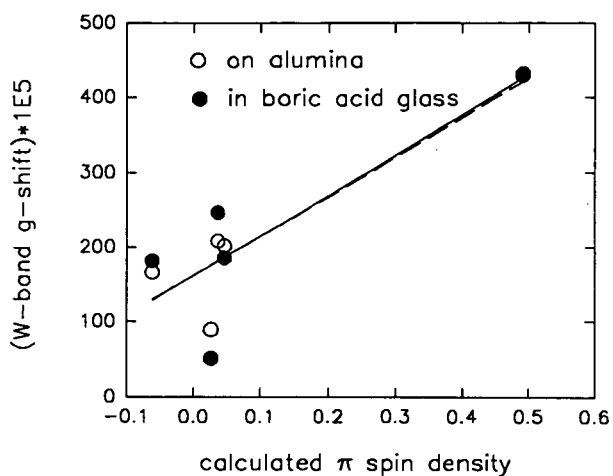
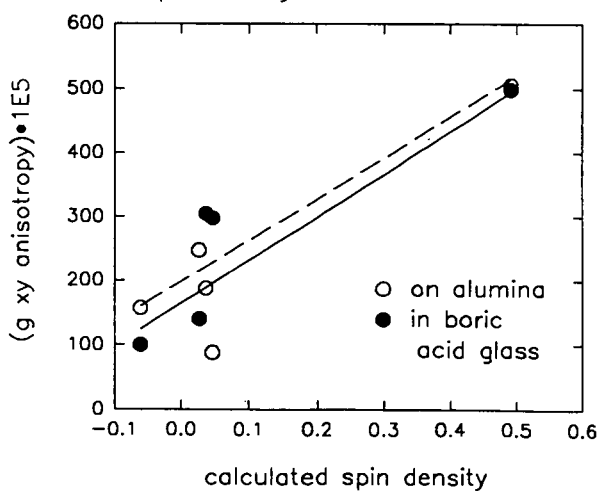


Fig. 7. g xy anisotropy vs. calculated π spin density on sulfur



AN EPR SPIN PROBE METHOD FOR CHARACTERIZING CHANGES IN THE ACCESSIBLE REGIONS OF COAL UPON OXIDATION

Wojciech Sady, Lowell D. Kispert, and Dennis R. Spears

Box 870336, Chemistry Department
The University of Alabama, Tuscaloosa, AL 35487-0336

KEYWORD: porosity, oxidation, coal swelling, EPR, nitroxyl spin probe

ABSTRACT

Eight Argonne Premium Coal Samples (APCS) were weathered in air and the structural and chemical changes that occurred upon swelling with toluene and pyridine were examined by an EPR spin probe method developed in this laboratory. Under mild oxidation conditions and swelling with toluene large structural changes were observed for lignite (Beulah-Zap) which suggested the collapse of the coal structure. This did not occur for higher rank coal. Upon oxidation and swelling with toluene and pyridine an increase occurred in the amino substituted spin probe concentration for coals with the carbon percent above 80%. A maximum was found for the creation of 5 Å diameter pores upon swelling with pyridine at 85% C.

INTRODUCTION

The conversion of coal by an economically feasible catalytic method is an area of research for our future energy requirements. However, knowledge of the coal structure (1, 2) is necessary before optimum use of a catalyst can be made. For instance, in addition to the normal surface catalysis, the catalyst must be able to diffuse into the coal, enabling catalysis to occur from within. This requires knowledge of the pore molecular accessibility size and shape in the coal. Any conversion process, however, involves exposure of the pore structure to solvents of various polarity, temperature and pressure variation, and catalytic action. Complicating the process can be oxidation processes that occurred before the coal is processed.

Oxidation (3) is of the utmost importance in many respects. Autogenous heating in a coal stockpile causes oxidation and even combustion of coal. In either case, severe detrimental changes to coal properties occur. Oxidation affects thermal and swelling properties which are important in coke production. Oxidation also affects solvent swelling properties, important in catalytic conversion.

However, the oxidation process is difficult to study, quantitatively or qualitatively. The amount of oxygen has been determined by neutron activation analysis (4) and by XPS analysis of the coal surface (5,6). Relative changes in the properties of the coal have also been used to measure oxidation. These include FTIR signatures, (7) pH, (8) Gieseler fluidity, (9,10) pyrolysis response, (11, 12) and free swelling index (13). In spite of these advance techniques, it is difficult to quantify the low temperature oxidation, as the amount of solid oxidation products are small (14). XPS measurements in conjunction with GC analysis of the gas products and thermal gravimetric analysis (GA) of the fuels (15) can be useful in determining the oxidation process.

In addition, drying of the coal results in pore collapse which changes the mechanical properties (1, 2) so the coal becomes more friable. Reswelling the dried coal is believed (1, 2) to cause autogenous heating of the coal.

The micropore structure of coal has been characterized by both sorptive methods (16-18) and spectroscopic methods. The spectroscopic methods have included small-angle X-ray (SAXS)

(19) and neutron (SANS) (20-22) scattering where micropores can be observed in the presence of solvent molecules. Low field NMR spin lattice relaxation measurements (23, 24) of the water in the pores of the coal enabled a study of pore radius from <0.5 mm to 0.5 mm.

EPR spin probe studies in the absence of oxidation

Previous electron paramagnetic resonance (EPR) spin probe (25-30) studies of APCS samples have dealt with the effect of swelling temperature, micropore size and shape, solvent polarity, spin probe imbibition, and polarity of the spin probes. The results of these studies have correlated well with SANS (19), SAXS (20-22) and NMR (23, 24) studies of APCS coals upon coal swelling.

It was observed by the EPR spin probe method that APCS samples swelled at 298 K in toluene did not change the micropore structure in any significant way (29). It was found (28, 29) that coals swelled in toluene contained small, spherically shaped pores and a broad distribution of cylindrical shaped pores of short length. Elevating the swelling temperature from 298 K to 333 K had no effect on nonpolar solvents (toluene), only a mild effect on slightly polar solvents (nitrobenzene) and a significant effect on very polar swelling solvents (pyridine).

Polar solvents caused elongation of the micropores (29). The greater the swelling temperature and the greater the swelling solvent polarity, the greater the degree of micropore elongation. Nitrobenzene at 298 K showed only small micropore elongation. However, small spherical pores did disappear entirely. At 333 K in nitrobenzene, significant pore elongation did occur, with the creation of a bimodal pore size distribution. Coals swelled in pyridine at 298 K exhibited significant pore elongation, and the creation of a bimodal pore size distribution. Elevation of the swelling temperature to 333 K caused much greater micropore elongation. This bimodality was confirmed through the use of alkylammonium spin probes, which behaved more like nonpolar spin probes than as cationic moieties.

The effect of solvent polarity was found to be related to the types of cross-linking in coal. Toluene did not disrupt either covalent or noncovalent linkages and so did not swell coal significantly under these conditions. Polar solvents like nitrobenzene and pyridine swelled coal by disrupting hydrogen bonds. A solvent which was more polar (i.e., had a greater hydrogen bond accepting ability) could disrupt more bonds and swell coal to greater degree. More polar solvents took longer to reach swelling equilibrium. Increasing the swelling temperature had the effect of hastening the approach to equilibrium and so caused greater pore swelling and elongation.

Micropore elongation was ascribed to swelling anisotropy in coal. It was determined that most of the micropore elongation took place parallel to the bedding plane. This led to the development of a "zipper" model for coal swelling (29).

Rank effects was shown to be an important factor in spin probe imbibition (29). Coals at 85% carbon (dmmf) and above typically showed similar spin probe retention curves. Spin probe concentration, where significant retention occurred, decreased with rank. The retention curves showed a minimum in the range 85-92% carbon (dmmf). For coals swelled in toluene, the minimum was directly related to a minimum in porosity in this range.

For coals swelled in polar solvents, the decrease in spin probe concentration was associated with rank, and the increase in covalent cross-links. The decrease in hydrogen bond cross-link density in APCS coals was in turn associated with the decrease in oxygen functionality concentration, especially hydroxyl content, with rank.

Spin probes with polar R groups showed selective retention over nonpolar spin probes of same size. Spin probe retention was dependent on the polarity of the R group, which proceeded in

the order $-H \ll -OH < -CO_2H < NH_2$. Spin probe retention for moderately polar spin probes increased with swelling temperature for coals swelled in toluene. This increase was ascribed to hydrogen bond disruption by the spin probes. The most polar spin probe ($R = -NH_2$) showed no temperature effects up to 333 K, apparently because its R group was strong enough to cause significant hydrogen bond disruption.

Varying the swelling solvent polarity resulted in a competition of the solvent molecules with the polar spin probes for hydrogen bonding sites. Raising the swelling temperature resulted in increased solvent competition for hydrogen bonding sites. The effect of temperature was significantly greater as solvent polarity increased.

It was shown that "acidity" and "basicity" were incorrect terms in considering coal micropore wall chemistry. The terms "hydrogen bond donor" and "hydrogen bond acceptor" were used instead. Polar spin probes interacted with coal primarily as hydrogen bond acceptors. Acidic spin probes showed some indication of acting as hydrogen bond donors, but the primary mechanism of interaction was as an acceptor.

For coal swelled in polar solvents, the decrease in spin concentration was associated with the decrease in hydrogen bond-type cross-link concentration with rank, and the increase in covalent cross-links. The decrease in hydrogen bond cross-link density in APCS coals was in turn associated with the decrease in oxygen functionality concentration, especially hydroxyl content, with rank.

Recently, measurements of Argonne Premium Coal Samples (APCS) in our lab using the EPR spin probe technique that we developed suggests that the study of the oxidation processes and the change in structure upon drying can be followed by the EPR spin probe technique. This paper details the study of oxidizing coal for eight days and outlines additional experiments which lead to a further understanding of the oxidation process in the pore structures of coal.

EXPERIMENTAL

Ampoules containing all eight APCS coals were opened and their content was placed in a number of vials, 250 mg of coal in each vial. The vials with coals were weighed, and then placed on a shelf in room temperature and humidity about 60% protected from dust. The coals were stirred every day.

At the beginning samples from fresh coals were made, then samples were prepared from coals weathered for 8, 15, 36, 64 and 119 days. The vials with weathered coals were weighed, the values of the loss of weight after n days of weathering are given in Table 1.

Our standard procedure of imbibing spin probes into the pore structure of coals in the presence of swelling solvent was applied (28, 29). Coals were swelled in 60 °C for 18 hours in toluene or pyridine. Spin probes used were VI (3-carboxy-2,2,5,5-tetramethylpiperidine-1-oxyl), VII (TEMPAMINE, 4-amino-2,2,6,6-tetramethylpiperidine-1-oxyl), and VIII (TEMPO, 2,2,6,6-tetramethylpiperidine-1-oxyl). All spin probes are spherically shaped and are similar in size, the difference between them is the polarity of the R group [Figure 1]. Spin probes I-X were previously defined (26).

EPR spectra of the spin probe doped coal samples were recorded. The method of computing the nitroxide radical spin probe concentration was described previously (26,27). The results of the first 8 days of oxidation are presented in Figures 2-4.

RESULTS AND DISCUSSION

The concentration of spin probe VI (carboxyl substituent, polar group interactions) as a function of toluene and pyridine as the swelling solvent for APCS coal in the absence of air is given in Figure 2a. A general increase in the number of hydrogen bonding sites is observed as the rank decreases. It is known that the lignites contain more hydroxyl functional groups than the higher rank coals, thus the observed increase in the concentration of trapped spin probe VI for both solvents. The lower concentration of VI in pyridine is due to competition of pyridine for the polar sites, which does not occur in the case of toluene. Upon weathering the coal for 8 days in air (Figure 2b), a large decrease in the concentration of VI is observed for lignite (74-76% C) swelled in toluene. This can be explained by the data of Yost and Creasy (31) that the loss of water from the coal structure (which we also observed) collapses the structure, making it more difficult to trap the small spin probe VI in the coal structure unless the energy barrier can be overcome. A weight loss of 20-25% occurred for 74% C but none for 92% C (Table 1). However, the use of pyridine disrupts the collapsed coal structure so no difference is observed for pyridine solvent in the concentration of spin probe VI over the entire coal rank, while the same is true above 76% C when toluene is the swelling solvent. This observation suggests that we can follow changes in the hydrogen bond energy distribution. Further oxidation for 15 days shows an increase in spin probe concentration at 85% C content when toluene solvent is used indicating an increase in the formation of oxygen groups. This suggests that we can follow oxidation kinetics as well as changes in pore shape and size.

The biggest effect upon weathering in an oxygen atmosphere occurs when solutions of spin probe VII (NH_2 substituent) is slurried with the APCS coals. In the absence of air (Figure 3a) the concentration of VII is similar to VI using toluene as the swelling solvent but is larger for VII than VI when pyridine is the swelling solvent. However upon exposing the coal for 8 days to air a dramatic increase occurs in the concentration of VII for both toluene and pyridine as the swelling solvent above 76% carbon (Figure 3b). Below 76% C, the collapse of the coal structure upon loss of water is observed when toluene is used preventing the trapping of VII. Use of pyridine as the swelling solvent opens up the collapsed structure, allowing the trapping of VII. Upon oxidation for 15 days, the concentration of spin probes VII in pyridine solvent continues to increase due to the interaction of the NH_2 group with the oxidized coal.

The concentration of a spin probe with no substituent (VIII) and thus only size effects are studied, is depicted in Figure 4a. The concentration of VIII for both toluene and pyridine solvents is an order of magnitude or more lower for VIII than for VI and VII. Interestingly the concentration of VIII in toluene increases with decreasing rank while VIII in pyridine reaches a maximum at 86% C. These features can be rationalized by the opening of the coal structure by the pyridine - allowing all the spin probe concentrations to be washed out at low rank and the coal structure opened sufficiently in some places to trap VIII at 86% C. Upon weathering in air (Figure 4b), the concentration of VIII increases with the maximum still at 86% in a pyridine solvent while the loss of structure can be detected when swelled in a toluene solvent. Further oxidation for 3 weeks shows the maximum at 86% C - suggesting some interesting changes in the swelling characteristics as a function of oxidation. It is important to note that the concentration of VIII is very small but the polar VI and VII spin concentration is large. This observation indicates that even small degrees of oxidation can be detected.

CONCLUSION

The large decrease in the concentration of the spin probe after oxidation of lignite (74%) for eight days and swelled in toluene, appears to be due to the collapse of the coal structure upon oxidation as a result of water loss. However swelling with pyridine reopens the collapsed structure and no detectable difference is observed upon oxidation. For higher rank coal, a larger concentration of amino substituted spin probes was trapped upon swelling with toluene and pyridine after air oxidation for 8 days. The decrease in amino substituted spin probe for fresh Beulah-Zap showed a measurable increase upon oxidation and swelling in pyridine. Swelling with pyridine opens up small pores for 81-86% which is not observed for swelling with toluene. Changes in coal structures due to oxidation can followed by the EPR spin probe method.

ACKNOWLEDGMENT

This work was supported by the U. S. Department of Energy, University Coal Research Program under grant no. DE-FG22-90PC90284.

REFERENCES

1. N. Berkowitz, "An Introduction to Coal Technology" Academic Press, New York, 1979.
2. E. L. Fuller, Jr., In "Coal Structure, "Ed. by M. L. Gorbaty and K. Ouchi, Adv. in Chem. Series, Washington, DC, 1981, Chapter 19.
3. L. Petrakis and J. P. Fraissard, "Magnetic Resonance, Introduction Advanced Topics and Applications to Fossil Energy"
4. W. D. Ehmann, D. W. Koppelaar, C. E. Hamrin, Jr., W. C. Jones, M. N. Prasad and W. Z. Tian, *Fuel*, **65**, 1563 (1986).
5. D. L. Perry and A. Gint, *Fuel*, **62**, 1029 (1983).
6. D. T. Clark and R. Wilson, *Fuel*, **62**, 1034 (1983).
7. P. M. Fredericks and N. T. Moxon, *Fuel*, **65**, 1531 (1986).
8. Y. Yun, B. Hoesterey, H. I. C. Meuzelaar and G. R. Hill, *ACS Fuel Div. Preprints*, **32**, 302 (1987).
9. G. P. Huffman, F. E. Huggins, G. E. Dunmyre, A. J. Pignocco and M. Lin, *Fuel*, **64**, 849 (1985).
10. A. Grint and D. L. Perry, *Proc. Int. Conf. Coal Sci.* 879 (1985).
11. B. S. Ignasiak, D. M. Clugston and D. S. Montgomery, *Fuel*, **51**, 76 (1972).
12. H. Iyuhara, R. Tanibata and S. Nishida, *Proc. Conf. Coal Sci.*, 491 (1985).
13. J. W. Larsen, D. Dee, T. Schmidt and A. Grint, *Fuel* **65**, 595 (1986).
14. J. S. Gethner, *Fuel*, **66**, 1091 (1987); J. J. Isaacs and R. Liotta, *J. Energy & Fuels*, **1**, 349 (1987).

15. S. R. Kilemen and H. Freund, *ACS Div. Fuel Prepr.* **33**, 706 (1988).
16. S. Fuji; H. Tsuboi *Fuel* **46**, 361 (1967).
17. O. P. Mahajan and P. L. Walker, Jr. In *Analytical Methods for Coal and Coal Products*, vol. 1.; C. Karr, Jr., Ed.; Academic; New York: 1978.
18. M. L. Gorbaty, *Fuel*, **57**, 796 (1978).
19. Z. Spitzer and L. Ulicky, *Fuel*, **55**, 212 (1976).
20. R. E. Winans and P. Thiagarajan, *Energy & Fuels*, **2**, 356 (1988).
21. J. S. Gethner *J. Appl. Physics*, **59**, 1068 (1986).
22. J. S. Gethner *Prepr. Pap.-Am. Chem. Soc., Div. Fuel Chem.*, **32**, 239 (1987).
23. C. L. Graves, P. J. Davis, D. P. Gallegos and D. M. Smith, *Energy and Fuel* (1988).
24. C. H. Bartholomew, W. E. White, D. Thornock, W. F. Wells, W. C. Hecker, L. D. Smott, D. M. Smith and F. L. Williams, *ACS Div. Fuel Chem. Prepr.*, **33**(3), 24 (1988).
25. S.-K. Wu and L. D. Kispert, *Fuel* **64**, 1681 (1985); M. L. S. Cooray, Sc. Thesis, University of Alabama, 1988.
26. J. Goslar and L. D. Kispert, *Fuel* **69**, 564 (1990).
27. J. Goslar and L. D. Kispert, *Energy & Fuels* **3**, 589 (1989).
28. D. R. Spears; L. D. Kispert, and L. Piekara-Sady *Prepr. Pap.-Am. Chem. Soc., Div. Fuel Chem.* **36**, 29 (1991); D. R. Spears; L. D. Kispert, and L. Sady, *Fuel*, In Press, 1992; D. R. Spears; L. D. Kispert, and W. Sady, *Prepr. Pap.-Am. Chem. Soc., Div. Fuel Chem.* **36**, 1277 (1991).
29. D. R. Spears, Ph.D. Dissertation, The University of Alabama, 1991.
30. J. Goslar, L. S. Cooray and L. D. Kispert, *Fuel*, **68**, 1402 (1989).
31. R. S. Yost and D. E. Creasy, *Fuel*, **69**, 648 (1990).

Table 1. Weight loss ($\pm 0.4\%$) of APCS coals after n days of weathering.

Coal	Carbon Content	8	15	days 36	64	114
Beulah-Zap	74.05%	21	25	23	23	25
Wyodak-Anderson	76.04%	19	20	20	21	21
Illinois #6	80.73%	4.5	5.5	5.5	5	5.3
Blind Canyon	81.32%	1.2	2	1.5	1.6	1.2
Pittsburgh #8	84.95%	0	0	0.2	0.4	1.2
Lewiston-Stockton	85.47%	0.8	1	1	1.4	1
Upper Freeport	88.08%	0.6	0.8	1	1	0.6
Pocahontas	91.81%	0	0	0	0	0

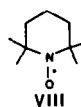
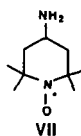
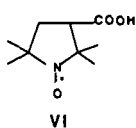


Figure 1. Spin probes VI, VII, and VIII.

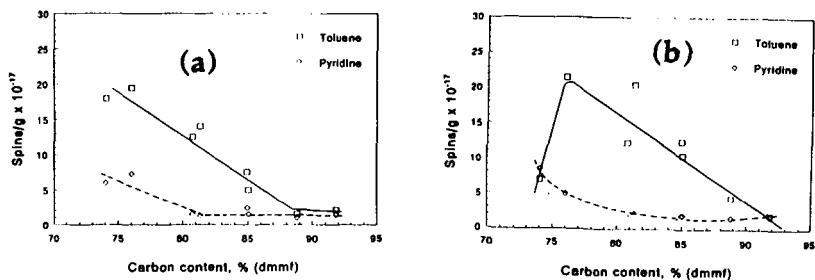


Figure 2. Concentration of spin probe VI versus percent carbon content (dmmf) in APCS coal swelled at 60 °C in toluene (□) and in pyridine (●), (a) as received and (b) after weathered for 8 days in air at room temperature.

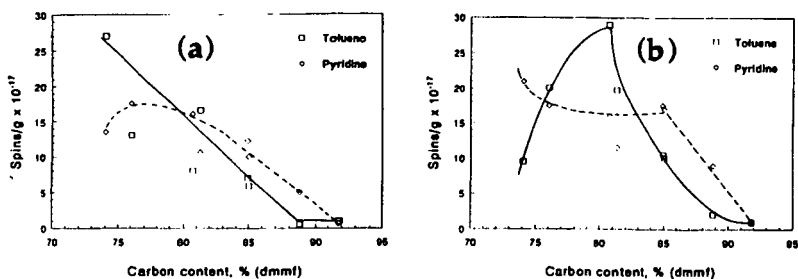


Figure 3. Spin probe VII versus percent carbon content (dmmf) in APCS coal swelled at 60 °C in toluene (□) and in pyridine (○), (a) as received and (b) after weathered for 8 days in air at room temperature.

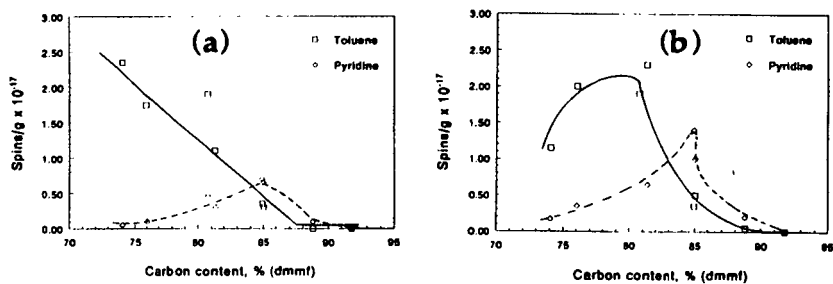


Figure 4. Spin probe VIII versus percent carbon content (dmmf) in APCS coal swelled at 60 °C in toluene (□) and in pyridine (○), (a) as received and (b) after weathered for 8 days in air at room temperature.

ENDOR Characterization of Free Radicals in Coals at Temperatures Upto 200°C

Naresh Dalal and Jeffrey P. DeLooze, Chemistry Department
West Virginia University, Morgantown, WV 26506-6045

Summary

The lack of information about the chemical structure of coal-based radicals has been a major obstacle in the understanding of the structural-chemical reactivity relationship. Our past research has indicated that the electron nuclear double resonance (ENDOR) technique has the potential of providing the most accurate structural information on the coal-based radicals. Unfortunately, the sensitivity of the best available ENDOR instrumentation was too low for liquefaction studies. We have developed an ENDOR probe which yields an increase in the sensitivity of the technique that enables us to investigate the structural-chemical reactivity patterns of coal-based free radicals under mild conditions suitable for liquefaction. We have used this technique to examine chemically characterized Illinois #6 coal at temperatures up to 200°C. Analysis of the resulting ENDOR signals identified at least three different types of protons. Analyses were also performed on the temperature dependence of the ENDOR signal intensity. Efforts are currently being made to enhance the measurement methodology's sensitivity above 200°C.

Introduction

It is well established that free radicals must play a dominant role in coal liquefaction [1]. Thus, a detailed understanding of the reaction mechanism(s) of the free radicals in coal is thought to be essential for the further improvement in the efficiency of coal liquefaction. However, a lack of knowledge concerning the chemical structure(s) of these same coal-based radicals has been a major hindrance in the development of the possible reaction mechanism(s) and, hence, an impediment to the improvement of liquefaction technology. The difficulty in this aspect has been that the structure(s) of the radicals is (are) complex and, hence, standard methods of radical structure determination, such as ESR, are not adequate. Following earlier leads [2-4], it was felt that the high resolution possible with the electron nuclear double resonance (ENDOR) technique would enable us to provide the much needed structural information on the radicals.

Commercially available ENDOR instrumentation does not provide the sensitivity for the required measurements at temperatures of interest to coal liquefaction scientists. Thus, our first task was the development of a new probe that would enable us to make measurements at 200°C and higher. We have developed such a probe, as described elsewhere [5] and the results obtained with it in the studies of Illinois #6 coal are summarized below. Illinois #6 was chosen because it has been accepted by many researchers as a model coal for liquefaction studies. Thus, it is possible to obtain large amounts of uniformly processed coal along with a detailed analysis of the chemical constituents of each sample.

Experimental Results

The ENDOR measurements were made with a Bruker ER-200-D ENDOR spectrometer, using an ENDOR probe designed in our laboratory, as described in our earlier report [4]. The ENDOR spectral lineshape was found to be quite sensitive to the instrumental parameters as well as sample preparation. A most important factor was the removal of oxygen from the sample via evacuation: the lower

the overall pressure in the sample tube, the stronger became the ENDOR signals, especially those corresponding to the larger couplings. In order to find the experimental parameters which would lead to the optimum signal-to-noise ratio, we carried out systematic ENDOR measurements on the Illinois #6 coal, by varying the microwave power, radio frequency (rf)-power, and sample temperature.

Figure 1 is a typical plot of the ENDOR spectrum of protons in an Arkwright, West Virginia, coal as reported earlier [4] with the original, non-optimized probe under the previously stated operating parameters. The spectrum shows quite high baseline noise and a poor signal-to-noise ratio.

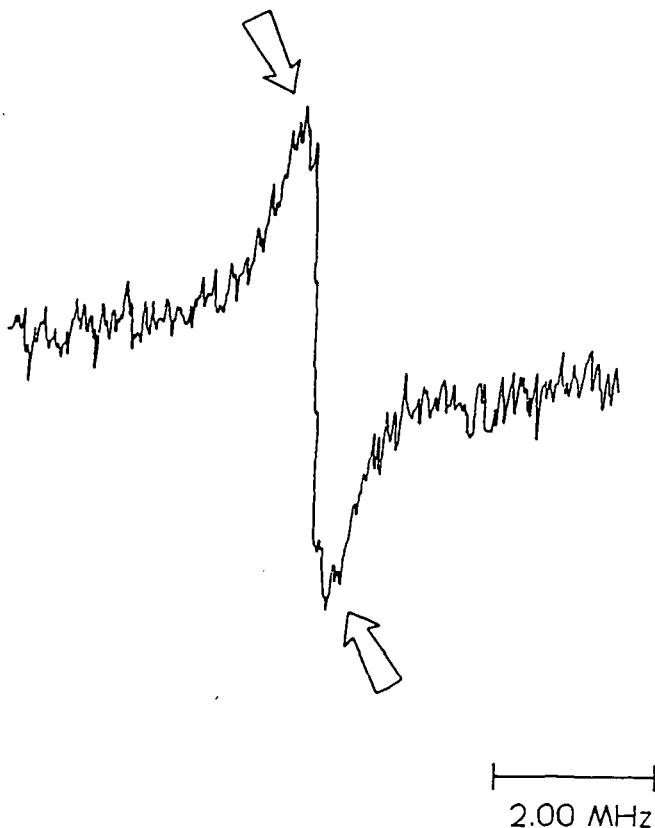


Figure 1: ENDOR spectrum of Arkwright, West Virginia coal sample
Arrows indicate the sidebands separated by approximately 750 kHz

Figure 2 shows a typical ENDOR spectrum of the Illinois #6 coal, obtained with the new probe; the greatly reduced noise level and, hence, the much higher signal-to-noise ratio is readily apparent. The improvement in the signal-to-noise ratio was found to be at least a factor of 200. This improvement in signal-to-noise also made it possible to obtain still higher spectral resolution via second harmonic detection, as demonstrated by the lower plot in figure 2.

Comparison of First and Second Derivative ENDOR Spectra

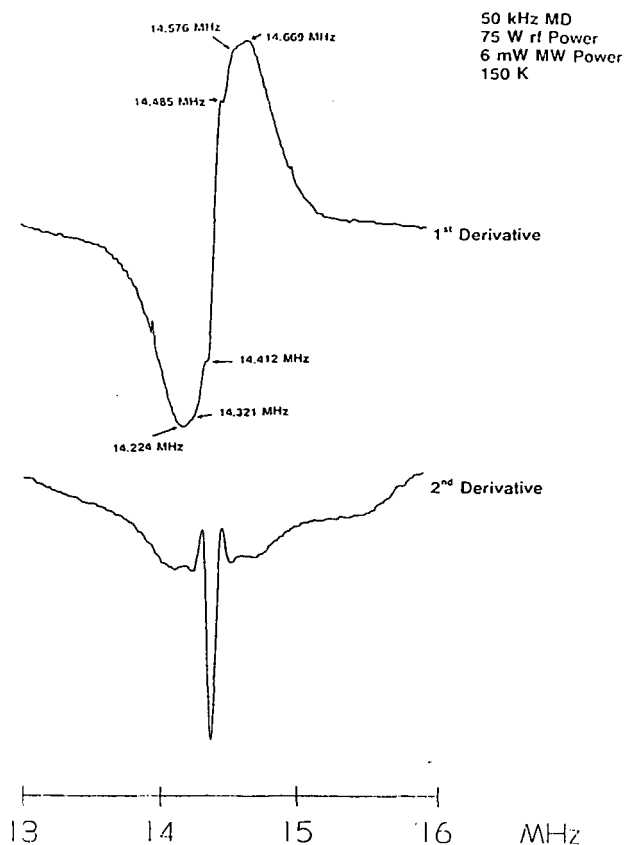


Figure 2: ENDOR spectra of Illinois #6 coal (a) first derivative and (b) second derivative. The higher resolution of the second-derivative presentation (as compared to the first-derivative presentation) can be noted from a comparison of (a) and (b).

Figure 3 is an expanded scale view of the optimized spectra in Figure 2. Note that the apparent discrepancies in the measured ENDOR frequencies is due to the re-tuning of the cavity for optimum response.

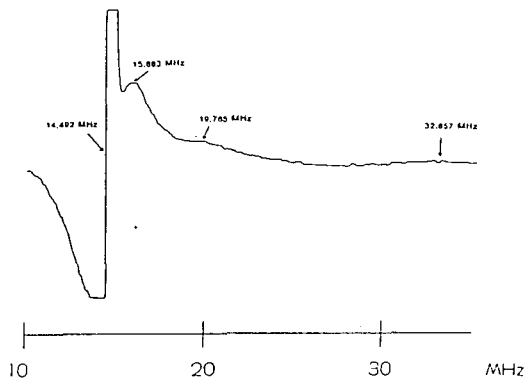


Figure 3: A wide-scan, optimized ENDOR spectrum of Illinois #6 coal at 150K.

Figure 4 shows typical ENDOR spectra of Illinois #6 as a function of temperature. It can be clearly seen that the new probe allows not only for a significant improvement in the room temperature signal, but also provides spectra at previously unheard of temperatures higher than that ever achieved before.

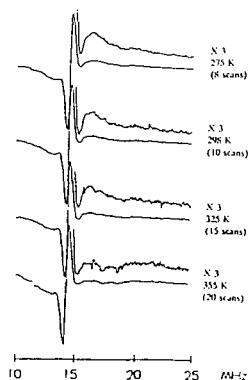


Figure 4: Temperature dependence of the ENDOR spectra of Illinois #6 coal.

Figure 5 shows a plot of the intensity of the ENDOR response as a function of temperature. It is clearly seen that the ENDOR intensity drops as a near-quadratic power function above room temperature to the point that the signals become undetectable above ≈ 425 K ($\approx 150^\circ\text{C}$).

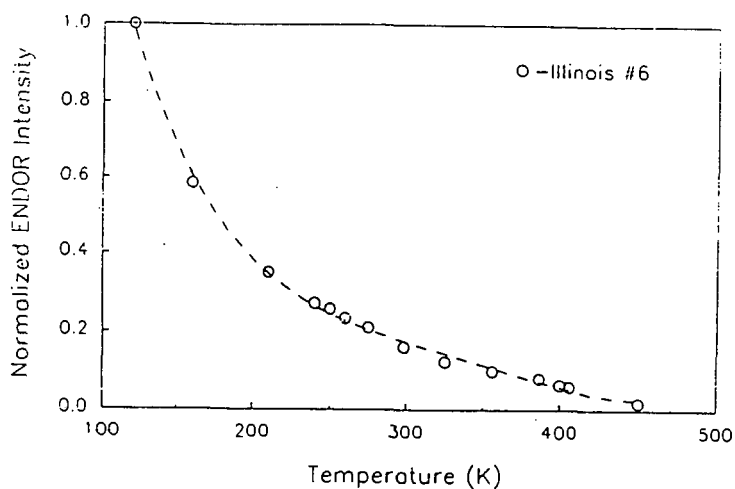


Figure 5: ENDOR signal intensity (optimized) versus temperature for Illinois #6 coal. Signal intensity normalized to $I_{\text{ENDOR } 120} = 1$.

Analysis Procedure

The measured ENDOR frequencies, ν_E , were analyzed in terms of the corresponding hyperfine coupling, Δ_H , via the following effective spin Hamiltonian [6, 7]:

$$\mathcal{H} = \langle S \rangle \Delta_H \cdot \hat{I} \cdot g_n \beta_n \hat{H} \cdot \hat{I}, \quad (1)$$

where $\langle S \rangle$ is the effective electron spin; \hat{I} , the electron spin; \hat{H} , the applied magnetic field; and $g_n \beta_n$, the magnetic moment of the nucleus under consideration, in this case, protons. The general solution of equation (1) will give the energy levels as a function of the applied magnetic field \hat{H} and the properties of the hyperfine coupling tensor, Δ_H . The ENDOR transitions are then given by the differences in the energy levels, with the selection rules $\Delta m_s = 0$, $\Delta m_I = 1$, where m_s and m_I are the electronic and nuclear spin quantum numbers. In the high-field approximation, i.e., when $\hat{H} \gg \Delta_H$ (in Gauss), and along the principal directions, the ENDOR transition frequencies, ν_E , are related to Δ_H and \hat{H} via:

$$\nu_E = \Delta_H / 2 + g_n \beta_n H \quad (2)$$

For the spectrum shown in figure 3, $g_n \beta_n H$ was equal to 14.492 MHz, and thus equation (2) provides a direct method of calculating hyperfine couplings from the measured ENDOR frequencies. The hyperfine couplings calculated via equation (2) are listed below in Table 1.

Table 1: Proton ENDOR transition frequencies, ν_E , and hyperfine couplings, Δ_H , for the free radicals in Illinois #6 coal.

Proton #	ν_E / MHz	Δ_H / MHz	Assignment
1	14.448 (two)	0.0	coal matrix
2	15.448	2.87	meta- para-
3	19.765	10.63	ortho-, para-

It is clear that the ENDOR measurements show that there are essentially three types of protons in the structure of the free radicals in Illinois #6 coal. The majority of the protons, labeled #1 in the table (ref. figure 3), exhibit no measurable isotropic hyperfine coupling with the unpaired electron. These protons are assigned to the coal matrix, although some of these might belong to the radical itself but located at positions of negligible spin density. The second set of protons, labeled #2, exhibits a coupling of about 3 MHz. The third set of protons (labeled #3) exhibits the largest hyperfine coupling (≈ 10.6 MHz).

The above results indicate that the free radicals imbedded in the matrix of the Illinois #6 coal are essentially highly delocalized aromatic structures: protons of type #3 being located at the positions of high spin density, i.e. ortho-to the free electron center. Protons of type #2 might be located at either the meta - or para - positions.

Theoretical Model

While exact details of the model explaining the rapid decrease in the ENDOR intensity upon heating the Illinois #6 coal have not yet been worked out, it is well established [6] that the ENDOR response is determined by an effective electron-nuclear spin-lattice relaxation time (T_{1e}). In general, one then sees that the temperature dependence of the ENDOR signals simply reflects the decrease in T_{1e} . For simple model compounds, T_{1e} is a sensitive function of the molecular motion of the radical, given by the autocorrelation function, $J(\omega_L)$, as:

$$(T_{1e})^{-1} \approx B_1 J(\omega_L), \text{ where} \quad (3)$$

$$J(\omega_L) = 2 / \tau (1 + \omega_L^2 \tau^2) \quad (4)$$

$$\tau = \tau_0 \exp (E / k_B T) \quad (5)$$

Where τ is the correlation time for the relevant molecular motion, τ_0 the pre-exponential factor, and E the activation energy. From these relationships, it is seen that T_{1e} will decrease rapidly with increase in temperature when $\omega_L^2 \tau^2 < 1$ (i.e., fast motion limit).

We are now carrying out a detailed analysis of temperature dependence of the ENDOR intensity as shown in figure 4 as assuming different values for τ_0 and E . A satisfactory set of these parameters fitting the data in Figure 4 will provide us with further insight into the chemical structure and, more importantly, the relevant molecular motions in the radical entities in the Illinois #6 coal, and likely also in other coals.

References Cited:

- [1] See for example, H.L. Retcofsky, *Coal Science* **1**, 43 (1982).
- [2] I. Miyagawa and C. Alexander, *Nature* **278**, (1979).
- [3] S. Schlick, P.A. Narayana, and L. Kevan, *J. Am. Chem. Soc.* **100**, 3322 (1978).
- [4] H.L. Retcofsky, M.R. Hough, M.M. Maguire, and R.B. Clarkson, *Appl. Spectrosc.* **36**, 187 (1982).
- [5] N.S. Dalal and J.P. DeLooze, paper presented at the Fifth Annual Technical Meeting of the consortium for fossil Fuel Liquefaction Science, Lexington, Kentucky, August 14, 1991.
- [6] *Electron Spin Double Resonance*, L. Kevan and L.D. Kispert, Wiley Interscience, New York, 1976.
- [7] N.S. Dalal, *Advances in Magnetic Resonance* **10**, 119-218 (1982).

SELECTIVE FLUORINATION OF COALS: STRUCTURE AT REACTIVE SITES BY HIGH RESOLUTION TRIPLE RESONANCE SOLID STATE NMR

Edward W. Hagaman and Suk-Kyu Lee
Chemistry Division, Oak Ridge National Laboratory
Oak Ridge Tennessee 37831-6201

Keywords: fluorinated coal, ^1H - ^{19}F - ^{13}C triple resonance solid state NMR

INTRODUCTION

As part of our program to define the chemical reactivity of coals, we are systematically investigating methods to introduce fluorine into specific sites in the organic matrix of these materials. The methodology is guided by analysis methods appropriate for solid derivatives. The spectroscopic technique that we use most heavily is solid state NMR.¹ In addition to the triple resonance experiments of reference (1), we have recently achieved the capability to observe ^{19}F directly. The utilization of the large ^{19}F chemical shift dispersion and cross correlation with the ^{13}C chemical shift will provide a powerful approach for analysis in these complex materials. We use Fourier transform infrared spectroscopy (FTIR) as a rapid method to assess fluorine incorporation into the coal matrix.

RESULTS AND DISCUSSION

Treatment of North Dakota lignite (Argonne Premium Coal No.8) with Sulfur Tetrafluoride. The chemistry of sulfur tetrafluoride with organic carbonyl compounds is well known.^{2,3} Under mild reaction conditions it converts carboxylic acid functionality into acyl fluoride moieties. The reaction proceeds with aliphatic and aromatic acids although the latter require acid catalysis in some cases. The following experimental reports our initial trials using SF_4 to convert carboxylic acid functional groups in coal into acyl fluoride residues. Dry lignite (110°C vacuum oven, 24 h), 0.5 g, is placed in a monel pressure vessel and evacuated. Sulfur tetrafluoride, 15 g, is transferred to this vessel, cooled in a dry ice/acetone bath. The reaction is accomplished by warming the vessel to the desired temperature and allowing the mixture to stand for the prescribed time. Excess SF_4 and gaseous byproducts of the reaction are destroyed in aqueous KOH traps. The coal is then washed with water until the filtrate is neutral and then dried at 110°C.

The reactivity of the coal with SF_4 is dependent on pretreatment. Lignite, as received, produces a material that shows minor reaction after contact with SF_4 for 72 h at 110°C. Reaction progress is judged by the relative intensity of the acid fluoride absorption in the infrared spectrum (IR) at 1830 cm^{-1} and by the ^1H - ^{19}F - ^{13}C double cross polarization (DCP)/MAS ^{13}C NMR spectrum. Washing the coal with 1N HCl or with citric acid⁴ and then with water until the filtrate is neutral to pH paper, followed by overnight drying, yields a much more reactive coal. The source of the difference in reactivity is suggested in the FTIR spectra of the APC #8 lignite and of the HCl washed material, shown in Figure 1a and b, respectively. The change in the carbonyl absorption indicates the

REFERENCES

1. F. Bergius, "Chemical Reactions Under High Pressure", Nobel Lecture, May 21, 1932.
2. A. N. Stranges, *Fuel Proc. Tech.*, **16**, 205 (1987).
3. W. R. K. Wu and H. H. Storch, "Hydrogenation of Coal and Tar", Bulletin 633, Bureau of Mines, U.S. Department of the Interior, Washington, DC, 1968.
4. E. E. Dovath, *Fuel Proc. Tech.*, **1**, 3 (1977).
5. A. Eamsiri, W. R. Jackson, K. C. Pratt, V. Chreston and M. Marshall, *Fuel*, **71**, 449 (1992).
6. J. M. Lee, C. E. Cantrell, S. V. Gollakota, O. L. Davies, M. M. Corser and P. Vimalchand, *ACS Div. Fuel Chem. Preprints*, **36**, 1915 (1991).

Table 1

Crystalline Phases in Fe-S System

Formula	Crystal Structure	Lattice Parameters Å		
Fe ₇ S ₈	HCP	a = 6.867	c = 17.062	
FeS	HCP	a = 5.967	c = 11.735	
Fe ₃ S ₄	HCP	a = 3.47	c = 34.5	
Fe _{1-x} S	HCP	a = 6.88	c = 22.90	
FeS ₂	Cubic	a = 5.417		
FeS	Cubic	a = 5.423		
Fe ₇ S ₈	Monoclinic	a = 11.902	b = 6.859	c = 22.787
β-Fe _{1-x} S	HCP	a = 6.894	c = 40.15	
Fe ₉ S ₈	Tetragonal	a = 3.679	c = 5.047	
FeS ₂	Orthorhombic	a = 4.436	b = 5.414	c = 3.381
Fe ₃ S ₄	Cubic	a = 9.876		
FeS	Tetragonal	a = 3.676	c = 5.032	

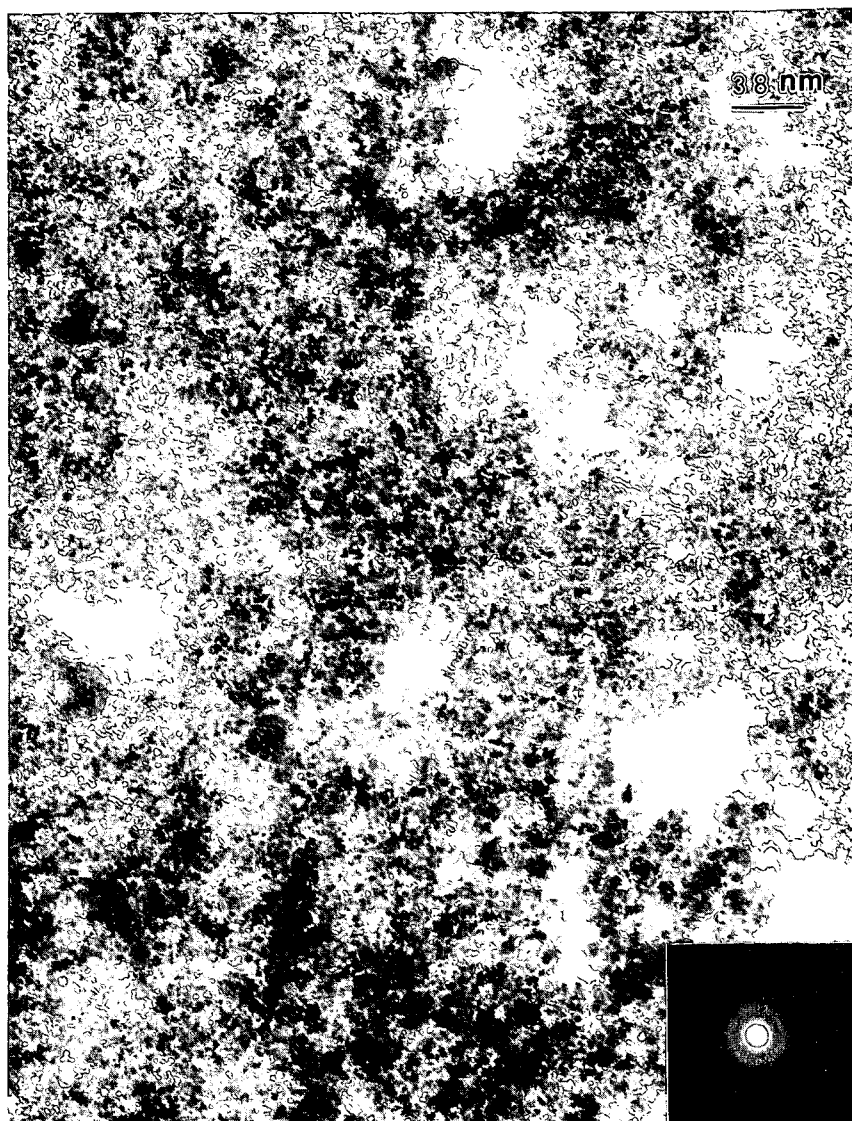


Figure 1. Transmission electron micrograph from the as-received Fe_2O_3 catalyst (inset). Microdiffraction pattern showing diffuse rings.

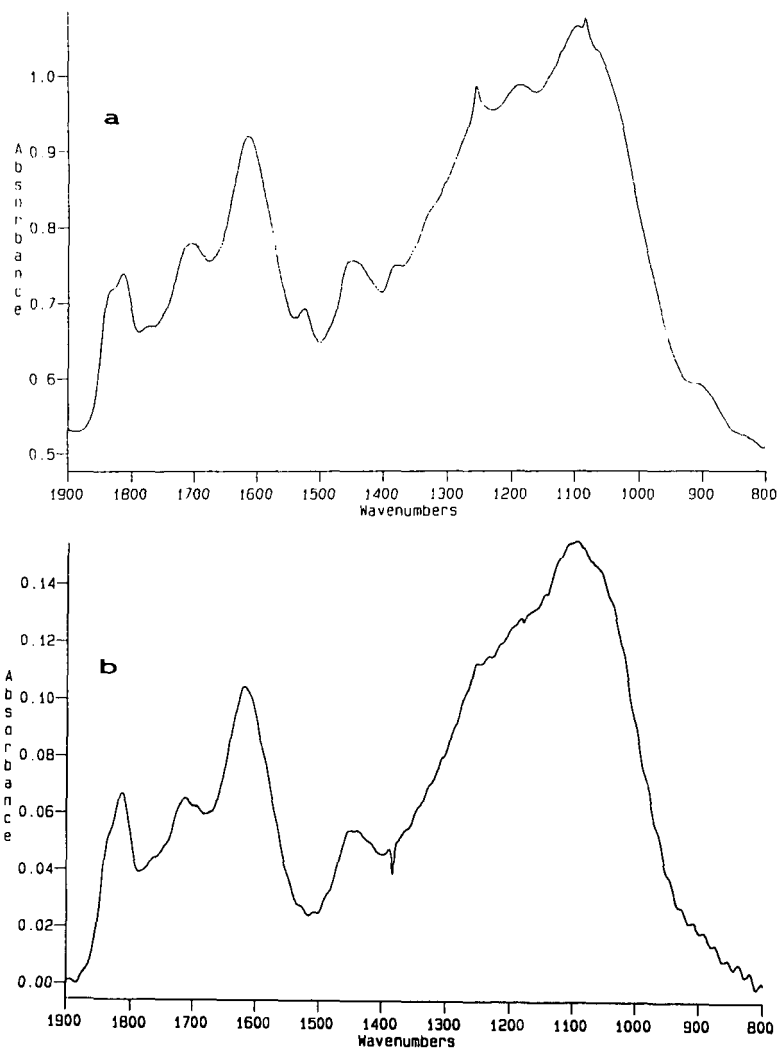


Figure 2. Infrared spectra (KBr pellet) of the products obtained from fluorination of North Dakota lignite with SF_6 , (a) at 110°C for 15 h, (b) at 170°C for 18 h.

AUTOMATED ANALYTICAL SCANNING ELECTRON MICROSCOPY AND IMAGE ANALYSIS METHODS FOR CHARACTERIZING THE INORGANIC PHASES IN COAL AND COAL COMBUSTION PRODUCTS

K.C. Galbreath, D.W. Brekke, and B.C. Folkedahl
Energy and Environmental Research Center, University of North Dakota,
Box 8213, University Station, Grand Forks, North Dakota 58202

Keywords: scanning electron microscopy, digital image analysis, coal and coal ash

ABSTRACT

Particle-by-particle scanning electron microscopy (PBPSEM) and scanning electron microscopy point count (SEMP) are being developed and applied for characterizing the inorganic phases in coal and coal combustion products. PBPSEM sizes, identifies, and quantifies coal mineral constituents and the degree of mineral-coal association. SEMPC determines the chemical composition and abundance of inorganic phases in coal ashes and deposits. Both methods are automated to minimize operator bias and to facilitate the acquisition of a statistically significant number of analyses to fully characterize heterogeneous samples.

INTRODUCTION

This paper describes two analysis methods: particle-by-particle scanning electron microscopy (PBPSEM) and scanning electron microscopy point count (SEMP), being developed and applied at the Energy and Environmental Research Center (EERC) for characterizing the inorganic phases in coal, coal ashes, and deposits. Both methods employ an automated analytical scanning electron microscope (SEM) integrated with a digital image analysis system. This instrumentation is very useful for characterizing complex heterogeneous materials because it provides the capability to efficiently analyze a statistically significant number of individual microparticles for both compositional and morphological information.

In recent years, considerable attention has been focused on developing and applying image processing and analysis techniques for quantifying the association of mineral grains with the organic coal matrix (1-3). Most image processing and analysis systems provide algorithms for acquiring the required morphological data for such an analysis. These algorithms are based on the creation of binary images from an original gray-scale image. The binary transformation process requires operator intervention to select thresholds for segmenting the coal and mineral phases from the gray-scale image. Unfortunately, this process can be very time-consuming and involves subjective judgement by the operator to create binary images that accurately represent the original image. At the EERC, we have formulated an automatic threshold selection algorithm and incorporated it into an image analysis application program. The program completely automates image acquisition and processing, thus enhancing the objectivity of analysis results. The PBPSEM method integrates this automated image analysis capability with electron-probe microanalysis to measure various morphological and compositional parameters for individual mineral grains in coal. These data are compiled and classified according to

compositional criteria into various mineral/chemical categories using a modified version of the Particle Characterization (PARTCHAR) program (4). The program provides a complete statistical summary for all the mineral/chemical phases in a sample, including the proportion of each phase directly associated with coal.

The SEMPC method for chemically characterizing and classifying the crystalline and amorphous phases in coal ashes and deposits has been improved greatly since its initial development (5). The method involves performing quantitative electron-probe microanalysis on a statistically significant number of randomly selected points on a sample. The compositional analyses are compiled and then classified according to stoichiometric criteria into standard phase categories using a best-fit algorithm (6). Applications of the method are presented elsewhere (7, 8). Recent improvements discussed in this paper include an automation routine for randomly selecting discrete image areas and analysis points on the sample, the capability to store digital images with documented analysis locations, and a more efficient and comprehensive phase classification program.

DESCRIPTION OF THE PBPSEM METHOD

Sample Preparation and Instrumentation. Coals to be analyzed by PBPSEM are pulverized to a standard combustion grind (i.e., approximately 80% of the particles -200 mesh), mounted in carnauba wax (9), cross-sectioned, and polished using standard petrographic procedures. Samples are then sputter-coated with carbon to minimize electron-beam charging artifacts. A JEOL JSM-35 analytical SEM equipped with a NORAN Instruments (formally Tracor Northern, TN) Micro-Z ultrathin window x-ray detector, TN-5500 x-ray analyzer, TN-5600 stage automation system, TN-8500 image analyzer, and GW Electronics annular solid-state backscattered electron (BSE) detector is utilized for performing PBPSEM analyses.

Digital Image Acquisition, Processing, and Analysis. The automated analytical SEM, operating in the BSE imaging mode, is programmed to analyze preselected areas on the sample. The electron microbeam is rastered across the analysis areas to acquire a digital image at a spatial resolution of 512 pixels in both the line-scan (x-) and frame-scan (y-) directions. Frame averaging is employed to enhance image quality.

A modified version of NORAN Instruments Locked and Liberated image analysis program is used to locate particles and measure various morphological, phase correlation, and compositional parameters. Coal and mineral particles are delineated based on the atomic number contrast inherent in BSE imaging. An automatic threshold selection algorithm has been formulated to segment the coal and mineral phases from the gray-scale BSE image into separate binary images. The selection algorithm utilizes the image's gray-level histogram. Gray-level histograms of prepared coal samples are generally bimodal consisting of two peaks corresponding to the average brightness (i.e., mean atomic number) of mounting medium and coal, a valley that separates the peaks and represents the less heavily populated intermediate gray levels of coal particle edges, and an essentially featureless region corresponding to a large range in mineral gray level intensity as a result of compositional variation. In some coal samples, the mounting medium and coal peaks are poorly resolved, and the selection algorithm has difficulty in

locating the histogram valley separating the two peaks (Figure 1a). A median filter is applied to the image to create a more strongly bimodal histogram (Figure 1b). The filtered histogram facilitates the selection of thresholds by the method described in this section. The median filter was chosen because it suppresses digital image noise without significantly affecting particle edges or other image features (10). The automatic threshold selection algorithm searches for the mounting medium and coal peaks and then selects a threshold at the minimum intensity value in the histogram valley (Figure 1b). This method of threshold selection is referred to as the mode method or standard histogram method (11, 12). The threshold segments coal from the mounting medium. Another threshold is selected to segment the coal from minerals. The placement of this threshold involves a peak-modeling procedure to account for any asymmetry of the coal peak caused by the overlapping of coal and mineral gray levels. The procedure models the coal peak assuming a Gaussian distribution of gray levels and then establishes a threshold at the base of the modeled peak (Figure 1b). Thresholds are determined for each area of the sample analyzed. Automatic thresholding eliminates operator bias in the results and compensates for instrument drift.

After transforming the gray-scale image into coal and mineral phase binaries, the following morphological parameters are determined for each phase of a given particle using standard image analysis routines: minimum, maximum, and average cross-sectional diameter; area; and external perimeter. Two correlation parameters are also determined for each mineral phase: an indication of whether the mineral grain is included, attached, or excluded relative to the coal matrix; and the amount of mineral perimeter in contact with the coal or mounting medium. In addition to this morphological and phase correlation data, compositional information is obtained by acquiring an energy-dispersive x-ray (EDX) spectrum from each mineral grain's center. Spectral regions-of-interest (ROI) are defined to measure the characteristic x-ray emission intensities of twelve common, mineral-forming, major and minor elements (Na, Mg, Al, Si, P, S, Cl, K, Ca, Ti, Fe, and Ba). Relative intensities are calculated by dividing the net counts for each element by the total ROI counts for all elements. Morphological, phase correlation, and compositional data for approximately 3000 particles are collected at three magnifications to provide the spatial resolution necessary to analyze particles ranging widely in size. These data are transferred on-line to a personal computer where they are tabulated and stored to disk for subsequent reduction, report generation, and archival. The acquired BSE images with the locations of EDX analysis are stored to tape.

Data Reduction and Reporting. A modified version of the PARTCHAR data reduction program (4) classifies the mineral compositional analyses based on elemental relative intensities, relative-intensity ratios, and stoichiometric criteria into one of 33 mineral/chemical and mineral association categories. Analyses that do not conform to any of the specified criteria are termed unclassified. The program allocates the classified particles according to average diameter into six intervals so that the size distribution of mineral/chemical phases can be determined. A report is generated that summarizes the results in a series of tables containing information on the number, area, and proportions of mineral/chemical phases in their respective size intervals and according to their association with the coal matrix (i.e., included, attached, or excluded). Mineral weight percentages are calculated assuming that particle area is proportional to particle volume (13) and mineral densities are constants.

DESCRIPTION OF THE SEMPC METHOD

Sample Preparation and Instrumentation. Coal combustion products to be analyzed by SEMPC are mounted in epoxy resin, cross-sectioned, and polished; or dispersed ultrasonically and mounted on filter paper. Samples are sputter-coated with carbon prior to analysis. The SEMPC analysis is performed with a NORAN Instruments Automated Digital Electron Microscope (ADEM). The ADEM is a fully integrated analytical SEM and image analysis system equipped with a Z Max 30 diamond window EDX detector and LaB₆ gun. The ADEM has the capability to perform SEMPC analyses on multiple samples with unattended operation.

Digital Image Acquisition and Electron-Probe Microanalysis. The stage/electron-beam automation system is programmed to randomly select discrete locations on a representative area of the sample for digital imaging and quantitative electron-probe microanalysis. Specifically, the analyst specifies a rectangular analysis area on the sample. The number of analysis frames available in this area is calculated based on the magnification employed. An analysis frame is randomly selected, and a digital image is acquired. Brightness, contrast, and focusing adjustments are performed automatically by the instrument for each frame analyzed. A location grid is established on the image, and the electron beam is sent to an address on the grid to acquire an EDX spectrum for eight seconds. The x-ray count rate is monitored during the 8-second acquisition to exclude points that emit insufficient x-ray counts for complete chemical characterization. The count rate must exceed a predefined threshold value, typically 1000 counts/second, for the analysis to be accepted. If the count rate is less than the threshold value, the beam is moved to another location. However, if the point is acceptable, the acquisition continues for an additional 17 seconds. The spectrum is then transferred to another memory location for processing, while the next point is selected and analyzed. Elemental peaks are deconvoluted, and their net intensities are extracted from the spectrum using the filter-fit method (14). The x-ray intensity data are corrected for matrix effects, and concentrations are calculated using the ZAF correction procedure. Mineral standards are used to calibrate the procedure. A maximum of 18 elements may be included in the analysis. Quantitative analyses for typically 250 points per sample are collected and transferred on-line to a personal computer for reduction and archival purposes. The acquired digital images with documented analysis locations can be archived for additional analysis.

Data Reduction and Reporting. An off-line program classifies each compositional analysis according to stoichiometric criteria into one of 56 standard phase categories using a best-fit algorithm (6). The program has the option to incorporate a maximum of 10 additional user-defined phase categories in the classification scheme. Analyses that do not conform to any of the specified criteria are termed unclassified. The program calculates the abundance of each phase in frequency percent and a normalized cumulative bulk composition for the sample on a weight percent oxide basis.

SEMP analysis results, when combined with crystalline phase identifications obtained by x-ray powder diffraction (XRD), can be used to infer a composition for the vitreous (i.e., liquid) phase of a deposit. This inferred liquid phase composition can be used as input for a subroutine of the program to calculate base-acid ratio and viscosity (15).

Liquid phase chemistry and viscosity is important for understanding deposit strength and development (7).

Quality Control. Bulk analysis techniques are utilized to validate SEMPC analysis results. The SEMPC calculated bulk composition is compared to the bulk composition determined directly by EDX fluorescence analysis to assess whether the SEMPC analysis is strictly representative of the sample. In addition, XRD crystalline phase identifications are referred to for confirmation of SEMPC phase identifications. Comparisons of SEMPC analysis results to mineralogical and chemical data obtained by bulk analysis techniques are presented elsewhere (5).

DISCUSSION

Development of the PBPSEM method is in its infancy, and several refinements are required before it can be used routinely for characterizing coal mineralogy. The automatic threshold selection algorithm requires a bimodal gray-level histogram for segmenting the coal particles from the mounting medium. This requirement is violated when the area imaged on a sample consists of only coal or mounting medium. Currently, the analysis is performed at low magnifications, generally less than 500, to prevent such an occurrence. This practice, however, results in rather poor spatial resolution, thereby limiting the method to analyzing relatively large particles, generally greater than about three microns in average cross-sectional diameter. Other methods for automatic threshold selection are being investigated to negate this particle-size restriction. Another limitation of the method is the inability to distinguish and quantify mineral-mineral associations for agglomerated particles. This information is extremely important when considering inorganic transformations that occur during combustion. Additional development of the data reduction program is needed to present quantitative mineral-coal association results in formats appropriate for various applications, such as in the field of physical coal cleaning or ash modeling. Work also needs to be done to optimize and validate the method.

In contrast to the PBPSEM method, the SEMPC method is in a mature stage of development. Efforts are primarily focused on developing automated image analysis methods for utilizing the stored digital images to relate the morphology in the vicinity of an analysis point to chemical composition. Porosity and the recognition and quantification of neck-growth development between particles are measurements being investigated for assessing deposit strength.

CONCLUSION

The PBPSEM and SEMPC analysis methods have been developed to provide detailed morphological and compositional information on the inorganic phases in coal and coal combustion products. Developmental efforts are in progress to optimize the methods and assess their performance characteristics (i.e., limitations, repeatability, and reproducibility). Work will also continue to extract and quantify the wealth of information provided by these methods for various applications.

ACKNOWLEDGEMENT

This work was supported by the U.S. Department of Energy under Cooperative Agreement No. DE-FC21-86MC10637. The authors are grateful to the Contracting Officer's Representative, Mr. Philip M. Goldberg, for permission to publish.

REFERENCES

1. Huffman, G.P.; Shah, N.; Huggins, F.E.; Casuccio, G.S.; Mershon, W.J. "Development of Computer-Controlled Scanning Electron Microscopy (CCSEM) Techniques for Determining Mineral-Maceral Association," *ACS Fuel Chem. Division Preprints* 1991, 36 (3), 1155-1163.
2. Straszheim, W.E.; Markuszewski, R. "Automated Image Analysis of Minerals and Their Association with Organic Components in Bituminous Coals," *Energy & Fuels* 1990, 4 (6), 748-754.
3. Straszheim, W.E.; Markuszewski, R. "Automated Image Analysis of the Association of Ash-Forming Mineral Matter with Coal Particles," *ACS Fuel Chem. Division Preprints* 1991, 36 (1), 216-222.
4. Zygarlicke, C.J.; Steadman, E.N. "Advanced SEM Techniques to Characterize Coal Minerals," *Scanning Microscopy* 1990, 4 (3), 579-590.
5. Kalmanovitch, D.P.; Montgomery, G.C.; Steadman, E.N. "Computer-Controlled Scanning Electron Microscope Characterization of Coal Ash Deposits," *ASME Paper* 87-JPGC-FACT-4, 1987.
6. Folkedahl, B.C.; Brekke, D.W.; Steadman, E.N. "Advanced SEM Techniques for Determining Mineralogy of Coal Combustion Products," *Scanning Microscopy*, in press.
7. Steadman, E.N.; Benson, S.A.; Zygarlicke, C.J.; Brekke, D.W. "Characterization of Liquid Phase Components in Coal Ashes and Deposits," *In proceedings of the Seventh Annual International Pittsburgh Coal Conference*; 1990, pp 43-51.
8. Jones, M.L.; Kalmanovitch, D.P.; Steadman, E.N.; Zygarlicke, C.J.; Benson, S.A. Application of SEM Techniques to the Characterization of Coal and Coal Ash Products," *Advances in Coal Spectroscopy*; Meuzelaar, M.L.C., Ed.; Plenum Publishing Corp.: New York, 1992, Chapt. 1, pp. 1-27.
9. Straszheim, W.E.; Younkin, K.A.; Greer, R.T.; Markuszewski, R. "Mounting Materials for SEM-Based Automated Image Analysis of Coals," *Scanning Microscopy*, 1988, 2 (3), 1257-1264.
10. Twogood, R.E.; Sommer, F.G. "Digital Image Processing," *IEEE Transactions on Nuclear Science* 1982, NS-29 (3), 1076-1086.

11. Weszka, J.S. "A Survey of Threshold Selection Techniques," *Computer Graphics and Image Processing* 1978, 7, 259-265.
12. Kohler, R. "A Segmentation System Based on Thresholding," *Computer Graphics and Image Processing* 1981, 15, 319-338.
13. DeHoff, R.T.; Rhines, F.N. *Quantitative Microscopy*; Materials Science and Engineering Series, McGraw Hill Book Company, 1968.
14. McCarthy, J.J.; Schamber, F.H. "Least-Squares Fit with Digital Filter: A Status Report," *National Bureau of Standards Special Publication 604*, 1981, pp. 273-296.
15. Kalmanovitch, D.P.; Frank, M. "An Effective Model of Viscosity for Ash Deposition Phenomena," Conference on Mineral Matter and Ash Deposition from Coal, The Engineering Foundation, Santa Barbara, CA, Feb. 21-26, 1988.

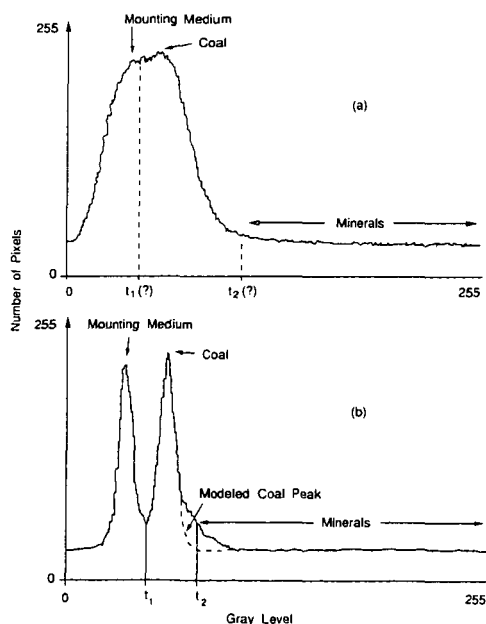


Figure 1. Grey-level histograms, (a) original histogram, the selection of thresholds segmenting mounting medium from coal (t_1) and coal from minerals (t_2) is arbitrary; (b) median filtered histogram (5 x 5 filter), mounting medium and coal peaks are resolved, thus facilitating automatic threshold selection by the method described in the text.

COAL SURFACE THERMODYNAMICS BY INVERSE GAS CHROMATOGRAPHY*

A. S. Glass and J. W. Larsen
Department of Chemistry
Lehigh University
Bethlehem, PA 18015

(Keywords: coal surfaces, surface thermodynamics, inverse gas chromatography)

Introduction

Determination of coal surface interactions is important for the development of improved coal liquefaction and beneficiation methods. Knowledge of interactions at coal interfaces will aid the development of such technologically important coal reactions.

Although coals possess pores, they probably do not possess interconnected internal surfaces^{1,2}. Coals have the properties of absorbents, including an external surface and the ability to absorb molecules in the bulk. A technique that determines coal surface interactions must be sensitive to interactions at the external coal surface.

Many techniques are available for studying interactions at surfaces, but most are not suitable for measuring interaction thermodynamics of complex coal surfaces. Static adsorption and calorimetric techniques measure coal-solute interactions, but they are plagued by diffusion of the solute into the coal³⁻⁵. In contrast, inverse gas chromatography (IGC) is a dynamic sorption technique. Only those interactions that occur during the time of travel of the solute contribute to the signal in IGC. Therefore, IGC is sensitive to coal-solute interactions that occur in the rapid uptake regime rather than those that occur during the slow approach to equilibrium that characterizes static sorption measurements of coals.

Theory

IGC is most straightforward in the regime of linear chromatography. In this regime, also called the "Henry's Law" or "infinite dilution" regime, the retention volume is most characteristic of the interaction between the solute and the stationary phase. For a single type of retention mechanism, i.e., surface adsorption, the Henry's Law constant, K_s , expresses the equilibrium thermodynamic interaction between the adsorbate and the stationary phase. K_s is the retention volume per accessible surface area of the stationary phase and per unit pressure of adsorbate in the gas phase⁶:

$$K_s = \frac{V_N}{SRT} = \frac{V_s}{RT} \quad (1)$$

where V_N is the net retention volume, S is the surface area of the stationary phase that is accessible to the solute, R is the gas constant, T is the column temperature, and V_s is the specific

retention volume.

The dependence of retention volume on surface area has been used to determine S for stationary phases. If V_s is determined for a given probe molecule on a stationary phase of known S , then S can be calculated for a column of unknown S from⁶:

$$S = \frac{V_N}{V_s} \quad (2)$$

For polymers below T_g where adsorption occurs on the external geometrical surface, it has been shown that S is equivalent to the external geometrical surface, S_{geom} ⁷. For spherical particles of radius r and particle density ρ , S_{geom} is given by⁸

$$S_{geom} = \frac{3}{\rho r} \quad (3)$$

Since K_s is the equilibrium constant for surface adsorption, then

$$K_s = K_{s,o} e^{\frac{q_{st}}{RT}} \quad (4)$$

where q_{st} is the isosteric heat of adsorption. Substituting equation 1 and converting to natural logarithms gives

$$\ln(V_N/T) = \frac{q_{st}}{RT} + \ln K_{s,o} + \ln SR \quad (5)$$

The slope of a plot of $\ln(V_N/T)$ vs. $1/T$ gives q_{st} . The adsorption entropy, ΔS° , may be determined from^{9,10}

$$\Delta S^\circ = \frac{-q_{st}}{T} + 31.61 + R \ln V_s \quad (6)$$

Experimental

Experiments were conducted by injecting gas samples at pressures of 0.01 to 10.0 Torr from a glass manifold via an 8-port Valco GC valve with 0.015 and 0.100 ml sample loops. Pressures were measured with a 1 Torr Baratron gauge (MKS Instruments, Inc.) or a mercury manometer attached to the sample reservoir.

Gases were 99% purity or better. Liquids obtained from Aldrich in "sure-seal" bottles were subjected to at least three freeze-pump-thaw cycles before being introduced as gases at pressures below their vapor pressures.

Argon premium Illinois No. 6 coal was sieved to give the desired fraction (80/100, 60/70, or 40/60 mesh) and about 4g was packed into a 1/8 inch O.D., 2.1mm I.D. ss column about 1.5m in length. The particle density was 1.3 g/ml¹¹. The coal was degassed overnight at 150°C before each day's experiments. The

GC was a Hewlett-Packard 5890A equipped with both TCD and FID detectors. 0.03 inch I.D. ss tubing was used between the GC valve and the column inlet to minimize dead volume.

Data were collected over the range 30 to 150°C, with injector and detector temperatures at 180°C. The temperature of the chromatograph oven was accurate to $\pm 0.1^\circ\text{C}$ and was constant to within 0.2°C over different parts of the oven. Flow rates ranged from 5 to 35 ml/min. They were determined using a bubble meter and were corrected for the effect of water vapor. The pressure drop was determined using a pressure transducer (Omega Engineering, Inc.) on the column inlet and a barometer for measuring atmospheric pressure. Typical pressure drops were about 1 atm. Retention volumes were corrected using the pressure drop correction term, j^{12} .

Column dead volumes were determined from geometrical considerations for the different mesh fraction particle sizes and checked using columns of the same length and diameter packed with the same mesh fraction of nonporous glass beads. Retention times for various solutes on the glass bead columns were characteristic of the dead volume.

Data were collected using Lab Calc software (Galactic Industries Corp.) at rates of one point per second. Retention times were determined as first moments of the peaks using Simpson's rule. Adsorption entropies were calculated using de Boer's approach⁹, assuming a standard gaseous state with a pressure of 1.01×10^8 dyne/cm² and a standard adsorbed state with a pressure of 0.338 dyne/cm.

Results and Discussion

I. Technique

With injection sizes greater than about 10^{-4} μmole of adsorbate, peak tailing increased greatly. With injection sizes below this saturation limit, peak shapes and retention times were independent of injection size. This behavior resembles that seen with column overload¹³. Assuming close packing of adsorbates on the coal surface, the injection sizes corresponding to the onset of column saturation gave specific surface areas of about 0.02 m²/g, similar to the geometrical surface area of coal in the column. This indicates that the accessible surface of coal in the column was equal to the external surface of the coal. All thermodynamic data were obtained using injection sizes below the saturation limit.

Table I shows accessible and geometrical surface areas calculated using equations 2 and 3 for columns containing different particle sizes of coal using three different adsorbates. From the table it is seen that the agreement between S and S_{geom} for methane and *n*-butane is good. The agreement for neopentane is worse and this will be discussed in the next section. These results show that the accessible surface is equal to the external surface of the coal, and provide further support for the idea that coal behaves as an absorbent in IGC.

The surface areas in Table I, when corrected for the amount

of coal in the column, give specific surface areas on the order of $0.05 \text{ m}^2/\text{g}$. Assuming coal particle sizes of $25 \mu\text{m}$, typical of those used in static sorption experiments, gives an external geometrical specific surface area of $0.10 \text{ m}^2/\text{g}$. This value is smaller than specific surface areas determined by static sorption by at least 1 to 2 orders of magnitude^{1,4}. This provides evidence that static sorption determines a "coal surface area" which contains a contribution from absorption. In contrast, IGC measures a coal surface area that is due to surface adsorption only.

II. Thermodynamics

Figure 1 is a plot of q_{st} vs. polarizability, α , for linear alkanes, neopentane, and cyclopropane on Illinois No. 6 coal determined by IGC. In plot 1A, it is seen that the strength of interaction with the coal surface increases linearly with the polarizability of the adsorbate. The increase in q_{st} from methane to ethane is 3.2 kcal/mol , while that between ethane and propane is 2.8 kcal/mol . Between propane and *n*-hexane, the increase in q_{st} per CH_2 group of the adsorbate levels off to a constant value of about 2.1 kcal/mol . On carbon surfaces, the increase in q_{st} per CH_2 group of the adsorbate varies between about 1.0 and 3.0 kcal/mol , depending on the history of the carbon^{10,14}. Our values for Illinois No. 6 coal are higher than for graphitized carbon black surfaces and fall within the range for non-graphitized and oxidized surfaces.

While the adsorption enthalpies for the linear alkanes scale with polarizability, neopentane does not fall on the line. The effect of increased branching of the adsorbate on retention is well known for graphitized carbon surfaces¹⁵. This effect is probably responsible for the relatively low adsorption enthalpy of neopentane on Illinois No. 6 coal. In this context, it is interesting to reconsider the data in Table I. The data for neopentane show larger errors than those for methane and *n*-butane. This is probably due to the smaller coal surface area accessed by neopentane.

Plot 1B corresponds to adsorption heats on Illinois No. 6 coal extracted with tetrahydrofuran. The linear hydrocarbons show the linear relation between q_{st} and α , while neopentane falls slightly below the line. The decrease in the values of q_{st} for Plot 1B compared to 1A are greatest at high values of α , corresponding to the larger hydrocarbons. This indicates a decrease in carbon atom density as a result of extraction. For polyethylene glycol vs. carbon black, a decrease in the slope of a plot of q_{st} vs. carbon number was ascribed to a decrease in the energy of nonspecific interaction due to a decrease in the density of carbon atoms at the surface¹⁶.

Figure 2 is a plot of q_{st} vs. ΔS° for linear hydrocarbons and neopentane on both the extracted and original Illinois No. 6 coal. The linear relationship is an example of the well-known isokinetic effect¹⁷. The fact that the isokinetic effect holds supports the existence of a common surface adsorption interaction of these molecules with the coal.

Conclusion

Thermodynamic data for adsorption at the external surface of Illinois No. 6 coal have been determined by IGC. The behavior of Illinois No. 6 coal in these experiments fits with the view that coals are crosslinked macromolecular networks capable of taking up molecules into their bulk^{18,19}. This supports the position that coals do not contain interconnected pore networks^{1,2}.

The surface thermodynamic data are reasonable as they fall within the limits of those for non-graphitized carbon surfaces. The determination of surface thermodynamics for various coals and modified coals by IGC will enable the creation of a coal surface interaction database. This will aid the development of improved coal reaction strategies.

References

1. Larsen, J. W.; Wernett, P. C. Energy Fuels 1988, 2, 719.
 2. Larsen, J. W.; Wernett, P. C. Prepr. Pap.-Am. Chem. Soc., Div. Fuel Chem. 1992, 37, 849.
 3. Hsieh, S. T.; Duda, J. L. Fuel 1987, 66, 170
 4. Marsh, H. Fuel 1965, 44, 253.
 5. Fowkes, F. M.; Jones, K. L.; Li, G.; Lloyd, T. B. Energy Fuels 1989, 3, 97.
 6. Kiselev, A. V.; Yashin, I. Gas-Adsorption Chromatography; Plenum: New York, 1969; p. 121.
 7. Braun, J.-M.; Guillet, J. E. Macromolecules 1975, 8, 882.
 8. Lowell, S. Introduction to Powder Surface Area; Wiley & Sons: New York, 1979; p. 5.
 9. de Boer, J. H. The Dynamical Character of Adsorption; Oxford University: London, 1953; Chapter 6.
 10. Crescenti, G.; Mangani, F.; Mastrogiamco, A. R.; Palma, P.; J. Chromatogr. 1987, 392, 83.
 11. Van Krevelen, D. W. Coal; Elsevier: New York, 1961; p. 128.
 12. Littlewood, A. B. Gas Chromatography, 2nd ed.; Academic: New York, 1970; p. 30.
 13. Ruthven, D. M. Principles of Adsorption and Adsorption Processes; Wiley & Sons: New York, 1984; p. 226-227.
 14. Elkington, P. A.; Curthoys, G. J. Phys. Chem. 1969, 73, 2321.
 15. Littlewood, A. B. Gas Chromatography; Academic: New York, 1970; p. 102ff.
 16. Kiselev, A. V.; Yashin, I. Gas-Adsorption Chromatography; Plenum: New York, 1969; pp. 56-58.
 17. Isaacs, N. S. Physical Organic Chemistry; Wiley & Sons: New York, 1987; pp. 102-103.
 18. Van Krevelen, D. W. Coal; Elsevier: New York, 1961; pp. 127ff.
 19. Larsen, J. W. In New Trends in Coal Science, NATO ASI Ser. vol 244; Yürüm, Y., Ed.; Kluwer Academic: Netherlands, 1988; p. 73.
- *A full paper on this topic has been submitted to The Journal of Physical Chemistry.

Table I. Geometrical and Accessible Surface Areas for Columns Containing 4 grams of Illinois No. 6 Coal of Different Particle Sizes.

Column	1	2	3
Mesh Fraction	80/100	60/70	40/60
$r \text{ (}\mu\text{m)}^{\dagger}$	82.5	115.5	169.0
$S_{\text{geom}} \text{ (m}^2)^*$	0.110	0.080	0.055
$S^a \text{ (m}^2)^{\ddagger}$	--	0.091	0.061
$S^b \text{ (m}^2)^{\ddagger}$	--	0.150	0.038
$S^c \text{ (m}^2)^{\ddagger}$	--	0.078	0.051
Diff $S^a-S_{\text{geom}}, \%$	--	13.8	10.9
Diff $S^b-S_{\text{geom}}, \%$	--	87.5	-32.7
Diff $S^c-S_{\text{geom}}, \%$	--	-1.25	-7.27

[†]particle radius for the average particle size of the given mesh fraction.

*Calculated from equation 3 assuming spherical particles.

[‡]Determined using equation 2 by setting the accessible surface area of column 1 to its geometrical surface area.

^aCH₄ from data at 90°C; ^bneo-C₃H₁₂ from data at 115°C; ^cn-C₄H₁₀ from data at 120°C.

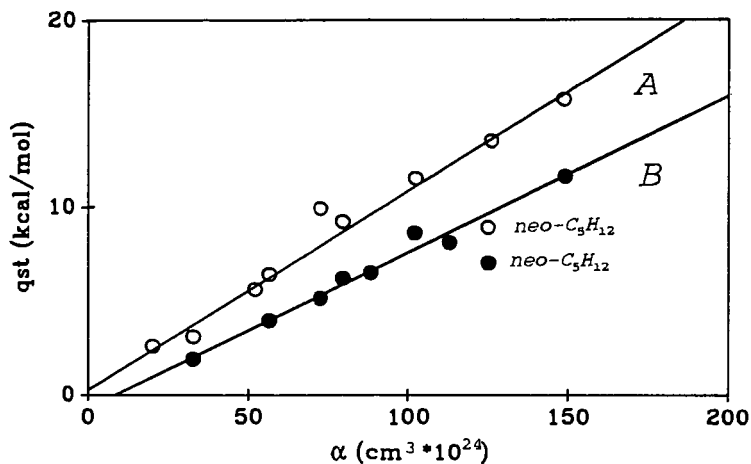


Figure 1. Heats of adsorption vs. polarizability for hydrocarbons on Illinois No. 6 coal. A, Original coal, o. B, Coal extracted with tetrahydrofuran, •.

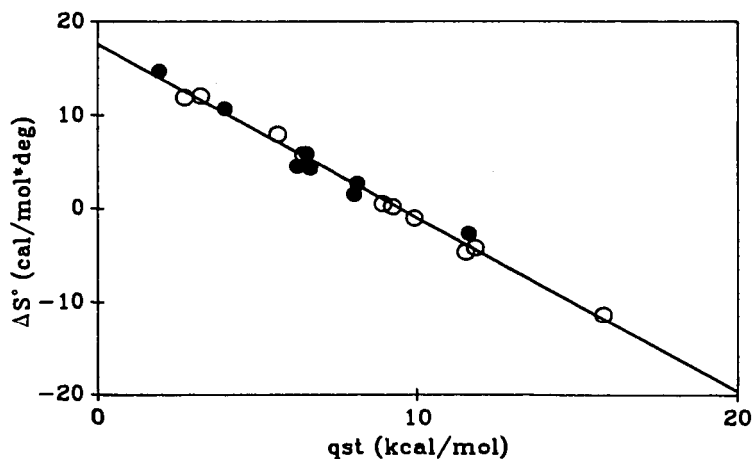


Figure 2. Heats of adsorption vs. entropies of adsorption for hydrocarbons on original and THF-extracted Illinois No. 6 coal. o, Original Coal; •, THF-extracted Coal.

Oxidation-Induced Structural Changes in Argonne Coals Studied by Differential Scanning Calorimetry and Solvent Swelling

Yongseung Yun and Eric M. Suuberg
Division of Engineering, Brown University
Providence, RI 02912

Key Words: Oxidation, Differential Scanning Calorimetry, Solvent swelling, Argonne coals

INTRODUCTION

It is widely known that oxidation/weathering has a profound effect on many important coal properties such as coking characteristics, slurry pH, flotability, tar yield, extractability, etc., as well as on coal utilization processes such as combustion, pyrolysis, gasification and liquefaction [1-5]. In addition, there have been many reports as to the high sensitivity of coal structure to aerial oxidation, especially in steam-pretreated coal. For example, Graff and Brandes [6] reported the decrease of liquid yield from 61% to 25% after exposing steam-treated Illinois No. 6 coal to air at room temperature for just two minutes. Because of these reports that have established the extreme vulnerability of coal structure to air, even at room temperature, major accommodations, to prevent air contact, have ensued in many studies on coal. The basic question here is how air causes change in coal structure, even at room temperature in such a short time (minutes). At higher temperatures, e.g., at temperatures which can cause the thermal degradation of coal structure, the sensitivity of the response of oxidized coal to heat or solvents has been well established, and can be easily understood, since even small amounts of oxidized functional groups might act as initiators of chain processes that can magnify the total response.

This paper is concerned with the effect of aerial oxidation on the solvent swelling ratio of several pretreated coal samples (i.e., water-treated, heat-treated). Our former studies [7,8] have clearly illustrated that heating under an inert environment renders coal structure relaxed in such a way that solvent and/or catalysts for liquefaction can be efficiently employed or incorporated into coal structure. The question that we pose here is whether the effects of oxidation make themselves known at low temperatures, in terms of changes in macromolecular structure, that might mitigate some pretreatment effects.

EXPERIMENTAL

Aliquots of three coal samples, obtained from the Argonne National Laboratory - Premium Coal Sample Program, were analyzed by differential scanning calorimetry (DSC) and solvent swelling techniques. These samples included Upper Freeport (-100 mesh), Pittsburgh No. 8 (-100 mesh), and Illinois No. 6 (-20 mesh) coals. Detailed petrographic, chemical, and physical analysis data on these coals can be found elsewhere [9]. Detailed experimental procedures for DSC and solvent swelling can be also found elsewhere [8,10]. One point should be carefully noted with respect to the latter measurements, the supernatant swelling solvent was replaced every day. This is important, because the coal is effectively solvent extracted by this procedure. Aerial oxidation was performed in two ways. One method involved oxidizing the coal sample in a tube furnace at 115°C or 120°C for one day under room air. Another method involved oxidizing the sample inside the DSC at 120°C for 15 hr with dry air flow of 100 ml/min over the aluminum pan containing the coal sample.

RESULTS AND DISCUSSION

First, we examined the effect of aerial oxidation on solvent swellability by comparing as-received and oxidized coals (this can give us some hint as to changes of structure). For this purpose, Upper Freeport medium volatile bituminous coal was oxidized at 120°C in the tube furnace for one day, under room air, and the resulting oxidized coal as well as as-received coal were heat-

treated inside the DSC under the continuous flow of nitrogen up to the specified temperature, followed by quench-cooling and pyridine swelling. The results are illustrated in Figure 1 in which pyridine swellability is shown as a function of heat-treatment temperature. In Figure 1, it is noteworthy that the aerial oxidation rendered the final pyridine swelling values higher than the corresponding values in as-received coal. Probably the newly formed oxygenated functional groups on the surface of coal provided additional capacity to hold pyridine molecules because of increased polarity of the coal surface. Thus, it is safe to say that aerial oxidation seems to have a significant impact on pyridine swellability, at least, in Upper Freeport coal.

The oxidation results in a considerable increase in swellability prior to thermal relaxation of the coal's structure (below 250°C). One would have to surmise that the thermodynamically favorable mixing of the new oxygen functional groups and pyridine overwhelms some of the thermally labile non-covalent interactions (though many are preserved). The very slow nature of the swelling in this low temperature regime favors this explanation over one based upon the oxidation itself destroying some of the interactions.

Once the thermally labile interactions are destroyed by heating the coal to over 300°C, the time dependence of swelling apparently shifts (higher swelling is seen in shorter times). This is because the coal becomes quite extractable after thermal relaxation as compared to before, and the decrease in swellability with time is an artifact due to extraction of some of the coal. Temperatures above 350°C have not been explored in the case of the oxidized coal because the extraction already starts to become quite significant in the sample obtained at 350°C.

The main concern of this paper is with what kind of sensitivity an already relaxed coal structure (normally achieved here by heat treatment) might have upon exposure to air. Two coals, i.e., Upper Freeport and Pittsburgh No. 8 coals, were heat-treated and followed by aerial oxidation in this case inside the DSC at 120°C for 15 hr with air flowrate of 100 ml/min. Note that in this case heat treatment precedes oxidation, the opposite of the situation in the experiments of Figure 1. The temperature of heat treatment was selected based upon the difference DSC results reported in our earlier studies [7,8,10]. The differences in sensitivity to aerial oxidation were measured by pyridine swellability and the results are shown in Figure 2.

Figure 2 reveals several interesting results. While heat-treated-plus-oxidized Upper Freeport coal exhibits higher pyridine swellability compared to heat-treated-only coal (which agrees with the data of Figure 1), the opposite case was observed in Pittsburgh No. 8 coal. It appears that in the case of the Upper Freeport coal initial values of swelling ratio are more or less identical regardless of oxidation. However, appreciable differences in pyridine swelling ratios start to appear with further swelling time. The decrease of the pyridine swelling ratio with time is believed to be caused by extraction as noted earlier. In this case, note that the increase in swellability with oxidation of the Upper Freeport coal is modest at short swelling times. This makes sense, in that the structure is fully relaxed already by heat treatment, and the addition of oxygen functional groups does not provide pyridine an extra "handle" for relaxing the structure, as it does in non-heated coals. The actual short-time swelling ratio is quite similar to what it was for heat treated, non-oxidized coal itself (around 2.22 at 350°C from Figure 1, compared to 2.25 for non-oxidized coal in Figure 2 and 2.29 for oxidized coal in Figure 2).

Since the decrease in apparent swellability with time is attributed to extraction of the coal, it appears that the unoxidized coal is more extractable. While measurements need to be performed to establish quantitatively the relative extents of extraction, at present, we believe that this is the most likely explanation for the observed behavior. Because both the oxidized and non-oxidized Upper Freeport samples swell equally readily to their comparable maximum values, the later differences in extractability appear to indicate that oxidative crosslinking occurred in the oxidized sample. Thus we see evidence of a deleterious effect of 120°C aerial oxidation on the macromolecular structure of this coal, as regards any attempt to break down that structure or solubilize it.

In the case of the Pittsburgh No. 8 sample, oxidation is seen to be immediately deleterious. The Pittsburgh coal has a significant concentration of polar functional groups already, so it does not benefit from added oxygen providing more strong interaction sites for swelling. Evidence of oxidative crosslinking is visible in the first data points for swelling in pyridine. From that point on, the two curves for oxidized and non-oxidized Pittsburgh No. 8 samples, track each other closely, meaning that comparable amounts of extractable are lost from both samples. The effect

is not as large as in the Upper Freeport coal. This means that the incremental effect of aerial oxidation is not nearly as significant in the Pittsburgh No. 8 coal as in the Upper Freeport coal.

Figure 3 shows the effect of aerial oxidation on the DSC signatures of Upper Freeport coal. First, the coal was heat-treated inside DSC up to 350°C and the water evaporation process around 110°C as well as structural relaxation process around 310-350°C are both clearly visible (see thick-solid line (1) in Figure 3). Then the heat-treated coal sample was exposed to an air flow of 100 ml/min inside DSC for 12 hr at 120°C, followed by another two consecutive DSC scans up to 350°C (the first and second scans shown as a solid line (2) and a dotted line (3), respectively, in Figure 3). A clear exotherm, extending from 150-230°C with maximum at around 195°C, can be seen in (2). There was an earlier report [11] of observed an exotherm around 195°C in Upper Freeport coal following long exposure to air. The difference DSC (shown as solid line (4) in Figure 3) illustrates concisely the effect of aerial oxidation on coal structure, which results in an exotherm centered at around 195°C.

It has already been established in connection with the data of Figure 2 that oxidation at 120°C probably causes chemical reactions in the structure. The existence of this exothermic peak centered at 195°C suggests that a different set of processes is involved in that exotherm. Consequently, the search for oxidation effects by DSC can be misleading, if it implies that the peak at 195°C represents the beginning of oxygen functional group chemistry.

Figure 4 shows the effect of aerial oxidation on heat-treated Pittsburgh No. 8 coal. The coal's structure was relaxed by heat treatment, as is evident in the upper panel of Figure 4 from the fast swelling time for the heat-treated coal compared to as-received coal. Both the tetrahydrofuran (THF) and pyridine swelling ratios are higher for heat treated coal than for as-received coals. No appreciable differences can be noted between THF swelling responses from 5 hr and 15 hr oxidized samples, indicating that, after 5 hr of oxidation, further exposure to air does not cause any significant changes in the structure of Pittsburgh No. 8 coal.

We find it curious that in contrast to the results in pyridine, the swellability in THF is not strongly influenced by whether the sample is oxidized or not. Consistent with THF being a poorer solvent for this coal (note the lower swelling ratio compared to pyridine), the THF shows much less evidence of extraction. The visual appearance of the THF solvent also suggests a much lesser amount of extract compared to pyridine. So it appears that with a "weaker" solvent, oxidation effects are not as notable. This could be because the swellability of the coal structure is not linear in numbers of crosslinks; THF is unable to dissociate some non-covalent crosslinks that pyridine can, and existence of a few more covalent crosslinks makes little difference in swelling.

Pyridine swellability after heat-treatment exhibits quite different characteristics. The swelling time required to reach the maximum swelling ratio in pyridine is comparable to that for THF swelling after heat treatment. Before heat treatment, the pyridine is taken up much more quickly by the coal. This is again understood in terms of the pyridine's ability to dissociate some non-covalent crosslinks that THF cannot. A possibility is that there are strong acid-base interactions that pyridine, a strong base, can participate in, whereas THF cannot. Following oxidation, the same pattern of extraction is displayed in the data of Figure 4 as was shown in Figure 2, and the differences compared with THF, are large.

The mass gain upon oxidation was determined for the sample shown in the lower panel of Figure 4. The oxygen uptake (assuming no loss of any material during oxidation) was 1.83 wt%. This corresponds to an addition of 1.1×10^{-3} mol O/g coal, or using a density of 1.3 g/cc for this coal, the oxygen uptake was 1.4×10^{-3} mol O/cc. To help put this figure in perspective, the uptake of pyridine by the coal is initially about 18.8×10^{-3} mol pyridine/cc. Thus there is not a major addition of potential pyridine-holding groups to the coal. The actual loss of pyridine capacity as a result of oxidation is about 0.9×10^{-3} mol pyridine/cc, based on the earliest swelling points. The comparability of the equivalents of oxygen uptake and the loss of pyridine capacity is intriguing, but we cannot ascribe any significance to the comparability of these values at this time.

The DSC results on oxidized Illinois No.6 and Pittsburgh No.8 coals are shown in Figure 5. The difference DSC spectra clearly illustrate the exotherm around 200°C caused by added

oxygen. It should be pointed out that the temperature range of the exothermic peaks is remarkably similar to that observed in the Upper Freeport medium volatile coal (see Figure 3). These observations might suggest that aerial oxidation is actually concerned with certain specific components irrespective of coal rank (and pretreatment conditions).

In order to confirm the reportedly high sensitivity of Illinois No. 6 coal to air exposure after steam treatment [6], four sets of Illinois No. 6 coal samples were prepared and compared in terms of solvent swellability. Treatment was performed in water in a sealed bomb under a self generated pressure of 1000 psig for about one hour and then the sample was cooled to room temperature, so that the resulting sample remained submerged in water. Thus it is fair to call the treatment process as "water-treatment" instead of steam treatment. From the steam pressure, the temperature is known to be 285°C. The water was removed by drying under vacuum at room temperature for about three days. The tube-furnace was employed for quick oxidation experiments. As-received and water-treated coal samples were oxidized under room air for one day at 115°C. Figure 6 is the result on four sets of samples, in which dotted lines denote oxidized samples.

When the four sets of samples were compared as to solvent swellability in pyridine, no significant difference in pyridine swellability was caused by oxidation during the course of one day at 115°C. If there were any changes due to oxidation, they involved rather slight increases in equilibrium pyridine swelling ratio. The water treatment appears to have no significant effect on the pyridine swelling ratio, either with or without oxidation. We have no explanation for the curiously slower initial pyridine swelling that the oxidized coals experience. The fact that this feature is, however, unaffected by water treatment again supports the notion that not very much is changed in the structure by the treatment. The temperature of the treatment was below the range normally thought to be needed to see significant benefit [6] and is at the very beginning of what we believe to be a pre-pyrolytic structural relaxation in this coal. Thus, the lack of effect was not surprising.

What was, then, surprising was the significant effect of water treatment on THF swellability. First, water treatment decreases THF swellability. The lack of a corresponding decrease in pyridine swellability strongly suggests that covalent crosslinking is not involved. Water pretreatment in this temperature range appears to be promoting the formation of stronger, new non-covalent interactions. It is unclear from these data alone whether this involves formation of new intracoal bonding interactions, because the coal can rearrange structurally, or whether this involves addition of new oxygen functional groups, which contribute new interactions. Whatever the mechanism is, the oxidation promotes even more such non-covalent bonding interactions that THF is unable to dissociate.

The results of Figure 6 are replotted in a more concise form, with respect to each treatment, in Figure 7. After one day of swelling, pyridine swelling ratio reaches relatively similar values regardless of treatment, while THF swelling ratios indicate that oxidation was an important factor in reducing swelling.

The DSC results of Figure 8 show the effect of oxidation on the samples whose behavior was illustrated in Figures 6 and 7. As before with the Pittsburgh No. 8 and Upper Freeport coals, oxidation gives rise to an exothermic peak centered near 200°C. Unlike the situation in the earlier described coals, the peak does not have a well-defined upper temperature limit, in the case of Illinois No. 6 coal. This apparent peak "tailing" is independent of the fact that the coal experienced a temperature of 285°C during water treatment (thus the 200°C peak is caused by treatment), and is the same in both water treated and untreated coals. Thus the conclusion must be that the exotherm "tail" is a result of oxidation of this coal's structure in a manner different than observed in the Pittsburgh No. 8 coal or the Upper Freeport coal.

Careful examination of the peaks in Figure 8 strongly suggests that the "tail" does not in fact represent continuation of the exotherm to higher temperatures than those seen in Upper Freeport and Pittsburgh No. 8 coals. Instead, it actually appears that mass loss results in a "baseline shift" in the difference spectrum. Loss of mass, associated with the exotherm at near 200°C, would tend to decrease the apparent heat capacity of the sample after 200°C, during the first scan. When a second scan, which involves no mass loss, is subtracted from the first scan, the expected result would be a negative difference before the peak and a zero difference after the peak. The

former is seen, but the latter is not; the difference spectrum shows a positive baseline value after the peak, although it is heading towards zero. Some further processes apparently do occur above 250°C, but their magnitude is considerably less than a cursory look at Figure 8 might otherwise suggest. (The processes might include relaxations of the coal structure between 300 and 350°C, as we have discussed earlier; these relaxations may not have occurred during water treatment since the temperature was only 285°C). Further experiments to explore the effects of water and steam pretreatment are scheduled.

CONCLUSIONS

- Aerial oxidation in Upper Freeport coal rendered the pyridine swellability values higher than those in the corresponding as-received coal. This is due to addition of oxygen functionality, in all probability.
- Heat-treated Upper Freeport and Pittsburgh No.8 coals (in which coal structure was relaxed) show an appreciable impact of aerial oxidation. However, the nature of the effect was quite different. Aerial oxidation appears to cause less extraction from Upper Freeport medium volatile bituminous coal, due to crosslinking. Crosslinking is also promoted in Pittsburgh No. 8 coal, but relative extractability is unaffected.
- THF swellability of Pittsburgh No. 8 coal is not significantly affected by oxidation, whereas pyridine swellability is reduced. By contrast, the Illinois No.6 coal exhibits a significant decrease with oxidation of the THF swellability, while pyridine swellability remaining more or less the same.
- The comparison of DSC thermograms obtained from as-received and oxidized coal samples at 8°C/min demonstrate that an exothermic peak centered around 200°C was caused by the added oxygen and, interestingly, does not depend upon coal rank. These observations might suggest that the oxidation is actually concerned with certain specific components in coal structure, irrespective of coal rank as well as pretreatment conditions. However, this must be considered in light of the result below.
- According to DSC thermograms obtained from oxidized coal samples, the Illinois No.6 coal appears to be attacked in a different manner than the Upper Freeport and Pittsburgh No.8 coals. It appears to lose mass at the time of the exotherm.

ACKNOWLEDGEMENT The work reported here was financially supported by the Department of Energy Contract No. DE-AC22-91PC91027.

REFERENCES

1. Gray, R.J.; Rhoades, A.H.; King, D.T. *AIChE Trans.* **1976**, *260*, 334.
2. Cronauer, D.C.; Ruberto, R.G.; Jenkins, R.G.; Davis, A.; Painter, P.C.; Hoover, D.S.; Starsinic, M.E.; Schyler, D. *Fuel* **1983**, *62*, 1124.
3. Khan, M.R.; Jenkins, R.G. In *Chemistry of Coal Weathering*; Nelson, C.R. Ed.; Elsevier: Amsterdam, 1989; pp. 107-132.
4. Wu, M.M.; Robbins, G.A.; Winschel, R.A.; Burke, F.P. *Energy & Fuels* **1988**, *2*, 150.
5. Furimsky, E.; MacPhee, J.A.; Vancea, L.; Ciavaglia, L.A.; Nandi, B.N. *Fuel* **1983**, *62*, 395.
6. Graff, R.A.; Brandes, S.D. *Energy & Fuels* **1987**, *1*, 84.
7. Yun, Y.; Suuberg, E.M., accepted for publication in *Energy & Fuels*, 1992.
8. Yun, Y.; Suuberg, E.M., submitted to *Fuel*, 1992.
9. Vorres, K.S. *User's Handbook for the Argonne Premium Coal Sample Program*; Argonne, Illinois, 1989.
10. Yun, Y.; Otake, Y.; Suuberg, E.M. *Prepr. Pap.-Am. Chem. Soc., Div. Fuel Chem.* **1991**, *36(3)*, 1314.
11. MacDonald, R.A.; Callanan, J.E.; McDermot, K.M. *Energy & Fuels* **1987**, *1*, 535.

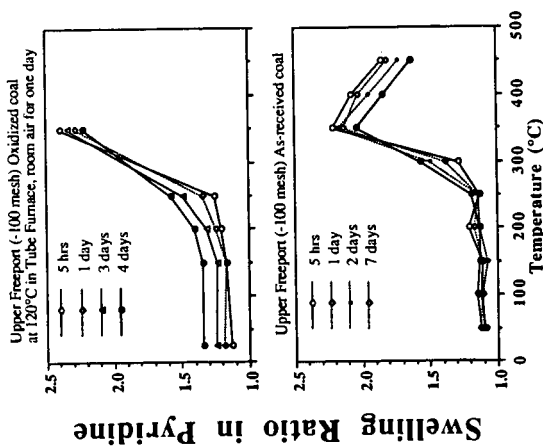


Figure 1. Comparison of pyridine swelling ratios with heat-treatment temperature between as-received and air-oxidized Upper Freeport medium volatile bituminous coal.

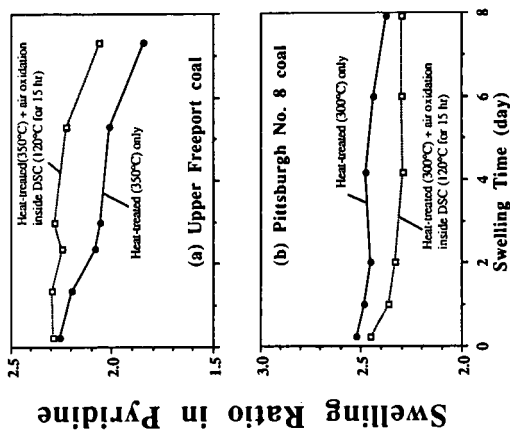


Figure 2. Effects of aerial oxidation on pyridine swelling characteristics in heat-treated and oxidized Upper Freeport, Pittsburgh No. 8 coals.

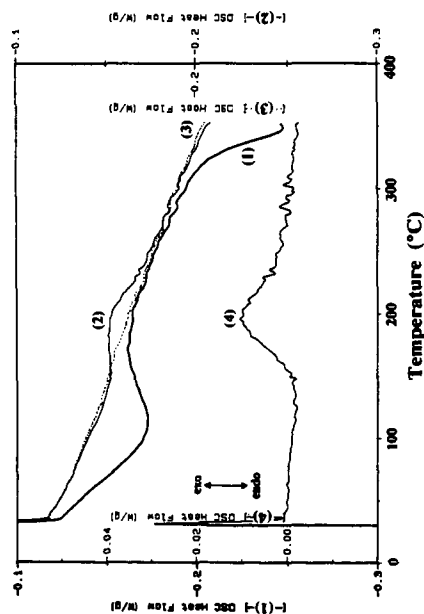


Figure 3. DSC and difference DSC thermograms obtained at 8°C/min from Upper Freeport medium volatile bituminous coal. The experiment was performed as follows: First, as-received coal was heat-treated up to 300°C; the result of which is denoted as (1) in the figure. Second, the purge gas inside the DSC was switched from nitrogen to air (100 ml/min) and the sample was cooled down to 120°C. Third, the heat-treated coal was scanned once. The results of the DSC, the results of which are (2) and (3). The difference DSC thermogram of the two consecutive DSC thermograms (2) and (3) is denoted as (4).

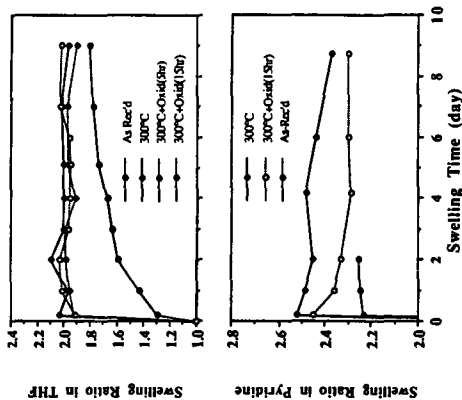


Figure 4. Effects of aerial oxidation on changes of THF and pyridine swelling ratios with swelling time in as-received and heat-treated Pittsburgh No. 8 coal. The notation of 300°C in the figure denotes that the sample was pretreated inside the DSC up to 300°C at 8°C/min under a nitrogen atmosphere. Oxidation was performed inside the DSC at 120°C with 100 ml/min air for 5 or 15 hr.

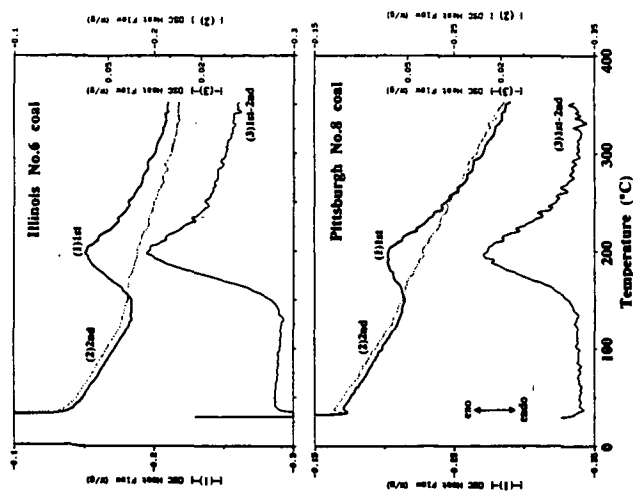


Figure 5. First and second DSC thermograms as well as the corresponding difference DSC thermograms for oxidized Illinois No. 6 and Pittsburgh No. 8 coals. Oxidation condition was 120°C for 15 hr while the sample was kept under air flow of 100 ml/min inside the DSC.

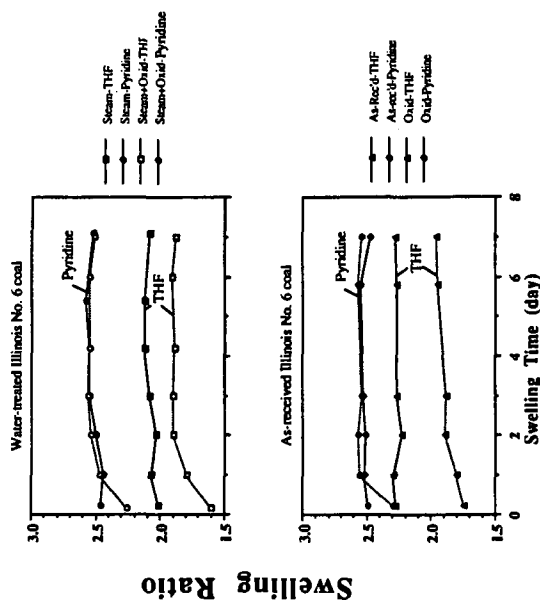


Figure 6. Effects of serial oxidation and water treatment on changes of solvent swelling ratios with swelling time in Illinois No. 6 high volatile bituminous coal. Oxidation was performed in tube furnace at 115°C for one day with room air.

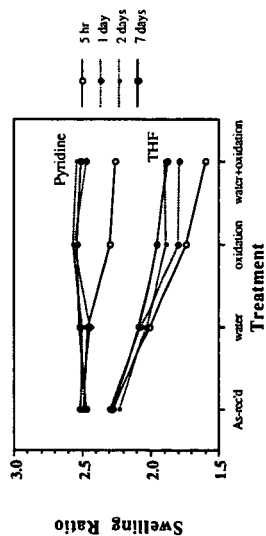


Figure 7. Comparison of solvent swelling ratios with respect to pretreatment conditions in Illinois No.6 high volatile bituminous coal. Water-treatment condition was at 1000 psig for about 1 hr and oxidation condition was at 115°C for 1 day with room air.

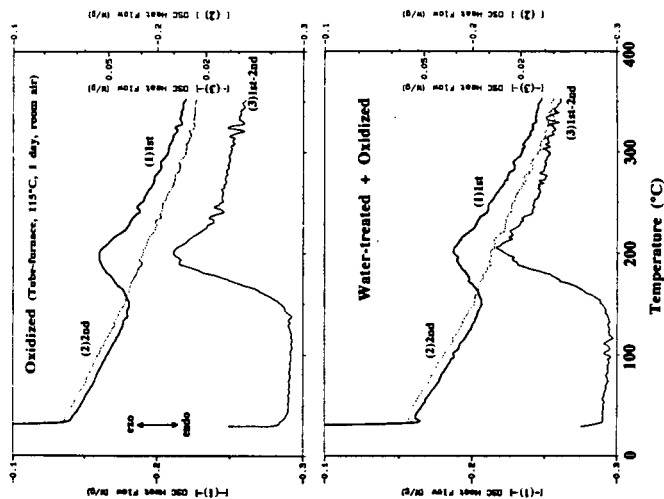


Figure 8. DSC (1st and 2nd) thermograms and the corresponding difference DSC thermogram obtained at 8°C/min from oxidized and water-treated-and-oxidized Illinois No.6 coal.

X-RAY DESCRIPTORS OF THE "NEAR" DIFFRACTION PEAK IN SOME ARGONNE PREMIUM COALS.

David L. Wertz
Department of Chemistry & Biochemistry
Center for Coal Product Research
University of Southern Mississippi
Hattiesburg, MS 39406 USA

Key words: [00L] peaks, PAC layering.

INTRODUCTION

The Argonne Premium Coals are being thoroughly characterized by many research groups.

Four of the bituminous coals in the Argonne Premium Coal Program samples have been utilized to determine the ability of x-ray diffraction methodology to define several of the non-crystalline features of these coals.

Three of the subject coals, Pocahontas #3 (APC 501), Pittsburgh #8 (APC 401), and Upper Freeport (APC 101), reportedly have very low moisture contents, 0.5-1.5 %. The fourth coal, Lewiston-Stockton, has a higher moisture content, 4.6 %. Three of the subject coals reportedly contain ca. 75 % carbon, of which at least 75 % has been classified as aromatic. Both the carbon percentage and its aromatic fraction are reportedly much higher in Pocahontas #3.^{1,4}

The subject coals differ in considerably in inorganic content, producing from 4.5% - 13.0% high temperature ash.¹ Furthermore, the coals differ considerably in volatile matter, ranging from 43.7 % for the Lewiston coal (high volatile bituminous) to 18.5% in Pocahontas #3 (low volatile bituminous). The coals also differ considerably in the reported volatile matter content.¹

The extent to which diffraction may be used to measure the crystalline entities in coals has been established.⁵ The effects of important other features on the diffractogram of a coal have not been so well established.⁶ The purpose of this study is to determine which parameters that are important to coal scientists and/or environmental scientists may be measured by x-ray diffraction methods.

EXPERIMENTAL

COALS. The Argonne Premium Coals, well defined in numerous references, were provided as finely powdered samples sealed into an inert atmosphere. For these samples, the particle diameter < 0.15 mm.

A more detailed description of these subject coals is presented in Table One.

Division of carbon into aromatic and aliphatic fractions is based on the average of values reported by two different groups who analyzed these coals by MAS ¹³C nmr methods.^{2,3} Except for Pittsburgh #8, the aromatic (and aliphatic) fraction reported by each group differ by less than the experimental uncertainty of their results. The difference between the aromatic fraction reported by the two groups is ca. 0.10, which exceeds the

experimental uncertainty suggested by each of the nmr groups.

X-RAY EXPERIMENTS. A 0.5 gram sample of each finely powdered coal was mounted into our θ - 2θ x-ray diffractometer which is equipped with a theta-compensating slit, a sample spinner, and a LiF crystal monochromator in the secondary x-ray beam. A diffractogram of each coal was obtained over the region from $2\theta = 5.00^\circ$ to 50.00° by measuring the secondary intensity for five seconds at angular increments of 0.02° . Diffractograms acquired over a much wider angular range but using a much shorter count time at each angle have already been presented.^{5,6}

TABLE ONE. PARTIAL COMPOSITIONS OF THE HIGHEST RANK COALS IN THE ARGONNE PREMIUM COAL PROGRAM SAMPLES¹

COAL DESCRIPTOR	COAL DESIGNATION			
	A	A	A	A
	P	P	P	P
	C	C	C	C
	1	4	5	6
	0	0	0	0
	1	1	1	1
A. Rank	mvb	hvb	lvb	hvb
B. Volatile Matter	27.14%	37.20%	18.48%	43.72%
C. Moisture	1.13%	1.65%	0.65%	4.63%
D. High Temperature Ash	13.03%	9.10%	4.74%	4.49%
E. Carbon Content	73.34%	74.25%	86.15%	73.32%
E.1. Aromatic Fraction ^{2,3}	0.83	0.77	0.87	0.75
E.2. Aliphatic Fraction ^{2,3}	0.17	0.23	0.13	0.25

RESULTS

The abbreviated diffractograms of the four Argonne Premium Coals are presented in Figure One. Diffractograms of these four (and the other) Argonne Premium Coals obtained over a considerably wider angular range have been previously presented. The mass absorption coefficient (previously determined for these coals for Cu K α x-rays⁶) was used to calculate the absorption corrected intensity. These diffractograms were partitioned into diffraction peaks (due to crystalline species in the coals) and a residual intensity which describes the amorphous scattering, as shown in Figure Two. Included in Figure Two is experimentally measured curve (2.A), the diffraction intensity due to the minerals (2.C), and the residual intensity (2.B). The latter is due to non-crystalline scattering, including the amorphous scattering due to the average poly-cyclic aromatic structural unit in each coal as well as other structural features.

The residual intensity curve, due to non-crystalline scattering, is shown for each of the four coals in Figure Three.

From the maxima and minima observed in each diffractogram, the molecular scattering associated with the average poly-cyclic aromatic hydrocarbon unit in each coal was calculated and then removed from the amorphous scattering intensity, as shown in Figure Four for APC 501. A well define peak results. Shown in Figure Five is the resulting "diffraction" peak, which (a) dominates the diffractogram, (b) is much broader than a typical diffraction peak, and (c) is asymmetrical.

In graphite, an ideal poly-cyclic aromatic compound (PAC), a corresponding diffraction peak, much more intense and much less broad, occurs at 3.35 Å and describes the stacking of its [00L] planes.

This unusually broad diffraction peak is due to imperfect diffraction from the [00L] planes present in each of the coals. As noted in Figure Five the shapes of the [00L] peak differ considerably, although each appears to be composed a symmetrical peak and a broad maximum. The symmetrical peak was simulated by the method of Kurita⁸, i.e.

$$I(2\theta) = Q \cdot \exp(-a' \Delta s^2) = Q \cdot \exp(-a' \cdot HW^2) \quad (1)$$

where Q is the maximum peak intensity and s is the half width at half maximum (HW) measured for the diffraction peak in reciprocal space. A summary of the symmetrical peak simulated for each coal is presented in Table Two.

TABLE TWO. SUMMARY OF SOME X-RAY DESCRIPTORS OF THE NEAR DIFFRACTION PEAK.

COAL	dmax	I*max (CPS)	HW (rad)	s (Å ⁻¹)
APC 501	3.541 Å	1,880	0.0332	0.0210
APC 101	3.578 Å	1,471	0.0387	0.0244
APC 401	3.749 Å	1,328	0.0707	0.0447
APC 601	3.755 Å	1,271	0.0775	0.0490
*GRAPHITE	3.354 Å	75,466	0.0174	0.0027

PEAK MAXIMUM. The intensity of the broad [00L] peak, as measured by the peak height in the absorption corrected diffractograms, is related to the % aromatic character by:

$I_{max} = m'(\% C_{ar}) + b$; where m and b are coefficients determined by linear least squares methods. For this analysis, R = 0.9989.

The [00L] maximum shifts, from 3.54 Å in APC 501 (the low volatile bituminous) to ca. 3.75 Å in the two high volatile bituminous coals -- APC 401 AND APC 601. This increase in the average inter-planar spacing parallels decreasing aromatic (and concomitant increasing aliphatic) content in the coals, suggesting that the aromatic PAC lamellae become further separated, on the average, as the rank of the coal decreases.

PEAK WIDTH. The width of a diffraction peak may be affected by several factors. However, to a first approximation, $\Delta 2\theta$ (in radians) = $ef + (0.9\lambda/T\cos\theta) + (2(\Delta d/d)\tan\theta)$; (2) where ef is a characteristic function of the diffractometer, λ is the x-ray wavelength, T is the particle size of the diffracting material(s), $\Delta d/d$ is the deviation (strain) in the inter-planar spacing that cause diffraction peak characterized by the inter-planar spacing d .

(1) The Diffractometer Contribution. $\Delta d/d \rightarrow 0$ for graphite, as evidenced by the very intense and very narrow diffraction peak observed from the finely powdered graphite used as the reference in this study. As a consequence, the observed peak width ($0.25^\circ = 0.0174$ rad) has been attributed to our diffractometer.

(2) Effect of Particle Size. The coal particles provided via the Argonne Premium Coal Sample Program and the graphite particles are 10^4 - 10^6 Å in diameter. Since $\lambda = 1.5404$ Å, $\lambda/T \rightarrow 10^{-4}$, which is considerably smaller than experimental uncertainty in these diffraction experiments. Consequently, for neither the coals nor the graphite is peak broadening due to particle size effects important.

(3) Effect of Inter-Planar Strain due to Distortions ($\Delta d/d$). For these coals, the peak broadening due to distortions in the distance between the PAH planes is given by:

$$\Delta 2\theta = 2\Delta d/d \tan\theta. \quad (3)$$

(4) Approximate Solution to the Peak Broadening Effect for the Argonne Premium Coals. Since $\lambda/t \rightarrow 0$, the observed peak broadening, $\Delta 2\theta$, may be related only to $\Delta d/d$ by:

$$\Delta d/d = (HW - 0.0174)/\tan\theta \quad (4)$$

Shown in Table Three in the strain associated with the [00L] planes for these coals.

TABLE THREE. ESTIMATE OF THE STRAIN IN THE [00L] PEAK.

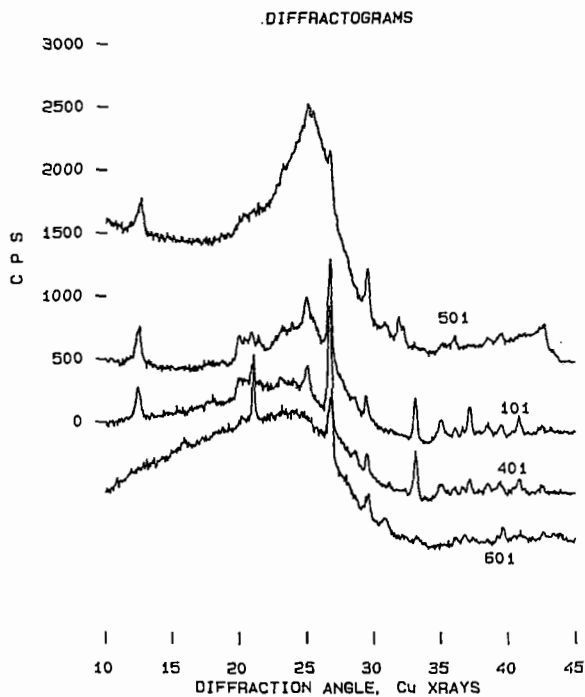
COAL	$\Delta d/d \cdot 100$
APC 101	9.6 %
APC 401	23.7 %
APC 501	7.1 %
APC 601	27.1 %

KEY REFERENCES

1. Vorres, K. S., Energy Fuels, 1990 (4) 420.
2. Solum, M. S., Pugmire, R. J., and Grant, D. M., Energy Fuels, 1989 (3) 187.
3. Shin, S. C., Baldwin, R. M., and Miller, R. L., Energy Fuels, 1989 (3) 193.
4. Weitzsacker, C. J. and Gardella, J. A., Anal. Chem., 1992 (64) 1068.

5. Wertz, D. L., Powder Diff., 1990 (5) 44.
6. Wertz, D. L., Energy Fuels, 1990 (4) 442.
7. Wertz, D. L., Powder Diff., 1988 (3) 153.
8. Kurita, M., Adv. X-Ray Anal., 1987 (31) 277.
9. Specht, E. D., Clausing, R. E., and Heatherly, L., J. Material Res., 1990 (5) 2351.

FIGURE ONE



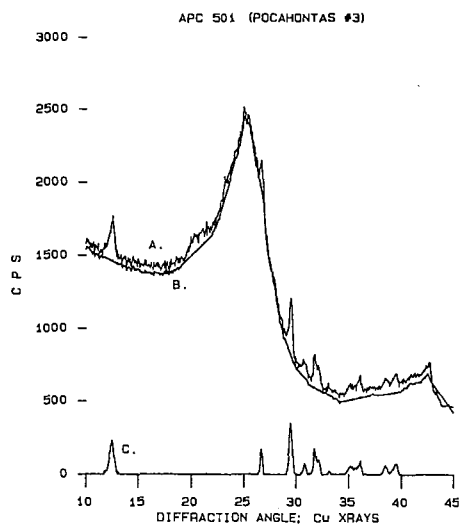


FIGURE TWO

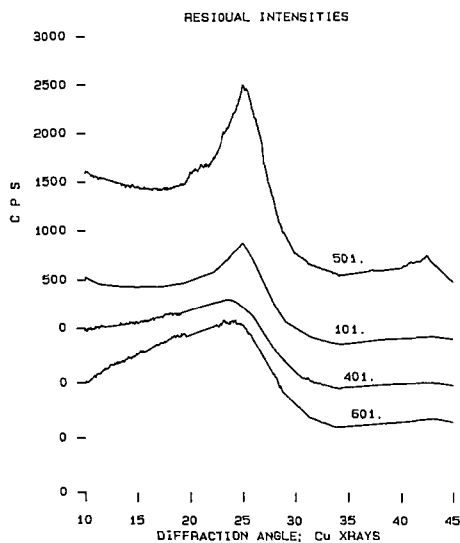


FIGURE THREE

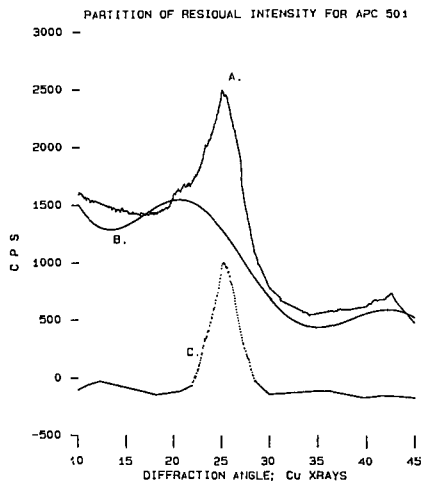


FIGURE FOUR

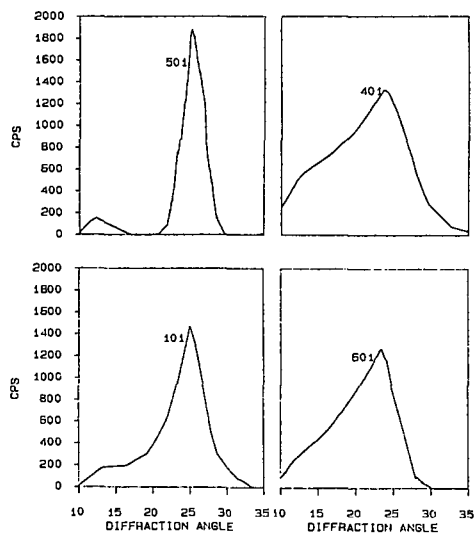


FIGURE FIVE

CO₂ Adsorption Techniques On High Surface Area Activated Carbons.

Mark L. Stewart and John M. Stencel.
Center for Applied Energy Research
University of Kentucky
Lexington, Kentucky
40511-8433

1. INTRODUCTION

For years the subject of CO₂ adsorption on activated carbons has been both challenged and supported. The question remains whether or not CO₂ is a valid adsorbate for characterizing pore structures of activated carbons. The predominance of nitrogen adsorption as a routine experimental technique for BET surface area approximations has more or less overshadowed the limitations of this technique in terms of activated diffusion phenomena[1]. As a result, it is thought that nitrogen adsorption at 77K generally underestimates the surface area of coals[1]. In some super-activated carbons, CO₂ is an attractive adsorbate for characterization due to its small molecular diameter and it's access to supermicropores. Although CO₂ adsorption models are not completely understood, for particular cases in which N₂ adsorption may be problematic or inconclusive, CO₂ adsorption may offer additional pore structure information.

The purpose of this communication is to address the concept of CO₂ adsorption phenomena experimentally and conceptually. Experimental data are compared for CO₂ adsorbed onto very high surface area activated carbons. From this information, optimal experimental conditions are theorized on the basis of ease and understanding. It is hoped that an adsorption procedure involving the benefits of N₂ and CO₂ together will provide insight into the pore structures of very high surface area activated carbons.

2. EXPERIMENTAL

Materials used:

Two activated carbons were used in the experiments; they were supplied by Amoco Research and Development, and Norit N.V. Activated Carbon. They are classified as Amoco Super-A and Norit A-8982. The surface areas, as measured by nitrogen BET method[2], were 1500-1800 m²/g for Norit A-8982 and 2500-2800 m²/g for Amoco Super-A.

Experimental methods:

Adsorption analysis was performed on a Coulter Omnisorp 100CX Automated Gas Sorption System. Approximately 0.25 grams of sample was weighed prior to outgassing. All samples were outgassed at 250°C and sealed under vacuum prior to

analysis. Static volumetric mode was used for all CO₂ and N₂ adsorption measurements. N₂ was adsorbed at 77K in the relative pressure range (P/P_0) of 0.001 to 0.98. CO₂ was adsorbed at three different temperatures and relative pressure ranges(P/P_0) as follows:

195K: 0.0001 to 0.48
273K: 0.0001 to 0.027
298K: 0.0002 to 0.015

CO₂ saturation vapor pressures for each temperature were taken as follows:

195K: 1,410 torr[3]
273K: 26,068 torr
298K: 45,041 torr

Molecular diameters used for N₂ and CO₂ were 3.64 and 3.3 angstroms, respectively. All surface areas were calculated from the BET equation[2] and pore volumes were approximated using the Dubinin-Radushkevich equation[4].

3. RESULTS AND DISCUSSION

The CO₂ adsorption isotherms for the A-8982 and the Amoco Super-A carbons at 195K, 273K, and 298K are plotted in Figures 1 and 3, respectively. Upon initial examination for the Norit carbon, the CO₂ uptake at 195K in this low pressure region is markedly higher than in the other two temperature cases. At 273K and 298K, the isotherms are virtually identical with very little deviation in CO₂ uptake. The Amoco Super-A carbon exhibits similar characteristics in this region but with a noticeable difference in the 273K and 298K temperature cases. These results suggest that, at 195K, complete micropore filling may occur giving higher potential for CO₂ adsorption. It is likely that incomplete micropore filling occurs at temperatures of 273-298K since the saturation vapor pressure of CO₂ is extremely sensitive to temperature changes and is very high. However, it seems reasonable to assume that, at 195K, a better estimate of internal pore uptake can be obtained.

The CO₂ DR plots for A-8982 and Amoco Super-A are indicated in Figures 2 and 4, respectively. In estimating pore volumes, a comparable range for each temperature was taken for extrapolation to the y-axis. The pore volumes are as follows:

Norit 195K = 1.22 cc/g	Amoco 195K = 2.00 cc/g
Norit 273K = 0.93 cc/g	Amoco 273K = 1.40 cc/g
Norit 298K = 1.09 cc/g	Amoco 298K = 1.64 cc/g

At an adsorption temperature of 195K the pore volumes are the highest which relates to the increased uptake observed in the adsorption isotherms in figures 1 and 3. Pore volume calculations from N₂ adsorption are slightly less than the 195K CO₂ case but higher than 273K and 298K CO₂ cases. Results obtained from BET surface

area calculations for the 195K CO₂ case yield higher surface areas than N₂ BET estimates.

4. CONCLUSIONS

CO₂ adsorption at 195K appears to be a valid technique for approximating pore volumes of high surface area activated carbons if complete micropore filling is assumed. Experimentally, due to instrumental limits, a larger relative pressure range can be analysed for 195K due to the temperature and vapor pressure sensitivities present at 273K and 298K. Because of this fact, CO₂ and N₂ surface areas can be compared. Since the relative pressure ranges for 273K and 298K are so low, (maximum $p/p_0 = 0.02-0.03$), the micropore filling is incomplete, giving pore volumes that are underestimated. Although a strict comparison between CO₂ and N₂ needs to be investigated further, molecular size differences may still give some insight on the possible presence of any super microporosity.

5. REFERENCES

1. Om P. Mahajan, Carbon Vol. 29 No. 6. pp. 735-742. 1991.
2. Brunauer S., Emmett P.H., Teller E. J.A.M. CHEM. SOC., pg 6309. 1938.
3. H. Marsh, D. Crawford, T.M. O'Grady, and A. Wennerberg, Carbon Vol. 20 No 5, pp. 419-426, 1982.
4. Dubinin M.M., and Radushkavich L.V. Proc. acad. Sci. USSR Vol. 55 pg 331 1947.

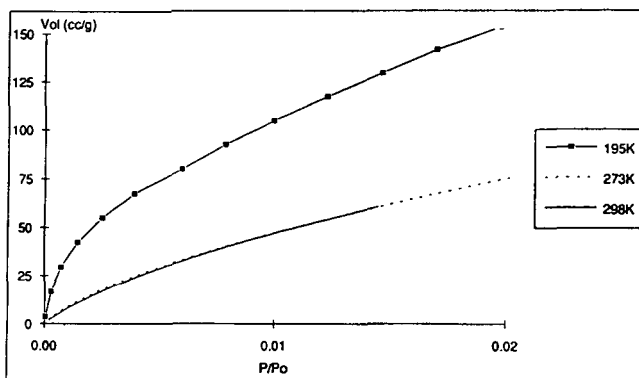


Fig. 1. CO₂ adsorption isotherms on Norit activated carbon at 195K, 273K, and 298K.

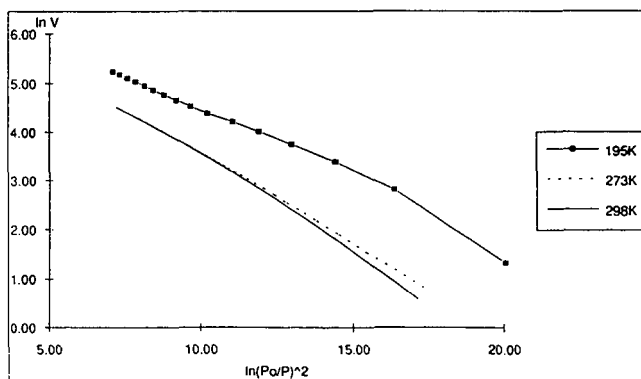


Fig. 2. CO₂ DR plots corresponding to isotherms in Fig. 1.

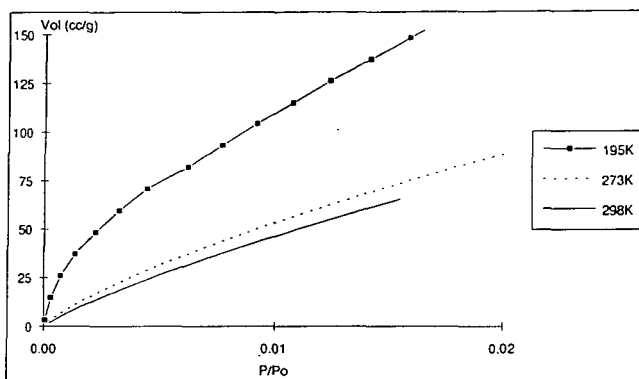


Fig. 3. CO₂ adsorption isotherms on Amoco Super-A activated carbon at 195K, 273K, and 298K.

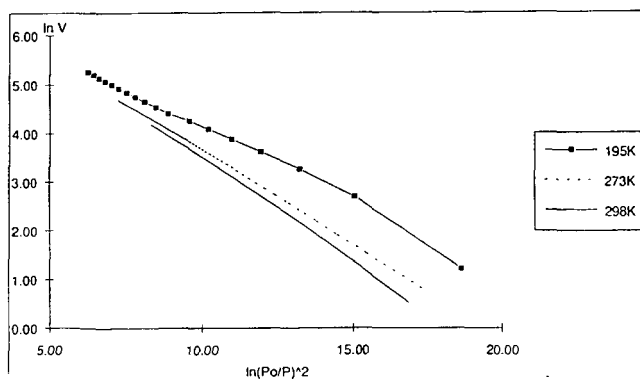


Fig. 4. CO₂ DR plots corresponding to isotherms in Fig. 3.

**SYMPOSIUM ON ANALYTICAL TECHNIQUES FOR CHARACTERIZING
COAL AND COAL CONVERSION PRODUCTS
AMERICAN CHEMICAL SOCIETY
WASHINGTON, DC MEETING, AUGUST 23-28, 1992**

TG-MS FOR CHARACTERIZATION OF ACTIVATED CARBONS FROM COAL

By

A.M. Rubel, M. Jagtoyen, J.M. Stencel, S. N. Ahmed, F. J. Derbyshire
University of Kentucky, Center for Applied Energy Research
3572 Iron Works Pike, Lexington, KY 40511-8433

Keywords: thermogravimetry, mass spectrometry, coal-based activated carbons

INTRODUCTION

The application of thermogravimetry coupled with a quadrupole mass spectrometer (TG-MS) to study coal-based materials was examined. First, TG-MS was used to analyze the gaseous decomposition products from activated coal-based carbons to obtain structural information related to their synthesis conditions. Secondly, adsorption/desorption profiles of physisorbed and chemisorbed gases were determined through temperature programmed desorption/evolved gas analysis (TPD/EGA).

There are a number of reviews on the use of TG-MS systems to study decomposition and kinetics of biological, organic, and inorganic compounds.^{1,2,3} This method has several advantages over other instrumentation used for TPD/EGA. For example, methods that utilize gas chromatography (GC) to monitor gas release are limited to only a few gases and the time required for each analysis results in discontinuous gas evolution profiles^{4,5}. Newer methods, which couple MS to the reactors used for TPD, provide a significant improvement; however many of these systems do not have continuous sample weight monitoring^{6,7}.

The TG-MS system used for this study provided the ability to accurately and continuously monitor weight changes simultaneously with evolved gas composition. The quadrupole MS system employed allows determination of multiple gas components in the range of 0-300 atomic mass units. Procedures for determining relative gas evolution rates and quantities have been developed. The system is equipped with multiple sweep and reaction gas purge, gas switching, and gas blending capabilities which make possible the study of adsorption and desorption of gases under a wide variety of conditions.

EXPERIMENTAL

Instrumentation

A Seiko TG/DTA 320 was coupled to a VG Micromass quadrupole MS. The TG was connected to a disk station which provided for programmable control of the furnace, continuous weight measurements, sweep gas valve switching, data analysis, and export of data to other computers. The TG has a temperature range of room temperature to

1300°C. The MS has a Nier type enclosed ion source, a triple mass filter, and two detectors (a Faraday cup and a secondary emissions multiplier). The MS was controlled by a dedicated personal computer which was also used to acquire and review scans before export to a spreadsheet for data manipulation.

The two instruments were coupled by a fused silica capillary transfer line leading from above the sample pan in the TG to an inert metrasil molecular leak which interfaced the capillary with the enclosed ion source of the MS. Connections at both ends of the capillary allowed sampling of very small fractions of the gases. The transfer line was heated to 170°C at which temperature the flow rate through the capillary was approximately 12 ml/min.

TG-MS procedures

The TG conditions used to study the relationship between the structure and synthesis parameters of carbons were: heating rate of 10°C/min to a 5 min hold at 900°C; sweep gas, 225 ml/min; constant sample volume weighing 10-25mg. The MS was scanned over a 0-100 amu range with measurement intervals of approximately 30 seconds.

The TG heating profile for TPD/EGA measurements was more complex and incorporated segments for outgassing, cooling, adsorption, desorption, and temperature-induced desorption (Table I). During outgassing and subsequent cooling of the sample to an adsorption temperature (segments a and b, Table I), an inert (He) gas sweep was usually used after which the gas to be adsorbed was introduced. After completion of an adsorption interval, He was again used to purge the system during segments d and e. Multiple and consecutive adsorption/desorption cycles were performed by recycling the temperature programmer to segment b.

The relative amounts of effluent gases monitored by the MS was determined using the He peak intensity, at a constant flow rate, to determine a sensitivity factor for each analysis. The area under the gas evolution curve for each gas was determined, normalized for the sample weight, and multiplied by the sensitivity factor obtained by arbitrarily assigning a value of one to the He intensity of one of the runs to be compared. This run was referred to as the standard run. The sensitivity factor was then calculated by dividing the He intensity of the standard run by the intensity of He in all subsequent runs. The intensities of all other gases of interest were multiplied by the sensitivity factor for relative comparisons.

Materials

Activated carbons produced by chemical and thermal procedures were studied during the first part of this work. They were produced from Illinois Basin bituminous coals supplied by the Illinois Basin Coal Sample Program and were prepared according to procedures detailed elsewhere^{8,9,10}. Two types of chemical activation were examined, H₃PO₄ and KOH. Temperature treatments were 170 and 500°C for acid treated carbons and 75, 400 and 800°C for base treated carbons. All carbons were leached to a pH of 7 and dried before TG-MS analysis.

During the TPD/EGA study, a commercially (Carbotech) produced coal-based

carbon was used. This carbon was produced by thermal activation and had a N_2 BET surface area of $450 \text{ m}^2/\text{g}$. The adsorption gas mixture was 2% NO , 10% O_2 , 15% CO_2 with He the balance.

RESULTS AND DISCUSSION

Structural determinations

TG-MS experimental data enables the correlation of weight loss to individual gas evolution. The temperature of evolution has been related to different functional groups on the surface of the carbon matrix¹¹. For example, the data in Figure 2 were from a carbon sample thermally treated at 500°C . Maxima in the evolution profiles for CH_4 and H_2 were at 620 and 820°C . Dealkylation is a likely source of the CH_4 release¹². H_2 and CH_4 evolution began at about the same temperature but H_2 continued to be evolved after CH_4 release had stopped. This suggests that H_2 from more than one source contributes to its evolution profile. Possible sources are the decomposition of aliphatics at lower temperatures and aromatics at higher temperatures¹². Very little CO_2 (mass 44) was evolved which suggests that the CO_x (mass 28) evolution profile represents primarily CO release. Presently work is being done to correlate these TG-MS CO and CO_2 evolution determinations to carbonyl and aromatic C-O measurements by FTIR.

No significant amounts of other gases were detected by MS. Gas identification was based on a comparison of several ions. For instance, the identification of CH_4 was based on a comparison of mass 16 with mass 32 (O_2). Mass 32 did not deviate significantly from barely detectable levels. In this example, weight loss cannot be assigned to a specific gas since evolution profiles overlap. However, weight loss corresponded well with the onset of gas evolution.

Important to this study was a comparison of the relative amount of gas evolved from carbons produced under different synthesis conditions. A number of factors (condition of the capillary transfer tube, the ion source, and the efficiency of the vacuum system) affect the sensitivity of the MS. Therefore, comparison of spectra required the development of a method to correct for the sensitivity of the MS. Helium was used as an internal standard to calculate a sensitivity correction factor for each spectra. Since the flow rate and concentration of He was held constant for each experiment and the amount of gases evolved from the sample was negligible in comparison to the concentration of He, each spectra was corrected to the same He intensity arbitrarily chosen from the spectra to be compared. Further, comparison of gases on a unit basis required normalization of the relative amount of gas evolved for the differing initial sample weights.

Using the above approach, carbons produced under a number of thermal, acid and base treatments were examined. H_2 and CH_4 evolution profiles were compared for three carbons treated as follows: low followed by high temperature treatment (170°C and 500°C); low followed by high temperature treatment with H_3PO_4 ; and high temperature treatment with acid (Figure 3 and 4). These three samples, though activated at the same maximum temperature, had quite different H_2 evolution profiles. The acid treatment appeared to remove more low temperature H_2 since evolution began at 460°C for the thermal only sample and at nearly 600°C for acid treated samples. Additionally, the

temperature of maximum H_2 evolution was shifted slightly higher for acid treated carbons. CH_4 evolution was observed only for the carbon sample that had a thermal treatment without acid. If the CH_4 results from the pyrolytic cleavage of aliphatic carbon side chain in the parent coal structure, then acid treatment promoted these dealkylation reactions. The calculated relative amounts of H_2 released indicated that acid treatment promotes dehydrogenation (Figure 3 and 5) during synthesis. The relative amounts of evolved H_2 were consistent with H/C atomic ratios calculated from elemental analysis of the carbons.

TG-MS data of four activated carbons produced under different thermal and base (KOH) treatments were also compared (Figure 6). The relative amount of evolved H_2 and CH_4 decreased with increased severity of treatment. The base activated carbon evolved substantially more CO and CO_2 than the thermal only treated sample. This is consistent with FTIR analyses of these samples which showed carbonyl group development in base treated samples which was not present in the parent coal⁹.

TPD/EGA determinations

The NO adsorption/desorption profiles (Figure 7) of a commercial coal-based activated carbon will be used as an example of a TPD/EGA determination performed by TG-MS. Adsorbing samples must be heated to a temperature as high as the maximum desorption temperature to remove any adsorbed gases. After this pre-conditioning step and sample cooling to 70°C, NO plus CO_2 , O_2 , and He were passed over the sample until its weight approached saturation. The NO was turned off and a He sweep gas was passed over the sample at the adsorption temperature for a period of time. This interval allowed purging of the NO from the system and removal of any physically bound NO from the carbon. The sample was then heated at 10°C/min to a maximum desorption temperature of 400°C. In Figure 7, some weight loss occurs during the low temperature desorption period but the MS spectrum showed an intense peak at mass 30 which correlated well with the weight loss during heating. The temperature at which maximum evolution occurred was 132°C. This temperature indicates NO is not strongly bound to the carbon matrix. The only gas evolved during desorption was NO which allows the direct correlation of weight loss with NO desorption. Any number of adsorption/desorption cycles can be consecutively run. The sample in Figure 6 was repeated three times.

SUMMARY AND CONCLUSIONS

TG-MS has been successfully applied to the study of coal-based activated carbons providing information which relates synthesis parameters to the structure of the carbons. Procedures were developed to compare the relative quantities of evolved gases. The instrumentation was also used to do TPD/EGA analyses of activated carbons. Their adsorption and desorption properties are important in evaluating the practical applications.

REFERENCES

1. Dollimore, D., G.A. Gamlen, and T.J. Taylor. *Thermochimica Acta* 75 (1984)59.
2. Wendlandt, W.W. *Thermal Methods of Analysis*, 3rd edn., Wiley, New York, 1986,482.

3. Eppler, H. and H. Selhofer. *Thermochimica Acta* 20 (1977)45.
4. Carrizosa, I. and G. Munuera. *J. Catal.*, 49 (1977)174.
5. Cvetanovic, R.J. and Y. Amenomiya. *Adv. Catal.*, 17 (1967)103.
6. Bernal, S., R. Garcia, and J.M. Rodriguez-Izquierdo. *Thermochimica Acta* 70 (1983)249.
7. Causton, P. and B. McEnaney. *Fuel* 64 (1985)1447.
8. Derbyshire, F.J., J. Stencel, B. McEnaney, M. Thwaites, and M. Jagtoyen. Final Technical Report to CRSC, "An Investigation of the Conversion of Illinois Coals to Activated Carbons," for the period Sept. 1, 1990 through Sept. 3, 1991.
9. Derbyshire, F.J., M. Jagtoyen, R. Rathbone, and J. Stencel. Quarterly Report to the CRSC, "Synthesis of Adsorbent Carbons from Illinois Coals," for the period of Dec. 1, 1991 through February 29th, 1992.
10. Derbyshire, F.J., M. Jagtoyen, J. Stencel, and B. McEnaney. Quarterly Report to the CRSC, "Synthesis of Adsorbent Carbons from Illinois Coals," for the period of Sept. 1 through Nov. 30, 1991.
11. Wang, J. and B. McEnaney. *Abstracts 19th American Conference on Carbon*, Pennsylvania State Univ. (1989)590.
12. Wen, C.Y. and S. Dutta. In *Coal Conversion Technology*, C.Y. Wen and E.S. Lee, Eds., Addison-Wesley Publishing Co., Reading, MA(1979)57.

Table I. TG heating profile for ADP.

Step	Temp C	Rate C/min	Hold min
a	0-400	20	10
b	400-70	50	10
c	70 (1)	0	60
d	70 (2)	0	30
e	70-400	20	10

¹Adsorption

²Low temperature desorption

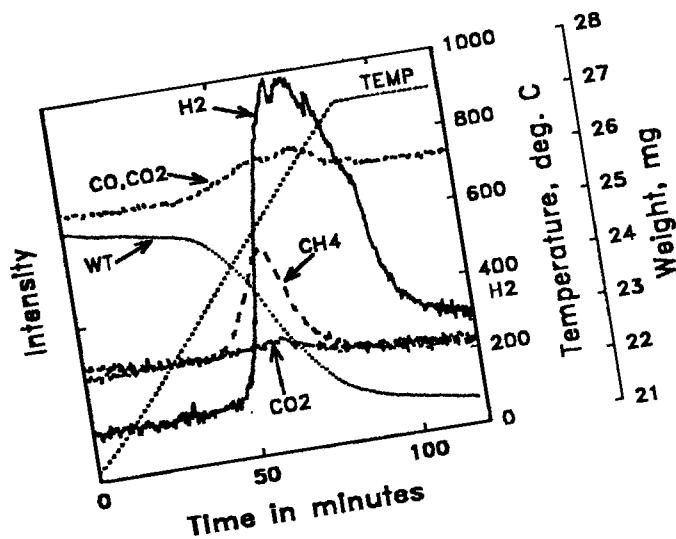
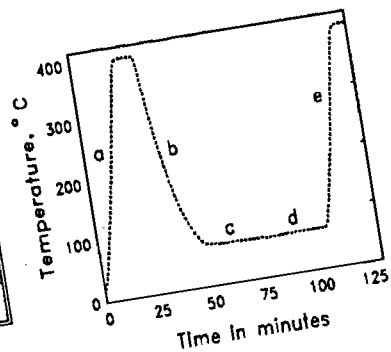


Figure 1. TG-MS analysis of thermally treated activated carbon from IBC sample.

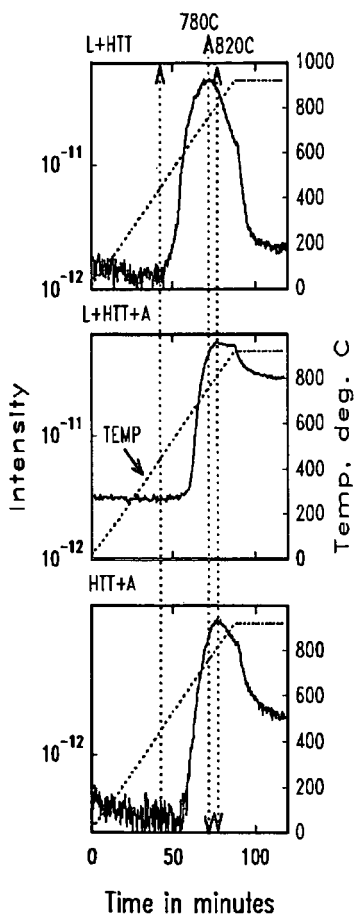


Figure 3. H_2 evolution curves from TG-MS analysis of acid and heat treated coal-based active carbons. A= H_3PO_4 ; L=low; HTT=high temperature treatment

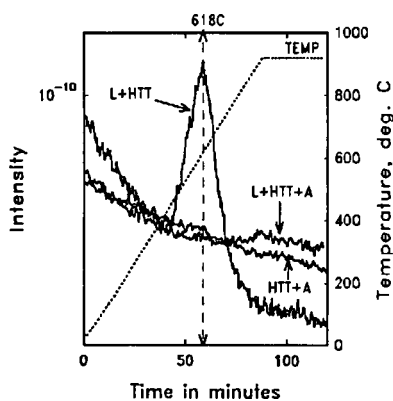


Figure 4. CH_4 evolutions curves from TG-MS analysis of acid and thermally activated coal-based carbons. A= H_3PO_4 ; L=low; HTT=high temperature treatment

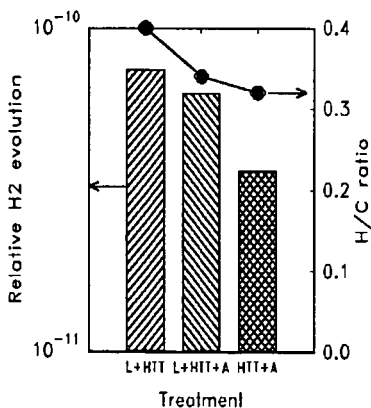


Figure 5. Relative amounts of H_2 evolved from acid and heat treated coal-based carbons. A= H_3PO_4 ; L=low; HTT=high temperature treatment

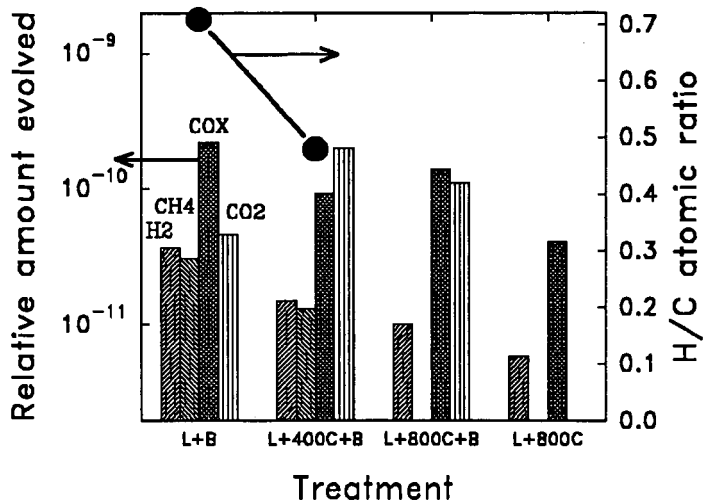


Figure 6. Relative amounts of H₂, CH₄, CO, CO₂ evolution from KOH activated carbons. B=KOH, L=low temperature treatment, 75°C

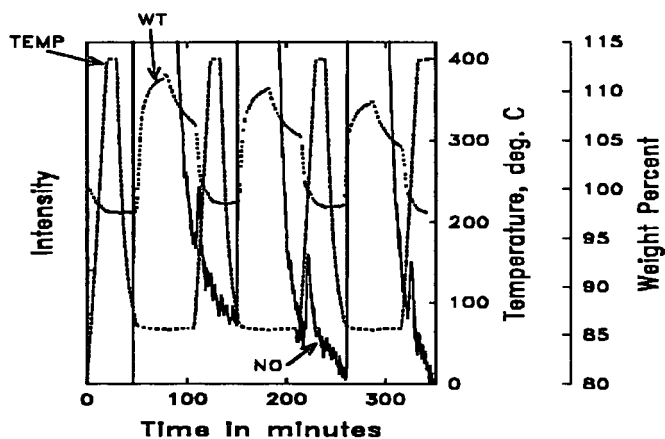


Figure 7. NO adsorption/desorption profile for coal-based activated carbon as determined by TG-MS.

FIELD IONIZATION MASS SPECTROMETRY FOR CHARACTERIZING COALS AND COAL-DERIVED LIQUIDS

Ripudaman Malhotra and Donald F. McMillen
Molecular Physics Laboratory
SRI International
Menlo Park, CA 94025-3493.

Keywords: FIMS, Coals, Coal Liquids, Heavy Oils

INTRODUCTION

The fossil fuel research program at SRI International has greatly benefited from the availability of on-site FIMS capability. In this paper we present a potpourri of FIMS applications from various aspects of coal research to demonstrate the technique's versatility. These applications include (a) differentiating coal types (b) analyzing coal tars, (c) determining the fate of a nitrogen-containing donor solvent in coal liquefaction, (d) identifying species responsible for catalyst deactivation, and (e) understanding why certain liquefaction resids are more difficult to upgrade. This list includes examples of characterization of individual species from peak intensities, which is possible in certain instances, and the use of overall FIMS profiles to identify trends in a series of samples.

EXPERIMENTAL

The technique of field ionization (FI) consists of passing the vapors of a material through a region of intense electric field to polarize and ultimately ionize the molecules. The ions are then mass analyzed using standard mass spectrometric techniques. For most organic compounds, this procedure causes minimal fragmentation and produces only the molecular ions. (1) Thus, complications arising from fragmentation during ionization are minimized. Another advantage of field ionization is that the relative field ionization efficiencies of various hydrocarbon types are within a factor of two of alkyl aromatics except for saturated acyclic hydrocarbons, which ionize about a third as efficiently. For many other ionization techniques, such as field desorption, low-voltage electron impact, secondary ion mass spectrometry (SIMS), or fast-atom bombardment (FAB), the relative ionization efficiencies can differ by more than one or two orders of magnitude. Thus, even without any corrections for sensitivity, the FI mass spectra represent the true molecular weight profile fairly accurately. This is particularly useful in complex unknowns where extensive calibration is not feasible. It should be noted that practical advantage can be taken of this similarity in ionization efficiency *only* if appropriate technique and care is used in preparing and operating the tantalum foil ion sources that are used at SRI.

SRI's FIMS instrument consists of a foil-type field ionizer interfaced with a 60-degree magnetic-sector mass analyzer and a PDP 11/23 computer for instrument control, data acquisition, and report production, as previously described.(2) The spectrometer has a resolving power ($M/\Delta M$) of 1300, although it is capable of scanning up to 3000 Da. The sample is weighed into a melting point capillary and introduced into the spectrometer with a heatable direct insertion probe. It is heated at a fixed rate from ambient (or $\sim 67^\circ\text{C}$ for samples with sufficiently high vapor pressure) to about 700°C . The spectra of the evolving volatiles are continuously recorded, and at the end of a run, they are added to produce a "sum" spectrum of the total volatiles. The capillary is weighed afterward to determine the percent volatilization.

The sum spectra consist of (a) intact molecular ions from individual chemical species originally present in the sample, (b) ions produced from any ion fragmentation that may occur, and (c) molecular ions of fragments that are generated thermally during the ramped heating. The ion fragments are most often totally negligible, as asserted above, but the thermal fragments can be substantial, depending on the volatility and reactivity of the sample. However, in both cases, the manner of presentation of the spectral intensities can generally indicate the extent to which (b) and (c) contribute. Since ion fragments will accumulate at the masses corresponding to the common stable positive ions, the typical absence of significant intensity at, for example, m/z 57 (where the

easily generated t-butyl ion fragment appears) indicates that the percent fragmentation at each of the other hundreds of masses that may have had attached t-butyl fragments must have been very small indeed. For cases where there is significant formation of volatiles through thermal decomposition in the heated source, this is usually revealed by the appearance of some smaller ions as the source is progressively heated. Contributions from pyrolysis during heating are of course significant for heavy coal conversion fractions such as preasphaltenes and vacuum resids. These pyrolytically generated volatiles, when recognized, can sometimes provide valuable information.

RESULTS AND DISCUSSION

1. Differentiating Coals

We analyzed the eight coal samples from the Argonne Premium Coal Sample Program (APCSP) by programmed temperature pyrolysis directly in the inlet of the field ionization mass spectrometer.(3) The spectra of the evolved tars, but not of gases such as CO, CO₂, CH₄, and H₂O, were obtained. From these data we could identify several salient rank-dependent trends. Some of these trends are known from other studies, but FIMS provides an easy means for quantifying them and developing indices that could be used in modeling. In general, the spectra appear to be composed of two groups of peaks: (a) a cluster of peaks in the low molecular weight range corresponding to homologous series of phenols and dihydric phenols and (b) a broad, roughly Gaussian, distribution of peaks spanning the mass range of 150 to 1000 Da.

The low molecular weight cluster is particularly dominant in the Beulah Zap lignite and the Wyodak subbituminous coal, as shown in Figure 1. With increasing rank, the prominence of this cluster decreases relative to the broad Gaussian envelope, whose mean appears to shift to higher masses with increasing rank. Furthermore, the ratio of monohydric to dihydric phenols generally increases with rank. A detailed examination of the broad envelope revealed the buildup of polycyclic aromatic structures in the higher rank coals. Thus molecular species with five and more aromatic rings were discernible in the spectra of the Upper Freeport and Pocahontas coals. The observed periodicity revealed homologation via both benzolog formation ($\Delta m/z = 50$ as in naphthalene to phenanthrene and $\Delta m/z = 24$ as in phenanthrene to pyrene) and also in the formation of biaryl linkages (most noticeably in the formation of naphthyl substituted aromatics with a $\Delta m/z = 126$). (3) The shift toward higher molecular weight and away from phenolic fragments with increasing coal rank is entirely consistent with the previously articulated view (4) that low-rank, high-oxygen coals are more crosslinked to begin with and/or become so during heating, such that the molecular weight between crosslinks is small and primarily small fragments are released. These observations parallel some of those recently reported by Schulten and coworkers.(5)

2. Characterizing Coal Liquids

Chemical analysis of coal- or petroleum-derived liquids as well is best accomplished by first fractionating the oil into different compound classes by HPLC and then subjecting these fractions to FIMS analysis. The most evident feature in these spectra is a 14-Da periodicity arising from the various alkyl-substitution homologous series. The HPLC-FIMS approach has been used by many investigators to follow the chemical changes that accompany processing.(6-10) In general, severe processing leads to dealkylation and formation of larger PAH structures. The net result is a simplification of the FI-mass spectra, which show an increasing dominance of a 50-Da periodicity instead of the more common 14-Da periodicity. An extreme of this behavior can be seen in high-temperature coal tars, which can consist almost exclusively of dealkylated aromatics, as shown in Figure 2.(7)

3. Fate of Amine Solvents during Coal Liquefaction

We examined liquefaction products obtained with and without 1,2,3,4-tetrahydroquinoline (THQ) as a solvent component to determine the fate of THQ.(8) At the time this study was undertaken, it was well recognized that (a) use of THQ dramatically increased coal conversion to soluble products, but these products were much less distillable than the normal toluene solubles, and (b) a

substantial portion of the THQ was not recovered from the solvent. The nitrogen content of the resid produced in batch autoclave liquefaction was significantly greater than without THQ. It was postulated that THQ was adducted into the resid by means of H-bonds that limited its recovery in the normal fashion, but that some physical or simple chemical separation would still make THQ available under recycle conditions.

FIMS of the resid showed a complete absence of a peak at 133 Da corresponding to THQ. Since even the strongest of hydrogen bonds would provide only a vanishingly small degree of association at the high vacuum field ionization condition, this observation provided incontrovertible evidence that THQ was not lost merely by H-bonding. FIMS also showed that after correcting for natural ^{13}C -content, the profile of the odd masses was significantly more intense for the resid obtained with THQ as a solvent component, as shown in Figure 3. The increase in the intensity of the entire odd-mass envelope indicated that THQ was incorporated by covalent linkages into a whole host of resid components, and is hence, for all practical purposes, irretrievably lost to the resid. FIMS and GC-MS analysis of the lighter fractions showed many specific coupling products, thereby providing insight into the types of reactions contributing to THQ loss.

4. Resid Reactivity

In a recent study (11,12) we analyzed fifteen recycle resids from five runs conducted at the Wilsonville facility to help address the question of what structural and process factors help make some resids much more convertible than others. At first glance, the spectra looked very similar with only a broad, featureless envelope. Closer examination, however, revealed that the mass spectra consistently showed the same set of a few prominent peaks in the low mass end, where the distillate-resid cut had sent lower boiling components (i.e., aliphatics) of similar molecular weights into the distillate fraction. Some of these prominent peaks are identified in Figure 4. Interestingly, these prominent masses left in the resid were identical to those previously identified by Sullivan et al. and associated (10) with increased difficulties in hydrotreating vacuum gas oils derived from petroleum resids. This coincidence is remarkable and we believe that a quantitative analysis could lead to an index of resid reactivity and help as well to understand the kinetic factors that control the ring-growth processes.

Apart from information contained in these few specific peaks, we can also derive useful information from overall FIMS profiles. Many of the liquefaction resid samples exhibited a bimodal molecular weight distribution. The relative amounts of the low and high molecular weight components differ significantly from sample to sample, and a simple mathematical deconvolution into Components A and B revealed a correlation between the variations in A and B on the one hand and coal type, process conditions, and process performance on the other. The deconvolution led to several conclusions reasonably in concert with what is already recognized in coal liquefaction. For example, this analysis clearly showed the occurrence of retrograde reactions after the second-stage reactor, while the oil was held at temperature and handled through the ROSE-SR unit.(13) This retrogression was evidenced by an increase in the amount of component B. It was satisfying to see this and other observations about reactivity reiterated, not on the basis of yields, but on the basis of differences in molecular weight distribution, when the streams are already constrained by process conditions and product fractionation to be as similar as possible.

5. Catalyst Fouling

In order to determine the types of compounds that strongly adsorb on supported liquefaction catalysts and likely deactivate them, we used FIMS to characterize the carbonaceous deposits on the spent catalysts from DOE's Wilsonville facility.(14) The spent catalyst extrudates (Ni/Mo on alumina) were washed with tetrahydrofuran (THF) to remove any weakly adsorbed oil, and only tenaciously held materials remained. The washed extrudates were analyzed by heating a single pellet in the direct insertion probe of the mass spectrometer, and the evolved volatiles were then field ionized to produce the molecular ions. The spectra appeared very much like that in Figure 2 above, except that they are dominated not by PAH, but by the corresponding azaaromatics and their alkylated derivatives. These basic compounds are expected to adsorb strongly to alumina and

may have indeed caused the deactivation. Peaks due to some purely hydrocarbon structures such as alkyl pyrenes and perylenes were also present, albeit at lower intensity than the azoaramatics.

CONCLUSIONS

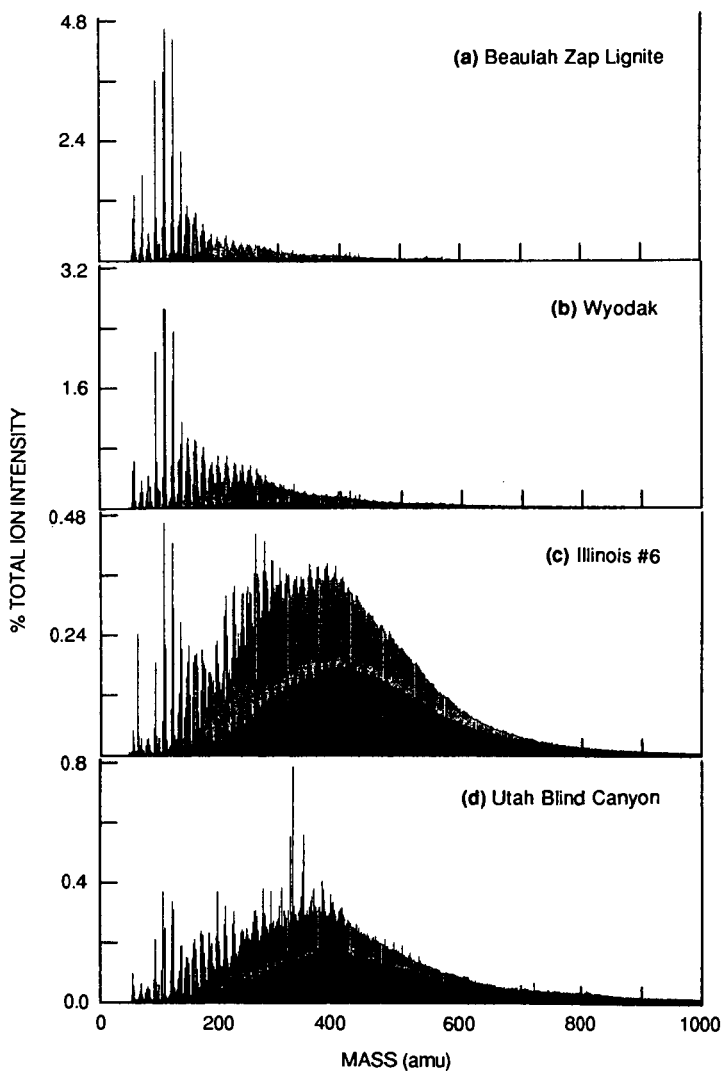
Field ionization mass spectrometry, through definitely not a panacea, has been very useful in a wide range of fossil-fuel-related research. The vapor pressure requirements for desorption/ionization under FIMS conditions definitely constitute a limitation relative to methods such as field desorption and fast atom bombardment. However, with FIMS the extent of fragmentation is often much lower than one typically observes in FAB spectra. Furthermore, the variation in substrate sensitivity is usually much less for FIMS, providing a reasonably accurate quantitative analysis without the necessity for calibration.

When field ionization is coupled with mass analysis at nominal mass resolution, it is of course often not strictly able to provide definitive molecular formula identification, let alone structural identification. However, observation of homologous series, together with any knowledge of the structural types present in the product mixture and the results of previous compound-class separation/FIMS analyses, often provide very good "provisional" identification of the structures at various masses. Furthermore, for very complex mixtures, the absence of discrimination between structural isomers can collapse hopelessly complex spectra to provide useful analyses. (For instance, considering that there are 15 different isomers among the dimethylpyrenes alone, it will generally be very useful, even in systems much simpler than coal liquefaction products, to have these isomers grouped together at m/z 230.) In the examples reviewed above, a complete separation of structural and geometric isomers, such as could be provided in principle by a chromatography-MS technique, would have presented severe problems in data-handling and chemical correlation and provided little, if any, net benefit. In summary, we find that field ionization mass spectrometry, coupled with judicious use of prior separation techniques, can provide useful information on the extremely complex mixtures that constitute coal liquefaction fractions.

Acknowledgment. Support for various aspects of this work from the U.S. Department of Energy, Electric Power Research Institute, Advanced Fuel Research, and several other commercial concerns is gratefully acknowledged.

REFERENCES

1. Beckey, H. D.; *Field Ionization Mass Spectrometry*, Pergamon Press, Elmsford, NY, 1971.
2. St. John, G. A.; Buttrill, S. E., Jr.; Anbar, M., in *Organic Chemistry in Coal*, J. Larsen, Ed.; ACS Symposium Series 71, Washington, D. C., 1978, p. 223.
3. Malhotra, R.; McMillen, D. F.; Huestis, D. L. *Am. Chem. Soc., Div. Fuel Chem. Preprints*, 1991, 36(3), 1252.
4. Solomon, P. R.; Serio, M. A.; Deshpande, G. V.; Kroo, E. *Energy Fuels* 1990, 4, 42.
5. Schulten, H.-R.; Marzec, A.; Czajkowska, S. *Energy Fuels* 1992, 6, 103.
6. Boduszynski, M. M. *Energy Fuels* 1988, 5, 597.
7. Rahimi, P. M.; Fouda, S. A.; Kelly, J. F.; Malhotra, R.; Malhotra, R. *Fuel* 1989, 68, 422.
8. Ueda, K.; Matsui, H.; Malhotra, R.; Nomura, M. *J. Japan Pet. Inst.* 1991, 34, 53.
9. McMillen, D. F.; Chang, S. -J.; Fleming, R. H.; Laine, R. M.; Malhotra, R.; Nigenda, E.; Ogier, W., "Effect of of Amine Solvents and Oxygen Functionalities on Coal Liquefaction," EPRI Research Project 2147-5 1985.
10. Sullivan, R. F.; Boduszynski, M. M.; Fetzer, J. C. *Energy Fuels* 1989, 3, 603.
11. Malhotra, R.; McMillen, D. F.; "Characterization of Coal Liquids," Final Report prepared for Consolidation Coal Co., under U.S. DOE Contract No. DE-AC22-89PC89883, 1991.
12. Malhotra, R.; McMillen, D. F.; Huestis, D. L. *Am. Chem. Soc., Div. Fuel Chem. Preprints*, 1992, 37(2), 908.
13. Brandes, S. D.; Winschel, F. P.; private communication, 1992.
14. Stohl, F. V., *Am. Chem. Soc., Div. Fuel Chem. Preprints*, 1988, 33(3), 210.



CA-2302-2

Figure 1. FI-Mass spectra of the four lower rank coals from the Argonne Premium Coal Sample Program.

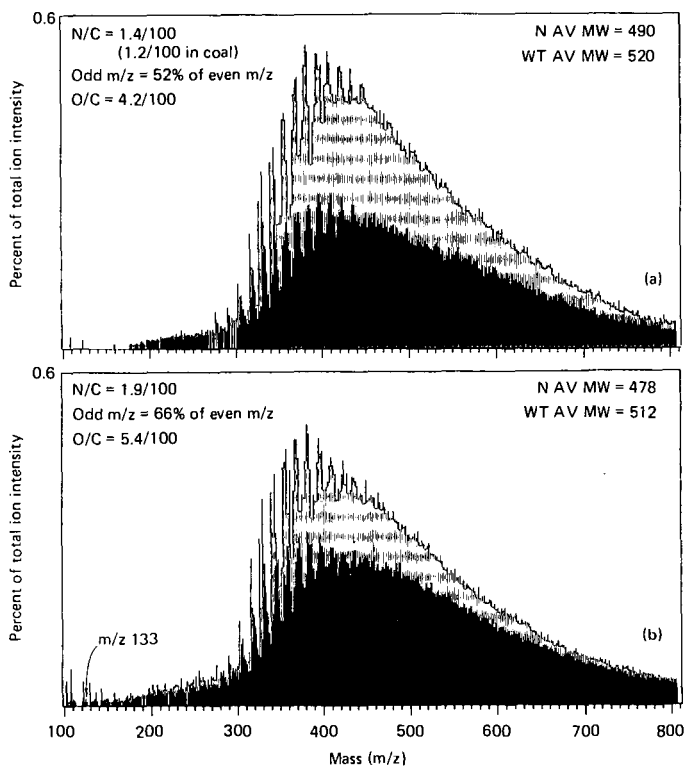


Figure 3. FI-Mass Spectrum Showing Increased Intensity of Odd Masses When THQ is Used in Liquefaction Solvent.

- (a) 1090° F+ residue, without THQ in liquefaction solvent for Wyodak coal.
- (b) 090° F+ residue obtained with 16% THQ in liquefaction solvent. Spectra in this figure are corrected for ^{13}C contributions to odd masses on the basis of an average 86 wt% carbon.

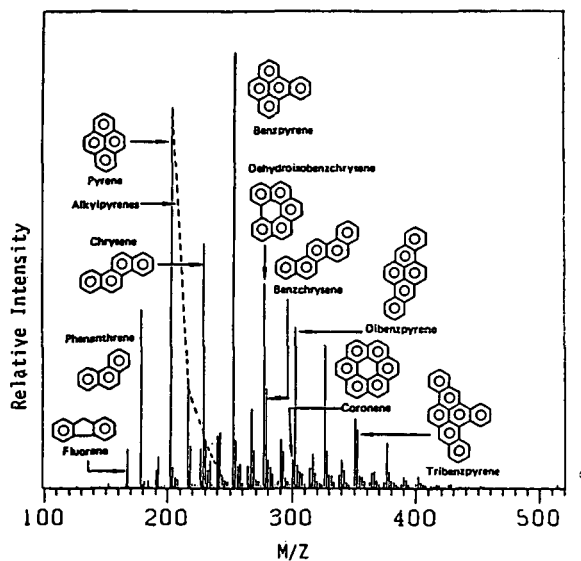


Figure 2. FI-Mass Spectrum of PCAH Fraction from Coal Tar

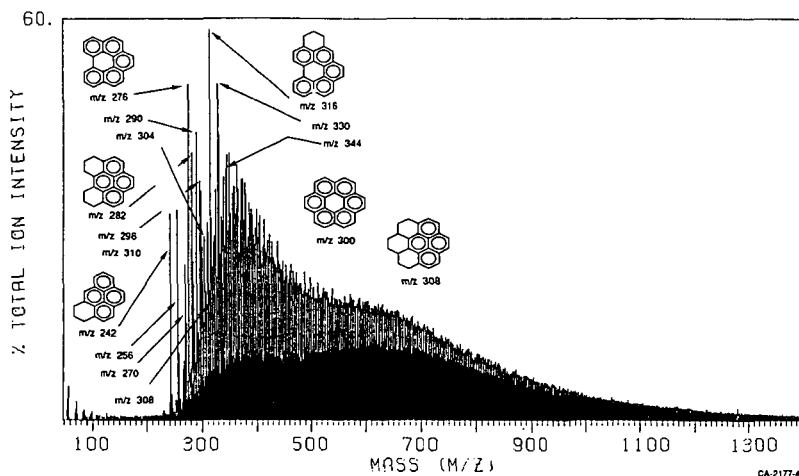


Figure 4. FI-Mass Spectrum of the 850°F+ Recycle Oil from Pittsburgh Coal (Wilsonville Run 259) Showing the Prominent PCAH Structures in the 200-350 Da Range.

APPLICATION OF ^{252}Cf -PLASMA DESORPTION MASS SPECTROMETRY
TO ANALYSIS OF DIRECT COAL LIQUEFACTION HEAVY PRODUCTS.

Andrzej R. Lapucha and John W. Larsen

Lehigh University, Department of Chemistry,
Bethlehem, PA 18015

Keywords: Plasma Desorption Mass Spectrometry, Coal Liquefaction.

ABSTRACT

Californium Plasma Desorption Mass Spectrometry (PDMS) has been used to analyze heavy distillation residues obtained from direct coal liquefaction processes. The characteristics of the ^{252}Cf -PDMS technique for the analysis of these non-polar materials were determined, especially the ionization efficiency of molecules of different chemical type. The molecular weight distributions of several THF soluble 850°F+ materials ("resids") from the Wilsonville pilot plant were determined. These data were compared to the results obtained by Field Ionization Mass Spectrometry (FIMS) and Gel Permeation Chromatography (GPC). In general, number average molecular weights for all three techniques agreed well. Both GPC and PDMS give higher weight average molecular weights than FIMS and agree with each other for weight averages below 1500 amu.

INTRODUCTION

Field ionization and field desorption mass spectrometry have been applied to the analysis of coal liquefaction products.¹⁻³ ^{252}Cf -PDMS, a different kind of mass spectrometry,⁴⁻⁶ has been incompletely explored for the analysis of coal products.^{7,8}

The ^{252}Cf plasma desorption technique utilizes energetic fission fragments from the decay of ^{252}Cf to volatilize and ionize a solid sample. The ionization source is typically a 10- μCi californium sandwiched between two thin sheets of nickel foil. A sample is dissolved in an appropriate solvent and the solution is electrosprayed over a 1 cm^2 area on an aluminized poly(ethylene terephthalate) foil (Mylar disk). ^{252}Cf -PDMS is capable of producing mass spectra consisting primarily of molecular ions for a wide variety of compounds, including amino acids,⁴ peptides,⁹ nucleotides,¹⁰ geoporphyrins,¹¹ polynuclear aromatic hydrocarbons,¹² polyethers¹³ and other synthetic polymers.¹⁴⁻¹⁶

Gel Permeation Chromatography (GPC), also known as Size Exclusion Chromatography (SEC), has been used to determine the molecular weight distribution of coal extracts.¹⁷⁻¹⁹ The limits of the method and lack of calibration standards for coal derived materials are well known.²⁰ Relative molecular weights values obtained using the same standards (often polystyrenes) and conditions can be satisfactorily compared.

EXPERIMENTAL

Mass spectra were obtained using a BIO-ION 20 commercial time-of-flight mass spectrometer (Bio-Ion Nordic, Upsala, Sweden) equipped with PDP-11 microcomputer data acquisition system (DAS). The instrument is

equipped with 10 μCi ^{252}Cf source and a short 15 cm flight tube. We used a positive 10kV acceleration voltage and the time resolution was set to 1ns/channel. Data collection was terminated at a preset count and 10^6 primary ion events were acquired. This took about 12 minutes. The samples of analyzed distillation resids were dissolved in THF (10 mg/mL) and 40 μL of each solution was electrosprayed onto nitrocellulose coated Mylar disks using the BIO-ION electrospray apparatus. Thin homogenous coverages were obtained. We also developed a software package (CFINT) that can be used on any IBM compatible PC to calculate the number average and weight average molecular weights using data imported from the Bio Ion 20 PDP-11 computer. In addition, this software package allows us to subtract the background spectrum which comes from the mylar film. The software supplied with the spectrometer also adds counts from surrounding channel to enhance the signal-to-noise ratio. This is undesirable for the determination of molecular weight distribution and has been removed from our data analysis.

The molecular weight distributions of five selected resids (#7, #13, #16, #19 and #22) provided by Consolidation Coal Company dissolved in pyridine were measured by a computer interfaced GPC with a mass sensitive detector. The components of the instrument were all commercially available. It consists of a Waters Liquid Chromatograph (Model ALL 201) equipped with high pressure pump, injector, and four μ -styragel columns ($10^4 + 10^3 + 500 + 100 \text{ \AA}$). The mass detector, built by Applied Chromatography Systems Ltd. (Model 750/14), works by nebulizing the liquid stream emerging from the column and then passing this uniform distribution of droplets down a heated tube in a flow of dry nitrogen, evaporating the solvent. The resulting solid passes a light scattering detector whose output is directly proportional to the mass of solid material passing in front of it. Between the mass detector and the columns is a digital thermal pulse flow meter. The outputs from the mass sensitive detector and the flow meter are directed to a Zenith Model 158 microcomputer, the former through a 12 bit resolution A to D converter (Data Translation Model DT 2805). The programs for data collection and manipulation were written in a high level language using the Asyst package (McMillan Software Co.). The instrument was carefully calibrated with polystyrene standards. HPLC grade pyridine was used as the eluting solvent with flow rate of ca. 1 mL/min. 50 μL of each sample with concentration of 10 mg/mL was loaded through the injector valve. For each run data were collected for the period of one hour.

RESULTS AND DISCUSSION

Five THF soluble samples of solid $850^\circ\text{F}+$ materials ("resids") obtained in the Wilsonville pilot plant during direct liquefaction of different coals were analyzed by ^{252}Cf - Plasma Desorption Mass Spectrometry. Molecular Weight Distribution curves were obtained and number average molecular weights (M_n) and weight average molecular weights (M_w) were calculated. These data are compared to the results obtained by Field Ionization Mass Spectrometry and Gel Permeation Chromatography.

Figure 1 shows the PDMS spectra of Mylar film (a), the software converted spectrum of resid #7 which includes the Mylar background (b), and of resid #7 with the Mylar background subtracted (c). As can be seen only traces of Mylar background remain in the range between 0-100 m/z.

Despite different coal feeds and processing conditions, all the samples show similarities. Table 1 summarize origin and physico/ chemical parameters of the analyzed recycle products. In Table 2. and Fig. 2 (a-c) PDMS results are compared with those obtained from FIMS and GPC. The PDMS M_n values are essentially identical to those from FIMS and GPC. PDMS M_w values are about twice the field ionization results. The FIMS spectra do not show any peaks with molecular weights higher than 1200 - 1300 m/z. Both PDMS and GPC detect molecules having molecular weight greater than 1300 amu. In fact, the PDMS intensity does not return to zero before 2000-2500 m/z. Based on these observations, much higher M_w values can be expected from PDMS and GPC. Probably the field ionization technique is not able to efficiently volatilize high boiling, high molecular weight species. GPC M_w values are higher than the corresponding PDMS results with an exception of resid #19. There are three possible explanations for this phenomenon. 1) The integral of GPC molecular weight distribution curve is very sensitive to small amounts of high molecular weight analytes which are not detected by PDMS. This leads to enormously high M_w values. 2) The recycle oils are fragmenting in PDMS. 3) PDMS is capable of producing mass spectra from a wide variety of natural products but less polar polymeric materials very often give low responses or no peaks at all. PDMS may not be detecting all of the sample.

As can be seen in Table 2, the molecular weights of Resid #19 are much lower than of the other samples. This sample has the highest percentage of condensed aromatics and is low in sulphur and beta and gamma protons (Table1). For this sample PDMS and GPC M_n and M_w values are in overall good agreement. Resids #7, #13 and #22 contain relatively low amounts of condensed aromatics, high numbers of cyclic and alkyl beta and gamma protons, and the highest percentage of oxygen. These resids show higher weight average molecular weights in GPC than in PDMS. The relatively low polarity and highly polymeric nature of these fractions are both unfavorable factors for PDMS. The instrument may not be providing a reliable analysis.

CONCLUSIONS

²⁵²Cf-PDMS is easy to operate, fast and less expensive than most other mass spectrometric techniques and is suitable for quantitative measurements of the molecular weight distributions of some coal conversion products.

Comparison of PDMS molecular weight distributions to the GPC and FIMS shows that, in general, number average molecular weights agree well. Both GPC and PDMS give higher weight average molecular weights than does FIMS.

ACKNOWLEDGMENTS

We thank Dr. Susan D. Brandes at the Consolidation Coal Company for providing samples for this study. This research was financed by the subcontract from Consolidation Coal Co. under DOE contract DE-AC22-89PC89883. We are most grateful to Dr. Patrick Wernett for writing the software used and to William Anderson for his instrumental advice and expertise.

REFERENCES

1. Aczel, T.; Laramee, J.; Hansen, G.J. in *Proceedings of the 30th Annual Conference on Mass Spectrometry and Allied Topics*, p.808 (1982)
2. Aczel, T.; Dennis, L.W.; Reynolds, S.D. in *Proceedings of the 35th Annual Conference on Mass Spectrometry and Allied Topics*, p.1066 (1987)
3. Larsen, B.S.; Fenselau, C.C.; Whitehurst, D.D.; Angelini, M.M. *Anal. Chem.* (1986), **58**, 1088
4. MacFarlane, R.D.; Torgeson, D.F. *Science* (1976), **191**, 920
5. MacFarlane, R.D. *Anal. Chem.* (1983), **55**, 1247 A
6. Cotter, R.J. *Anal. Chem.* (1988), **60**, 781 A
7. Lytle, J.M.; Tingey, G.L.; Macfarlane, R.D. *Anal. Chem.* (1982), **54**, 1881
8. Zingaro, R.A.; Macfarlane, R.D.; Garcia, J.M.; Vindiola, A.G.; Zoeller, J.H. in *Chemistry of Coal Liquefaction*, ACS Symposium Ser., Vol. 29, No 5, p. 22 (1984)
9. Alai, M.; Demirev, P.; Fenselau, C.; Cotter R.J. *Anal. Chem.* (1986), **58**, 1303
10. Scanlan, G.; Benson, L.; Tsarbopoulos, A.; Jardine, I. in *Proceedings of the 36th Annual Conference on Mass Spectrometry and Allied Topics*, Denver, CO. (1987), 80
11. Wood, K.V.; Bonham, C.C.; Chou, M.M. *Energy Fuels* (1990), **4**, 747
12. Zoeller, J.H.; Zingaro, R.A.; Macfarlane, R.D. *Int. J. Mass Spectrom. Ion Processes* (1987), **77**, 21
13. Chait, B.T.; Shpungin, J.; Field, F.H. *Int. J. Mass Spectrom. Ion Processes* (1984), **58**, 121
14. MacFarlane, R.D.; McNeal, C.J.; Martin, C.R. *Anal. Chem.* (1986), **58**, 1091
15. Gehrig, C.C.; Wood, K.V. *The 38th ASMS Conference on Mass Spectrometry and Allied Topics* (1990), 255
16. Keough, T.; Lacey, M.P. *Anal. Chem.* (1991), **63**, 1482
17. Larsen, J.W.; Choudry, P. *J. Org. Chem.* (1979), **44**, 2856
18. Larsen, J.W.; Mohammadi, M.; Yiginsu, J.; Kovac, J. *Geochim. Cosmochim. Acta* (1984), **48**, 135
19. Larsen, J.W.; Wei, Y.C. *Energy Fuels* (1988), **2**, 344
20. Buchanan, D.H.; Warfel, L.C.; Biley, S.; Lucas, D. *Energy Fuels* (1988), **2**, 32

Table 1. Analysis of the Soluble Portion of the Distillation Resids

	Res.#7	Res.#13	Res.#16	Res.#19	Res.#22
Weight %	Ill.#6	Tex.Lign.Pitt.#8	Wyodak	Wyodak	
C	88.75	89.39	90.54	90.90	89.46
H	8.15	7.12	6.74	6.32	6.69
N	0.66	1.23	0.91	1.11	1.13
S	0.14	0.09	0.39	0.03	0.05
O	2.30	2.17	1.42	1.64	2.67

Proton Dist.(%)

Cond. Aromatics	16.7	22.4	26.1	32.2	22.5
Uncond. Aromatics	4.4	4.3	5.4	5.1	5.1
Cyclic Alpha	17.9	19.2	18.9	18.1	16.8
Alkyl Alpha	9.4	9.5	9.4	9.2	9.3
Cyclic Beta	18.6	15.9	14.8	13.6	14.4
Alkyl Beta	20.4	18.5	14.6	13.9	21.2
Gamma	12.5	10.3	10.8	7.8	10.8
Phenolic -OH Conc.	0.50	0.71	0.69	0.67	0.89

Table 2. Number Average and Weight Average Molecular Weights Obtained from Field Ionization Mass Spectrometry, Plasma Desorption Mass Spectrometry and Gel Permeation Chromatography.

Resid #	FIMS	PDMS	GPC	FIMS	PDMS	GPC
	M _n			M _w		
7	620	600	600	730	1370	1930
13	570	570	570	680	1340	2050
16	590	590	610	690	1340	1840
19	-	580	500	-	1300	1430
22	-	600	700	-	1460	2160

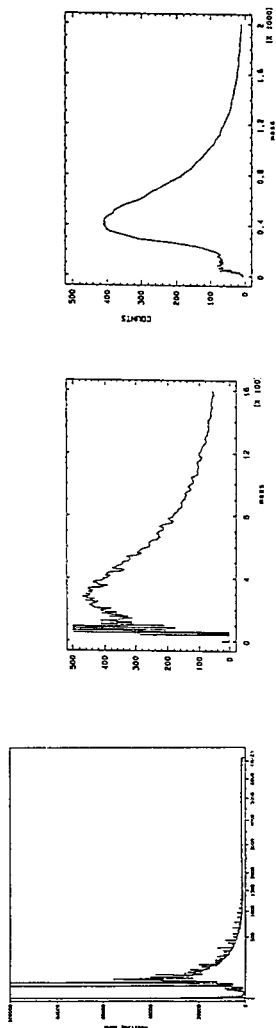


Figure 1. PDMS Spectra of Mylar Background (a), Software Converted Spectrum of Resid #7 which Include Mylar Background (b) and Resid #7 with Mylar Background Subtracted (c).

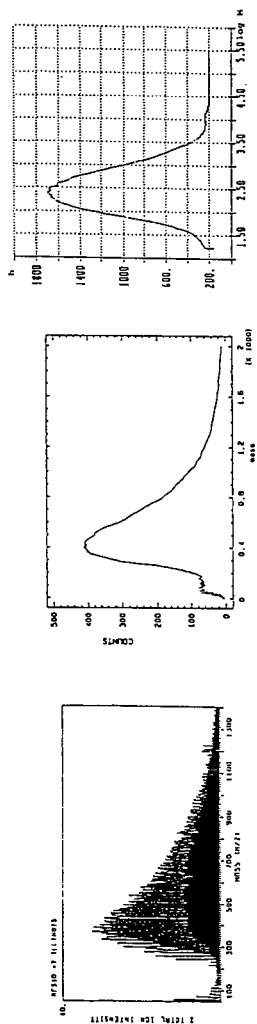


Figure 2. FIMS (a), PDMS (b) and GPC (c) Molecular Weight Distribution of Resid #7

TWO-DIMENSIONAL HPLC ANALYSIS OF FCC DECANT OILS

Y. Liu, S. Eser, P. G. Hatcher

Fuel Science Program, Department of Materials Science and Engineering
The Pennsylvania State University, University Park, PA 16802

Keywords: Decant oil, HPLC, mass spectrometry

INTRODUCTION

Fluid catalytic cracking decant oils (FCC-DO) are used as feedstocks for producing highly graphitizable petroleum cokes (needle cokes) in delayed cokers¹. The chemical composition of decant oils depends on the nature of catalytic cracker feeds and the conditions used in the crackers. It is known that the quality of the needle coke product is, in turn, strongly dependent on the chemical constitution of the starting decant oil. Therefore, the need for a detailed analysis of FCC-DO is well recognized; elemental analysis, various solvent fractionation techniques, NMR, and gas chromatography and gas chromatography/mass spectrometry (GC/MS) have been used to analyze these materials^{2,3}. One limitation of ordinary GC and GC/MS methods is that heavy ends and some polar compounds cannot be analyzed because of their low volatility.

High performance liquid chromatography (HPLC) and HPLC/MS can be used to separate and analyze high molecular weight and polar fractions of feedstocks^{4,5}. However, traditional HPLC instruments with mono-UV wavelength detectors are not amenable to identify the molecular components of the fractions eluted from the LC columns. The development of on-line HPLC/MS has greatly facilitated the analysis of heavy hydrocarbons without, however, the capability of distinguishing between the isomers of polycyclic aromatic compounds⁶. A distinct advantage of a two dimensional HPLC technique, which provides UV spectra of separated fractions as a function of time, is its capability to identify the molecular components of the eluates, including the isomers of polycyclic aromatic compounds. In this paper, we present the results of a two dimensional HPLC and heated probe/MS analyses of some FCC-DO samples.

EXPERIMENTAL

HPLC analyses were carried out with a Waters 600 micro-flow syringe pump and a 4.6x150 mm column packed with C-18 stationary phase. A Waters Model 990 UV detector was used to collect UV spectra ranging from 200 nm to 400 nm. A mixture of distilled water and acetonitrile (EM Science, HPLC grade) was used as mobile phase. Decant oil samples and some model compounds were diluted in acetonitrile (4 µg/µL), and 1 µL sample was injected. The scan time used was 50 ms and every four scans were averaged to obtain a UV spectrum. At a column temperature of 50 °C and mobile phase flow rate of 1 mL/minute, the separation of components took 40-50 minutes, collecting 2400-3000 UV spectra during each analysis. Two dimensional and contour graphs as well as single UV spectra obtained from each analysis were plotted and studied.

Selected FCC-DO were also analyzed by a heated probe/MS technique to assist in component identification. A KRATOS MFC 1500 instrument was used for these analyses with electron impact ionization potential of 70 eV. Samples were placed in a probe which was introduced into the MS source. The probe was heated from 50°C to 250°C at a heating rate of approximately 15°C/min and mass spectra were collected at every 2.5 °C temperature interval during heating.

RESULTS AND DISCUSSION

Before analyzing the FCC-DO samples, mixtures of six model compounds were analyzed by HPLC. Figure 1a and 1b show the two dimensional plots of the two ternary mixtures of naphthalene/anthracene/fluoranthene and phenanthrene/pyrene/chrysene, respectively. The

abscissa in the plots represents the retention time in the column, and the ordinate shows the UV wavelength. The UV absorption intensity is shown on the z axis. Samples of naphthalene, anthracene and fluoranthene were eluted at 4.90, 8.45 and 10.45 minutes, respectively, and well separated, as shown at the top of Figure 1. Similarly, phenanthrene, pyrene and chrysene, shown at the bottom of Figure 1, are also well separated with retention times of 7.75, 10.90 and 14.20 minutes, respectively. In addition to the different retention times, these six model compounds have distinctly different UV spectra which facilitate their positive identification in a mixture. For example, the isomers, phenanthrene and anthracene which give exactly the same mass spectra have quite different UV absorption characteristics; and pyrene and its homologues can be easily identified by the peaks located around the 340 nm region.

Figure 2 shows a classification of various PAH's according to the number of rings, cata- and peri-condensation, and linear versus angular configurations which are responsible for different UV absorption characteristics. For each aromatic compound shown in Figure 2, UV absorption wavelength increases as the number of aromatic rings increases. Also, one can distinguish between the aromatics of the same ring number with respect to differences in their molecular configurations, e.g., linear PAH's extend their absorption to the longer UV wavelengths than the angular PAH's.

A good separation of the components of the FCC-DO samples was obtained at a column temperature of 50°C and water/acetonitrile ratio of 2/3. Adding water to acetonitrile up to an optimum 40% in the mixture steadily improved the separation of the constituent compounds. All the FCC-DO samples were analyzed under the same conditions.

Figure 3 shows a two-dimensional plot of the HPLC results obtained for FCC-DO #1, indicating the series of identified compounds. One should note that the UV absorption intensities for the components in a mixture should not be taken as a quantitative measure of concentrations, since the observed intensity is not only a function of concentration, but also a function of molecular structure for each compound. Figure 4 shows the data for FCC-DO #1 as a contour graph. Contour lines in Figure 4 represent UV absorption intensities as a function of retention time and wavelength. The more lines cross a given region, the higher is the absorption intensity. One can see in Figure 4 that the highest intensity peaks are located at retention times of 11, 15 and 16 minutes. Peaks located around 21-22 minutes also appear as relatively strong but broad peaks. The use of a contour plot for plotting the data makes it easy to determine the right wavelength through which a representative HPLC chromatogram can be obtained. The trace shown at the bottom of Figure 4 is an HPLC chromatogram of the sample at a UV wavelength of 254 nm, showing a good separation of the constituent compounds. One should note that the identified compounds in Figure 4 are only the aromatic compounds present in FCC-DO #1, since aliphatic compounds do not absorb UV radiation in the wavelength range studied here. It is known that decant oils can contain high concentrations of paraffins and alicyclic compounds^{2,3}.

The UV spectra corresponding to the retention times of strong peaks seen in Figure 4 are plotted in Figure 5 to identify the individual compounds with respect to their retention time and the attendant UV spectra. The solid line in Figure 5a is assigned to phenanthrene. The spectrum shown with a dotted line in Figure 5a is assigned to pyrene structures. As different from the spectrum of pure pyrene, the dotted line trace has a shoulder at 260 nm which may be assigned to alkyl substituted pyrenes or phenanthrenes. The third spectrum shown in Figure 5a with a broken line can be attributed to chrysene and benzo(c)phenanthrene. Any contribution from naphthacene or benzo(a)anthracene can be ruled out, since there is no UV absorption beyond 340 nm in this spectrum. All of these four ring aromatics have the same molecular weight of 228.29 and similar fragmentation patterns which make their differentiation by mass spectroscopy very difficult.

Figure 5b shows the UV spectra obtained at retention times of 15.15, 16.10 and 21.80 minutes. The three spectra obtained at retention times of 15.15 minutes (solid line), 16.1 minutes (dotted line), and 21.8 minutes (broken line) have similar traces to the pyrene spectrum with a clear shift to longer wavelengths, and can be assigned to benzo- and alkyl- pyrenes. One should note again

that MS alone would not readily distinguish between the alkyl substituted homologues of pyrene, fluoranthene, 1,2-benzofluorene, and 3,4-benzofluorene. The molecular weight of pyrene and fluoranthene is 202.26, benzofluorenes is 216.28 and the alkylated homologues of these compounds have molecular weights of 216.28, 230.29, 244.31 and 258.33, etc., with similar fragmentation patterns.

To compare with the HPLC data, a heated probe/mass spectroscopy analysis was carried out on the same decant oil sample. The collection of mass spectra was started at 50 °C, obtaining one mass spectrum at every 2.5 °C interval up to 250 °C. As the probe temperature increased, the decant oil sample evaporated gradually starting with lower boiling point fractions and progressing to higher boiling materials with reasonable separation. Major compounds in FCC-DO #1 were identified by their mass spectra, pointing out the two most dominant compound series. One series has $m/z=202+14n$ ($n=0,1,2,3...$) (pyrene+ alkylpyrenes), and the other has $m/z=252+14n$ ($n=0,1,2,3...$) (benzopyrene + alkylbenzopyrenes). Typical mass spectra of these compound series collected at probe temperatures of 70 °C and 120 °C are shown in Figure 6a and 6b, respectively. Although the separation processes involved in HPLC and heated probe/MS are different, the general order of compounds released from LC column and the heated probe appears to be the same, controlled apparently by the molecular weight of the constituent molecules.

Comparing the HPLC and heated probe/MS data, one can see that the first major HPLC fraction eluting at 11 minutes is pyrene (MW=202.26), which corresponds to a probe temperature of 70 °C in the mass source. As the temperature of the probe increases, compounds with $m/z=228+14n$ ($n=0,1,2,3...$) emerge starting with chrysene (MW=228.29) detected at HPLC elution time of 14.2 minutes, followed by the second major fraction with $m/z=252+14n$ ($n=0,1,2,3...$) namely, benzopyrene at 15.2 minutes and alkylbenzopyrenes starting at 16.1 minutes of LC retention time. At a probe temperature of 165 °C, a compound series of $m/z=290+14n$ ($n=0,1,2,3...$) appears with a corresponding LC retention time of 21.8 minute, assigned as dibenzopyrene and its alkyl homologues.

Figures 7 shows the contour plots of the HPLC data on two other decant oil samples, FCC-DO #2 and FCC-DO #3. By comparing the contour graphs of the three decant oil samples, one can clearly see that FCC-DO #2 and FCC-DO #3 contain more lower molecular weight aromatic compounds than FCC-DO #1. These lighter compounds consist of naphthalene, alkylnaphthalenes, phenanthrene and alkylphenanthrenes, which were eluted from the HPLC column in less than 10 minutes.

CONCLUSIONS

A two-dimensional HPLC technique is useful for separation and identification of aromatic compounds present in fluid catalytic cracking decant oils. This method combined with a heated probe/MS analysis provides a positive, and convenient identification of high-molecular-weight aromatic compounds. The analysis of three different FCC-DO's has shown significant variations in the composition of their aromatic fractions.

ACKNOWLEDGEMENTS

This study is part of a research project sponsored by the Carbon Graphite Group, Inc., Pittsburgh, PA. Helpful and stimulating discussions with Samuel Hoff, Peter Lefrank, and James Baldwin are gratefully acknowledged. We thank Barton Schober and Bernard Gordon of Polymer Science Program at Penn State for their help with the HPLC experiments. Jeffrey Blank and Robert Minard of the Department of Chemistry at Penn State provided the data from the heated probe/MS experiments.

REFERENCES

1. Stocks, C. A. and Guercio, V. J., *Erdöl Kohle Erdgas Petrochem.* 38, 31, 1985.

2. Nesumi, Y., Oyama, T., Todo, Y., Azuma, A., Mochida, I. and Korai, Y., *Ind. Eng. Chem. Res.* **29** (9), 1793, 1990.
3. Eser, S., Liu, Y., and Hatcher, P.G., Unpublished data.
4. Hsu, C. S., McLean, M. A., Qian, K., Aczel T., Blum S. C., Olmstead, W. N., Kaplan, L. H., Robbins, W. K., and Schulz, W. W., *Energy & Fuel* **5**, 395, 1991.
5. Vreuls, J. J., de Jong, G. J., and Th. Brinkman, U. A., *Chromatographia* **31**, 113, 1991.
6. Herod, A. A., Stokes, B. J., Major, H. J., and Fairbrother, A. E., *Analyst* **113**, 797, 1988.

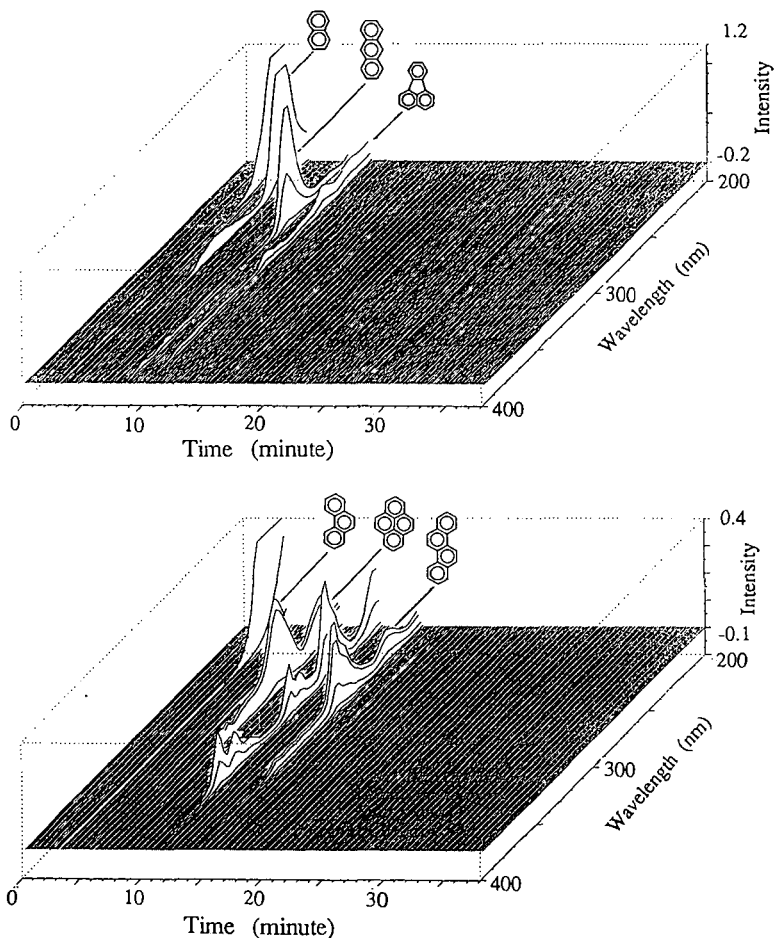


Figure 1. Two-dimensional HPLC plots for the two ternary mixtures naphthalene/anthracene/fluoranthene (top, a) and phenanthrene/pyrene/chrysene (bottom, b).

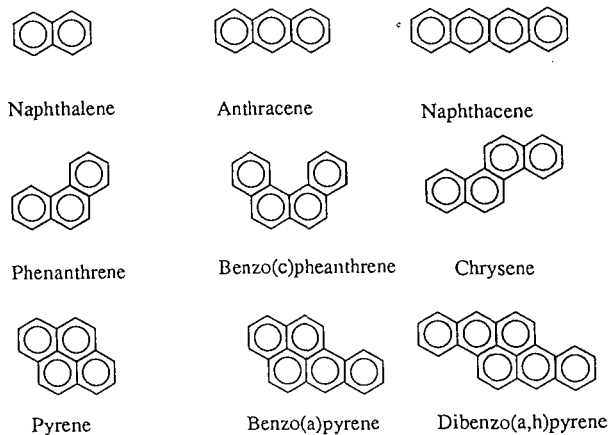


Figure 2. Different aromatic compounds found in FCC-DO.

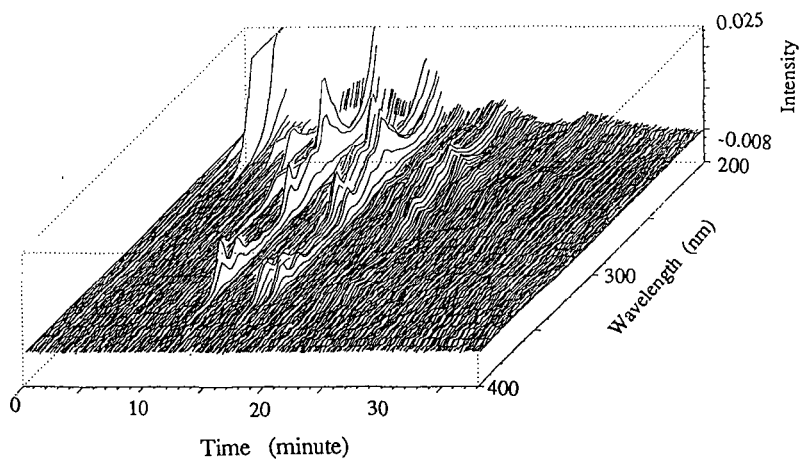


Figure 3. Two-dimensional HPLC plots for the sample FCC-DO #1.

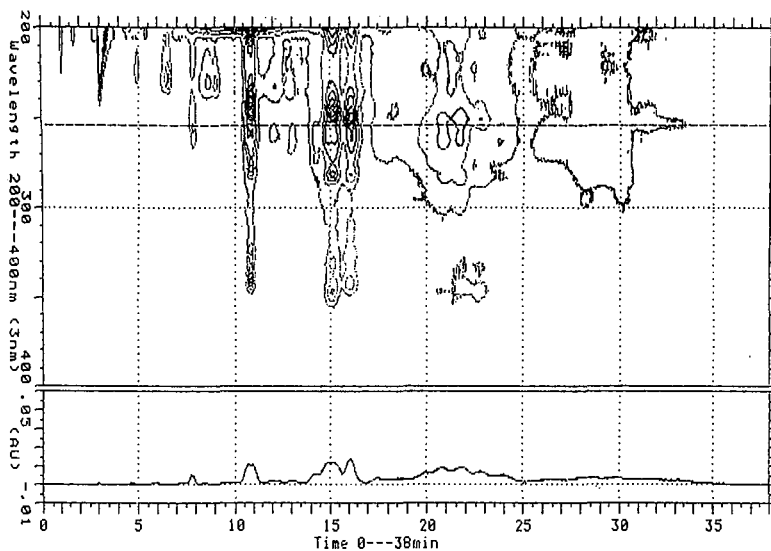


Figure 4. The HPLC contour plot for FCC-DO #1.

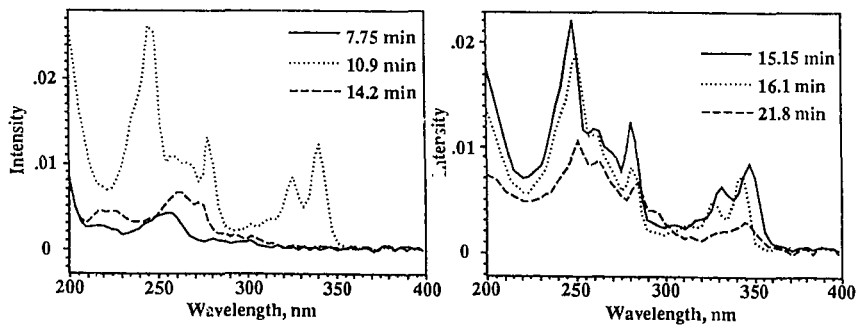


Figure 5. UV spectra of the compounds which elute at the indicated retention times.

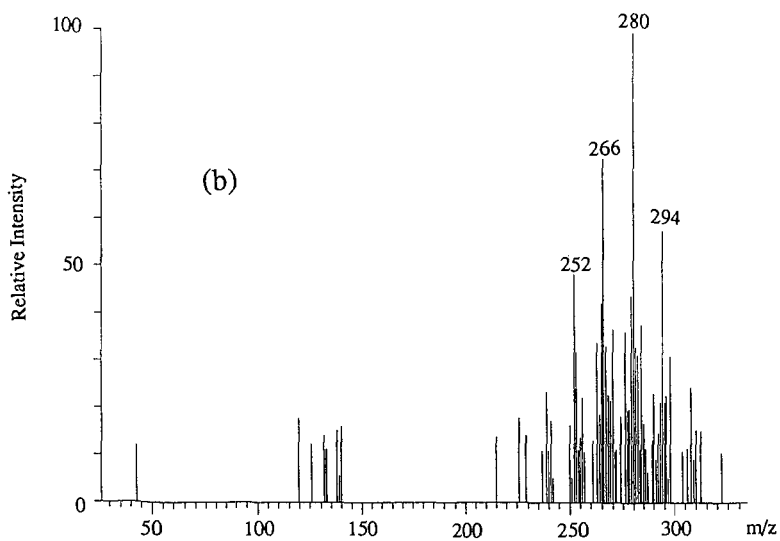
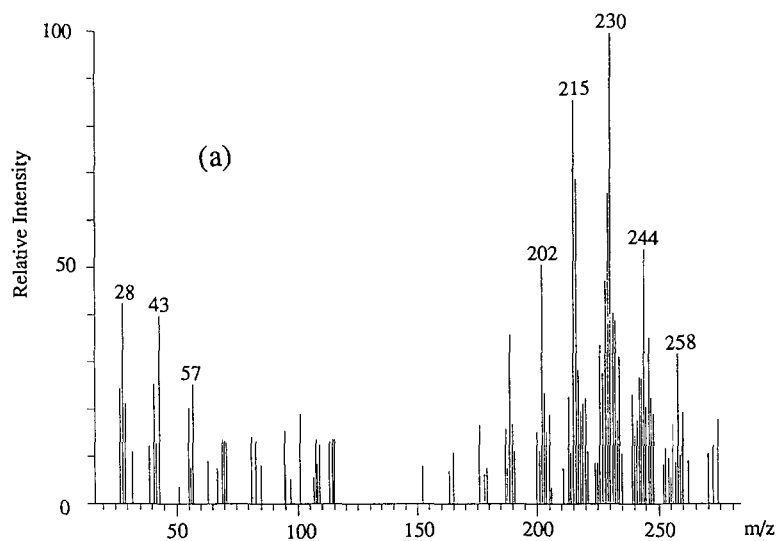


Figure 6. Mass spectra for sample FCC-DO #1 from the heated probe/MS experiment.

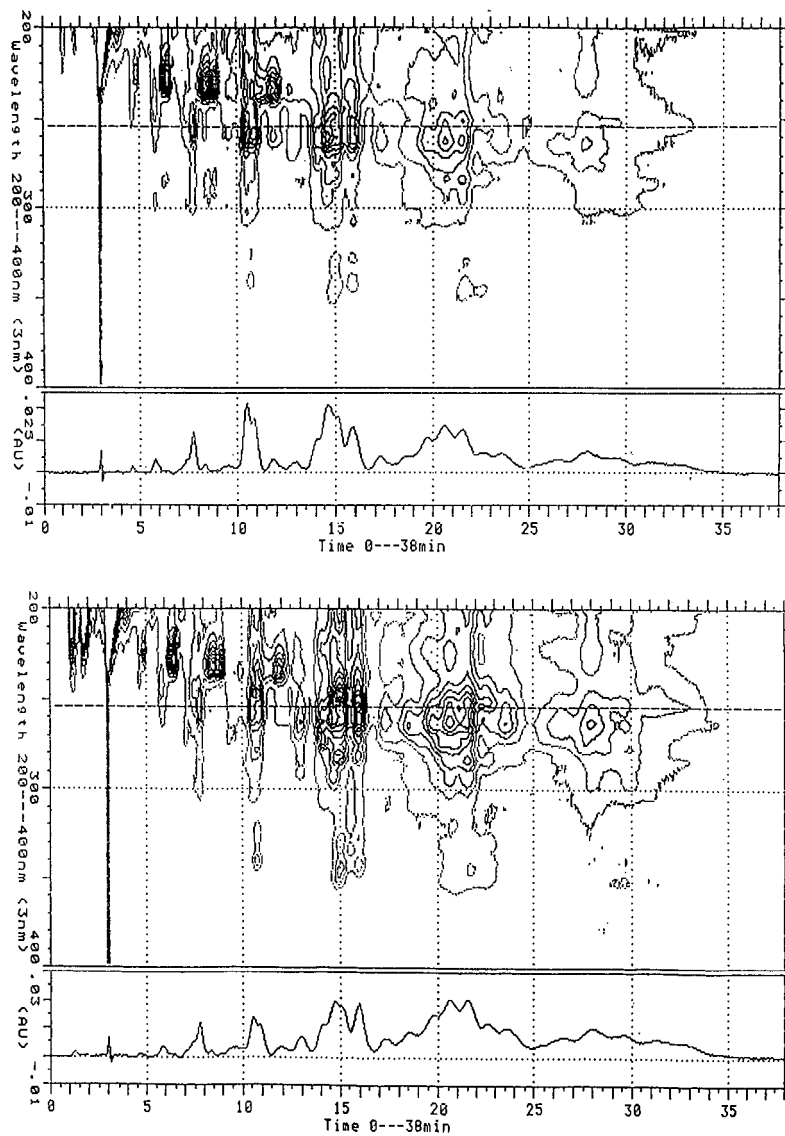


Figure 7. The HPLC contour plot for FCC-DO #2 (top) and FCC-DO #3 (bottom).

Characterization of Coal Structure and Low-Temperature Liquefaction Reactions by Pyrolysis-GC-MS in Combination with Solid-State NMR and FTIR.

Ajay K. Saini, Chunshan Song, Harold H. Schobert and Patrick G. Hatcher

Fuel Science Program, Department of Material Science and Engineering, 209 Academic Projects Building, The Pennsylvania State University, University Park, PA 16802, USA

Keywords: Solid-state ^{13}C NMR, Pyrolysis-GC-MS, Low-Temperature Liquefaction

INTRODUCTION

Coal conversion into liquids is an extremely complex process and involves both chemical and physical transformations. The dissolution of coal requires homolytic cleavage of bonds to yield free radicals and their immediate stabilization with a hydrogen, otherwise they may recombine or crosslink to form more refractory material. The rate of thermal fragmentation is mainly determined by coal reactivity and reaction conditions. Low-rank coals such as Wyodak subbituminous coal are more reactive than had been thought before. The thermally initiated reactions of coal can take place very rapidly (1,2) and especially for low-rank coals, can occur at lower temperatures (3,4). The previous work in our laboratory has demonstrated that more bonds in low-rank are thermally broken at lower temperature as compared to bituminous coals, and a concept of bond energy distribution has been developed from temperature-programmed pyrolysis (3,4).

It has been also demonstrated that the combination of low-temperature catalytic reaction followed by the high-temperature catalytic reaction using dispersed molybdenum catalyst significantly enhanced coal conversion (5-12). The work presented here is a part of an on-going project on the effects of low-temperature catalytic pretreatment on coal structure and reactivity in liquefaction. Recently, we have demonstrated that the combined use of solid-state NMR and pyrolysis-GC-MS has the potential to reveal the major and minor structural changes in the macromolecular network of coal induced by liquefaction (13, 14). The specific objectives of the present work are to identify the basic changes in coal structure induced by catalytic and thermal pretreatments by using modern analytical techniques.

EXPERIMENTAL

The coal used was a Wyodak subbituminous coal provided by the Penn State Sample Bank (DECS-8). The characteristics of this coal are as follows: 32.4% volatile matter, 29.3 % fixed carbon, 9.9% ash and 28.4% moisture, on a as-received basis; 75.8% C, 5.2% H, 1.0% N, 0.5% S and 17.5% O, on a dmmf basis. The coal was dried in a vacuum oven at 100°C for 2 h before use.

The liquefaction of coal was carried out at 300 and 350°C with and without catalyst (ammonium tetrathiomolybdate, 1% wt. of molybdenum of the dmmf coal) and solvents. The solvents used were tetralin, a known H-donor, and 1-methylnaphthalene (1-MN), a non-donor. Liquefaction was carried out in 25 ml microautoclaves using 4 g of coal and 4g of solvent, under 1000 psi H_2 pressure. The reaction time was 30 minutes plus 3 minutes for the heat-up time for autoclave to attain the reaction temperature. After the reaction, the liquid and solid products were separated by sequential extraction with hexane, toluene and THF. After the extraction the THF-insoluble residues were washed first with acetone and then with pentane in order to remove all the THF, followed by drying at 110°C for 6 h under vacuum.

The residues were analyzed by Py-GC-MS, and solid state CPMAS ^{13}C NMR and FTIR techniques as described elsewhere (14). The FTIR analysis of the samples was performed on a Digilab FTS 60 FTIR spectrometer. The samples were analyzed as KBr pellets. A accurately weighed amount (approximately 3 mg) of the vacuum dried samples were grinded with pre-weighed amount of KBr (approximately 300 mg). The pellets were pressed under a pressure of 10 tones. The pellets were dried at 100°C under vacuum for 24 h before recording their infrared spectra.

RESULTS AND DISCUSSION

Products Distribution

The liquefaction at 300°C (with H_2 , solvent and no catalyst) shows a very small conversion (11-15%). This conversion is not very significant as compared to the total THF-soluble materials (8%) extracted from the raw coal. The presence of solvents (tetralin or 1-methylnaphthalene) seems to have no appreciable effect on the

conversions. The presence of catalyst also did not cause any appreciable increase in the conversion at 300°C, because at low temperature ATTM is less likely to decompose into catalytically active phase.

The results from the liquefaction at 350°C, given in Table 1, show an appreciable effect of catalyst and solvent on the total conversion and quality of the products. In the non-catalytic liquefaction the variation in the total conversion with the solvent is quite significant, with a maximum conversion in presence of tetralin. The total conversions in a solvent-free run and the run with 1-MN are not much different from that at 300°C but with tetralin as a solvent the difference is significant. The presence of catalyst (ATTM) in the liquefaction at 350 °C shows a drastic increase in the total conversion with or without solvent. The larger increase in conversion is in the solvent free liquefaction, though the total conversion is maximum in the presence of tetralin.

Characterization of DECS-8 Wyodak subbituminous coal

The CPMAS ^{13}C NMR spectrum of THF-extracted DECS-8 raw coal, shown in Figure 1, did not show any noticeable difference as compared to that of the unextracted raw coal in terms of aromaticity and functionality. The loss of 8% of organic materials of coal did not produce any apparent changes in its chemical structure. This may not be true for some coals; the THF-extracted sample may display a substantially different spectrum. The NMR spectrum shows two major very broad bands between 0-60 ppm and 90-165 ppm. The first band (0-60 ppm) is due to aliphatic carbons and may also include aliphatic ether carbons. The second region (90-165) is identified as an aromatic region. This band consists of three types of aromatic carbons: an intense peak around 130 ppm (aromatic C), first shoulder at 142 ppm (catechol-like C) and another at 152 ppm (phenolic or aromatic ether C). The other weak and broad bands at 181 and 212 ppm are attributed to carboxylic and ketonic carbons, respectively. The FTIR spectrum of the THF-extracted raw coal was also recorded and compared with that of the unextracted raw coal and there was no significant difference between the two samples.

Figure 2 shows the total ion chromatogram (TIC) from Py-GC-MS of the THF-extracted raw coal up to the retention time 30 minutes, which is a part of the total pyrogram. All the major structural units produced by the flash pyrolysis of the coal other than the alkanes and alkenes are listed in Table 2. The low-rank coals are known to have higher oxygen functionalities: therefore, phenol, alkylphenols, catechol and alkylcatechol are the most intense peaks in the pyrogram of the raw coal. The other minor oxygen-containing compounds identified are indanol, alkyl-indanol and hydroxyindene. Among the most abundant hydrocarbons other than alkanes and alkenes are toluene, xylenes and C₃-benzenes. Indene, alkyl indene, dihydroindene, alkyl dihydroindene and alkyl naphthalenes are also identified in minor amounts. There are several intense peaks between 0-2 min (RT) of the pyrogram (Figure 2). These peaks are C₅-C₈ alkanes plus alkenes which coelute. There is another quite intense peak around 25 minutes (RT); it is a branched alkene with m/z 266. There are many more peaks over the whole pyrogram, and selective ion monitoring at m/z 71 indicates that they are long chain alkanes and alkenes. Overall, Py-GC-MS of the THF-extracted raw coal indicates that Wyodak subbituminous coal contains significant amount of oxygen containing structures including phenol, alkylphenols, catechol and other benzenediols as well as indanols. These observations are consistent with our earlier findings (13,14).

Characterization of the residues from the liquefactions.

CPMAS ^{13}C NMR

Figure 1 compares the CPMAS ^{13}C NMR spectra for the THF-extracted raw coal and the coal after liquefaction at 300 and 350°C without any solvent or catalyst. The residue from the reaction at 300°C displays a spectrum very much similar to that of the residue from the raw coal. Integration of the spectrum gives only a slight increase in the aromaticity. The residues produced after the liquefaction at 300°C in presence of solvents with and without catalyst were also analyzed by NMR, and there was no significant difference observed, except a slight increase in the relative intensity of the aromatic region. This increase was relatively less in the case when catalyst was used in the liquefaction reaction.

The residues from runs at 350°C show different spectra as compared to the raw coal. The catecholic (142 ppm) and carboxylic (181 ppm) bands almost disappeared after the run at 350°C and there is a slight decrease in the intensity of the phenolic (152 ppm) band (Figure 1). The residue, obtained from the liquefaction at 350 °C in presence of a solvent (tetralin or 1-MN) were also characterized by NMR. As compared to that of the solvent-free run, the residue from the run with tetralin shows slightly more of catechol-like carbons, but less intense than that of the THF-extracted raw coal. Also a decrease in the aliphatic band is observed. With 1-MN as a solvent the decrease in the aliphatic band is very prominent but the aromatic region shows similar functionality to that of the residue from solvent-free run.

We have seen that the presence of catalyst improves the total conversion at 350°C. However, CPMAS NMR spectra of the samples from catalytic runs appear to be similar to those from thermal runs.

FTIR

The analysis of the residues produced from liquefaction at 300°C showed no marked changes in the FTIR spectrum as compared to that of the THF-extracted raw coal, except a slight decrease in the aliphatic band in the 2950 cm^{-1} region. Using a solvent during the liquefaction also did not cause any appreciable difference in the FTIR spectra of the residues. The residue produced after the liquefaction in presence of catalyst showed a slight decrease in the ether region (1110-1300 cm^{-1}).

Figure 3 shows the FTIR spectra of the residues from liquefaction at 350°C (solvent-free) with and without catalyst, along with that of the residue from the raw coal. There are substantial changes apparent in the structure of coal after liquefaction at 350°C. There is a significant decrease in the carbonyl band at 1700 cm^{-1} and hydroxyl region at 3400 cm^{-1} (presumably carbonyl loss). In presence of catalyst, which improves the total conversion at 350°C, the effect on the ether region is very significant. It appears that catalyst has enhanced the cleavage of the ether bonds in the coal network.

PYROLYSIS-GC-MS

Figure 2 shows the selected retention time region of the Py-GC-MS chromatogram of the THF-extracted raw coal and the residues from the liquefaction at 300 and 350°C (solvent- and catalyst-free). The major peaks which are identified are listed in Table 2. Compared to the pyrogram of the THF-extracted raw coal, all the major species such as phenol, alkylphenols, alkylbenzenes, as well as alkanes and alkenes, are formed from the pyrolysis of the residues from the liquefied coal, but there are apparent differences. A substantial decrease in the intensity of the catechol and alkylcatechol peaks in the pyrogram of the residue from the run at 300°C, and the disappearance of these peaks from the pyrogram of the residue from 350°C run, are the most significant. This change in the residue from the 300°C run is not apparent from NMR, but after liquefaction at 350°C the shoulder at 142 ppm in the CPMAS ^{13}C NMR spectrum disappears completely. From this it is clear that reaction at 300°C did cause some structural changes in the coal network.

The residues from the liquefaction experiments at 300 and 350°C in presence of solvents and with and without catalyst were also characterized by Py-GC-MS. The pyrogram of the residues from liquefaction at 300 and 350 °C in presence of tetralin as solvent (with and without catalyst) are shown in Figure 4. The peaks identified are given in Table 2. The peaks marked with an alphabet in the pyrograms are the new peaks observed after liquefaction in presence of a solvent. An intense methyl-naphthalene peak observed here was also seen in the case of a solvent-free run, but with a very low intensity. These new peaks appear to have come from the adduction of solvent because they were not observed in the Py-GC-MS profiles of the residues from the solvent-free runs. When methyl-naphthalene was used as solvent, the tetralin and dihydronaphthalene peaks were not observed and the 1-methyl-naphthalene peak was very intense, showing that it is due to the solvent. The naphthalene peak was relatively weak in presence of 1-methyl-naphthalene, as compared to that in the presence of tetralin. Since the residue was extracted with THF for 24 h and dried, the solvent remaining in the residue must be either chemically bound or physically entrapped in the solvent-inaccessible micropores, or both, as also noted in an earlier work (14). In the residue from the liquefaction in the presence of catalyst and solvent, the adduction of solvent was decreased, as shown by the decreased intensity of the solvent peak in the pyrogram. The reason for the decreased adduction of solvent molecules could be due in part to the formation of reduced number of free radicals from the solvent molecules in presence of catalyst. This is also supported by the decreased amount of hydrogen transfer from tetralin and increased amount of hydrogen gas consumption during liquefaction in presence of catalyst compared to that of the catalyst-free experiment.

Table 3 shows the relative ratios of the oxygen-containing units to the alkylbenzenes before and after liquefaction. For oxygen-containing species the areas of the phenol, alkylphenols and catechol peaks were added and for alkylbenzenes, toluene, xylenes and C₃-benzenes were used. As compared to that for raw coal, the ratio decreased for the sample from solvent-free run at 300°C, and the sample from the run at 350 °C with 1-MN or without solvent. These ratios show that the presence of solvent does make a difference in the loss of specific type of species from the coal network and it is independent of the catalyst. In solvent-free reaction and with non-donor solvent (1-MN), more oxygen containing species are lost during liquefaction. In presence of tetralin during the liquefaction, this ratio did not decrease much from that of the raw coal and is highest as compared to the others.

The results of this work, though preliminary, have shown that there are significant changes in the coal structure as a consequence of the low-temperature catalytic pretreatments. Further work on the identification of specific changes in the coal structure is now in progress.

ACKNOWLEDGEMENT

This project was supported by the U. S. Department of Energy, Pittsburgh Energy Technology Center under contract DE-AC22-91PC91042. We wish to thank Dr. M. Baird of DOE/PETC for his kind support.

REFERENCES

1. Whitehurst, D. D., "Coal Liquefaction Fundamentals", Am. Chem. Soc. Sym. Ser. 1980, 139, 132.
2. Whitehurst, D. D., Mitchell, T. O. and Farcasiu, M., "Coal Liquefaction", Academic Press, New York, 1980.
3. Song, C. and Schobert, H. H., "Temperature-Programmed Liquefaction of Low-Rank Coals in H-donor and Non-donor Solvents", Am. Chem. Soc. Div. Fuel Chem. Prepr., 1992, 37(2), 976.
4. Song, C., Nomura, M., Ono, T., Am. Chem. Soc. Div. Fuel Chem. Prepr., 1991, 36 (2), 586-596.
5. Davis, A., Derbyshire, F. J., Finseth, D. H., Lin, R., Stansberry, P. G. and Terrer, M-T., Fuel, 1986, 65, 500.
6. Davis, A., Derbyshire, F. J., Mitchell, G. D. and Schobert, H. H., "Enhanced Coal Liquefaction by Low-Severity Catalytic Reactions", U. S. Department of Energy, Final Report DOE-PC-90910-F1, July, 1989, 175p.
7. Derbyshire, F. J., Davis, A., Lin, R., Stansberry, P. and Terrer M-T., Fuel Proc. Technol., 1986, 12, 127.
8. Derbyshire, F. J., Davis, A., Epstein, M. and Stansberry, P., Fuel, 1986, 65, 1233.
9. Derbyshire, F. J., Energy and Fuels, 1989, 3, 273.
10. Stansberry, P. G., Lin, R., Terrer, M-T., Lee, C. W., Davis, and Derbyshire, F., Energy and Fuels, 1987, 1, 89.
11. Burgess, C. and Schobert, H. H., ACS Fuel Chem. Prepr., 1990, 35, 31.
12. Burgess, C., Artok, L., Schobert, H. H., ACS Fuel Chem. Prepr., 1991, 36 (2), 462.
13. Song, C., Schobert, H. H., Hatcher, P. G., Energy & Fuel, 1992, 6, in press.
14. Song, C., Schobert, H. H., Hatcher, P. G., Am. Chem. Soc. Div. Fuel Chem. Prepr., 1992, 37(2), 638.

TABLE 1. Products distribution (dmmf wt %) for the liquefaction at 350°C with and without catalyst.

Solvent	Gas	Oils	Asphaltenes	Preasphaltenes	Total Conversion
Thermal					
none	3.3	2.1	2.6	4.5	12.5
Tetralin	4.2	4.1	7.6	10.0	25.9
1-MN	4.0	1.1	5.8	7.4	18.3
Catalytic					
none	3.0	10.0	5.4	11.4	29.8
Tetralin	3.0	10.2	12.9	10.6	36.4
1-MN	2.6	6.1	10.1	12.3	31.1

TABLE 2. Major identified peaks in pyrograms.

No.	MW	Identified Compounds
1	92	Toluene
2	106	p-Xylene
3	106	o-Xylene
4	120	C ₃ -benzene
5	120	C ₃ -benzene
6	120	C ₃ -benzene
7	94	Phenol
8	118	Indane
9	116	Indene
10	108	o-Cresol
11	108	m-p-Cresol
12	132	Methylindane
13	130	Methylindene
14*	132	Tetralin
15	122	Ethylphenol
16	130	Dihydronaphthalene
17	122	Ethylphenol
18	122	Dimethylphenol
19	128	Naphthalene
20	146	Dimethylindene
21	122	Dimethylphenol
22	136	C ₃ -Phenol
23	136	Caatechol
24	144	C ₃ -Phenol
25	136	Dimethylindene
26	124	Methylcatechol
27	124	Methylcatechol
28	142	2-Methylnaphthalene
29	142	1-Methylnaphthalene
30	110	1,3-Benzenediol
31	134	Indanol
32	134	Indanol
33	132	Hydroxyindene
34	138	C ₂ -Caatechol
35	156	C ₂ -Naphthalene
36	170	C ₃ -Naphthalene

* The compounds identified in Py-GC-MS profiles (Figure 4) of the residues from the liquefactions in presence of tetralin.

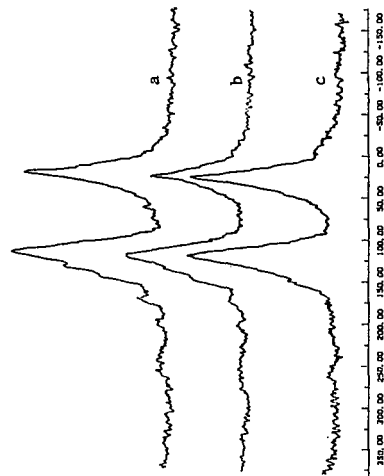


FIGURE 1 CPMAS ¹³C NMR spectra of (a) 1Ht-extracted raw coal and the residues from the solvent free thermal liquefactions at (b) 300°C, and (c) 350°C.

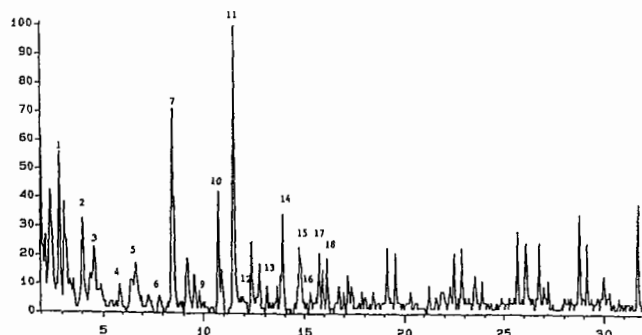
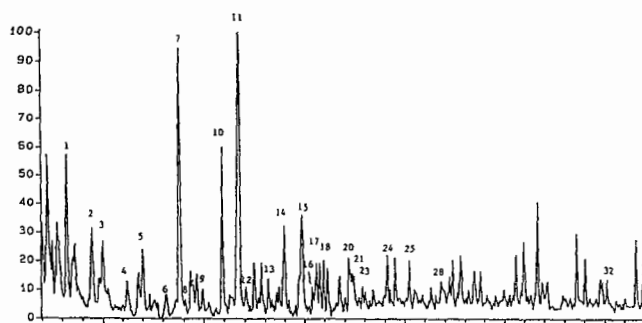
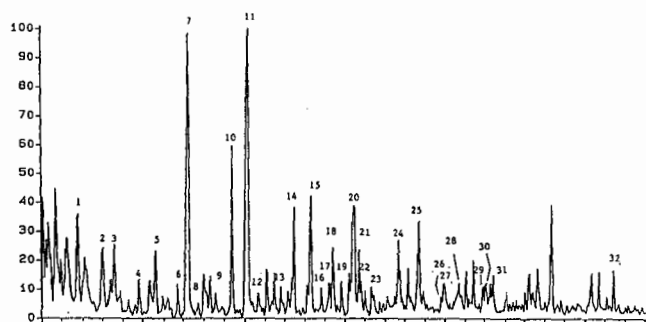


FIGURE 2. Py-GC-MS profiles of (a) THF-extracted raw coal and the residues from the thermal liquefactions at (b) 300°C, and (c) 350 °C.

TABLE 3. Ratios of the amount of the oxygen-containing units to the alkylbenzene units.

Temperature (°C)	Solvent	Ratio Phenolic/Alkylbenzenes	
		Thermal	Catalytic
Raw Coal		3.6	
300	none	2.4	2.5
300	Tetralin	3.5	3.1
300	1-MN	3.6	3.2
350	none	2.3	2.4
350	Tetralin	3.2	3.1
350	1-MN	1.9	2.3

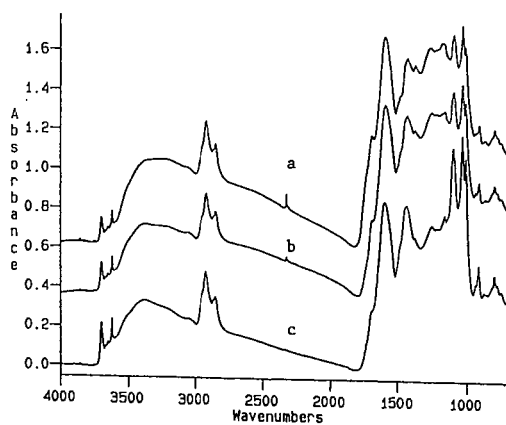


FIGURE 3. FTIR spectra of (a) THF-extracted raw coal and the residues from the solvent-free, (b) thermal, and (c) catalytic liquefactions at 350°C

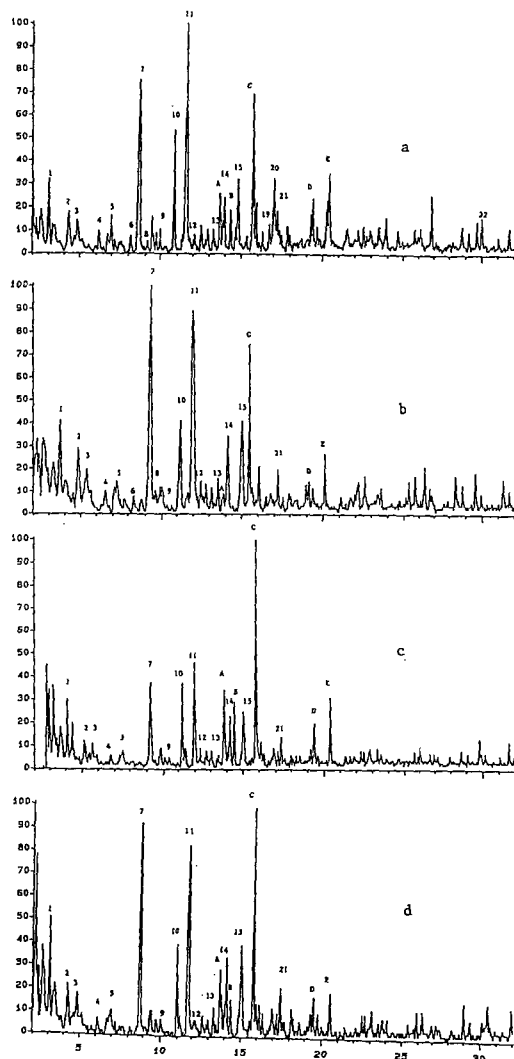


FIGURE 4. Py-GC-MS profiles of the residues from the liquefactions in presence of tetralin, (a) thermal, (b) catalytic at 300°C, and (c) thermal, (d) catalytic at 350°C.

THE CHEMICAL NATURE OF COAL LIQUID RESIDS AND THE IMPLICATIONS FOR PROCESS DEVELOPMENT

S. D. Brandes, R. A. Winschel, F. P. Burke
CONSOL Inc.

Research & Development
4000 Brownsville Road
Library, PA 15129

Key words: coal liquids, resid

INTRODUCTION

The informational needs for the advancement of direct coal liquefaction process development include the knowledge to choose the appropriate analytical tools. CONSOL Inc. is working with a number of research groups to evaluate various methods for analyzing direct coal liquefaction process-derived samples.¹ Each individual method was applied to process-derived samples and the advantages (and some drawbacks) for each have come to light.²⁻⁸ The large database accumulated in the study may be useful in choosing analytical methods for process development and design of facilities. This paper will explore the usefulness of these data for that purpose by examining a few specific examples.

Close-coupled integrated two-stage direct coal liquefaction, on a pilot plant scale, is a continuous, multi-step operation. The process steps include mixing feed coal with recycled coal liquid to form a slurry; thermal and/or catalytic liquefaction of the coal in the slurry; stripping of the light, high-value products; and recycling of the heavy residues to near extinction. The coal concentration in the feed slurry is typically 30 wt %. The slurry oil consists mostly of relatively high molecular weight material (resids) and some light distillable materials. Each process stream, with the exception of the distillation column overheads, also is comprised of 50% or more of non-distillable (850°F) resid. Because of the preponderance of the resid in the system, and its influence on the overall properties of the process streams, the program described above was directed to the study of these materials.

RESULTS AND DISCUSSION

The results of the analyses of six 850°F⁺ distillation resid samples, obtained from two process runs (Run 257⁹ and Run 259¹⁰) conducted at the Wilsonville Advanced Two-Stage Direct Coal Liquefaction facility, will be used to demonstrate the potential usefulness of these data for process development. Each of the samples are composites of many daily samples obtained over the length of the liquefaction test. These tests lasted for a number of months and included numerous changes in operating conditions. The feed to Wilsonville Run 257 was Illinois No. 6 coal from Burning Star No. 2 Mine and the feed to Run 259 was Pittsburgh seam coal from Ireland Mine. The resid from Run 259 was notably more difficult to convert to distillate products, based on Wilsonville operating results. Both runs were carried out with catalyst in both reactors. Both runs operated, for the most part, with the first of the two reactors at a higher temperature than the second reactor. Samples were obtained from three locations in the plant (Figure 1): between the two reactors (Interstage), after the second reactor but before the deasher (2nd Stage Product), and at the vessel used to accumulate different process flows to form the slurry solvent that is recycled back through the system (Recycle). Samples obtained from these different locations during a single run are expected to represent different degrees of coal conversion in the direct liquefaction process. The samples analyzed were the 850°F⁺ distillation resids of these three process streams, and, in some cases, the tetrahydrofuran-soluble portion of the resids.

The analyses performed by CONSOL on the samples include elemental analyses, proton NMR (and classification of the proton signal into defined groups), and determination of phenolic -OH by Fourier transform infrared spectroscopy (FTIR). Pyrolysis and subsequent detection and analysis of the pyrolysate by thermogravimetric (TG)-FTIR, fluorescence microscopy, reflectance microscopy, field ionization mass spectrometry (FIMS), and various separation techniques, including liquid chromatography were performed by Advanced Fuel Research,⁷ University of Kentucky,⁴ The Pennsylvania State University,³ SRI International,⁵ and Virginia Polytechnic and State University,² respectively.

Table 1 presents the elemental analyses of the six composite resid samples and the parent coals. It is readily apparent that the hydrogen content is increased and the heteroatom content is decreased in the resid as the coal slurry proceeds through the liquefaction process. Also given in Table 1 are the phenolic -OH contents of the tetrahydrofuran (THF)-soluble portion of each resid. Figure 2 shows that the phenolic -OH contents, determined by FTIR, correlate relatively well with the yield of the most polar liquid chromatography fraction of the THF-soluble portion of resids.² The data presented in Figure 2 were obtained from a number of resids obtained from different liquefaction runs made at different facilities, including Runs 257 and 259 made at Wilsonville.

The TG-FTIR results, presented in Table 2, show a reduction in gas make in the pyrolysis of the resids with a corresponding increase in tar yield as the coal is converted in the liquefaction system. The remaining -2 to -10% of the resid, not accounted for in these analyses, is converted to additional gases (NH_3 , COS) and light hydrocarbons, such as C_2H_4 and benzene. It is notable that the resids produced in the Illinois No. 6 coal run generate a much larger proportion of these volatile materials and more tar than the resids produced from the Pittsburgh seam coal resid. The char yields from the distillation resids correlate with the phenolic -OH content of the THF-soluble portion of the resid, which, as discussed above, correlates to the very polar material found in the resid.

The proton NMR data for the THF-soluble portions of the resids (Table 3) are divided into five spectral regions corresponding to five proton types. These types are condensed aromatics, uncondensed aromatics, alpha protons, beta protons, and gamma protons. The condensed aromatic component of the Run 257 resids decreases from interstage to second-stage product samples and is relatively unchanged in the recycle stream by partial deashing. The increase in aromaticity from recycle to interstage samples comes about from the addition of fresh feed coal to the slurry which is then liquefied in the first reactor. The conversion of the 850°F resid in each stage of the liquefaction process is not the same; it was approximately two times greater in the first stage than in the second stage for Run 257, and about 1.5 times greater in the first stage than the second stage in Run 259. Nonetheless, it is concluded that for Run 257, the aromatic coal structure is broken down in the first stage of the liquefaction system with little additional change of aromaticity in the second reactor. The liquefaction process conditions in Run 259 were more severe than in Run 257 (higher temperature, lower space velocity) and the rejection of resid in the deasher was lower. This accounts for the total aromaticity being higher in the Run 259 samples. However, within Run 259, an interesting trend is seen. The percent of condensed aromatic protons decreases and that of the uncondensed aromatic materials increases sequentially from the interstage to second stage product to recycle resid. This indicates that the process stream (which is mostly resid) is being converted to less-condensed aromatic moieties, but the unconverted resid is not being saturated. This is supported by a number of other analyses. For example, total volatile material of the resids (100% char) determined from the TG-FTIR experiment is essentially the same as the percentage of uncondensed aromatic protons for each sample from Run 257. However, for the Run 259 samples, there is

a large increase observed for total volatiles and uncondensed aromatic protons in the recycle sample.

Microscopy proved to be a useful technique in the examination of the resids, which are solid at room temperature. It was possible to distinguish different petrographic components in the samples that are related to the extent that the coal slurry had reacted. Point counts and mean random reflectance measurement were made of three components: the high-reflecting vitroplast, the partially reacted vitrinite, and the low-reflecting vitroplast. Values for the interstage and recycle materials in this example data set are given in Table 4. The concentration of low-reflecting vitroplast is higher for the interstage samples than the recycle samples in both Runs 257 and 259. However, for the recycle samples, its concentration is considerably lower in Run 259 than in Run 257. This indicates that across the second stage reactor and deasher, the Pittsburgh coal resid is less upgraded than the Illinois coal-derived materials, and may, in fact, be undergoing retrogressive reactions. This supports the NMR results described above.

Fluorescence microscopy^{4,11} provides a great deal of qualitative information and some quantifiable values including the wavelength of maximum fluorescence (L_{max}) and the fluorescence intensity at L_{max} . It is possible to relate the intensity and the wavelength at L_{max} to the relative degree of aromaticity, and thus to the relative reactivity of the material; the lower the intensity and the longer the wavelength, the higher the aromatic concentration and therefore the lower the reactivity. Resids from Run 257 were found to contain two distinct populations; values of L_{max} and intensity are given in Table 5 for both. Comparison of samples from Run 257 (either population) and Run 259 (Table 5) shows the intensity of the Run 259 interstage sample is relatively low and the L_{max} is high (approaching 700nm). This suggests that the interstage resid from Run 259 is comprised of a more-condensed aromatic structure than the Illinois No. 6 interstage resid and it is thus inferred to be less reactive. The recycle resid samples follow the same trend; the Run 259 sample is also more aromatic and is inferred to be less reactive. Another quantifiable value is the quotient of the fluorescence intensities measured at 700nm (red) and 525nm (green). These red:green quotients (Q) can be used to assess the variability of the fluorescence properties within a heterogeneous sample. A shift to longer wavelengths (red) indicates a more extended pi-bond conjugation or a larger proportion of condensed aromatics. The red:green quotients usually are reported as histograms. Figure 3 shows the histograms for the Runs 257 and 259 interstage and recycle resid samples. The Run 259 samples exhibit much higher proportion of the material at higher Q values than the Run 257 samples. This is consistent with the ¹H-NMR data where ~20% of all protons are aromatic in the Run 257 recycle sample and ~32% are aromatic in the Run 259 recycle sample. Across the second-stage reactor (and including the part of the process stream that has been deashed), there is a considerable shift of the fluorescence of the material to the green (or shorter wavelength, lower aromaticity) in Run 257, but not in Run 259. This may help explain the greater propensity of the Run 259 resids to form char in the TG-FTIR experiments.

FIMS data and their interpretation for these samples have been presented elsewhere.¹² Because of a distinct bimodality, the FIMS profiles of the distillation resids were deconvoluted into two overlapping components, A and B. Component A represents a molecular weight (m/e) range centered at approximately 350 Da, component B is centered around 600 Da. The relative weight fractions of A and B were used to compare the resid samples. Table 6 presents the weight percent of component A for each of the six samples obtained from both the even- and odd-mass FIMS profiles. In agreement with the data discussed above, the concentration of component A in the Run 257 resid almost doubles as the coal slurry passes through the first-stage reactor indicating that the molecular weight of the resid was

reduced in the first-stage reactor. As discussed above, conversion of the resid in the first-stage reactor was approximately twice that of the second-stage reactor for Run 257, and correspondingly the concentration of component A in the second-stage product sample increases from the interstage sample, but is only about 1.5 times that of the interstage sample. In comparison, Run 259 interstage and second-stage samples are less enriched with lower molecular weight material. The concentration of low molecular weight material decreases across both the first-stage and second-stage reactors. It increases in the recycle sample only after part of the second-stage product stream passes through the deasher where high molecular weight materials are rejected along with the ash.

SUMMARY AND CONCLUSION

To briefly summarize the information presented above; relative to the Illinois No. 6 resids, the Pittsburgh seam resids are less hydrogenated, higher molecular weight, less fluorescent and they produce fewer volatiles upon pyrolysis. In addition, the Pittsburgh seam resids are more phenolic, more aromatic and contain more nitrogen. These characteristics are consistent with the lower observed reactivity of the Pittsburgh seam resids, which must have arisen from a combination of the coal and operating conditions. The NMR, FIMS and TG-FTIR data indicate that in Run 257, the upgrading of Illinois No. 6 coal to lower molecular weight, more volatile, less aromatic materials was primarily achieved in the first stage of the two-stage system. Additionally, reflectance microscopy data show that the resid derived from the Illinois No. 6 coal in the first-stage reactor is more upgraded in passing through the second-stage reactor and deasher than the Pittsburgh seam coal first-stage resid. Phenolic -OH determinations made on the THF-soluble portion of the distillation resids correlate with the amount of very polar fraction isolated from the resids by liquid chromatography and also with the char yield from the TG experiments. Fluorescence microscopic examination of the resids leads to inferences of resid reactivity. These inferences are supported by the other data. It is apparent that no single method fully describes process derived materials; however, the trends observed by any one method are generally mimicked in the response of the other methods. The implication for process development is that the choice of methodology for analytical use, among these methods tested, can be determined by the requirements of the process developer based on such factors as cost, time, or frequency of measurement.

ACKNOWLEDGEMENT

This work was funded by the U.S. Department of Energy under contract No. DE-AC22-89PC89883.

REFERENCES

1. Brandes, S. D.; Winschel, R. A.; Burke, F. P. "The Application of Advanced Analytical Techniques to Direct Coal Liquefaction," Am. Chem. Soc., Div. Fuel Chem. Preprints, 1991, 36(3), 1172.
2. Taylor, L. T.; Hellgeth, J. W.; Sequeira, A. "Coal Liquefaction Process Streams Characterization and Evaluation; Analysis of Coal Liquefaction Process Streams by Chromatographic and Spectroscopic Techniques, Topical Report," DOE/PC 89883-41, January 1992.
3. Mitchell, G.; Davis, A. "Coal Liquefaction Process Streams Characterization and Evaluation; Gold Tube Carbonization and Reflectance Microscopy, Topical Report," DOE/PC 89883-37, December 1991.
4. Rathbone, R. F.; Hower, J. C.; Derbyshire, F. J. "Coal Liquefaction Process Streams Characterization and Evaluation; Novel Analytical Techniques for Coal Liquefaction: Fluorescence Microscopy, Topical Report," DOE/PC 89883-30, October 1991.

5. Malhotra, R.; McMillen, D. F. "Coal Liquefaction Process Streams Characterization and Evaluation; Characterization of Coal Liquids by Field Ionization Mass Spectrometry and Iodotrimethylsilane Derivatization, Topical Report," DOE/PC 89883-39, January 1992.
6. Miknis, F. P. "Coal Liquefaction Process Streams Characterization and Evaluation; Solid-State NMR Characterization of Coal Liquefaction Products, Topical Report," DOE/PC 89883-36, November 1991.
7. Serio, M. A.; Hsisheng, T.; Bassilakis, R.; Solomon, P. R. "Coal Liquefaction Process Streams Characterization and Evaluation; FT-IR Methods for Characterization of Coal Liquefaction Products, Topical Report," DOE/PC 89883-45, April 1992.
8. Green, J. B.; Pearson, C. D.; Young, L. L.; Green, J. A. "Coal Liquefaction Process Streams Characterization and Evaluation; Application of Liquid Chromatographic Separation Methods to THF-Soluble Portions of Integrated Two-Stage Coal Liquefaction Resids, Topical Report," DOE/PC89883-47, May 1992.
9. Winschel, R. A.; Robbins, G. A.; Burke, F. P. "Coal Liquefaction Process Solvent Characterization and Evaluation, Technical Progress Report July 1 through Sept. 30, 1988," DOE/PC 70018-68, July 1989.
10. Winschel, R. A.; Robbins, G. A.; Burke, F. P. "Coal Liquefaction Process Solvent Characterization and Evaluation, Technical Progress Report April 1 through June 30, 1990," DOE/PC 89883-22, July 1991.
11. Rathbone, R. F.; Hower, J. C.; Derbyshire, F. J. "Application of Fluorescence Microscopy to Coal-Derived Resid Characterization," Am. Chem. Soc., Div. Fuel Chem. Preprints, 1991, 36(3), 1164.
12. Malhotra, R.; McMillen, D. F.; Huestis, D. L. "Characterization of Coal Liquefaction Resids by Field Ionization Mass Spectrometry: Correlation Spectral Features with Processing Parameters," Am. Chem. Soc., Div. Fuel Chem. Preprints, 1992, 37 (2), 908.

TABLE 1
ELEMENTAL ANALYSES AND PHENOLIC -OH CONTENTS OF 850°F*
DISTILLATION RESIDS AND PARENT COALS^{9,10}

	Run 257				Run 259			
	Feed Coal	Inter-stage Resid	2nd Stage Resid	Recycle Resid	Feed Coal	Inter-stage Resid	2nd Stage Resid	Recycle Resid
wt % of 850°F* Resid in Process Stream	-	81.9	77.5	79.8	-	72.3	67.9	73.1
Ash wt % as det.	11.76	12.52	13.49	9.28	4.68	8.74	10.21	8.51
C wt % MAF	79.52	88.05	87.99	88.64	81.24	90.12	90.24	91.01
H wt % MAF	5.51	7.70	7.87	8.08	5.97	6.19	6.39	6.50
N wt % MAF	1.53	0.86	0.77	0.78	1.37	1.15	1.05	1.04
S wt % MAF	3.68	1.34	1.20	0.79	3.28	1.50	1.49	1.25
O wt % (by diff) MAF	9.58	2.05	2.16	1.71	8.07	1.04	0.83	0.20
Phenolic -OH, meq/g ^(a)	-	0.68	0.57	0.50	-	0.92	0.70	0.69

(a) determined on the THF-soluble portion of the resid

TABLE 2
TG-FTIR ANALYSES OF 850°F⁺ DISTILLATION RESIDS⁷

TG Yield (wt % daf)	Run 257			Run 259		
	Interstage	2nd Stage	Recycle	Interstage	2nd Stage	Recycle
Tar	70.48	69.90	73.49	65.00	65.56	67.07
Gas ^(a)	4.85	4.32	3.71	5.59	3.89	3.61
Char	17.50	15.88	14.15	27.80	28.39	22.88
Unaccounted	7.17	9.90	8.65	1.61	2.16	6.44

(a) Gas = CH₄+CO+CO₂+SO₂

TABLE 3
PROTON NMR ANALYSES OF THF-SOLUBLE PORTION OF 850°F⁺ RESIDS^{9,10}

Proton Type (wt %)	Run 257			Run 259		
	Interstage	2nd Stage	Recycle	Interstage	2nd Stage	Recycle
Condensed Aromatic	18.1	16.9	16.8	30.7	27.8	26.1
Uncondensed Aromatic	3.7	3.4	3.1	2.6	3.8	5.4
Alpha	28.8	28.6	28.0	31.1	30.8	28.3
Beta	39.1	40.5	41.4	27.2	28.9	30.4
Gamma	10.4	10.7	10.6	8.4	8.7	10.8

TABLE 4
NORMALIZED CONCENTRATION OF PETROGRAPHIC COMPONENTS^(a)
OF 850°F⁺ DISTILLATION RESIDS³

Component, %	Run 257		Run 259	
	Interstage	Recycle	Interstage	Recycle
Low-Reflecting Vitroplast	78.0	73.5	79.0	63.5
Partially Reacted Vitrinite ^(b)	0.5	0.0	0.5	0.5
High-Reflecting Vitroplast	21.5	26.5	20.0	36.0

(a) 200 reflectance measurements made on each sample

(b) unreacted coal

TABLE 5
WAVELENGTH AND INTENSITY OF MAXIMUM FLUORESCENCE
OF 850°F* DISTILLATION RESIDS*

	Run 257		Run 259	
	Interstage	Recycle	Interstage	Recycle
Fluorescence Spectrum Maximum, L_{\max} , nm	646 ^(a) /604 ^(b)	633 ^(a) /585 ^(b)	696	696
Intensity at L_{\max} , counts	6714/12666	9284/32108	6658	8497

(a) Population 1

(b) Population 2

TABLE 6
wt % COMPONENT A OF 850°F* RESIDS
FROM EVEN- AND ODD-MASS FIMS PROFILES⁵

Weight %	Run 257			Run 259		
	Interstage	2nd Stage	Recycle	Interstage	2nd Stage	Recycle
A Even	22.4	32.0	13.1	13.7	9.2	18.5
A Odd	7.9	12.9	4.3	4.0	2.2	6.3

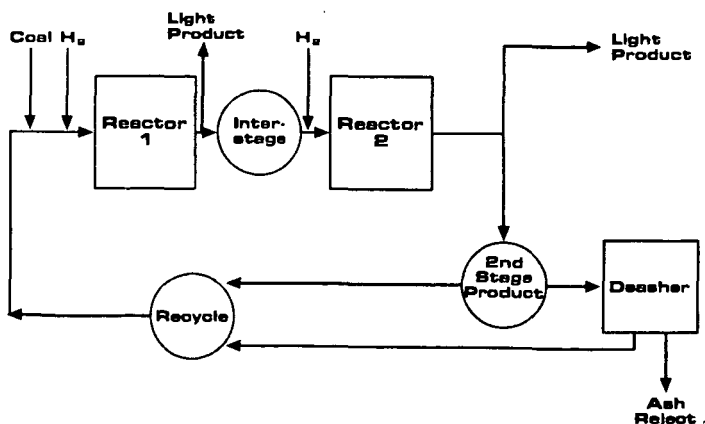


Figure 1. Simplified Flow Scheme Generic Integrated Two-Stage
Direct Coal Liquefaction Unit.

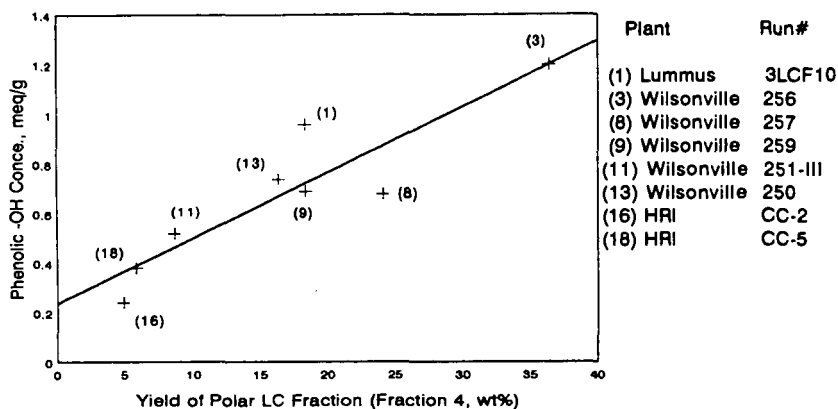


Figure 2. Phenolic -OH Concentration vs Yield of Liquid Chromatography Polar Fraction (F4).²

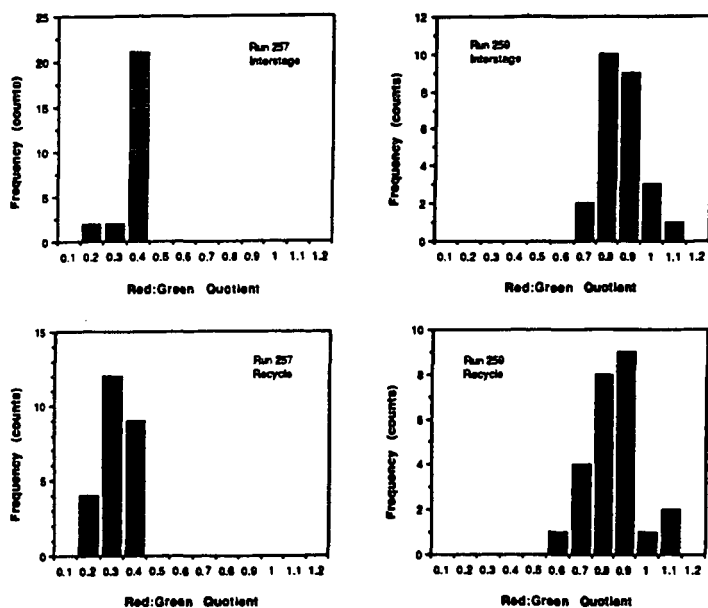


Figure 3. Red: Green Quotient Histograms for Run 257 and Run 259.⁴

Characterization of Petroleum Pitch Precursor Carbon Fibers Using Fourier Transform Infrared Photoacoustic Spectroscopy

Charles Q. Yang
Department of Textiles, Merchandising and Interiors
The University of Georgia
Athens, GA 30605

John R. Simms
Department of Chemistry
Marshall University
Huntington, WV 25701

key words: petroleum pitch, carbon fiber, infrared spectroscopy

Introduction

The production of carbon fiber from petroleum pitch proceeds in several stages: the formation of a precursor carbon fiber; stabilization of the precursor carbon fiber; and carbonization of the stabilized precursor carbon fiber (1-2). The stabilization process is the most important stage, at which thermal oxidation takes place in the precursor carbon fiber. Only a properly stabilized precursor carbon fiber can assure satisfactory performance of the final carbon fiber product.

The main interest of this research is to study the nature of the chemical changes in a pitch based precursor carbon fiber during the stabilization and carbonization processes using Fourier transform infrared photoacoustic spectroscopy (FT-IR/PAS). Gas chromatography has been widely used to investigate the volatile oxidation products of petroleum pitch and pitch based precursor carbon fibers (3-7). The applications of infrared spectroscopy, however, was focused on the oxidation of coal (8-12). The infrared spectroscopy studies of carbon fibers were carried out using transmission techniques (13,14). To obtain a transmission infrared spectrum, a carbon fiber must be either ground into a powder to make a potassium bromide (KBr) pellet or dissolved in an organic solvent to be deposited onto a window. One problem for both methods is the destruction of sample integrity. Another problem associated with the KBr pellet method is the high light scattering of carbon powders and the consequent opaqueness of the KBr pellet, which results in poor signal-to-noise ratio. It is also very difficult to find a organic solvent, in which a carbon fiber will totally dissolve.

Photoacoustic detection was used in this research to collect infrared spectra of carbon fiber samples. When a photoacoustic cell is used as a detector in a FT-IR spectrometer, the absorbed infrared radiation is first converted to photoacoustic signals, which are detected by a microphone and Fourier transformed to yield a single beam spectrum. With photoacoustic detection, it is not the transmitted or reflected IR radiation, but the photoacoustic signals converted from the absorbed radiation which are detected by a detector. Samples are not altered during the analysis. Opaque sample can be examined without experiencing difficulties with the detection of transmitted radiation. FT-IR/PAS can also be used as a near surface analysis technique (15-17).

Experimental

Instrumentation. A Nicolet 20DXB FT-IR spectrometer with a MTEC Model 100 photoacoustic cell was used to collect the infrared spectra. Resolution for all the spectra was 8 cm^{-1} . A 6-mm sample cup was used for PAS data collection. Carbon black was used as a reference material, and helium was used to purge the photoacoustic cell prior to data collection. The mirror velocity used was 0.139 cm/s for PAS and 0.556 cm/s for transmission experiments. No smoothing function or base-line correction was used.

Materials. (1) *Raw materials*—Both the enriched petroleum pitch and the green fiber produced by a melt blown process were provided by Ashland Carbon Fiber Division, Ashland Oil Company, Ashland, Kentucky. The pitch has a softening point of 260°C . The diameter of the precursor carbon fiber is 14 microns.

(2) *The stabilized precursor carbon fibers*—The precursor carbon fiber stabilized by a programmed thermal oxidation process was provided by Ashland Carbon Fiber Division. The stabilization process began at 157°C and ended at 341°C for a total heating period of 80 min. Air was used as the oxidizing

medium. The precursor carbon fiber was removed from the heating apparatus at 10-min intervals.

(3) *The carbonized carbon fibers*—The precursor carbon fibers at different stages of the carbonization process were also provided by Ashland Carbon Fiber Division. The carbonization process started at 300°C at a 15°C/min temperature ramp to the final temperature (500, 700, 900 and 1100°C, respectively). The carbonization was carried in a nitrogen atmosphere. Immediately after reaching the designated temperature, the samples were cooled to below 300°C under nitrogen before being removed. Samples were ground to a powder prior to analysis.

(4) *Solvent extraction*—A Soxhlet extractor was used to extract 1 g of a carbon fiber sample by 65 ml of a solvent for 4 hr. The solvents used included: methylene chloride, hexane, benzene and tetrahydrofuran. The extraction mixture was finally filtered to remove solid particles from the solution.

Results and discussion

The Raw Materials. The photoacoustic infrared spectra of the enriched petroleum pitch precursor and the green fiber made from the petroleum pitch are presented in Figures 1A and 1B, respectively. The bands at 2968 and 2921 cm^{-1} in Figure 1 are due to the asymmetric stretching of CH_2 - and $-\text{CH}_2$ -, respectively. Both the bands at 2968 and 2864 cm^{-1} increased their intensities relative to the band at 2921 cm^{-1} in the infrared spectrum of the tetrahydrofuran extract of the green fiber. Therefore, the band at 2864 cm^{-1} in Figure 1 can be assigned to the symmetric stretching mode of CH_2 -. The symmetric stretching mode of $-\text{CH}_2$ -, usually at 2850 cm^{-1} (18), is probably overlapped by the band at 2864 cm^{-1} in Figure 1.

The broad band at 3045 cm^{-1} in figure 1 is due to the unsaturated hydrocarbon stretching mode. In order to determine the nature of the unsaturated hydrocarbons contained in the raw materials, the green fiber was treated in a 5% solution of bromine in carbon tetrachloride for 5 min at room temperature, then analyzed by FT-IR/PAS. The intensity of the band at 3045 cm^{-1} was reduced in the spectrum of the bromine-treated green fiber. The reduction in the intensity of the band at 3045 cm^{-1} was due to the saturation of the aliphatic unsaturated hydrocarbons by bromine. Therefore, it can be concluded that the unsaturated hydrocarbons in the green fiber have both aliphatic and aromatic components.

The green fiber was extracted by benzene and hexane. It was found that both the aromatic hydrocarbon stretching band around 3045 cm^{-1} and the $-\text{CH}_2$ - asymmetric stretching band at 2918 cm^{-1} were significantly enhanced in the spectrum of the benzene extract compared with the spectrum of the green fiber (Figure 1B). This probably indicates that the $-\text{CH}_2$ - in the green fiber has a major contribution from the methylene bridges linking aromatic rings. It was also found that the CH_2 - asymmetric stretching band at 2960 cm^{-1} was much stronger while the band at 3045 cm^{-1} was weaker in the infrared spectrum of the hexane extract than in the spectrum of the green fiber (Figure 1B). Probably this can be explained by the fact that the methyl groups in the green fiber has a major contribution of methyl substitutes on the aromatic rings which have few hydrogens.

Three strong and distinct bands at 880, 834 and 750 cm^{-1} , respectively, due to aromatic out-of-plane C-H bending can be clearly identified in the spectra of the pitch precursor and the green fiber (Figures 1A and 1B). The assignment of the three aromatic out-of-plane C-H bending modes are listed in Table I. The strong band at 1600 cm^{-1} in Figure 1 is due to the aromatic ring stretching mode. The intensity of the aromatic ring stretching mode is enhanced by the presence of phenolic groups or methylene bridges linking the aromatic rings (19). It is very likely that some other aromatic C-H bending modes are superimposed by the three strong bands at 880, 834 and 750 cm^{-1} in Figure 1 as reported in the IR study of coal samples (18).

The two weak bands at 3550 and 3450 cm^{-1} shown in both the spectrum of the pitch precursor (Figure 1A) and the spectrum of the green fiber (Figure 1B) are probably associated with the stretching mode of free hydroxyl and hydrogen-bonded hydroxyl. A weak carbonyl band at 1697 cm^{-1} , which is not visible in the spectrum of the pitch precursor (figure 1A), is present in the spectrum of the green fiber (Figure 1B). The carbonyl was the oxidation product formed during

the melt blown process, by which the green fiber was produced. The functional groups present in the green fiber and the corresponding IR vibrational band frequencies are summarized in Table I.

Table I. The functional groups and the corresponding IR vibrational frequencies of green fiber.

Functional Groups	IR Vibrational Frequency (cm ⁻¹)	
-CH ₃	ν_{CH}	2968, 2866
	δ_{CH}	1444, 1377
-CH ₂	ν_{CH}	2918, 2850*
	δ_{CH}	1444*
Unsaturated Aliphatic Hydrocarbon	ν_{C-H}	3045
Aromatic Hydrocarbons	ν_{C-H}	3075-3035
1,2-bisubstituted Aromatic Hydrocarbons	γ_{C-H}	750
Trisubstituted Aromatic Hydrocarbons	γ_{C-H}	834
Aromatic Hydrocarbons with Isolated Hydrogens	γ_{C-H}	880
Aromatic Ring	$\nu_{C=C}$	1600
C=O	ν	1697
-OH	ν	3450, 3550

* Overlapped bands.

The Stabilization of the Pitch Precursor carbon Fiber. The petroleum pitch based precursor carbon fiber at different stages of the stabilization process were analyzed by FT-IR/PAS (Figures 2 and 3). It can be seen in the infrared spectra of the partially stabilized carbon fiber (Figures 2A-2D) that the band at 3550 cm⁻¹ associated with the stretching mode of the free hydroxyl and band at 1697 cm⁻¹ associated with the carbonyl stretching mode increased their intensities during the first 40 min of the programmed thermal stabilization process. This indicates that free hydroxyl and carbonyl were formed as the oxidation products at the early stages of the stabilization process. No changes are visible in the bands due to the C-H stretching and bending modes in Figure 2.

When the carbon fiber was oxidized for 50 min, the amount of the free hydroxyl was increased to such a extent that the hydroxyls form hydrogen bonding to each other as demonstrated by a broad band at 3400 cm⁻¹ with a increased intensity in Figure 3A. The intensity of the carbonyl band at 1697 cm⁻¹ is increased significantly, while the C-H stretching bands in the 3045-2864 cm⁻¹ region, the aliphatic C-H bending bands at 1444 and 1377 cm⁻¹, and the aromatic out-of-plane bending bands in the 880-750 cm⁻¹ region were reduced in Figure 3A. All the infrared spectroscopy data demonstrated that an accelerated oxidation occurred during the 40-50 min time period. A broad band around 1250 cm⁻¹ was formed in Figure 3A. This is mainly due to the C-O stretching mode, since large amount of -OH were formed during the same period. There is more reduction in the 880 cm⁻¹ band intensity than the bands at 835 and 750 cm⁻¹ so that the relative intensity of the 880 cm⁻¹ band is lower than those of the other two bands in the Figure 3A. This reveals that the isolated hydrogens in the aromatic rings were easier to be oxidized than the other types of hydrogens in the aromatic structures in the carbon fiber.

When the stabilization time was increased to 70 min, the hydroxyl

stretching band at 3400 cm^{-1} and the carbonyl stretching band at 1697 cm^{-1} continue to increase their intensities and to broaden, while bands due to both the aliphatic and aromatic C-H continue to reduce their intensities (Figure 3b and 3c). The broad band around 1250 cm^{-1} also increases its intensity. The band at 1600 cm^{-1} due to the aromatic ring stretching mode appears to have changed little in Figures 3b and 3c. Oxygen attacked both the aromatic and the aliphatic hydrocarbons while the aromatic ring remained intact during this stage of oxidation.

To determine the nature of the carbonyl-containing oxidation products formed during the stabilization process, the carbon fiber stabilized for 70 min was treated with an $0.1M$ NaOH solution at room temperature for 5 min. The spectrum of the carbon fiber thus treated showed a reduction in the intensity of the carbonyl band at 1697 cm^{-1} and the formation of a new band at 1380 cm^{-1} , which was due to the symmetric stretching of carboxylate carbonyl. The symmetric stretching band of the carboxylate was obviously overlapped by the strong band at 1600 cm^{-1} . Formation of carboxylate upon the treatment of the carbon fiber by a NaOH solution reveals that the carbonyl band at 1697 cm^{-1} in Figure 3c has a contribution of carboxyl. The carbonyl band at 1697 cm^{-1} was further reduced after the carbon fiber had been treated in a NaOH solution for 140 hr. Because an extended treatment of the carbon fiber in a NaOH solution allows saponification to take place, the further reduction of the intensity of the carbonyl band at 1697 cm^{-1} demonstrated that ester was also formed in carbon fiber during the stabilization process. The carbonyl band, which remained in the spectrum of the carbon fiber treated in the NaOH solution for 140 hr, was probably due to aldehyde and ketone.

The photoacoustic spectrum of the fully stabilized carbon fiber is shown in Figure 3d. The broad, intense band at 3400 cm^{-1} is due to the hydrogen-bonded -OH groups of alcohol and phenol. The carbonyl band appears to broaden toward the high frequency region so the peak is around $1735\text{--}1697\text{ cm}^{-1}$ region. When the fully stabilized carbon fiber was extracted in methylene chloride, the infrared spectrum showed two distinct carbonyl bands at 1841 and 1771 cm^{-1} , respectively, and a band at 896 cm^{-1} . When the methylene extract was exposed to moisture, the intensities of the two carbonyl bands at 1841 and 1771 cm^{-1} as well as the band at 896 cm^{-1} were reduced substantially while a strong and broad band at 1715 cm^{-1} due to carboxyl carbonyl was formed. Therefore, it can be concluded that anhydride was formed as an oxidation product in the carbon fiber. The anhydride formed in the carbon fiber is probably cyclic aromatic anhydride, the dehydration product of a 1,2-dicarboxylic acid which is in turn the oxidation product of two CH_2 - groups bonded to the adjacent carbons in an aromatic ring. The band at 896 cm^{-1} in the extract of the methylene chloride extract was due to the C-O stretching of five-member cyclic anhydride. The oxidation products in the stabilized carbon fiber is listed in Table II.

Table II. The oxidation products of the pitch precursor carbon fiber.

Oxidation Products	IR band Frequency (cm^{-1})
Carbonyls of ketone and aldehyde	" 1697
Carbonyls of carboxylic acid and ester*	" $1697\text{--}1735$
Carbonyl of aromatic cyclic anhydride	" $1841, 1771$
Isolated hydroxyl	" ~ 3550
H-bonded hydroxyl	" ~ 3450

* Overlapped bands.

The Carbonization Process. The photoacoustic infrared spectra of the pitch precursor carbon fibers at different stages of the carbonization process are presented in Figures 4B-4E. After the stabilized carbon fiber was heated from 300°C to 500°C , the amount of hydroxyl and carbonyl in the carbon fiber was decreased as demonstrated by the significant reduction in the intensities of the

two bands at 3400 cm^{-1} and 1697 cm^{-1} in Figure 4B. It is also found that most of the aliphatic hydrocarbons were eliminated during this period, because the aliphatic hydrocarbon bands in the 2968-2864 cm^{-1} region (the C-H stretching modes) and in the 1444-1377 cm^{-1} region (the C-H bending modes) decreased drastically in the infrared spectrum of the carbon fiber heated to 500°C (Figure 4B). The aromatic hydrocarbon bands at 3050 cm^{-1} (the C-H stretching modes) and in the 880-750 cm^{-1} region (the aromatic C-H out-of-plane bending), as well as the aromatic ring stretching band at 1600 cm^{-1} appears to be unchanged in Figure 4B compared with the spectrum of the stabilized carbon fiber (Figure 4A). The infrared spectrum of the carbon fiber heated to 700°C (Figure 4C) reveals that all the hydroxyl and most of the carbonyl groups were eliminated in the carbon fiber. Only a very weak carbonyl band at 1697 cm^{-1} is seen in Figure 4C. The intensities of the aromatic hydrocarbon stretching band at 3050 cm^{-1} as well as the out-of-plane bending of the 1,2-bisubstituted aromatic C-H band at 750 cm^{-1} were drastically reduced in Figure 4C. The intensity of the aromatic ring stretching band at 1600 cm^{-1} was also reduced significantly in Figure 4C. The infrared spectroscopy data indicated that the aromatic rings were condensing and the hydrogens in the aromatic rings were being eliminated when the carbon fiber was heated from 500 °C to 700 °C.

When the carbonization temperature reached 900 °C, all the vibrational bands in the infrared spectrum (Figure 4C) were diminished. As a result, the infrared spectrum (Figure 4D) appears to be a flat line. All the functional groups in the carbon fiber were totally eliminated at this stage of carbonization. The infrared spectrum of the carbon fiber heated to 1100°C (Figure 4E) is identical to Figure 4D.

Conclusions

1. The unoxidized pitch carbon fiber contains aromatic hydrocarbons, saturated and unsaturated aliphatic hydrocarbons, as well as small amount of carbonyl and hydroxyl.
2. Hydroxyls of alcohol and phenol, carbonyls of ketone/aldehyde, carboxylic acid, ester and anhydride are formed during the stabilization process of the pitch precursor carbon fiber.
3. All the carbonyls, hydroxyls and hydrocarbons in the stabilized carbon fiber were gradually eliminated during the carbonization process. The aromatic ring condensation started to take place when the temperature reached above 500°C. All the functional groups were eliminated at 900 °C.

References

1. Otani, S. Carbon 1965, 3, 31.
2. Sawran, W.R.; Turill, F.H.; Newman, J.W.; Hall, N.W. U.S. Patent 4,497,789, 1985.
3. Saneta, R.; Wlochowicz, A.; Wysocki, M. Angew. Makromol. Chem. 1986, 140, 161.
4. Poxon, D.W.; Wright, R.G. J. Chromatogr. 1972, 61, 142.
5. Searl, D.T.; Cassialy, F.J.; King, W.H.; Brown, R.A. Anal. Chem. 1970, 42, 945.
6. Geinko, R.A.; Lewis, I.C. Anal. Chem. 1975, 47, 2151.
7. Glajch, J.; Lubkowitz, J.A.; Roger, L.B. J. Chromatogr. 1979, 68, 355.
8. Albers, G.; Lenart, L.; Oelert, H. Fuel 1974, 53, 47.
9. Painter, P.C.; Yamada, Y.; Jenkins, R.G.; Coleman, M.M.; Walker, P.L. Fuel 1978, 58, 293.
10. Fuller, E.L.; Smyrl, M.R. Fuel 1985, 64, 1143.
11. Ito, I.; Seki, H.; Lino, M. Fuel 1988, 67, 573.
12. Zawadzki, T. Carbon 1988, 26, 619.
13. Sajak, K.; Wlochowicz, A.; Wysocki, M. Acta Polym. 1984, 35, 580.
14. Usami, T.; Itoh, T.; Ohtani, H.; Tsuge, S. Macromolecules 1990, 23, 2460.
15. Yang, C.Q. Anal. Chem. Acta. 1987, 194, 303.
16. Yang, C.Q. Appl. Spectrosc. 1987, 45, 102.
17. Yang, C.Q. Ind. Eng. Chem. Res. 1992, 31, 617.
18. Painter, P.; Starsinic, M.; Coleman, M. in Fourier Transform Infrared Spectroscopy; Ferraro, J.R.; Basile, L.J. Eds.; Academic Press: Orlando, 1985; pp. 177-182.
19. Painter, R.; Snyder, M.; Starsinic, M.; Coleman, M.; Kuehn, D.; Davis, A. Appl. Spectrosc. 1981, 35, 475.

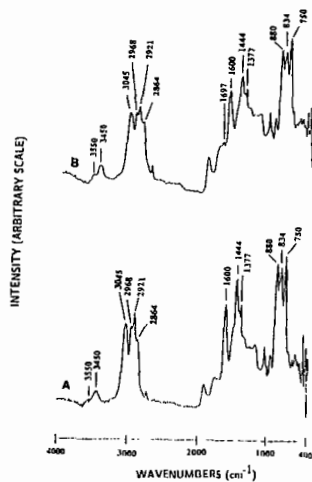


Figure 1 Photoacoustic infrared spectra of (A) the petroleum pitch; (B) the pitch precursor carbon fiber.

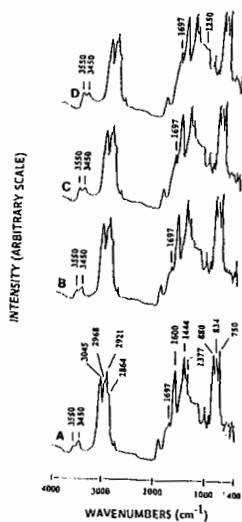


Figure 2 Photoacoustic infrared spectra of the pitch precursor carbon fiber stabilized for different times (min): (A) 10; (B) 20; (C) 30; (D) 40.

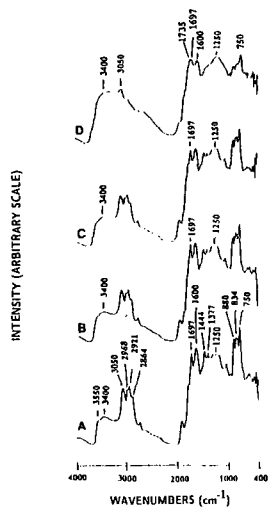


Figure 3 Photoacoustic infrared spectra of the pitch precursor carbon fiber stabilized for different times (min): (A) 50; (B) 60; (C) 70; (D) 80.

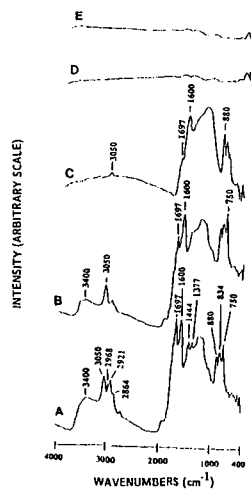


Figure 4 Photoacoustic infrared spectra of (A) the full stabilized carbon fiber. The photoacoustic infrared spectra of the carbon fiber heated to different temperatures during carbonization(°C): (B) 500; (C) 700; (D) 900; (E) 1100.

ON THE NATURE OF HYDROAROMATIC HYDROGEN IN MODEL COMPOUNDS AND IN COAL

Jianli Hu, James H. Whitcomb, John W. Tierney, and Irving Wender
Chemical and Petroleum Engineering Department,
University of Pittsburgh, Pittsburgh, PA 15261

Keywords: Catalytic Dehydrogenation, Hydroaromatic Hydrogen, Hydrogen Evolution/Transfer

ABSTRACT

The catalytic dehydrogenation of coal to yield molecular hydrogen using palladium on a support has been investigated by several workers. However, little has been reported on elucidation of the nature of the dehydrogenation reaction, the ease of removal of hydroaromatic hydrogen from different structural components or the effects of solvents of different boiling points, reduction potentials, hydrogen transfer ability, or the mechanism of hydrogen removal. The present study used model hydroaromatic compounds to gain information on the ease of catalytic removal of hydrogen either as H_2 or to a hydrogen acceptor. The course of the dehydrogenation of a number of model compounds was found to involve hydrogen transfer to intermediates, some of which have been identified. A mechanism for the palladium-catalyzed removal of hydrogen is proposed. The use of a hydrogen acceptor has permitted use of low-boiling solvents so as to minimize side reactions. Catalytic dehydrogenation, in addition to gaining information on hydrogen transfer to coal from hydroaromatic compounds, promises to be a valuable analytical technique to determine the amount and nature of hydroaromatic hydrogen in coal, recycle oils and heavy petroleum residues.

INTRODUCTION

The sources of hydrogen in direct coal liquefaction are molecular hydrogen and hydrogen in hydroaromatic structures in added solvents, recycle oils or in coal itself. It is important to have a measure of donatable hydrogen atoms available in hydroaromatic structures in coal and in oils derived from coal. Few efforts have been directed towards developing a direct method for determination of the nature and reactivity of hydroaromatic hydrogen that exists in coal. It is generally accepted that the main hydrogen sources in coal liquefaction are hydroaromatic structures containing two or more cyclic rings. Hydroaromatics may contain two available hydrogen atoms as in 9,10-dihydroanthracene (9,10-DHA), four as in a tetrahydroanthracene (THA), six as in a corresponding hexahydro compound (HHA) or eight as in an octahydroanthracene (OHA). Determination of the relative rates of hydrogen donation of hydroaromatics in recycle solvents is of particular important in achieving insights into the chemistry of coal liquefaction.

1H -NMR and ^{13}C -NMR⁽¹⁾ techniques have been used for the evaluation of hydroaromatic hydrogen. This approach can be applied to distillate fractions, but the residual material gives diffuse spectra and analysis becomes uncertain.

Reggel and coworkers^[2,3] studied the catalytic dehydrogenation of coal using a 5% Pd/CaCO₃ catalyst at the boiling point of a solvent. They found the compound phenanthridine (b.p. 350 °C), an excellent coal solvent, to be the most useful vehicle. It appeared that solvents with low reduction potentials were better than vehicles of higher reduction potentials in the removal of hydrogen from coal. With this technique, Reggel et al. concluded that high rank coals contain considerable hydroaromatic hydrogen with a maximum of about 40 atoms of hydrogen removed per 100 carbon atoms at coals of about 76% carbon (maf). Much of their work was aimed at studying coal structure and it was suggested that lignite and subbituminous coal contain substituted benzene rings with few hydroaromatic structures.

Heredy et al.^[4] felt that the use of high boiling solvents such as phenanthridine, which is also a polar solvent, might tend to adduction and condensation reactions leading to an incorrect measurement of hydroaromatic hydrogen.

The objectives of the present work are to study the catalytic dehydrogenation of model compounds and to relate the results to the catalytic dehydrogenation of coal, recycle solvents and liquefaction residues and to determine the fate of hydroaromatic hydrogen during these reactions. Kinetic analysis and the search for possible mechanistic pathways in catalytic dehydrogenation are also important aims of this research. In addition, these studies promise to shed light on the interchange and transfer of hydrogen involved between aromatic and hydroaromatic structures during coal liquefaction. It is hoped that an analytic method for determination and differentiation of hydroaromatic hydrogen will emerge from this research together with difficult to obtain information on the fate of hydrogen atoms attached to polynuclear systems during the liquefaction of coal.

We first investigated the effect of various high boiling solvents on the catalytic dehydrogenation of a number of model hydroaromatic compounds containing trinuclear polycyclic rings. Removal of hydrogen appears to be affected by both the boiling point of the vehicle and its reduction potential. We then found that solvents that boil as low as 245 °C could be used in the catalytic dehydrogenation of these model compounds if we added a good hydrogen acceptor such as stilbene. This unsaturated compound readily accepts hydrogen atoms to form bibenzyl under our typical catalytic dehydrogenation conditions.

EXPERIMENTAL

The dehydrogenation system is designed to provide for automatic data recording. Reactions were carried out in a three-necked flask at atmospheric pressure. The palladium catalyst was reduced with flowing hydrogen at 150°C for one hour prior to reaction. After the flask was cooled to room temperature under hydrogen, the model compound and vehicle were charged into the flask containing an Alnico stirring bar. The system was purged with He for 20 minutes and the flask then fitted with a mantle and heated. Evolved gases from the reaction were taken from the middle neck and collected over mercury in a burette. The mercury level used to maintain the pressure was controlled by a bulb mounted on a slide mechanism, by which the mercury level in both the bulb and burette were equalized. The level was recorded automatically, thus providing a continuous recording of the gas volume within the burette. The yield of hydrogen evolved was calculated from the difference of hydrogen evolved from the dehydrogenation of the model compound and a blank run. The hydrogen yield is expressed as the percentage of the theoretical available hydroaromatic hydrogen in the model compound. For example, the theoretical amount of hydroaromatic hydrogen in 9,10-DHA (2 atoms of hydrogen per molecule)

is 140.8 cc/gram, measured at 25 °C and 740 mm of Hg. In the presence of stilbene, a hydrogen acceptor, hydroaromatic hydrogen was mostly transferred to the hydrogen acceptor rather than evolved as hydrogen gas. The amount of hydrogen transferred was measured from the amount of bibenzyl formed.

Gas samples were removed from the sample port and analyzed by GC(Hewlett Packard 5880A). The residues were analyzed by GC and by GC-MS(The GC is a HP-5890 series II and the mass spectrometer is a HP-5970 series selective detector). Organic chemicals were obtained from Aldrich Chemical Inc.; catalysts were obtained from Strem Chemical Co. and from the Engelhard Corp.(Pd/CaCO₃, Pd/C).

RESULTS AND DISCUSSION

Effect of Boiling Point and Reduction Potentials on Hydrogen Evolution

Thermodynamically, high temperature and low pressure favor dehydrogenation; coal liquefaction, therefore, requires high hydrogen pressure. Reggel et al. postulated that the reduction potential, the energy required to accept an electron of the solvent, is of importance in catalytic dehydrogenation. This is borne out by the data obtained from catalytic dehydrogenation of 9,10-DHA with several vehicles. Pyrene, with a high boiling point (393 °C) and a comparatively low reduction potential(-1.56V) gives 95.1 percent of the theoretical yield of molecular hydrogen. p-Terphenyl, b.p. 383°C, but with a high reduction potential gives only 82.1% of H₂. Phenanthridine and anthracene, with lower boiling points and low reduction potentials, give high H₂ yields. Comparison of the use of phenanthrene and anthracene, molecular isomers, as vehicles is quite dramatic. The lowest H₂ evolution occurs with phenanthrene which boils only 3°C below anthracene but has a significantly higher reduction potential. This effect, the relative importance of boiling point and reduction potential of solvents on catalytic dehydrogenation, bears further investigation.

Dehydrogenation of 9,10-DHA with Various Solvents in the Presence of Stilbene, a Hydrogen Acceptor

The suggestion that use of a high-boiling solvent, indeed a nitrogen-containing vehicle, could lead to side reactions, may well be valid. We found that we could use low-boiling solvents in the presence of a hydrogen acceptor and the following experiments used stilbene as the hydrogen acceptor. Interestingly, depending on the vehicle, some hydrogen was evolved as molecular H₂ while some hydrogen was transferred to stilbene to form bibenzyl. The results are summarized in Table 2.

Initial experiments were carried out with two high boiling solvents (p-terphenyl and pyrene)which tended to yield more H₂ as gas than that transferred to the acceptor. Examination of the results reveals that the ratio of hydrogen evolution and hydrogen transfer may also depend on both temperature and reduction potential.

Experiments were then carried out with quinaldine (b.p. 248°C, reduction potential -1.50V) and 2-methylnaphthalene (b.p. 243°C, reduction potential -1.98V). Similar results were obtained with both solvents. 2-Methylnaphthalene is a good electron transfer agent and this probably is responsible for its effectiveness. With these low-boiling vehicles, hydrogen transfer to stilbene is the main step in the catalytic dehydrogenation of 9,10-DHA.

Also shown in Table 2, the surface area of the Pd support had essentially no effect. The reduced Pd on carbon catalyst, with a surface area of 1000 m²/g, gave the same or slightly higher amounts of hydrogen removal from 9,10-DHA as did reduced Pd on CaCO₃ (surface area

of 12m²/g).

An experiment with biphenyl (b.p. 255°C), a good electron transfer agent, resulted in 87% of the hydrogen in 9,10-DHA being transferred to stilbene with only 2.3% evolved as H₂ gas.

It is important that the palladium be in its lowest oxidation state; exposure of the catalyst to air affects the dehydrogenation deleteriously.

It is interesting to note that when 9,10-DHA is catalytically dehydrogenated in the presence of half the equivalent of stilbene, half the hydroaromatic hydrogen in 9,10-DHA is transferred to stilbene, half is evolved as gas (Table 2). It was observed that hydrogen evolution occurred after the stilbene was hydrogenated, indicating that hydrogen transfer to stilbene is preferred over H₂ gas evolution under these conditions.

Characterization of Hydrogen Transfer Mechanism of Hydroaromatics

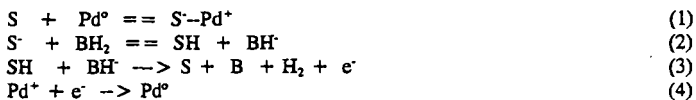
Several hydroaromatic compounds were dehydrogenated in the presence of stilbene with quinaldine as the vehicle in an attempt to elucidate the mechanism of hydrogen transfer. Dehydrogenation of 9,10-DHA gives only anthracene and hydrogen; it is unlikely that intermediate polynuclears are involved.

The model compound 1,4,5,8,9,10-hexahydroanthracene (HHA) is neither an aromatic nor a hydroaromatic compound. It does not contain an aromatic ring but has four isolated double bonds. But catalytic dehydrogenation of this compound in quinaldine in the presence of stilbene yields the hydroaromatic compounds 9,10-DHA, 1,2,3,4-tetrahydroanthracene (THA) and 1,2,3,4,5,6,7,8-octahydroanthracene (OHA) as well as bibenzyl formed by addition of hydrogen to the stilbene. As shown in Figure 1, the concentration of HHA decreases rapidly as the reaction proceeds. The yield of THA increases to a maximum after 5 minutes and decreases thereafter; it is then maintained at very low concentrations. The initial formation rate of OHA is very slow and then increases to a maximum value as the concentration of THA decreases; its concentration then falls slowly to a constant value. As for 9,10-DHA, its concentration increases smoothly at first and reaches a maximum in 10 minutes, following the maximum observed for THA by 5 minutes. The hydrogen transfer rate to stilbene is higher than the rate of formation of anthracene, particularly in the initial stages. It is noteworthy that the concentration of anthracene increases significantly after 10 minutes, when the concentrations of the hydroaromatics begins to drop, suggesting that the precursor of THA is a key intermediate through which both OHA and DHA are produced.

When the hydroaromatic, OHA, was dehydrogenated in the presence of stilbene, its concentration slowly decreased with time. After 40 minutes, only 10% of hydrogen was transferred and 15% of THA was formed. No 9,10-DHA was formed and only trace amounts of anthracene were detected. This indicates that OHA is a relatively poor hydrogen donor compared with THA and DHA. This is in keeping with the recent findings of Bate and Harrison⁽⁶⁾ who found, that for coal dissolution, the type of donor present may be more important than the total hydrogen donor content. The dehydrogenation of a mixture of DHA, HHA and OHA was carried out to compare hydrogen transfer rates of these model compounds (Figure 2).

On the Mechanism of Catalytic Dehydrogenation

Based on the above results, a mechanism of catalytic dehydrogenation and hydrogen transfer is proposed to explain the reaction pathways involved in dehydrogenation of these model compounds. The basic dehydrogenation pathway presented is based mostly on results of the dehydrogenation of 9,10-DHA both in the presence and in the absence of a hydrogen acceptor. S, BH₂, and B refer to vehicle, 9,10-DHA, and anthracene respectively.



It is assumed that the dehydrogenation step in the mechanism (eq.3) is rate controlling. A kinetic model expression based on this mechanism proposed describes the experimental curve of hydrogen evolved versus time very well. Further information is needed to improve this model and to apply it to the dehydrogenation of other substances containing hydroaromatic structures.

In the presence of a hydrogen acceptor, stilbene, a similar reaction pathway is involved, where the reduced solvent transfers hydrogen to adsorbed stilbene rather than further reacting with the BH^- intermediate to evolve hydrogen to gas phase.

CONCLUSIONS

For vehicles boiling above 340 °C, both boiling point and reduction potential of the solvent employed appear to influence the palladium-catalyzed dehydrogenation of model polynuclear hydroaromatic compounds to yield gaseous hydrogen. For certain solvents that boil about 100 °C lower (245 °C or so), the palladium-catalyzed dehydrogenation of the same compounds occurs readily in the presence of a good hydrogen acceptor such as stilbene. Depending on the model hydroaromatic compound and reaction conditions, hydroaromatic hydrogen may be evolved as molecular hydrogen or be transferred to the hydrogen acceptor. With lower boiling vehicles, addition reactions are minimized with selective removal of hydroaromatic hydrogen.

A pathway for palladium-catalyzed dehydrogenation is proposed. The first step involves transfer of an electron from zerovalent palladium to the solvent. The solvent then remove a proton from the hydroaromatic compound. The slow step is the removal of hydrogen from reduced solvent.

The mechanism of removal of different hydroaromatic hydrogens may occur through various intermolecular transfers. There is a need to quantify not only total hydroaromatic content in coal and recycle solvents but also to determine the contributions from individual types of hydroaromatic compounds.

ACKNOWLEDGEMENT

The authors acknowledge the financial support from U.S. Department of Energy under Contract No. DE-PS22-89PC89998.

REFERENCES

- [1].Burke, F.P. and Winschel, R.A., Annual Report to DOE, Contract No.DE-AC22-80-PC30027(1980)
- [2].Reggel, L.; Wender, I.; Raymond, R. *Fuel*, 1968,47,373-390
- [3].Reggel, L.; Wender, I.; Raymond, R., *Science*, Vol.137, 681-682(1962)
- [4].Heredy,L.A.; McCoy, L.R.; Skowronski,R.P.; Ratto,J.J. Final Report on the Chemistry of the Extractive Phase of Coal Liquefaction, US-DOE Contract No. N45569(1985).
- [5].Deshpande,A.P., M.S. Thesis, University of Pittsburgh,1991
- [6].Harrison, G., Bate, K., Proceeding of International Coal Conference, September, 1991, England, 739-742

Table 1. Dehydrogenation of 9,10-DHA with Pd/C in the Presence of Various Solvent

Polynuclear Aromatics	B.P. °C	Reduction Potential, -V	Dehydrogenation, H ₂ yield, cc	Blank, H ₂ , cc	Theoretical H ₂ yield, %
Phenanthridine	348	1.58	28.9	1.1	98.3
Phenanthrene	337	1.90	24.7	2.0	80.5
Pyrene	393	1.56	29.8	3.0	95.1
p-Terphenyl	383	2.01	26.4	3.2	82.1
Anthracene	340	1.46	27.0	1.1	91.8

Table 2. Dehydrogenation of 9,10-DHA with Pd/C in the Presence of a Hydrogen Acceptor

Catalyst	Vehicle Reduction Potential and B.P.	Feed		H ₂ Evolved, %	Bibenzyl %
		DHA, g	Stilbene, g		
Pd/C	p-Terphenyl 2.01, 383°C	0.2	0.2	79.7	20.3
Pd/C	Pyrene 1.56, 393°C	0.2	0.2	61.3	38.7
NONE	Phenanthridine 1.58, 348°C	0.2	0.2	11.1	16.5
NONE	o-Terphenyl 1.90, 337°C	0.2	0.2	1.0	9.1
Pd/C	Quinaldine 1.50, 248°C	0.2	0.2	2.7	92.5
Pd/CaCO ₃	Quinaldine 1.50, 248°C	0.2	0.2	14.5	74.0
Pd/C	2-Methylnaphthalene 1.96, 243°C	0.2	0.2	5.5	93.4
Pd/CaCO ₃	2-Methylnaphthalene 1.96, 243°C	0.2	0.2	8.8	90.4
Pd/CaCO ₃	Biphenyl 2.18, 255°C	0.2	0.2	2.3	87.2
Pd/C	Quinaldine 1.50, 248°C	0.3	0.15	50	50

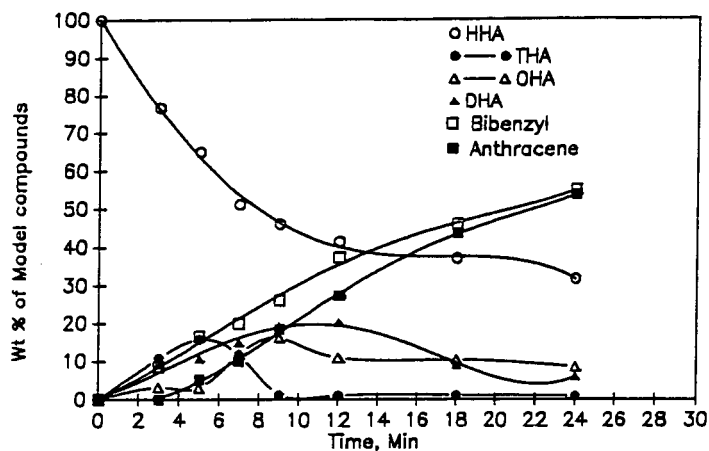


Figure 1. Dehydrogenation of HHA with Pd/CaCO_3 , quinaldine as vehicle in presence of stilbene as a hydrogen acceptor.

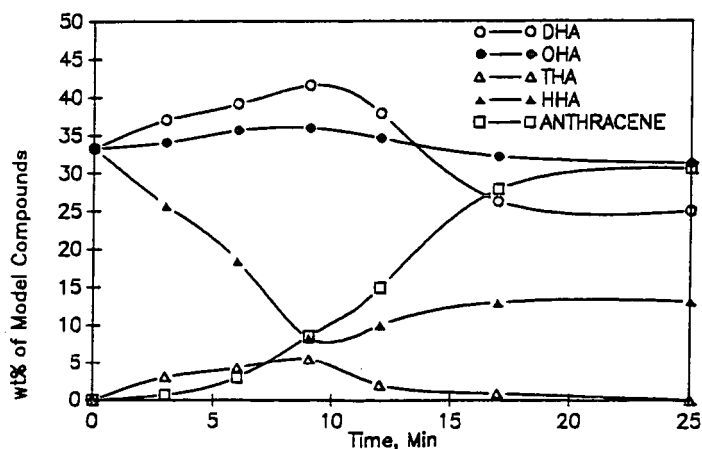


Figure 2. Dehydrogenation of mixture of model compounds on 0.5g reduced Pd/CaCO_3 with quinaldine as vehicle in presence of stilbene as a hydrogen acceptor.

CHARACTERIZATION OF IRON AND SULFIDED IRON OXIDE CATALYSTS BY ELECTRON MICRODIFFRACTION

Ram Srinivasan, Robert A. Keogh, and Burtron H. Davis
Center for Applied Energy Research
University of Kentucky
3572 Iron Works Pike
Lexington, KY 40511

Keywords: iron oxide, sulfidation, sulfation, microdiffraction, ferric naphthanate.

INTRODUCTION

The use of iron oxide as a catalyst for direct coal liquefaction was introduced soon after the initial discovery of the process (1-4). Iron oxide in the form of "red mud" has continued to be utilized (5). This was the catalyst of choice for the first stage reactor for many of the recent runs at the Wilsonville, Alabama Advanced Coal Liquefaction facility (6).

The availability of an ultrafine iron oxide catalyst (300 m²/g) provided an opportunity to follow with time the sulfidation of iron under mild direct coal liquefaction conditions. The use of transmission electron microscopy permitted a determination of the crystal structure and the elemental composition of individual catalyst particles.

EXPERIMENTAL METHODS

The Fe₂O₃ as-received powder was sulfided using dimethyldisulfide (DMDS) at 385°C for different periods ranging from 15 to 60 minutes.

For X-ray diffraction analysis, a Philips X-ray diffractometer equipped with an XRG-3100 generator, was used. The radiation used was CuK α ($\lambda_{\text{CuK}\alpha} = 1.548 \text{ \AA}$). A graphite monochromator was placed on the diffracted beam path. The data was acquired from the VAX/VMS V5.3-1 system.

Electron microscopy work was done using a Hitachi H800 NA scanning transmission electron microscope (STEM) at an operating voltage of 200 kV. This STEM is equipped with a silicon-lithium diode detector (Link) and a multichannel analyzer (Tracor 500). The X-rays emitted by the specimen upon electron irradiation were collected in the range 0-20 KeV for 60 seconds.

RESULTS AND DISCUSSION

The Fe-S system is so complex that various phases could be obtained as a result of sulfidation process. Numerous crystalline phases that exist in this system are presented in Table 1.

The precursor used for sulfidation studies was Fe₂O₃ (Mach Inc.). The surface area of these powders was 300 m²/g. The electron micrograph obtained from this as-received material is presented in Figure 1. An electron microdiffraction pattern obtained from a 5 nm region is shown in the inset in Figure 1, indicating that the material may be amorphous.

A particle size analysis indicates that the major fraction of the particles lies in the range 1-3 nm in diameter.

A typical X-ray diffraction pattern for the catalyst Fe_2O_3 -sulfided for 15 minutes at 385°C is shown in Figure 2. The X-ray peak intensities and the Bragg positions of 2θ correspond clearly to Fe_7S_8 phase. This is a hcp system with $a_0 = 0.686$ nm and $c_0 = 1.7062$ nm. All the $\{hkl\}$ indices corresponding to each profile are shown in this figure. The X-ray diffraction patterns obtained from other samples sulfided at longer times exhibited clearly the Fe_7S_8 (hcp) phase similar to that shown in Figure 2. However, the intensity was found to increase proportionately with the period of sulfidation time at 385°C . Thus, the crystal phase developed in all the catalysts is Fe_7S_8 according to the X-ray diffraction data (compare Table 1).

An electron micrograph obtained from the sample Fe_2O_3 sulfided at 385°C for 15 minutes is presented in Figure 3. Larger hexagonal crystals are formed after sulfidation at 385°C for 15 minutes. Several electron microdiffraction patterns were obtained from numerous individual crystals.

EDX analysis was also carried out along with the microdiffraction study. The particles appear to have grown into large hexagonal crystals, and yielded strong X-ray signals for $\text{Fe}_{K\alpha}$ and $\text{S}_{K\alpha}$ lines. Similar results were obtained for the Fe_2O_3 catalyst sulfided for 30 minutes. Likewise, large dense hexagonal crystals were observed for the one sulfided for 60 minutes. Similar size particles were obtained for either 15 minute and 60 minute sulfidation. Once the small oxide particles have undergone sulfidation for 15 minutes or more, they have grown to form hexagonal crystals which are larger than the precursor oxide particles, which show various iron sulfide phases. However, the majority of the diffraction patterns correspond to the Fe_7S_8 phase.

Ferric naphthanate was sulfided at 385°C for 15, 30 and 60 minutes respectively, under the same experimental conditions described above. A typical electron micrograph obtained from the 60 minute sulfided sample is shown in Figure 4(a) and a single hexagonal crystal is presented in Figure 4(b). The particle morphology for this catalyst is different from the other samples described above. The particles, although hexagonal in shape, consist of imperfections such as holes and dislocations. One such dislocation emanating from the boundary of the crystal can be seen in Figure 4(b). Several electron microdiffraction patterns revealed the structure to be FeS_2 , FeS and Fe_7S_8 .

The primary question plaguing the scientific community working in the area of direct coal liquefaction is the state of iron. Whether the iron oxide undergoes a phase transition directly to Fe_xS_y phases or it transforms to metallic iron first and then goes to form Fe_xS_y is the question to be addressed. While the major crystalline phase after sulfidation at 385°C for 15 minutes or more remains Fe_7S_8 , evidence was presented to show the existence of minor amounts of other Fe_xS_y phases. No evidence was found for the existence of metallic iron in the sulfided iron catalysts nor in the sulfided ferric naphthanate catalysts. It therefore appears that 15 minutes of sulfidation produces large iron sulfide crystals.

ACKNOWLEDGMENT

This work was supported by the DOE contract #DE-AC22-90PC90049 and the Commonwealth of Kentucky.

REFERENCES

1. F. Bergius, "Chemical Reactions Under High Pressure", Nobel Lecture, May 21, 1932.
2. A. N. Stranges, *Fuel Proc. Tech.*, **16**, 205 (1987).
3. W. R. K. Wu and H. H. Storch, "Hydrogenation of Coal and Tar", Bulletin 633, Bureau of Mines, U.S. Department of the Interior, Washington, DC, 1968.
4. E. E. Dovath, *Fuel Proc. Tech.*, **1**, 3 (1977).
5. A. Eamsiri, W. R. Jackson, K. C. Pratt, V. Chreston and M. Marshall, *Fuel*, **71**, 449 (1992).
6. J. M. Lee, C. E. Cantrell, S. V. Gollakota, O. L. Davies, M. M. Corser and P. Vimalchand, *ACS Div. Fuel Chem. Preprints*, **36**, 1915 (1991).

Table 1
Crystalline Phases in Fe-S System

Formula	Crystal Structure	Lattice Parameters Å		
		a	b	c
Fe ₇ S ₈	HCP	a = 6.867	c = 17.062	
FeS	HCP	a = 5.967	c = 11.735	
Fe ₃ S ₄	HCP	a = 3.47	c = 34.5	
Fe _{1-x} S	HCP	a = 6.88	c = 22.90	
FeS ₂	Cubic	a = 5.417		
FeS	Cubic	a = 5.423		
Fe ₇ S ₈	Monoclinic	a = 11.902	b = 6.859	c = 22.787
β-Fe _{1-x} S	HCP	a = 6.894	c = 40.15	
Fe ₉ S ₈	Tetragonal	a = 3.679	c = 5.047	
FeS ₂	Orthorhombic	a = 4.436	b = 5.414	c = 3.381
Fe ₃ S ₄	Cubic	a = 9.876		
FeS	Tetragonal	a = 3.676	c = 5.032	

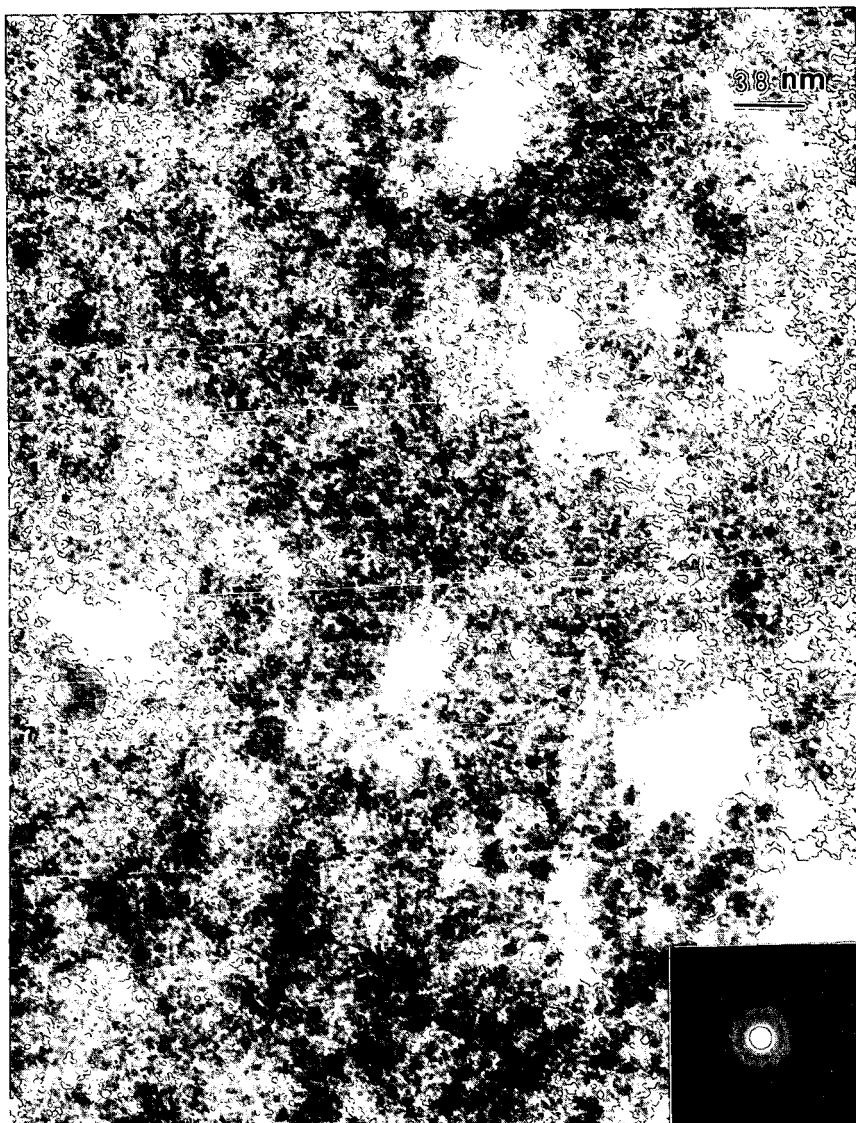


Figure 1. Transmission electron micrograph from the as-received Fe₂O₃ catalyst (inset). Microdiffraction pattern showing diffuse rings.

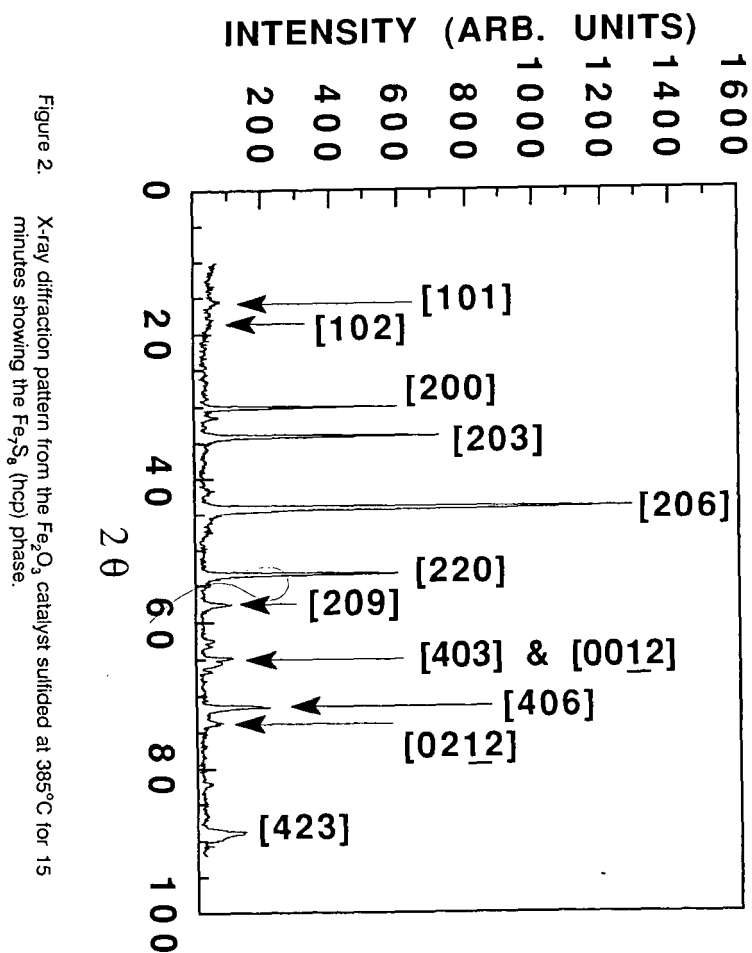


Figure 2. X-ray diffraction pattern from the Fe_7S_8 catalyst sulfided at 385°C for 15 minutes showing the Fe_7S_8 (hcp) phase.



Figure 3. Transmission electron micrograph from the as-received Fe₂O₃ catalyst after sulfiding at 385°C for 15 minutes showing large hexagonal crystals.

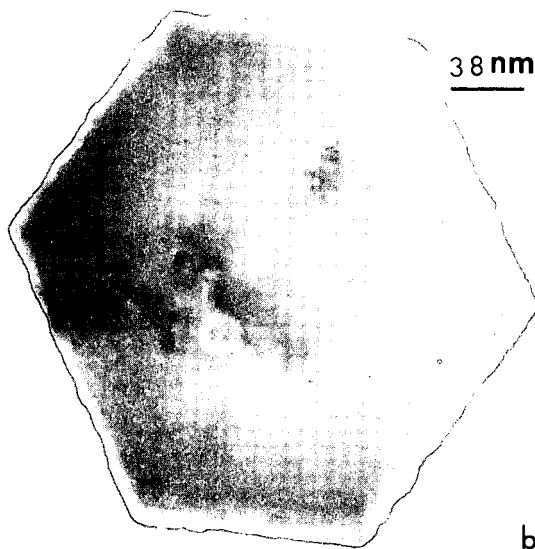
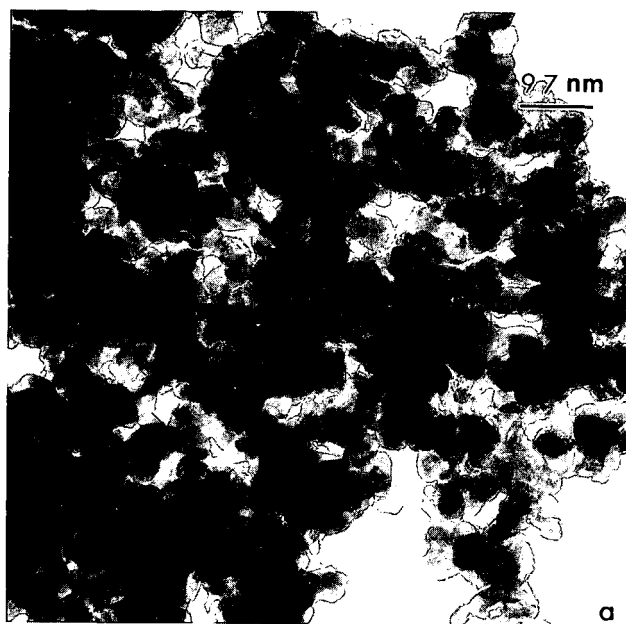


Figure 4. (a) A naphthalene electron micrograph obtained from ferric naphthanate after sulfidation at 385°C for 60 minutes. (b) A large single hexagonal crystal from the above sample.1